

THE FLORIDA STATE UNIVERSITY

COLLEGE OF ARTS AND SCIENCES

NEXT-TO-LEADING-ORDER CORRECTIONS TO WEAK BOSON
PRODUCTION WITH A MASSIVE QUARK JET PAIR AT HADRON
COLLIDERS

By

FERNANDO FEBRES CORDERO

A Dissertation submitted to the
Department of Physics
in partial fulfillment of the
requirements for the degree of
Doctor of Philosophy

Degree Awarded:
Fall Semester, 2007

a Kiko y Tefina...

TABLE OF CONTENTS

List of Tables	v
List of Figures	vi
Abstract	x
1. INTRODUCTION	1
2. NLO Calculation for $W/Z\ b\bar{b}$ Production at Hadron Colliders	8
2.1 Factorization Theorem for Hadronic Cross Sections	9
2.2 Hadronic Cross Section for $W/Z\ b\bar{b}$ Production: General Structure at NLO	10
2.2.1 Renormalization Scale Dependence of the NLO Cross Section	11
2.2.2 Calculating the Virtual Cross Section $\hat{\sigma}^{\text{virt}}$	12
2.2.3 Calculating the Real Cross Section $\hat{\sigma}^{\text{real}}$	16
2.3 NLO QCD Corrections to $Wb\bar{b}$ Production at Hadron Colliders	19
2.3.1 Virtual Corrections to $q\bar{q}' \rightarrow Wb\bar{b}$	20
2.3.2 Real Corrections to $Wb\bar{b}$ Production	26
2.3.3 Total Cross Section for $p\bar{p}(pp) \rightarrow Wb\bar{b}$	31
2.4 NLO QCD Corrections to $Zb\bar{b}$ Production at Hadron Colliders	36
2.4.1 Tree Level Cross Section for $Zb\bar{b}$ Hadronic Production	37
2.4.2 Virtual Corrections to $q\bar{q} \rightarrow Zb\bar{b}$	39
2.4.3 Virtual Corrections to $g\bar{g} \rightarrow Zb\bar{b}$	44
2.4.4 Real Corrections to $Zb\bar{b}$ Production	53
2.4.5 Total Cross Section of $p\bar{p}(pp) \rightarrow Zb\bar{b}$	60
3. Numerical Results	66
3.1 The Setup	66
3.2 $Wb\bar{b}$ Production at the Tevatron	68
3.3 $Zb\bar{b}$ Production at the Tevatron	75
4. CONCLUSION	84
4.1 Outlook	84
APPENDICES	86
A. Standard Model of Particle Physics	86

B. Tree Level Amplitudes for $W/Z\ b\bar{b}$ Production	93
C. Scalar Integrals for $W/Z\ b\bar{b}$ Production	96
D. Reducing Tensor Feynman Integrals	108
E. Using Quadruple Unitarity Cuts to Check Coefficients of Scalar Box Integrals	115
F. Phase Space Integrals for the Emission of a Soft Gluon in the two Cutoff PSS Method	118
REFERENCES	121

LIST OF TABLES

2.1	Diagram content of color amplitudes A_1^{ab} and A_1^{nab} whose color factor, when interfered with \mathcal{A}_0^{ab} or \mathcal{A}_0^{nab} respectively, is C_1	48
2.2	Diagram of content color amplitudes A_2^{ab} and A_2^{nab} whose color factor, when interfered with \mathcal{A}_0^{ab} or \mathcal{A}_0^{nab} respectively, is C_2	49
2.3	Diagram content of color amplitude A_3^{ab} whose color factor, when interfered with \mathcal{A}_0^{ab} or \mathcal{A}_0^{nab} respectively, is C_3	49
2.4	Diagram content of color amplitude A_4^{nab} whose color factor, when interfered with \mathcal{A}_0^{ab} or \mathcal{A}_0^{nab} respectively, is NC_2	49
2.5	Diagram content of color amplitude A_5^{ab} whose color factor, when interfered with \mathcal{A}_0^{ab} or \mathcal{A}_0^{nab} respectively, is $(N - 2/N)C_2$	50
3.1	LO and NLO total $Wb\bar{b}$ cross sections at the Tevatron for massive and massless bottom quarks, using $\mu_r = \mu_f = M_W + 2m_b$. The numbers in square brackets are the ratios of the NLO and LO cross sections, the so called K -factors. Statistical errors of the MC integration amount to about 0.1%.	67
3.2	LO and NLO total $Zb\bar{b}$ cross sections at the Tevatron for massive and massless bottom quarks, using $\mu_r = \mu_f = M_Z + 2m_b$. The numbers in square brackets are the ratios of the NLO and LO cross sections, the so called K -factors. Statistical errors of the MC integration amount to about 0.1%.	77

LIST OF FIGURES

1.1	Example of processes to which $Vb\bar{b}$ ($V = W$ or Z) is a main background. . .	4
2.1	Quadruple cut check of the calculation of a box diagram involving a top-quark loop.	15
2.2	Tree level Feynman diagrams for $q\bar{q}' \rightarrow Wb\bar{b}$	18
2.3	Gluon ($S_1^{(1,2)}$) and quark ($S_2^{(1,2)}$) $\mathcal{O}(\alpha_s)$ self-energy corrections contributing to the $q\bar{q}' \rightarrow Wb\bar{b}$ subprocess at NLO. The shaded blobs denote standard one-loop QCD corrections to the gluon and quark propagators, respectively. .	20
2.4	$\mathcal{O}(\alpha_s)$ vertex corrections contributing to the subprocess $q\bar{q}' \rightarrow Wb\bar{b}$ at NLO. The shaded blobs denote standard one-loop QCD corrections to the $q\bar{q}g$, $b\bar{b}g$ and $q\bar{q}'W$ vertices, respectively.	21
2.5	$\mathcal{O}(\alpha_s)$ box diagram corrections contributing to the $q\bar{q}' \rightarrow Wb\bar{b}$ process at NLO. The term <i>Crossed</i> refers to the box diagrams, $B_{3c}^{(1,2)}$ obtained from the $B_3^{(1,2)}$ boxes by flipping the b -quark fermion line.	22
2.6	$\mathcal{O}(\alpha_s)$ pentagon diagram corrections contributing to the $q\bar{q}' \rightarrow Wb\bar{b}$ process at NLO.	22
2.7	$\mathcal{O}(\alpha_s)$ real corrections: examples of initial and final real gluon emission and $q(\bar{q})g$ initiated subprocess.	26
2.8	Dependence of the total $Wb\bar{b}$ NLO QCD cross section on the δ_s PSS parameter.	34
2.9	Dependence of the total $Wb\bar{b}$ NLO QCD cross section on the δ_c PSS parameter.	35
2.10	Tree level Feynman diagrams for $q\bar{q} \rightarrow Zb\bar{b}$, with Z emitted from final fermion line.	36
2.11	Tree level Feynman diagrams for $gg \rightarrow Zb\bar{b}$. The circled crosses correspond to all possible insertions of the Z boson, each one representing a different diagram.	36

2.12	Gluon ($S_{1,f}^{(1,2)}$) and b -quark ($S_{2,f}^{(1,2)}$) $\mathcal{O}(\alpha_s)$ self energy corrections contributing to the $q\bar{q} \rightarrow Zb\bar{b}$ subprocess at NLO, when the Z boson is emitted from the final fermion line. The shaded blobs denote standard one-loop QCD corrections to the gluon and quark propagators respectively.	40
2.13	$\mathcal{O}(\alpha_s)$ vertex corrections contributing to the $q\bar{q} \rightarrow Zb\bar{b}$ subprocess at NLO when the Z boson is emitted from the final fermion line or from a closed fermion line. The shaded blobs denote standard one-loop QCD corrections to the $q\bar{q}g$ ($V_{1,f}^{(1,2)}$), $b\bar{b}g$ ($V_{2,f}^{(1,2)}$) and $q\bar{q}Z$ ($V_{3,f}^{(1,2)}$) vertices respectively. $V_{4,f}^{(1,2)}$ are b - and t -fermion loop vertices which are UV and IR finite (contributions of quarks from first and second family vanish).	41
2.14	$\mathcal{O}(\alpha_s)$ box diagram corrections contributing to the $q\bar{q} \rightarrow Zb\bar{b}$ subprocess at NLO, when the Z boson emitted from the final fermion lines (b or \bar{b}).	42
2.15	$\mathcal{O}(\alpha_s)$ pentagon diagram corrections contributing to the $q\bar{q} \rightarrow Zb\bar{b}$ subprocess at NLO, when the Z boson emitted from the final fermion lines (b or \bar{b}).	43
2.16	Gluon ($S_{1,s}^{(1,2)}$) and quark ($S_{1,s}^{(1,2)}$, $S_{2,s}^{(1,2)}$, $S_{3,(t,u)}^{(1,2)}$, and $S_{4,(t,u)}^{(1,2,3,4)}$) $\mathcal{O}(\alpha_s)$ self energy corrections contributing to the $gg \rightarrow Zb\bar{b}$ subprocess at NLO. The circled crosses correspond to all possible insertions of the Z boson, each one representing a different diagram.	45
2.17	$\mathcal{O}(\alpha_s)$ vertex corrections contributing to the $gg \rightarrow Zb\bar{b}$ subprocess at NLO. The shaded blobs denote standard one-loop QCD corrections to the ggg ($V_{1,s}^{(1,2)}$), $b\bar{b}g$ ($V_{2,s}^{(1,2)}$, $V_{7,(t,u)}^{(1,2,3)}$, and $V_{8,(t,u)}^{(1,2,3)}$) and $b\bar{b}Z$ ($V_{3,s}^{(1,2)}$ and $V_{9,(t,u)}^{(1,2,3)}$) vertices. The circled crosses correspond to all possible insertions of the Z boson, each one representing a different diagram.	46
2.18	$\mathcal{O}(\alpha_s)$ box diagram corrections contributing to the $gg \rightarrow Zb\bar{b}$ subprocess at NLO. The circled crosses correspond to all possible insertions of the Z boson, each one representing a different diagram.	47
2.19	$\mathcal{O}(\alpha_s)$ pentagon diagram corrections contributing to the $gg \rightarrow Zb\bar{b}$ subprocess at NLO. The circled crosses correspond to all possible insertions of the Z boson, each one representing a different diagram.	48
2.20	Examples of $\mathcal{O}(\alpha_s)$ real corrections to $q\bar{q} \rightarrow Zb\bar{b}$ production, with Z emitted from the final fermion line.	54
2.21	Examples of $\mathcal{O}(\alpha_s)$ real corrections to $Zb\bar{b}$ production. The circled crosses denote all possible insertions of a Z weak boson, each insertion corresponding to a different diagram.	54
2.22	Dependence of the total $Zb\bar{b}$ NLO QCD cross section on the δ_s PSS parameter.	64
2.23	Dependence of the total $Zb\bar{b}$ NLO QCD cross section on the δ_c PSS parameter.	65

3.1	Dependence of the LO (black solid band), NLO <i>inclusive</i> (blue dashed band), and NLO <i>exclusive</i> (red dotted band) $Wb\bar{b}$ total cross sections on the renormalization/factorization scales, including full bottom-quark mass effects. The bands are obtained by independently varying both μ_r and μ_f between $\mu_0/2$ and $4\mu_0$ (with $\mu_0 = m_b + M_W/2$).	68
3.2	Dependence of the LO and NLO <i>inclusive</i> and <i>exclusive</i> $p\bar{p} \rightarrow Wb\bar{b}$ total cross section on the renormalization/factorization scale, when $\mu_r = \mu_f = \mu$. The left hand side plot compares both LO and NLO total cross sections for the case in which the bottom quark is treated as massless (MCFM) or massive (our calculation). The right hand side plot shows separately, for the massive case only, the scale dependence of the $q\bar{q}'$ and $qg + \bar{q}g$ contributions, as well as their sum.	69
3.3	Dependence on the renormalization/factorization scale of the rescaled difference between our NLO calculation (with $m_b \neq 0$) of the total $Wb\bar{b}$ cross section and the corresponding result computed using MCFM (with $m_b = 0$) for the <i>inclusive</i> and <i>exclusive</i> cases (with $\mu_r = \mu_f = \mu_0$) respectively. The error bars indicate the statistical uncertainty of the Monte Carlo integration.	70
3.4	The distribution $d\sigma(p\bar{p} \rightarrow Wb\bar{b})/dm_{b\bar{b}}$ in LO and NLO QCD. The right hand side plot shows the ratio of the LO and NLO distributions.	72
3.5	The <i>inclusive</i> and <i>exclusive</i> distributions $d\sigma(p\bar{p} \rightarrow Wb\bar{b})/dm_{b\bar{b}}$ derived from our calculation (with $m_b \neq 0$) and from MCFM (with $m_b = 0$). The right hand side plot shows the ratio of the two distributions, $d\sigma(m_b \neq 0)/d\sigma(m_b = 0)$	73
3.6	The LO distribution $d\sigma(p\bar{p} \rightarrow Wb\bar{b})/dm_{b\bar{b}}$ derived from our calculation (with $m_b \neq 0$) and from MCFM (with $m_b = 0$). The right hand side plot shows the ratio of the two distributions, $d\sigma(m_b \neq 0)/d\sigma(m_b = 0)$	74
3.7	The $m_{b\bar{b}}$ distribution of the rescaled difference between our NLO calculation (with $m_b \neq 0$) and MCFM (with $m_b = 0$) for the <i>inclusive</i> (upper plot) and <i>exclusive</i> (lower plot) $p\bar{p} \rightarrow Wb\bar{b}$ production.	74
3.8	Dependence of the LO (black solid band), NLO <i>inclusive</i> (blue dashed band), and NLO <i>exclusive</i> (red dotted band) $Zb\bar{b}$ total cross sections on the renormalization/factorization scales, including full bottom-quark mass effects. The bands are obtained by independently varying both μ_r and μ_f between $\mu_0/2$ and $4\mu_0$ (with $\mu_0 = m_b + M_Z/2$).	76
3.9	Dependence of the LO and NLO <i>inclusive</i> and <i>exclusive</i> $p\bar{p} \rightarrow Zb\bar{b}$ total cross section on the renormalization/factorization scale, when $\mu_r = \mu_f = \mu$. The LHS plots compare both LO and NLO total cross sections for the case in which the bottom quark is treated as massless (MCFM) or massive (our calculation). The RHS plots show separately, for the massive case only, the scale dependence of the $q\bar{q}$, gg and $qg + \bar{q}g$ contributions, as well as their sum.	78

3.10	Dependence on the renormalization/factorization scale of the rescaled difference between our NLO calculation (with $m_b \neq 0$) of the total $Zb\bar{b}$ cross section and the corresponding result computed using MCFM (with $m_b = 0$) for the <i>inclusive</i> and <i>exclusive</i> cases (with $\mu_r = \mu_f = \mu_0$) respectively. The error bars indicate the statistical uncertainty of the Monte Carlo integration.	79
3.11	The distribution $d\sigma(p\bar{p} \rightarrow Zb\bar{b})/dm_{b\bar{b}}$ in LO and NLO QCD. The right hand side plot shows the ratio of the LO and NLO distributions.	80
3.12	The <i>inclusive</i> and <i>exclusive</i> distributions $d\sigma(p\bar{p} \rightarrow Zb\bar{b})/dm_{b\bar{b}}$ derived from our calculation (with $m_b \neq 0$) and from MCFM (with $m_b = 0$). The right hand side plot shows the ratio of the two distributions, $d\sigma(m_b \neq 0)/d\sigma(m_b = 0)$	81
3.13	The LO distribution $d\sigma(p\bar{p} \rightarrow Zb\bar{b})/dm_{b\bar{b}}$ derived from our calculation (with $m_b \neq 0$) and from MCFM (with $m_b = 0$). The right hand side plot shows the ratio of the two distributions, $d\sigma(m_b \neq 0)/d\sigma(m_b = 0)$	82
3.14	The $m_{b\bar{b}}$ distribution of the rescaled difference between our NLO calculation (with $m_b \neq 0$) and MCFM (with $m_b = 0$) for the <i>inclusive</i> (upper plot) and <i>exclusive</i> (lower plot) $p\bar{p} \rightarrow Zb\bar{b}$ production.	83
C.1	Topology of one-loop Feynman integrals. We denote by t the loop momentum, by $\{q_i\}$ the set of incoming momenta and by $\{m_i\}$ the set of masses in the internal propagators.	96
D.1	Topology of one-loop Feynman Integrals. We denote by t the loop momentum, $\{q_i\}$ the set of incoming momenta and $\{m_i\}$ the set of masses in the internal propagators.	108
E.1	Topology of the example presented. It corresponds to two Feynman Diagrams given by the two possible orientations of the fermion line. The loop in the fermion is a top quark (with mass m_t).	116

ABSTRACT

We present the calculation of Next-to-Leading-Order Quantum Chromo Dynamics corrections for the production of a W or Z weak boson associated with a bottom anti-bottom quark pair at hadron colliders ($p\bar{p}, pp \rightarrow W/Z b\bar{b}$), including the effects of a non-zero bottom-quark mass. We find a considerable reduction of the renormalization and factorization scale dependence of our results with respect to Leading-Order calculations. In particular, we study the impact of the corrections on the total cross section and invariant mass distributions of the bottom anti-bottom quark pair at the Fermilab Tevatron $p\bar{p}$ collider. We perform a detailed comparison with a calculation that considers massless bottom quarks and find significant deviations in regions of phase space with small invariant mass of the bottom anti-bottom quark pair.

Our results will be relevant to ongoing and future searches at hadron colliders, as the $W/Z b\bar{b}$ production mode is the main background to important signals, such as light Standard Model Higgs boson production or single top-quark production.

CHAPTER 1

INTRODUCTION

The *Standard Model* (SM) of particle physics is today the best mathematical framework to understand the dynamics of all elementary particles that have been observed in high-energy collisions. This quantum field theory has been amazingly successful in describing and predicting to an unprecedented level of precision observations made in all high energy particle accelerator experiments.

Extraordinary phenomenological efforts in the past few decades, both from the experimental side producing impressive amounts of precision data, and from the theoretical side producing powerful techniques to handle challenging calculations, show the SM to be a robust model of fundamental interactions. So much so that, if we consider only collider data, the SM fits all observables, with only a few showing statistical deviations of up to $2 - 3 \sigma$ ¹.

At the same time, however, we know that the SM is an incomplete theory, as it does not include gravitational interactions. Moreover, from cosmological data we know that the SM falls short of explaining the origin of Dark Matter and Dark Energy, and does not predict as large an asymmetry between matter and antimatter as observed in the universe. Another puzzle is the mechanism that breaks the electroweak $SU(2)_W \times U(1)_Y$ symmetry. In the SM this breaking occurs as a doublet of complex scalar fields acquires a non-zero vacuum expectation value (VEV), thus producing what is called spontaneous symmetry breaking. This mechanism gives rise to effective mass terms for weak force carriers, quarks, and leptons and leaves a physical scalar particle, the Higgs particle, which has so far eluded observation². Among others, these are the reasons why nowadays there are many models that posit physics beyond the SM, which often embed different mechanisms of electroweak symmetry breaking

¹See for example the LEPWWG website at <http://lepewwg.web.cern.ch/LEPEWWG> and the reviews on SM related topics of the PDG [1]

²A more detailed description of this mechanism and a brief introduction to the SM is given in Appendix A

(EWSB).

The current and future hadron colliders, i.e. the Tevatron, a $p\bar{p}$ collider currently taking data at 1.96 TeV center of mass energy at Fermilab, near Chicago, and the Large Hadron Collider (LHC), a pp collider with 14 TeV center of mass energy that will start in 2008 at CERN, Geneva, have as a main goal the elucidation of the mechanism of EWSB as well as the exploration of the energy spectrum beyond the weak scale, where physics beyond the SM (BSM) is expected. The processes studied in this thesis, i.e. the hadronic production of a weak force carrier with a bottom-antibottom quark pair ($p\bar{p}, pp \rightarrow W/Z b\bar{b}$), play a crucial role in some of the current studies of EWSB and BSM. They represent an important QCD background in the searches for a light SM-like Higgs boson (H) and for single top-quark production.

The Necessity of Higher Order Corrections in perturbative QCD

In order to improve our understanding of the behavior of fundamental particles at high energies, theorists are faced with the necessity to calculate signal and, often, background processes with high precision. This last task becomes essential when the signal to background ratio is small and the background cannot be easily extracted from data. Typically, this is the case for processes that involve a large number of kinematic variables and that have broad kinematic distributions, as often arises when final states consist of several jets and/or missing energy.

At hadron colliders, QCD effects are particularly important and must be taken into account to obtain precise theoretical predictions. Since at high energies QCD is a perturbative quantum field theory (pQFT), QCD effects at collider energies can be calculated order by order in the strong coupling constant. The lowest order at which a process can be calculated, the Leading Order (LO), typically has a large theoretical uncertainty associated with it. This is mainly due to the opening of new production channels at higher orders of the perturbative series and to the large dependence of LO calculations on renormalization and factorization scales, in certain renormalization prescriptions. Adding the first order QCD corrections, that is, Next-to-Leading-Order (NLO) corrections, usually improves the stability of theoretical predictions considerably and tests the behavior of the perturbative expansion. Occasionally, when the NLO corrections are unusually large, the reliability of the predictions can be improved by computing Next-to-Next-to-Leading Order (NNLO) QCD corrections.

In all known examples this is enough to reduce the theoretical uncertainty to an acceptable level.

Today the standard for hard scattering cross section calculations is NLO, and since the early nineties a wide set of processes have been studied at this level in perturbation theory (for an up-to-date review of some of them and a look at state of the art techniques that have been developed see Ref. [2]).

However, while several programs exist that allow automated calculations of partonic differential cross sections at LO (e.g. Madgraph [3, 4, 5], CompHEP [6], AMEGIC++ [7]), there are as yet no algorithms able to deal with all processes at NLO in a completely automatic way. There is a bottleneck that occurs with the calculation of virtual one-loop diagrams with many external partons or “legs”. Basically, following a traditional Feynman diagram approach, the complexity of the analytic expressions grows exponentially with the number of legs and the number of massive internal/external particles. This is mainly due to the number of Feynman diagrams, the increased number of kinematic variables and the increased complexity of the tensor integrals appearing in each Feynman diagram.

It has been observed that certain amplitudes (for example the so called Maximally Helicity Violating (MHV) amplitudes) show a surprising analytic simplicity, hidden by the cumbersome intermediate steps of standard calculations. A good part of the progress in the field is due to a better understanding of such amplitudes (the literature on MHV amplitudes is now extensive, but for a brief review see Refs. [8, 9, 10, 11]). Many new techniques have appeared that exploit general properties of gauge field theories such as gauge invariance, factorization, unitarity and the existence of representations in terms of Feynman integrals [10, 12, 2, 13]. An example of their success is the recently completed one-loop calculation of the set of all helicity amplitudes with six external gluons [14, 15, 16, 17, 18, 19, 20, 21, 22]. We have used generalized unitarity, specifically quadruple cuts [23], as a means to make non-trivial cross checks of coefficients of scalar box integrals of sets of Feynman diagrams. This represents the first direct application of this techniques to a phenomenologically relevant computation including massive internal and external particles.

In this dissertation we present the calculation of NLO QCD corrections to the production of a W or Z weak gauge boson in association with a bottom-antibottom quark pair at hadron colliders ($p\bar{p}, pp \rightarrow W/Z b\bar{b}$), including full bottom-quark mass effects. The main difficulty we encounter is the calculation of virtual one-loop diagrams with up to five legs that include the

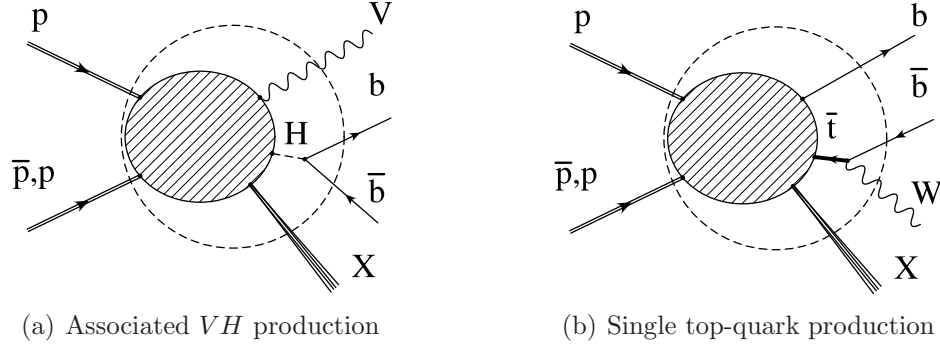


Figure 1.1: Example of processes to which $Vb\bar{b}$ ($V = W$ or Z) is a main background.

full effects of massive bottom-quarks. The latter increases the complexity of the calculation due to the addition of an extra kinematic invariant. We follow a traditional Feynman diagram approach to produce fully analytical expressions for one-loop amplitudes, which will allow non-trivial cross checks with on-shell recursion techniques, beyond the box coefficients checks presented in this work.

$W/Z\ b\bar{b}$ Production at Hadron Colliders

The associated production of a W/Z boson with a $b\bar{b}$ pair is by itself an interesting signature for hadron colliders, since it can be precisely studied experimentally. Sophisticated techniques exist to detect weak bosons at hadron colliders, especially when they decay into leptons. Even in the messy environment of a high energy hadron collider, Drell-Yan processes (W, Z or γ production) are often used as tools for detector calibration and luminosity measurements. Furthermore, b -quarks are very useful tools too, as the mesons in which they fragment have a life-time long enough to allow tagging. Nowadays the efficiency of this tagging is close to 50% for a large range of transverse momenta of the b -jets. These sorts of studies, in the context of $W/Z\ b\bar{b}$ production, allow non-trivial cross checks of experimental techniques, and provide further constraints on the SM, as long as the theoretical uncertainty on such signals is equal or smaller than the experimental precision.

The interest in $W/Z\ b\bar{b}$ production at hadron colliders is increased by the characteristic features of a light SM Higgs boson H . One of the strengths of the SM Higgs sector is that it is highly predictive as only one of its parameters is not yet constrained by direct observation,

the Higgs boson mass m_H . Electroweak precision measurements hint at the existence of a light Higgs boson, with mass below 144 GeV at 95% confidence level ³. For such a Higgs boson one of the main production channels is the W/Z H associated production, with the Higgs boson decaying most of the time into a $b\bar{b}$ pair, as depicted in Figure 1.1(a), for which W/Z $b\bar{b}$ represents a major background.

The production of a Higgs boson in association with an electroweak gauge boson, $p\bar{p} \rightarrow HV$ ($V=Z, W$) with $H \rightarrow b\bar{b}$, is indeed the most sensitive production channel of a SM Higgs boson at the Tevatron for a Higgs boson lighter than about 140 GeV [24, 25, 26, 27, 28]. The Tevatron with an integrated luminosity of 6 fb^{-1} will be able to exclude a Higgs boson with $115 \text{ GeV} < M_H < 180 \text{ GeV}$ at 95% confidence level [29], and will provide crucial guidance for the search strategy at the LHC.

On the other hand, due to the huge hadronic activity, the experiments at the CERN LHC will probably first look for a light SM-like Higgs boson in the $H \rightarrow \gamma\gamma$ decay channel. In spite of the small branching ratio, $H \rightarrow \gamma\gamma$ produces a clear peak in the invariant mass distribution of the pair of photons. In order to fully identify a potential Higgs boson candidate, however, the LHC experiments will have to measure $H \rightarrow b\bar{b}$ and this will have to be done when the Higgs boson is produced via associated production, either W/ZH or $t\bar{t}H$.

Finally, $Wb\bar{b}$ is among the most relevant irreducible background processes for single-top quark production [30, 31, 32], as illustrated in Figure 1.1(b), both at the Tevatron and at the LHC. This is particularly relevant to the Tevatron, where, via single-top production, the Wbt vertex is being measured for the first time [33, 34].

The cross section for $p\bar{p} \rightarrow HV$ has been calculated including up to NNLO QCD corrections [35, 36, 37] and $O(\alpha)$ electroweak corrections [38], while single-top production has been calculated at NLO in QCD [39, 40, 41, 42, 43, 44, 45, 46, 47], and at one-loop of electroweak (SM and MSSM) corrections [48]. Thus, to fully exploit the Tevatron's and LHC's potentials to detect the SM Higgs boson and to impose limits on its mass, as well as to test the third generation quark coupling to the W boson, it is crucial that the dominant background processes are also precisely calculated.

In the present experimental analyses⁴, the effects of NLO QCD corrections on the total cross section and the dijet invariant mass distribution of the W/Z $b\bar{b}$ background process

³For an update see the LEPWWG website at <http://lepewwg.web.cern.ch/LEPEWWG>

⁴For updated results, see the CDF and D0 websites at <http://www-cdf.fnal.gov/physics/exotic/exotic.html> and <http://www-d0.fnal.gov/Run2Physics/WWW/results/higgs.htm>.

have been taken into account by using the MCFM package [49]. In MCFM, the NLO QCD predictions of both total and differential cross sections for the $p\bar{p}(p) \rightarrow W/Z\ b\bar{b}$ production processes have been calculated in the zero bottom-quark mass ($m_b = 0$) approximation [50, 51, 52], using the analytical results of [53, 54]. From a study of the Leading Order (LO) cross section, finite bottom-quark mass effects are expected to affect both the total and differential $W/Z\ b\bar{b}$ cross sections mostly in the region of small $b\bar{b}$ -pair invariant masses [52]. Given the variety of experimental analyses involved both in the search for HW/Z associated production and single-top production, it is important to assess precisely the impact of a finite bottom-quark mass over the entire kinematical reach of the process, including complete NLO QCD corrections.

Using the MCFM package [49], we compared our results with the corresponding results obtained in the $m_b = 0$ limit. Numerical results are presented for the total cross section and the invariant mass distribution of the $b\bar{b}$ jet pair ($m_{b\bar{b}}$), at the Tevatron $p\bar{p}$ collider, including kinematic cuts and a jet-finding algorithm. In particular, we apply the k_T jet algorithm and require two tagged b -jets in the final state.

We have found that the NLO QCD corrections reduce considerably the theoretical uncertainty in the total hadronic cross section for $W/Z\ b\bar{b}$ production. We have found that NLO corrections are significant. The shape of the $m_{b\bar{b}}$ invariant mass distribution is changed by the NLO QCD corrections; that is, the effect does not amount to a simple NLO/LO rescaling factor (K -factor). Finally, we have found that mass effects affect the total cross section by about 8% to 10% at NLO. The influence is greatest in the small $m_{b\bar{b}}$ invariant mass region.

...

This dissertation is organized as follows. In Chapter 2 we present all the details of the full NLO calculation, including a thorough description of the techniques used to obtain both virtual and real corrections, first for $Wb\bar{b}$ production and then for $Zb\bar{b}$ production. We have included in the Appendices A-F a few complementary reviews and several collections of technical details, omitted for brevity and aesthetic reasons from the body of this dissertation. In Chapter 3 we present the results of our calculation. We show the LO and NLO dependence on renormalization and factorization scales, we study the impact of the corrections on the total cross sections and invariant mass distributions of the bottom quark-antiquark pair. We

show the m_b effects by comparing to a calculation that considers massless bottom-quarks. In Chapter 4 we conclude with a summary of the main results and discuss future studies of the $W/Z\ b\bar{b}$ production mode, as well as the natural generalization of our calculation to other processes.

CHAPTER 2

NLO Calculation for $W/Z\ b\bar{b}$ Production at Hadron Colliders

In this Chapter we present the details of the NLO QCD calculation of $Wb\bar{b}$ and $Zb\bar{b}$ hadronic production including full b -quark mass effects.

The NLO QCD calculation of the $W/Z\ b\bar{b}$ production cross section for massless b quarks has been available in the literature for quite some time [50, 51, 52]. It was performed by using the analytic expression of the scattering amplitudes for a weak gauge boson to four (massless) partons [53, 54], and simulating b -quark mass effects by imposing the kinematic conditions:

$$(p_b + p_{\bar{b}})^2 > 4Q^2, \quad p_b^T > Q, \quad p_{\bar{b}}^T > Q, \quad (2.1)$$

where Q is a scale of the order of the b -quark mass, $p_{b(\bar{b})}$ is the momentum of the $b(\bar{b})$ quark and $p_{b(\bar{b})}^T$ represents the $b(\bar{b})$ -quark transverse momentum.

We have improved on the massless calculation by considering a fully massive b quark both at the level of the scattering amplitude and in the integration over the final state phase space. We keep the weak bosons as on-shell particles, though the extension to include their leptonic decays does not present in principle any special complications. The rest of this Chapter is organized as follows. In Section 2.1 we present the main theoretical framework that allows the calculation of hadronic cross sections. We introduce briefly the parton model and the QCD factorization theorems. In Section 2.2 we present the main characteristics of the cross sections for $W/Z\ b\bar{b}$ hadronic production. Sections 2.3 and 2.4 present the core of the calculation for $Wb\bar{b}$ and $Zb\bar{b}$ production at hadron colliders respectively. They are organized into subsections which discuss the LO and the NLO virtual and real corrections of the calculation. We show explicitly the cancellation of UV singularities, by renormalization, and of IR singularities, by matching virtual and real corrections and by consistently absorbing all long-distant physics

into the renormalized parton distribution functions (PDFs) (see Section 2.1).

Due to the complexity of this calculation, all results have been cross checked using at least two independent sets of codes. The analytic calculation of the scattering amplitudes has been implemented using, at different stages, FORM [55], TRACER [56], *Maple* and *Mathematica*. Final numerical results have been obtained with codes built in *C* and FORTRAN, and we have used the FF package [57] and Madgraph [3, 4, 5] to cross check pieces of our code. Some of the figures in this Chapter have been produced using AXODRAW [58], FeynDiagram [59] and Grace [60].

2.1 Factorization Theorem for Hadronic Cross Sections

The *parton model* of hadron structure [61, 62] paved the way to the full formulation of QCD, as it created a framework to connect data from high energy hadronic collisions with the *quark model* according to which quarks are the elementary constituents of hadrons. The parton model basically states that when hadrons interact via a high momentum transfer, they appear as built of point-like, quasi-free constituents, the *partons* which we now know as the quarks and gluons of QCD. To each parton i in a given hadron A is associated a parton density function (PDF), $\mathcal{F}_i^A(x)$, which describes the probability of finding parton i in hadron A with a fraction x of the total momentum of the hadron (for more details on the development of the model see for example Ref. [62, 63, 64]).

Despite its success, the parton model remained without a firm theoretical basis until the 80's when a series of QCD factorization theorems rigorously proved that most hadronic observables can be calculated in QCD by disentangling the non-perturbative properties of hadrons and the asymptotically free behavior of partons into well defined building blocks¹ (see for example Ref. [65, 68, 69]). As a result, a given observable $\mathcal{O}_A(Q)$ involving an initial hadronic state A and a momentum transfer Q considerably larger than Λ_{QCD} can be decomposed as:

$$\mathcal{O}_A(Q) = \sum_i f_A^i(Q, \mu_f) \otimes \mathcal{O}_i(Q, \mu_f) , \quad (2.2)$$

¹Based on general physics principles these theorems have been extended to a wide variety of processes, although full proofs only exist for a few processes [65]. Recently it has been shown [66, 67] that certain processes in colliders with unpolarized beams can break factorization at Next-to-Next-to-Next-to-Leading Order (NNNLO), an order still far from being tested.

where the sum is over a full set of partons i , μ_f is the so called factorization scale and the operation \otimes is an integral convolution. The $\mathcal{O}_i(Q, \mu_f)$ are point-like operators that describe the short-distance parton interactions which, as the momentum transfer is large, can be calculated perturbatively. The functions $f_A^i(Q, \mu_f)$ contain all the long-distance physics information related to hadron A . They are universal (i.e. process independent) non-perturbative objects whose Q -evolution can be determined perturbatively starting from a data-driven non-perturbative core.

The factorization scale μ_f is introduced to define a boundary between the perturbative and non-perturbative regimes. Although the LHS of Eq. (2.2) is in principle independent of μ_f , this is only true when considering all orders in the perturbative expansion. In practice, the perturbative series is always truncated and that leaves a spurious μ_f dependence in the calculated $\mathcal{O}_A(Q)$, which can be argued that asymptotically is of the order of the next order in the perturbative expansion. That is why when a fixed-order calculation is performed in perturbative QCD, the spurious dependence on the factorization scale (and similarly on the renormalization scale) is used as an indicator of the theoretical uncertainty associated with the calculation. For the reader interested in expanding on this subject, see for example the review papers in Ref. [68, 69, 70] and references therein.

2.2 Hadronic Cross Section for W/Z $b\bar{b}$ Production: General Structure at NLO

Enforcing the factorization properties of QCD cross sections, we can write the NLO QCD total or differential cross section for $p\bar{p}(pp) \rightarrow W/Z$ $b\bar{b}$ as:

$$\sigma(p\bar{p}(pp) \rightarrow W/Z \ b\bar{b}) = \sum_{ij} \frac{1}{1 + \delta_{ij}} \int dx_1 dx_2 \left[\mathcal{F}_i^p(x_1, \mu) \mathcal{F}_j^{\bar{p}(p)}(x_2, \mu) \hat{\sigma}_{ij}(x_1, x_2, \mu) + (x_1 \leftrightarrow x_2) \right], \quad (2.3)$$

where $\mathcal{F}_i^{p(\bar{p})}$ are the PDFs for parton i in a proton (antiproton). The sum runs over all relevant subprocesses contributing to the hadronic differential cross section initiated by partons i and j . The partonic cross section for the subprocess $ij \rightarrow W/Z$ $b\bar{b}$ is denoted by $\hat{\sigma}_{ij}$. The hadronic process $p\bar{p}(pp) \rightarrow W/Z$ $b\bar{b}$ receives contributions from the initial state $q\bar{q}'$ at LO (where q and \bar{q}' represent quarks of up-type and down-type respectively), and from $q\bar{q}'$, qg and $\bar{q}g$ at NLO, while $p\bar{p}(pp) \rightarrow Z$ $b\bar{b}$ receives contributions from $q\bar{q}$ and gg at LO and from $q\bar{q}$, gg , qg and $\bar{q}g$

at NLO. The scale μ corresponds to both the factorization scale (μ_f) and renormalization scale (μ_r). The factor in front of the integral is a symmetry factor that accounts for the presence of identical particles in the initial state of a given subprocess (δ_{ij} is the Kronecker delta). The partonic center-of-mass energy squared, s , is given in terms of the hadronic center of mass energy square, s_H , by $s = x_1 x_2 s_H$.

We then write the NLO partonic cross section as follows:

$$\begin{aligned}\hat{\sigma}_{ij}^{\text{NLO}}(x_1, x_2, \mu) &= \alpha_s^2(\mu) \left\{ f_{ij}^{\text{LO}}(x_1, x_2) + \frac{\alpha_s(\mu)}{4\pi} f_{ij}^{\text{NLO}}(x_1, x_2, \mu) \right\} \\ &\equiv \hat{\sigma}_{ij}^{\text{LO}}(x_1, x_2, \mu) + \delta\hat{\sigma}_{ij}^{\text{NLO}}(x_1, x_2, \mu),\end{aligned}\tag{2.4}$$

where $\alpha_s(\mu)$ is the strong coupling constant evaluated at the scale μ , $\hat{\sigma}_{ij}^{\text{LO}}(x_1, x_2, \mu)$ is the $\mathcal{O}(\alpha_s^2)$ LO partonic cross section and $\delta\hat{\sigma}_{ij}^{\text{NLO}}(x_1, x_2, \mu)$ contains the $\mathcal{O}(\alpha_s)$ corrections to the partonic LO cross section. The $\delta\hat{\sigma}_{ij}^{\text{NLO}}(x_1, x_2, \mu)$ corrections can be decomposed in the following way:

$$\begin{aligned}\delta\hat{\sigma}_{ij}^{\text{NLO}} &= \int d(P S_3) \overline{\sum} |\mathcal{A}_{\text{virt}}(ij \rightarrow W/Z \, b\bar{b})|^2 + \int d(P S_4) \overline{\sum} |\mathcal{A}_{\text{real}}(ij \rightarrow W/Z \, b\bar{b} + k)|^2 \\ &\equiv \hat{\sigma}_{ij}^{\text{virt}} + \hat{\sigma}_{ij}^{\text{real}},\end{aligned}\tag{2.5}$$

where the term integrated over the phase space measure $d(P S_3)$ corresponds to the virtual one-loop corrections (three final-state particles), while the one integrated over the phase space measure $d(P S_4)$ corresponds to the real tree level corrections with one additional emitted parton (four final-state particles). The sum $\overline{\sum}$ indicates that the corresponding amplitudes squared, $|\mathcal{A}_{\text{virt(real)}}(ij \rightarrow W/Z \, b\bar{b}(+k))|^2$, have been averaged over the initial-state degrees of freedom and summed over the final-state ones. The final phase space integration have been performed using Monte Carlo techniques using the adaptive multi-dimensional integration routine VEGAS [71].

Intermediate stages of the calculation of $\delta\hat{\sigma}_{ij}^{\text{NLO}}$ contain both ultraviolet (UV) and infrared (IR) divergences, whose calculation will be discussed in detail in Sections 2.2.2, 2.2.3, 2.3 (for $Wb\bar{b}$ production) and 2.4 (for $Zb\bar{b}$ production).

2.2.1 Renormalization Scale Dependence of the NLO Cross Section

We observe that the scale dependence of the total cross section at NLO is dictated by renormalization group arguments. In order to assure the renormalization scale independence

of the total cross section at $\mathcal{O}(\alpha_s^3)$, $f_{ij}^{\text{NLO}}(x_1, x_2, \mu)$ has to be of the form:

$$f_{ij}^{\text{NLO}}(x_1, x_2, \mu) = f_{ij}^1(x_1, x_2) + \tilde{f}_{ij}^1(x_1, x_2) \ln \left(\frac{\mu^2}{s} \right), \quad (2.6)$$

where, taking into account that other sources of renormalization scale dependence in Eq. (2.4) are $\alpha_s(\mu)$ and the PDFs $\mathcal{F}_i^{p,\bar{p}}(x, \mu)$, we can prove that:

$$\begin{aligned} \tilde{f}_{ij}^1(x_1, x_2) = & 2 \left\{ 4\pi b_0 f_{ij}^{\text{LO}}(x_1, x_2) - \sum_k \left[\int_\rho^1 dz_1 P_{ik}(z_1) f_{kj}^{\text{LO}}(x_1 z_1, x_2) \right. \right. \\ & \left. \left. + \int_\rho^1 dz_2 P_{jk}(z_2) f_{ik}^{\text{LO}}(x_1, x_2 z_2) \right] \right\}, \end{aligned} \quad (2.7)$$

where $\rho = (2m_b + M_V)^2/s$ ($V = W, Z$), P_{ij} are the Altarelli-Parisi splitting functions as presented in Eqs. (2.43), (2.47), (2.88) and (2.92), and b_0 is determined by the one-loop renormalization group evolution of the strong coupling constant α_s :

$$\frac{d\alpha_s(\mu)}{d\ln(\mu^2)} = -b_0 \alpha_s^2 + \mathcal{O}(\alpha_s^3), \quad b_0 = \frac{1}{4\pi} \left(\frac{11}{3}N - \frac{2}{3}n_{lf} \right), \quad (2.8)$$

where $N = 3$ is the number of colors and $n_{lf} = 5$ the number of light flavors. To write Eq. (2.7) we have assumed that the b -quark mass does not run, given the mild dependence of the cross section on it. The origin of the rest of terms in Eq. (2.7) will become clear in Sections 2.3 and 2.4 where we describe in detail the calculation of virtual, real and total cross section corrections for both $Wb\bar{b}$ and $Zb\bar{b}$ production respectively.

2.2.2 Calculating the Virtual Cross Section $\hat{\sigma}^{\text{virt}}$

The $\mathcal{O}(\alpha_s)$ virtual corrections to the hadronic $W/Z b\bar{b}$ production tree level processes consist of self-energy, vertex, box and pentagon diagrams. The contributions to $\hat{\sigma}^{\text{virt}}$ in Eq. (2.5) can be written as:

$$\overline{\sum} |\mathcal{A}_{\text{virt}}(ij \rightarrow W/Z b\bar{b})|^2 = \sum_D \overline{\sum} \left(\mathcal{A}_0 \mathcal{A}_D^\dagger + \mathcal{A}_0^\dagger \mathcal{A}_D \right) = \sum_D \overline{\sum} 2\text{Re} \left(\mathcal{A}_0 \mathcal{A}_D^\dagger \right), \quad (2.9)$$

where \mathcal{A}_0 is the tree level amplitude and \mathcal{A}_D denotes the amplitude for the one-loop diagram D , with D running over all self-energy, vertex, box and pentagon diagrams corresponding to the ij -initiated subprocess.

The amplitude for each virtual diagram (\mathcal{A}_D) is calculated as a linear combination of Dirac structures with coefficients that depend on both tensor and scalar one-loop Feynman

integrals with up to five denominators. We solve the one-loop integrals in the coefficients either at the level of the amplitude or at the level of the amplitude squared (see Eq. (2.9)). These two independent approaches allow us to thoroughly cross check the calculation of each individual diagram. Indeed, the tensor structures present in the one-loop integrals of the amplitude are typically different from the ones present in the amplitude squared, as one can perform non-trivial reductions of the latter by canceling dot products of the integration momentum in the numerator with denominators in the Feynman integrals. In this way, the final analytical expression of a given diagram ends up being represented in terms of different building blocks. A possible incorrect relation between the building blocks would then naturally produce a discrepancy between the two approaches.

Tensor and scalar one-loop integrals are treated as follows. Using the Passarino-Veltman (PV) method [72, 73], the tensor integrals are expressed as a linear combination of tensor structures and coefficients, where the tensor structures depend on the external momenta and the metric tensor, while the coefficients depend on scalar integrals, kinematics invariants and the dimension of the integral (for a more detailed description of the technique see Appendix D). Numerical stability issues may arise at this level as a consequence of the proportionality of the tensor integral coefficients to powers of inverse Gram Determinants (GDs), specially when considering a full set of independent momenta $\{p_{a_i}\}$ ($i = 1, \dots, 4$) of the $ij \rightarrow W/Z b\bar{b}$ phase space, which is defined by $\text{GD} = \det(p_{a_i} \cdot p_{a_k})$. The problem becomes more serious for higher rank tensor integrals, since the higher the rank of the original tensor integral, the higher the inverse power of the GD that appears in the coefficients of its tensor decomposition.

To illustrate the problem, we parametrize the GD appearing in pentagon tensor integrals in terms of the $W/Z b\bar{b}$ phase space variables as

$$\text{GD} = -\frac{[s - (2m_b + M_V)^2]}{64} [M_V^4 + (s - \bar{s}_{b\bar{b}})^2 - 2M_V^2(s + \bar{s}_{b\bar{b}})] s \bar{s}_{b\bar{b}} \sin^2 \theta_{b\bar{b}} \sin^2 \phi_{b\bar{b}} \sin^2 \theta \quad , \quad (2.10)$$

where $s = x_1 x_2 s_H$ is the partonic center-of-mass energy squared, M_V is the mass of the weak vector boson ($V = W, Z$), and the $W/Z b\bar{b}$ phase space has been expressed in terms of a time-like invariant $\bar{s}_{b\bar{b}} = (p_b + p_{\bar{b}})^2$, polar angles $(\theta, \theta_{b\bar{b}})$ and azimuthal angles $(\phi, \phi_{b\bar{b}})$ in the center-of-mass frames of the incoming partons and of the $b\bar{b}$ pair, respectively. As can be seen in Eq. (2.10), the GD vanishes when the set of momenta become degenerate or co-planar,

for example at the boundaries of phase space. Near these regions of phase space it can become arbitrarily small, giving rise to spurious divergences which cause serious numerical difficulties, since large cancellations then appear between various parts of the calculation at the numerical level. The probability that the Monte Carlo integration hits a point close to these regions of phase space is not negligible and these points cannot just be discarded.

The numerical instabilities we just discussed can be considered as “spurious” or “unphysical” divergences, since it is well known that only two-particle invariants can give rise to a physical singularity. Indeed, these spurious divergences cancel when large sets of diagrams are combined [54], such as, for example, when one combines gauge invariant sets of color amplitudes (i.e. amplitudes with a common color factor). Explicit analytic cancellations have been found for example when using helicity amplitudes and the helicity product formalism (see for example Refs. [53, 54]), mainly because certain GD can be decomposed in terms of helicity products. As we have expressed our calculation in terms of kinematical invariants, the full cancellation only occurs between numerator and denominator at the numerical level, often between fairly large expressions. Nevertheless, when we consider gauge invariant sets of color amplitudes (as the ones presented in Tables 2.1-2.5) and full analytical reductions of all tensor integrals, we find cancellation of some powers of GD, which improves the behavior of the numerical code so that we can integrate, using Monte Carlo techniques, over the entire phase space, to obtain statistical errors from the numerical integration below 0.1%.

The fully reduced numerical amplitudes are often more demanding computationally, and because of that we have built numerical codes that use them only when close to regions of phase space where certain GD is small. With this the computer needs are reduced. All this was found particularly useful when considering E -PV functions (see Appendix D), and probably it would break down if one were to extend this technique to processes with even more legs, where probably using other techniques would be necessary.

We also checked parts of our result by using unitarity techniques [54], specifically the quadruple-cut technique [23]. As shown by Britto, Cachazo and Feng (BCF), from any set of Feynman diagrams (or more generally from any tensor integral [74]) one can extract the coefficient of a given scalar box integral by cutting the four corresponding propagators (see Fig. 2.1), i.e. by replacing $i/(\ell^2 - m^2 + i\epsilon) \rightarrow 2\pi\delta^{(+)}(\ell^2 - m^2)$ for each cutted propagator of momentum ℓ and mass m . This effectively freezes the momentum integration, and replaces it by a set of algebraic equations which determine the loop momentum entirely. We solved

this set of equations by using a BCF ansatz [23], and then compared the result to the corresponding box coefficient extracted from our analytic expression, and found agreement (for more details and specific solutions for the topology in Fig. 2.1 see Appendix E). This is a rather non-trivial check for the set of E -PV and D -PV functions (see Appendix D) we have employed at different stages, since they all contribute to the coefficients of the scalar D -functions occurring in the one-loop $W/Z\ b\bar{b}$ amplitudes. For instance, it has been particularly useful in the case of box diagrams like the one shown in Fig. 2.1, since this diagram and related ones contain up to $D4$ -PV functions that cannot be reduced even at the level of the amplitude squared. Since they involve up to four powers of inverse GDs, they are particularly subject to numerical instabilities and it is important to have their analytic expressions as compact as possible.

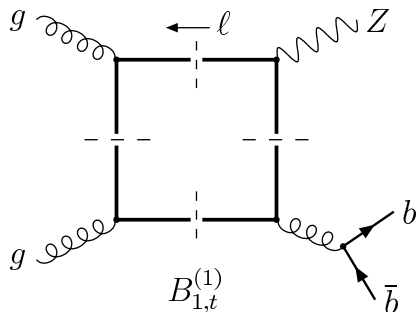


Figure 2.1: Quadruple cut [23] check of the calculation of a box diagram involving a top-quark loop. It corresponds to two Feynman diagrams ($B_{1,t}^{(1)}$ in Fig. 2.18) given by the two possible orientations of the fermion line.

After the tensor integral reduction is performed, the fundamental building blocks are one-loop scalar integrals with up to five denominators. They may be finite or contain both ultraviolet (UV) and infrared (IR) divergences.

The UV singularities of the virtual cross section are regularized in $d = 4 - 2\epsilon_{UV}$ dimensions and renormalized by introducing a suitable set of counterterms, while the residual renormalization scale dependence is checked from first principles using renormalization group arguments as in Eq. (2.6). The IR singularities of the virtual cross section are extracted in $d = 4 - 2\epsilon_{IR}$ dimensions and are canceled by analogous singularities in the $\mathcal{O}(\alpha_s^3)$ real cross section.

In our calculation we treat γ_5 according to the naive dimensional regularization approach, i.e. we enforce the fact that γ_5 anticommutes with all other γ matrices in $d = 4 - 2\epsilon$ dimensions. This is known to give rise to inconsistencies when, at the same time, the d -dimensional trace of four γ matrices and one γ_5 is forced to be non-zero (as in $d = 4$, where $\text{Tr}(\gamma^\mu \gamma^\nu \gamma^\rho \gamma^\sigma \gamma_5) = 4i\epsilon^{\mu\nu\rho\sigma}$) [75]. In our calculation, both UV and IR divergences are handled in such a way that we never have to enforce simultaneously these two properties of the Dirac algebra in d dimensions. For instance, the UV divergences are extracted and canceled at the amplitude level, after which the $d \rightarrow 4$ limit is taken and the renormalized amplitude is squared using $d = 4$. Thus, all fermion traces appearing at this point are computed in four dimensions and therefore have no ambiguities.

The finite scalar integrals are evaluated using the method described in Ref. [73] and cross checked with the numerical package FF [57]. The singular scalar integrals are calculated analytically by using dimensional regularization in $d = 4 - 2\epsilon$ dimensions. The most difficult integrals arise from IR divergent pentagon diagrams with several external and internal massive particles. We calculate them as linear combinations of box integrals using the method of Ref. [76, 77] and of Ref. [73]. Details of the box scalar integrals, including two that we calculated explicitly since they were not previously in the literature, and of the pentagon reduction used in this calculation are given in Appendix C, as well as the set of UV- and IR-divergent three and two point functions.

We note that the tree level amplitude \mathcal{A}_0 in Eq. (2.9) has generically to be considered as a d -dimensional tree level amplitude. This matters when the \mathcal{A}_D amplitudes in Eq. (2.9) are UV or IR divergent. Actually, as will be shown in the following, both UV and IR divergences are always proportional to pieces of the tree level amplitudes and they can be formally canceled without having to explicitly specify the dimensionality of the tree level amplitude itself. After UV and IR singularities have been canceled, everything is calculated in $d = 4$ dimensions.

2.2.3 Calculating the Real Cross Section $\hat{\sigma}^{\text{real}}$

The NLO real cross section $\hat{\sigma}^{\text{real}}$ in Eq. (2.5) corresponds to the $\mathcal{O}(\alpha_s)$ corrections to $ij \rightarrow W/Z \, b\bar{b}$ due to the emission of an additional real extra parton, i.e. to the process $ij \rightarrow W/Z \, b\bar{b} + k$. It contains IR singularities which cancel the analogous singularities present in the $\mathcal{O}(\alpha_s)$ virtual corrections and in the NLO PDFs. These singularities can be

either *soft*, when the emitted extra parton is a gluon and its energy becomes very small, or *collinear*, when the final state parton is emitted collinear to one of particles in the initial state. There is no collinear singularity from the final b and \bar{b} quarks, because the b -quark mass regularize the collinear divergence.

These IR singularities can be conveniently isolated by *slicing* the phase space of the final state particles into different regions defined by suitable cutoffs, a method which goes under the general name of *Phase Space Slicing* (PSS). The dependence on the arbitrary cutoffs introduced in *slicing* the final state phase space is not physical, and cancels at the level of the total real hadronic cross section, i.e. in σ^{real} , as well as at the level of the real cross section for each separate subprocess. This cancellation constitutes an important check of the calculation and will be discussed in detail in Sections 2.3.3 and 2.4.5.

We have calculated the cross section for the processes

$$i(q_1) + j(q_2) \rightarrow b(p_b) + \bar{b}(p_{\bar{b}}) + V(p_v) + h(k) \ ,$$

with $q_1 + q_2 = p_b + p_{\bar{b}} + p_v + k$, using the *two-cutoff* PSS method, which includes cutoffs of the soft and collinear kind. This implementation of the PSS method was originally developed to study QCD corrections to dihadron production [78] and has since then been applied to a variety of processes. (A nice review about it can be found in Ref. [79], to which we refer for more extensive references and details.)

In the following, we briefly review the structure of the real calculation using the two-cutoff PSS. We mention that the soft and collinear kernels employed throughout our calculation have been used also in the NLO calculation of $t\bar{t}H$ production at hadron colliders, where results have been checked using a PSS method with one-cutoff and a dipole cancellation method [80, 81, 82, 83]. Although the processes we are considering are different, the kinematics are equivalent, and the color structure and IR behavior are the same, so necessarily their soft and collinear kernels are the same.

Phase Space Slicing method with two cutoffs

The general implementation of the PSS method using two cutoffs proceeds in two steps. First, to isolate the soft singularities of a final state extra gluon we introduce an arbitrarily small *soft* cutoff δ_s and we separate the overall integration over the phase space of that gluon into two regions according to whether the energy of the final state gluon ($k^0 = E_g$) is *soft*,

i.e. $E_g \leq \delta_s \sqrt{s}/2$, or *hard*, i.e. $E_g > \delta_s \sqrt{s}/2$. The partonic real cross section of Eq. (2.5) can then be written as:

$$\hat{\sigma}^{\text{real}} = \hat{\sigma}^{\text{soft}} + \hat{\sigma}^{\text{hard}} , \quad (2.11)$$

where $\hat{\sigma}^{\text{soft}}$ is obtained by integrating over the *soft* region of the gluon phase space, and contains all the IR soft divergences of $\hat{\sigma}^{\text{real}}$. To isolate the remaining collinear divergences from $\hat{\sigma}^{\text{hard}}$, we further split the integration over the phase space of any final state parton according to whether the parton is ($\hat{\sigma}^{\text{hard/coll}}$) or is not ($\hat{\sigma}^{\text{hard/non-coll}}$) emitted within an angle θ from the initial state partons such that $(1 - \cos \theta) < \delta_c$, for an arbitrary small *collinear* cutoff δ_c :

$$\hat{\sigma}^{\text{hard}} = \hat{\sigma}^{\text{hard/coll}} + \hat{\sigma}^{\text{hard/non-coll}} . \quad (2.12)$$

The hard non-collinear part of the real cross section, $\hat{\sigma}^{\text{hard/non-coll}}$, is finite and can be computed numerically, using standard Monte Carlo techniques.

On the other hand, in the soft and collinear regions the integration over the phase space of the emitted gluon or quark can be performed analytically, thus allowing us to isolate and extract the IR divergences of $\hat{\sigma}^{\text{real}}$. More details on the calculation of $\hat{\sigma}^{\text{soft}}$ and $\hat{\sigma}^{\text{hard}}$ for each relevant subprocess will be given in Sections 2.3.2 and 2.4.4 for the hadronic production of $Wb\bar{b}$ and $Zb\bar{b}$ respectively.

The cross sections describing soft, collinear and IR-finite radiation depend on the two arbitrary parameters δ_s and δ_c . However, in the total real hadronic cross section σ^{real} , after mass factorization, the dependence on these arbitrary cutoffs vanishes for sufficiently small values of the cutoffs.

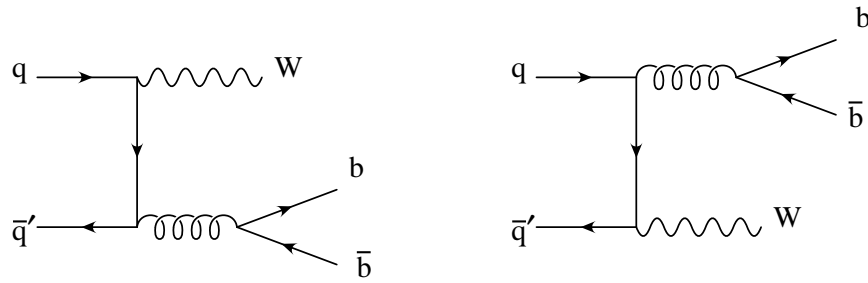


Figure 2.2: Tree level Feynman diagrams for $q\bar{q}' \rightarrow Wb\bar{b}$.

2.3 Calculation of NLO QCD Corrections to $Wb\bar{b}$ Production at Hadron Colliders

In this Section we present in detail the calculation of the partonic total or differential cross section $\hat{\sigma}^{\text{NLO}}(ij \rightarrow Wb\bar{b})$ [84], as defined in Eqs. (2.4) and (2.5).

There is only one subprocess contributing to $Wb\bar{b}$ at LO, $q\bar{q}' \rightarrow Wb\bar{b}$, where q and \bar{q}' represent quarks or antiquarks of up-type and down-type, respectively. We neglect contributions from third generation initial quarks as they are suppressed by either the initial state quark densities (PDFs) or by the corresponding Cabibbo-Kobayashi-Maskawa (CKM) matrix elements.

The contributing tree level Feynman diagrams are shown in Figure 2.2. Given the assignment of momenta

$$q(q_1)\bar{q}'(q_2) \rightarrow b(p_b) + \bar{b}(p_{\bar{b}}) + W(p_w) ,$$

the LO amplitude can be written as

$$\begin{aligned} \mathcal{A}_0(q\bar{q}' \rightarrow Wb\bar{b}) &= ig_s^2 \frac{g_w}{2\sqrt{2}} V_{q\bar{q}'} \epsilon_\mu^*(p_w) \frac{g_{\nu\rho}}{(p_b + p_{\bar{b}})^2} \bar{u}_b \gamma^\rho v_{\bar{b}} t_{ij}^a t_{kl}^a \\ &\quad \left[\bar{v}_{\bar{q}'} \gamma^\mu (1 - \gamma_5) \frac{-\not{q}_2 + \not{p}_w}{(-q_2 + p_w)^2} \gamma^\nu u_q \right. \\ &\quad \left. + \bar{v}_{\bar{q}'} \gamma^\nu \frac{\not{q}_1 - \not{p}_w}{(q_1 - p_w)^2} \gamma^\mu (1 - \gamma_5) u_q \right] , \end{aligned} \quad (2.13)$$

where g_s and g_w are the strong and weak coupling constants, respectively, $t^a = \lambda^a/2$ are given in terms of the Gell-Mann matrices λ^a and $V_{q\bar{q}'}$ are the entries of the CKM mixing matrix. (For more details see Appendix B.)

The partonic LO cross section is obtained by integrating $|\mathcal{A}_0|^2$ over the $Wb\bar{b}$ final state phase space:

$$\hat{\sigma}^{\text{LO}} = \int d(P S_3) \overline{\sum} |\mathcal{A}_0|^2 , \quad (2.14)$$

where the sums indicates average over initial and sum over final spins and colors of the fermion lines, as well as sum over polarizations of the vector boson. As we are considering an on-shell gauge boson, we have summed over its polarizations according to the prescription used for massive vector bosons, i.e.:

$$\sum \epsilon_\mu(k) \epsilon_\nu^*(k) = -g_{\mu\nu} + \frac{k_\mu k_\nu}{M_V^2} , \quad (2.15)$$

where M_V is the mass of the V weak boson ($V = W, Z$). For $Wb\bar{b}$ production the second term in Eq. (2.15) does not contribute, because in our calculation the W boson only couples to the initial massless fermion line. The full expression has to be considered, however, when calculating $Zb\bar{b}$ production.

At NLO one has to consider three processes: $q\bar{q}' \rightarrow Wb\bar{b}$, which contributes both at $\mathcal{O}(\alpha_s^2)$ and at $\mathcal{O}(\alpha_s^3)$ through the one-loop $\mathcal{O}(\alpha_s)$ virtual corrections, and the real $\mathcal{O}(\alpha_s)$ corrections, due to $q\bar{q}' \rightarrow Wb\bar{b} + g$ and $q(\bar{q})g \rightarrow Wb\bar{b} + q'(\bar{q}')$ which contribute at $\mathcal{O}(\alpha_s^3)$. In the following sections we will discuss in detail the structure of both virtual and real $\mathcal{O}(\alpha_s)$ corrections.

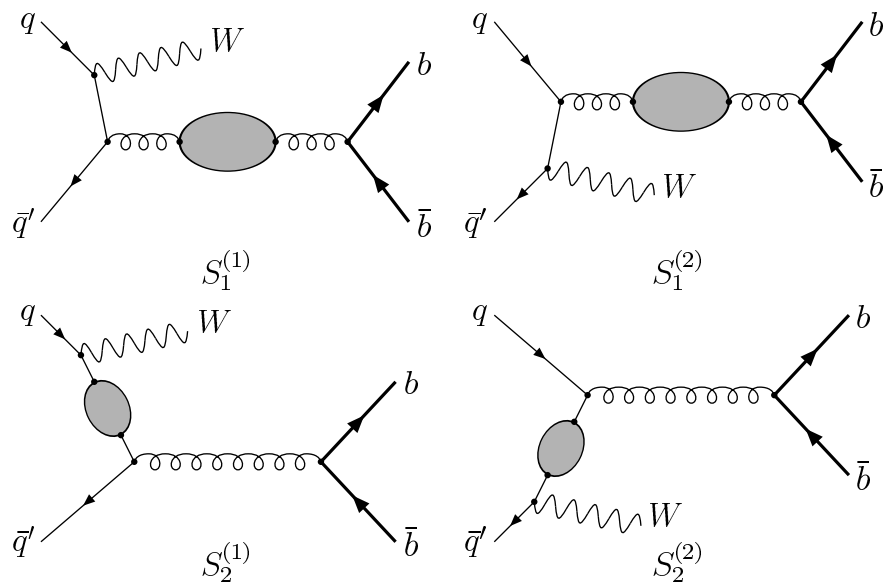


Figure 2.3: Gluon ($S_1^{(1,2)}$) and quark ($S_2^{(1,2)}$) $\mathcal{O}(\alpha_s)$ self-energy corrections contributing to the $q\bar{q}' \rightarrow Wb\bar{b}$ subprocess at NLO. The shaded blobs denote standard one-loop QCD corrections to the gluon and quark propagators, respectively.

2.3.1 Virtual Corrections to $q\bar{q}' \rightarrow Wb\bar{b}$

The $\mathcal{O}(\alpha_s)$ virtual corrections to the $q\bar{q}' \rightarrow Wb\bar{b}$ tree level process consist of the self-energy, vertex, box and pentagon one-loop diagrams illustrated in Figures 2.3, 2.4, 2.5 and 2.6. The

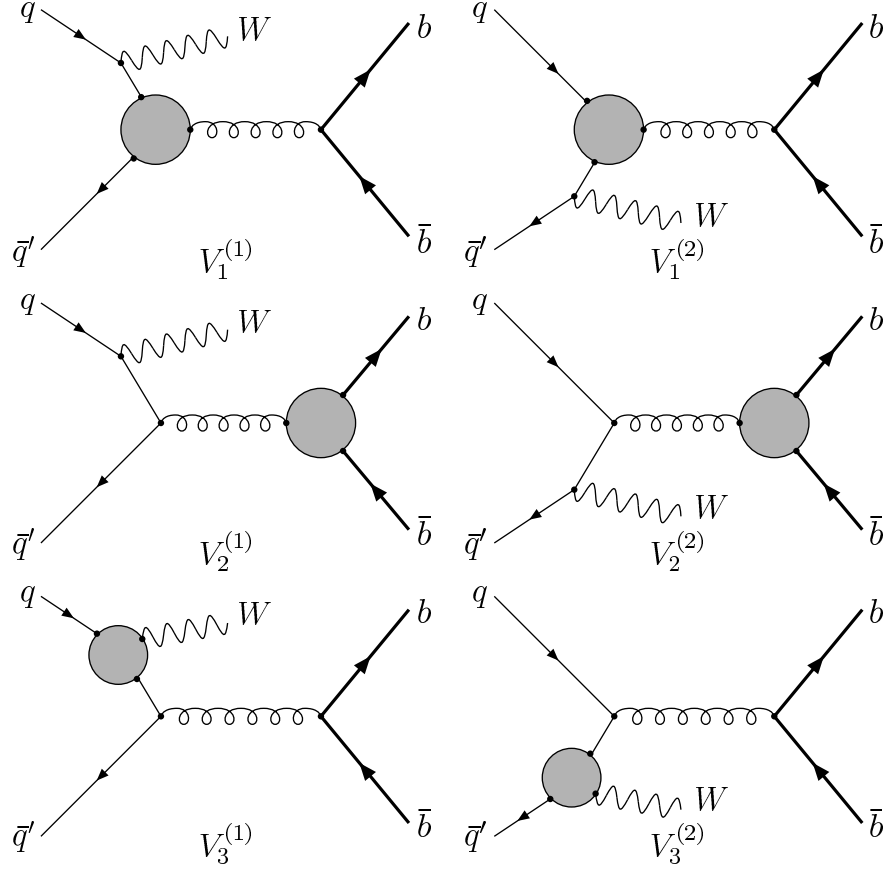


Figure 2.4: $\mathcal{O}(\alpha_s)$ vertex corrections contributing to the subprocess $q\bar{q}' \rightarrow Wb\bar{b}$ at NLO. The shaded blobs denote standard one-loop QCD corrections to the $q\bar{q}g$, $b\bar{b}g$ and $q\bar{q}'W$ vertices, respectively.

contributions to the virtual amplitude squared of Eq. (2.5) can then be written as:

$$\overline{\sum} |\mathcal{A}_{\text{virt}}(q\bar{q}' \rightarrow Wb\bar{b})|^2 = \sum_D \overline{\sum} \left(\mathcal{A}_0 \mathcal{A}_D^\dagger + \mathcal{A}_0^\dagger \mathcal{A}_D \right) = \sum_D \overline{\sum} 2\mathcal{Re} \left(\mathcal{A}_0 \mathcal{A}_D^\dagger \right), \quad (2.16)$$

where \mathcal{A}_0 is the tree level amplitude given in Eq. (2.13) and corresponding to the diagrams shown in Figure 2.2, and \mathcal{A}_D denotes the amplitude for the one-loop diagram D , with D running over all self-energy, vertex, box and pentagon diagrams illustrated in Figures 2.3, 2.4, 2.5 and 2.6.

The amplitude of each virtual diagram (\mathcal{A}_D) is calculated as described in Section 2.2.2. Inserting all diagram contributions into Eq. (2.16), we obtain the complete $\mathcal{O}(\alpha_s^3)$

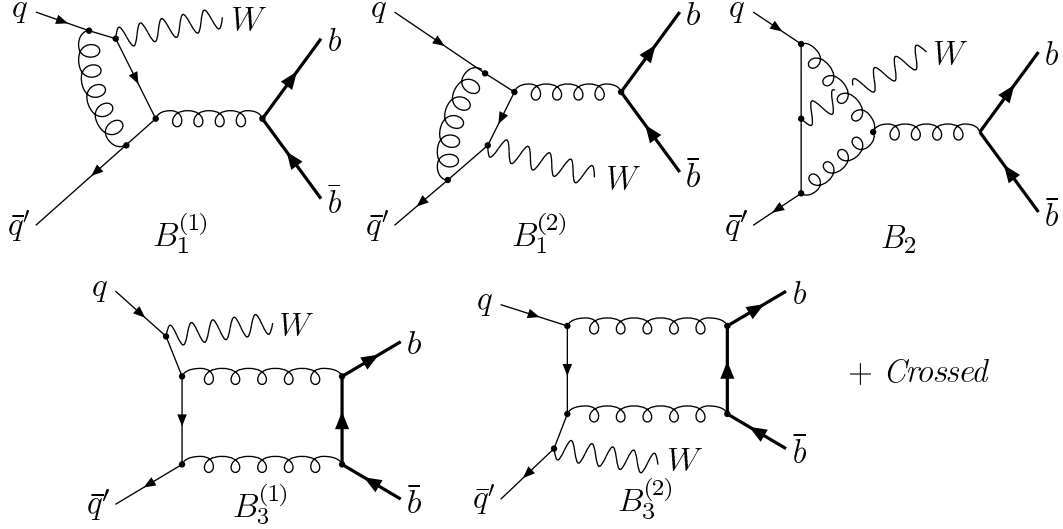


Figure 2.5: $\mathcal{O}(\alpha_s)$ box diagram corrections contributing to the $q\bar{q}' \rightarrow Wb\bar{b}$ process at NLO. The term *Crossed* refers to the box diagrams, $B_{3c}^{(1,2)}$ obtained from the $B_3^{(1,2)}$ boxes by flipping the b -quark fermion line.

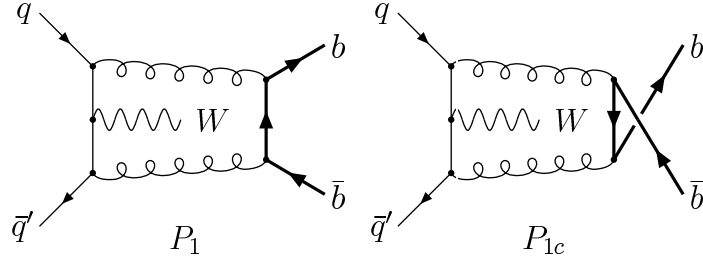


Figure 2.6: $\mathcal{O}(\alpha_s)$ pentagon diagram corrections contributing to the $q\bar{q}' \rightarrow Wb\bar{b}$ process at NLO.

contribution to the virtual amplitude squared, and integrating over the final state phase space we calculate $\hat{\sigma}_{q\bar{q}}^{\text{virt}}$ in Eq. (2.5).

Results for the renormalization of the one-loop corrections are shown in Section 2.3.1.1. The structure of the IR singular part of the virtual cross section is presented in Section 2.3.1.2, while the IR singularities of the real cross section are discussed in Section 2.3.2. The explicit cancellation of IR singularities in the total inclusive NLO cross section is outlined in Sections 2.3.2 and 2.3.3.

2.3.1.1 Virtual corrections: UV singularities and counterterms

The UV singularities of the $\mathcal{O}(\alpha_s^3)$ total cross section originate from the self-energy and vertex virtual corrections shown in Figures 2.3 and 2.4. These singularities are renormalized by introducing counterterms for the wave function of the external fields ($\delta Z_2^{(q)}$, $\delta Z_2^{(b)}$) and the strong coupling constant (δZ_{α_s}). If we denote by $\Delta_{\text{UV}}(S_i^{(1,2)})$ and $\Delta_{\text{UV}}(V_i^{(1,2)})$ the UV-divergent contribution of each self-energy ($S_i^{(1,2)}$) or vertex diagram ($V_i^{(1,2)}$) to the virtual amplitude squared (see Eq. (2.16)), we can write the UV-singular part of the total virtual amplitude squared as:

$$\begin{aligned} \overline{\sum} |\mathcal{A}_{\text{virt}}^{\text{UV}}|^2 &= \overline{\sum} |\mathcal{A}_0|^2 \left\{ \sum_{i=1}^2 \Delta_{\text{UV}}(S_i^{(1)} + S_i^{(2)}) + \sum_{i=1}^3 \Delta_{\text{UV}}(V_i^{(1)} + V_i^{(2)}) \right. \\ &\quad \left. + 2 \left[\left(\delta Z_2^{(q)} \right)_{\text{UV}} + \left(\delta Z_2^{(b)} \right)_{\text{UV}} + \delta Z_{\alpha_s} \right] \right\} . \end{aligned} \quad (2.17)$$

We denote by $|\mathcal{A}_0|^2$ the matrix element squared of the tree-level amplitude for $q\bar{q}' \rightarrow Wb\bar{b}$, computed in $d = 4$ dimensions (see Eq. (2.13) and Section 2.2.2).

The UV-divergent contributions due to the individual diagrams are given by:

$$\begin{aligned} \Delta_{\text{UV}}(S_1^{(1)} + S_1^{(2)}) &= \frac{\alpha_s}{2\pi} \left[\mathcal{N}_s \left(\frac{5}{3}N - \frac{2}{3}n_{lf} \right) - \mathcal{N}_b \frac{2}{3} \right] \left(\frac{1}{\epsilon_{\text{UV}}} \right) , \\ \Delta_{\text{UV}}(S_2^{(1)} + S_2^{(2)}) &= -\frac{\alpha_s}{2\pi} \mathcal{N}_b \left(\frac{N}{2} - \frac{1}{2N} \right) \left(\frac{1}{\epsilon_{\text{UV}}} \right) , \\ \Delta_{\text{UV}}(V_1^{(1)} + V_1^{(2)}) &= \frac{\alpha_s}{2\pi} \mathcal{N}_s \left(\frac{3N}{2} - \frac{1}{2N} \right) \left(\frac{1}{\epsilon_{\text{UV}}} \right) , \\ \Delta_{\text{UV}}(V_2^{(1)} + V_2^{(2)}) &= \frac{\alpha_s}{2\pi} \mathcal{N}_b \left(\frac{3N}{2} - \frac{1}{2N} \right) \left(\frac{1}{\epsilon_{\text{UV}}} \right) , \\ \Delta_{\text{UV}}(V_3^{(1)} + V_3^{(2)}) &= \frac{\alpha_s}{2\pi} \mathcal{N}_b \left(\frac{N}{2} - \frac{1}{2N} \right) \left(\frac{1}{\epsilon_{\text{UV}}} \right) , \end{aligned} \quad (2.18)$$

where $N = 3$ is the number of colors, $n_{lf} = 5$ is the number of light flavors and \mathcal{N}_s and \mathcal{N}_b are standard normalization factors defined as:

$$\mathcal{N}_s = \left(\frac{4\pi\mu^2}{s} \right)^\epsilon \Gamma(1 + \epsilon) , \quad \mathcal{N}_b = \left(\frac{4\pi\mu^2}{m_b^2} \right)^\epsilon \Gamma(1 + \epsilon) . \quad (2.19)$$

Moreover, we define the required counterterms according to the following convention. For the external fields, we fix the wave-function renormalization constants of the external fields

$(Z_2^{(i)} = 1 + \delta Z_2^{(i)}, i=q, b)$ using on-shell subtraction, i.e.:

$$\begin{aligned} (\delta Z_2^{(q)})_{\text{UV}} &= -\left(\frac{\alpha_s}{4\pi}\right) \mathcal{N}_s \left(\frac{N}{2} - \frac{1}{2N}\right) \left(\frac{1}{\epsilon_{\text{UV}}}\right), \\ (\delta Z_2^{(b)})_{\text{UV}} &= -\left(\frac{\alpha_s}{4\pi}\right) \mathcal{N}_b \left(\frac{N}{2} - \frac{1}{2N}\right) \left(\frac{1}{\epsilon_{\text{UV}}} + 4\right). \end{aligned} \quad (2.20)$$

We notice that both $\delta Z_2^{(q)}$ and $\delta Z_2^{(b)}$, as well as some of the vertex corrections ($V_1^{(1,2)}$ and $V_2^{(1,2)}$), have also IR singularities. In this section we limit the discussion to the UV singularities only, while the IR structure of this counterterm will be included in the IR-singularities shown in Section 2.3.1.2.

Finally, for the renormalization of α_s we use the \overline{MS} scheme, modified to decouple the top quark [85]. The first n_{lf} light flavors are subtracted using the \overline{MS} scheme, while the divergences associated with the top-quark loop are subtracted at zero momentum:

$$\delta Z_{\alpha_s} = \left(\frac{\alpha_s}{4\pi}\right) (4\pi)^\epsilon \Gamma(1+\epsilon) \left[\left(\frac{2}{3}n_{lf} - \frac{11}{3}N\right) \frac{1}{\epsilon_{\text{UV}}} + \frac{2}{3} \left(\frac{1}{\epsilon_{\text{UV}}} + \ln\left(\frac{\mu^2}{m_t^2}\right)\right) \right], \quad (2.21)$$

such that, in this scheme, the renormalized strong coupling constant α_s evolves with $n_{lf} = 5$ light flavors, as justified by the energy scale of the processes under consideration.

It is easy to verify that the sum of all the UV-singular contributions as given in Eq. (2.17) is finite. We also notice that the left over renormalization scale dependence, due to the mismatch between the renormalization scale dependence of $\Delta_{\text{UV}}(S_1)$ and $\delta(Z_{\alpha_s})$, is given by:

$$\overline{\sum} |\mathcal{A}_0|^2 \frac{\alpha_s(\mu)}{2\pi} \left(-\frac{2}{3}n_{lf} + \frac{11}{3}N\right) \ln\left(\frac{\mu^2}{s}\right), \quad (2.22)$$

and corresponds exactly to the first term of Eq. (2.7), as predicted by renormalization group arguments. We note that the presence of s in the argument of the logarithm of Eq. (2.22) has no particular relevance. Choosing a different argument would amount to reabsorbing some μ -independent logarithms in f_1^{ij} of Eq. (2.6).

2.3.1.2 IR singularities

This section describes the structure of the IR singularities originating from the $\mathcal{O}(\alpha_s)$ virtual corrections. The virtual IR singularities come from the following set of diagrams: vertex diagrams $V_1^{(1,2)}$ and $V_2^{(1,2)}$, box diagrams $B_1^{(1,2)}$, B_2 , $B_3^{(1,2)}$ and $B_{3c}^{(1,2)}$ and pentagon diagrams P_1 and P_{1c} , and from the wave function renormalization of the external fields, $\delta Z_2^{(q)}$ and $\delta Z_2^{(b)}$. After grouping all IR poles from this diagrams we obtain the total structure of the IR

singularity of the one-loop virtual corrections to $q\bar{q}' \rightarrow Wb\bar{b}$. Before writing such expressions, let us introduce the following set of kinematical variables:

$$\begin{aligned}
s &= (q_1 + q_2)^2 , \\
\tau_1 &= m_b^2 - (q_1 - p_b)^2 = 2 q_1 \cdot p_b , \\
\tau_2 &= m_b^2 - (q_2 - p_{\bar{b}})^2 = 2 q_2 \cdot p_{\bar{b}} , \\
\tau_3 &= m_b^2 - (q_2 - p_b)^2 = 2 q_2 \cdot p_b , \\
\tau_4 &= m_b^2 - (q_1 - p_{\bar{b}})^2 = 2 q_1 \cdot p_{\bar{b}} , \\
\bar{s}_{b\bar{b}} &= (p_b + p_{\bar{b}})^2 = 2 p_b \cdot p_{\bar{b}} + 2 m_b^2 .
\end{aligned} \tag{2.23}$$

Summing all the IR-divergent contributions yields:

$$\overline{\sum} |\mathcal{A}_{\text{virt}}^{\text{IR}}|^2 = \left(\frac{\alpha_s}{2\pi} \right) \mathcal{N}_b \overline{\sum} |\mathcal{A}_0|^2 \left\{ \frac{X_{-2}^{\text{virt}}}{\epsilon_{\text{IR}}^2} + \frac{X_{-1}^{\text{virt}}}{\epsilon_{\text{IR}}} + \delta_{\text{virt}}^{\text{IR}} \right\} , \tag{2.24}$$

with

$$\begin{aligned}
X_{-2}^{\text{virt}} &= - \left(N - \frac{1}{N} \right) , \\
X_{-1}^{\text{virt}} &= N \left[-\frac{5}{2} + \ln \left(\frac{\tau_1}{m_b^2} \right) + \ln \left(\frac{\tau_2}{m_b^2} \right) \right] \\
&\quad + \frac{1}{N} \left[-\ln \left(\frac{s}{m_b^2} \right) + \frac{5}{2} - \frac{\bar{s}_{b\bar{b}} - 2m_b^2}{\bar{s}_{b\bar{b}} \beta_{b\bar{b}}} \Lambda_{b\bar{b}} - 2 \ln \left(\frac{\tau_1 \tau_2}{\tau_4 \tau_3} \right) \right] ,
\end{aligned} \tag{2.25}$$

where we have used the kinematical invariants presented in Eq. (2.23) while $\beta_{b\bar{b}}$ and $\Lambda_{b\bar{b}}$ are defined by:

$$\begin{aligned}
\beta_{b\bar{b}} &= \sqrt{1 - \frac{4m_b^2}{\bar{s}_{b\bar{b}}}} , \\
\Lambda_{b\bar{b}} &= \ln \left(\frac{1 + \beta_{b\bar{b}}}{1 - \beta_{b\bar{b}}} \right) ,
\end{aligned} \tag{2.26}$$

and $\delta_{\text{virt}}^{\text{IR}}$ is a finite term that comes from having factored out a common factor \mathcal{N}_b and is given by:

$$\delta_{\text{virt}}^{\text{IR}} = \left(N - \frac{1}{N} \right) \left[\frac{3}{2} \ln \left(\frac{s}{m_b^2} \right) \right] + \frac{1}{N} \left[\frac{1}{2} \ln^2 \left(\frac{s}{m_b^2} \right) \right] . \tag{2.27}$$

Before finishing let us write the IR-pole contributions to the counterterms $\delta Z_2^{(q)}$ and $\delta Z_2^{(b)}$:

$$\begin{aligned}
\left(\delta Z_2^{(q)} \right)_{\text{IR}} &= \left(\frac{\alpha_s}{4\pi} \right) \mathcal{N}_s \left(\frac{N}{2} - \frac{1}{2N} \right) \left(\frac{1}{\epsilon_{\text{IR}}} \right) , \\
\left(\delta Z_2^{(b)} \right)_{\text{IR}} &= - \left(\frac{\alpha_s}{4\pi} \right) \mathcal{N}_b \left(\frac{N}{2} - \frac{1}{2N} \right) \left(\frac{2}{\epsilon_{\text{IR}}} \right) .
\end{aligned} \tag{2.28}$$

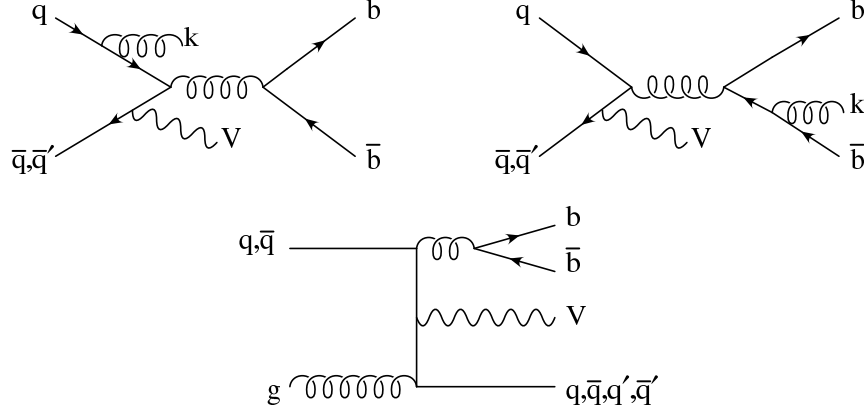


Figure 2.7: $\mathcal{O}(\alpha_s)$ real corrections: examples of initial and final real gluon emission and $q(\bar{q})g$ initiated subprocess.

In Sec. 2.3.2 we will show how the IR singularities of the real cross section exactly cancel the IR poles of the virtual cross section (see Eqs. (2.35)-(2.36)), as predicted by the Bloch-Nordsieck [86] and Kinoshita-Lee-Nauenberg [87, 88] theorems.

2.3.2 Real Corrections to $Wb\bar{b}$ Production

The $\mathcal{O}(\alpha_s)$ corrections to $q\bar{q}' \rightarrow Wb\bar{b}$ due to real gluon emission (see Figure 2.7) give rise to IR singularities which cancel exactly the analogous singularities present in the $\mathcal{O}(\alpha_s)$ virtual corrections (see Sec. 2.3.1.2). We also have real contributions from the subprocess $q(\bar{q})g \rightarrow Wb\bar{b} + q'(\bar{q}')$ that give rise to IR singularities of the collinear kind. We present results for the latter at the end of this section.

We have calculated the cross section for the process

$$q(q_1) + \bar{q}'(q_2) \rightarrow b(p_b) + \bar{b}(p_{\bar{b}}) + W(p_w) + g(k) \quad (2.29)$$

using the *two-cutoff* PSS method, as presented in Section 2.2.3. In the following subsections we explain in detail how we have applied this method to the calculation of the real contributions to $Wb\bar{b}$ hadronic production. We will present details of the calculation of the pieces of σ^{real} introduced in Section 2.2.3, namely σ^{soft} and σ^{hard} .

Soft gluon emission

The soft region of the $q\bar{q}' \rightarrow Wb\bar{b} + g$ phase space is defined by requiring that the energy of the gluon satisfies:

$$E_g < \delta_s \frac{\sqrt{s}}{2} , \quad (2.30)$$

for an arbitrary small value of the *soft* cutoff δ_s . In the limit when the energy of the gluon becomes small, i.e. in the *soft limit*, the matrix element squared for the real gluon emission, $\overline{\sum} |\mathcal{A}_{\text{real}}|^2$, assumes a very simple form, i.e. it factorizes into the LO matrix element squared times an eikonal factor Φ_{eik} :

$$\overline{\sum} |\mathcal{A}_{\text{real}}(q\bar{q}' \rightarrow Wb\bar{b} + g)|^2 \xrightarrow{\text{soft}} (4\pi\alpha_s) \overline{\sum} |\mathcal{A}_0|^2 \Phi_{eik} , \quad (2.31)$$

where the eikonal factor is given by:

$$\begin{aligned} \Phi_{eik} = & \frac{N}{2} \left[-\frac{m_b^2}{(p_b \cdot k)^2} - \frac{m_b^2}{(p_{\bar{b}} \cdot k)^2} + \frac{\tau_1}{(q_1 \cdot k)(p_b \cdot k)} + \frac{\tau_2}{(q_2 \cdot k)(p_{\bar{b}} \cdot k)} \right] \\ & + \frac{1}{2N} \left[\frac{m_b^2}{(p_b \cdot k)^2} + \frac{m_b^2}{(p_{\bar{b}} \cdot k)^2} - \frac{s}{(q_1 \cdot k)(q_2 \cdot k)} - \frac{\bar{s}_{b\bar{b}} - 2m_b^2}{(p_b \cdot k)(p_{\bar{b}} \cdot k)} \right. \\ & \left. + 2 \left(-\frac{\tau_1}{(q_1 \cdot k)(p_b \cdot k)} + \frac{\tau_4}{(q_1 \cdot k)(p_{\bar{b}} \cdot k)} + \frac{\tau_3}{(q_2 \cdot k)(p_b \cdot k)} - \frac{\tau_2}{(q_2 \cdot k)(p_{\bar{b}} \cdot k)} \right) \right] , \end{aligned} \quad (2.32)$$

where we have used the kinematical invariants defined in Eq. (2.23). Moreover, in the soft region the $q\bar{q}' \rightarrow Wb\bar{b} + g$ phase space also factorizes as:

$$\begin{aligned} d(PS_4)(q\bar{q}' \rightarrow Wb\bar{b} + g) & \xrightarrow{\text{soft}} d(PS_3)(q\bar{q}' \rightarrow Wb\bar{b}) d(PS_g)_{\text{soft}} \\ & = d(PS_3)(q\bar{q}' \rightarrow Wb\bar{b}) \frac{d^{(d-1)}k}{(2\pi)^{(d-1)}2E_g} \theta(\delta_s \frac{\sqrt{s}}{2} - E_g) , \end{aligned} \quad (2.33)$$

where $d(PS_g)_{\text{soft}}$ denotes the integration over the phase space of the soft gluon. The parton level soft cross section can then be written as:

$$\hat{\sigma}^{\text{soft}} = (4\pi\alpha_s) \mu^{2\epsilon} \int d(PS_3) \overline{\sum} |\mathcal{A}_0|^2 \int d(PS_g)_{\text{soft}} \Phi_{eik} . \quad (2.34)$$

Since the contribution of the soft gluon is now completely factorized, we can perform the integration over $d(PS_g)_{\text{soft}}$ in Eq. (2.34) analytically, and extract the soft poles that will cancel X_{-2}^{virt} and X_{-1}^{virt} of Eq. (2.25). The integration over the gluon phase space in Eq. (2.34) can be performed using standard techniques and we refer to Refs. [79, 89] for more details. For sake of completeness, in Appendix F we give explicit results for the soft integrals used in our calculation.

Finally, the soft gluon contribution to $\hat{\sigma}_{q\bar{q}}^{\text{real}}$ can be written as follows:

$$\hat{\sigma}^{\text{soft}} = \frac{\alpha_s}{2\pi} \mathcal{N}_b \int d(P S_3) \overline{\sum} |\mathcal{A}_0|^2 \left\{ \frac{X_{-2}^s}{\epsilon^2} + \frac{X_{-1}^s}{\epsilon} + N C_1^s + \frac{C_2^s}{N} \right\} , \quad (2.35)$$

where ϵ corresponds to ϵ_{IR} of Eq. (2.24) and

$$\begin{aligned} X_{-2}^s &= -X_{-2}^{\text{virt}} , \\ X_{-1}^s &= -X_{-1}^{\text{virt}} - \left(N - \frac{1}{N} \right) \left[\frac{3}{2} + 2 \ln(\delta_s) \right] , \\ C_1^s &= \frac{3}{2} \ln \left(\frac{s}{\mu^2} \right) + 2 \ln^2(\delta_s) - 2 \ln(\delta_s) \left[1 + \ln \left(\frac{m_b^2 \mu^2}{\tau_1 \tau_2} \right) \right] \\ &\quad + \frac{1}{2} \ln^2 \left(\frac{s}{m_b^2} \right) - \frac{\pi^2}{3} - \ln \left(\frac{s}{m_b^2} \right) \left[\frac{5}{2} + \ln \left(\frac{s m_b^2}{\tau_1 \tau_2} \right) \right] \\ &\quad + \frac{1}{2} \frac{1}{\beta_b} \ln \left(\frac{1 + \beta_b}{1 - \beta_b} \right) + \frac{1}{2} \frac{1}{\beta_{\bar{b}}} \ln \left(\frac{1 + \beta_{\bar{b}}}{1 - \beta_{\bar{b}}} \right) \\ &\quad + \frac{1}{2} (F_{qb} + F_{\bar{q}\bar{b}}) + \left[\frac{3}{2} + 2 \ln(\delta_s) \right] \ln \left(\frac{\mu^2}{m_b^2} \right) , \\ C_2^s &= -\frac{3}{2} \ln \left(\frac{s}{\mu^2} \right) - 2 \ln^2(\delta_s) - 2 \ln(\delta_s) \left[-1 \right. \\ &\quad \left. + \frac{\bar{s}_{b\bar{b}} - 2m_b^2}{\bar{s}_{b\bar{b}} \beta_{b\bar{b}}} \Lambda_{b\bar{b}} + \ln \left(\frac{s}{\mu^2} \right) + 2 \ln \left(\frac{\tau_1 \tau_2}{\tau_4 \tau_3} \right) \right] \\ &\quad - \frac{1}{2} \ln^2 \left(\frac{s}{m_b^2} \right) + \frac{\pi^2}{3} - \ln \left(\frac{s}{m_b^2} \right) \left[-\frac{5}{2} \right. \\ &\quad \left. + \frac{\bar{s}_{b\bar{b}} - 2m_b^2}{\bar{s}_{b\bar{b}} \beta_{b\bar{b}}} \Lambda_{b\bar{b}} + 2 \ln \left(\frac{\tau_1 \tau_2}{\tau_4 \tau_3} \right) \right] - \frac{1}{2} \frac{1}{\beta_b} \ln \left(\frac{1 + \beta_b}{1 - \beta_b} \right) - \frac{1}{2} \frac{1}{\beta_{\bar{b}}} \ln \left(\frac{1 + \beta_{\bar{b}}}{1 - \beta_{\bar{b}}} \right) \\ &\quad + \frac{\bar{s}_{b\bar{b}} - 2m_b^2}{\bar{s}_{b\bar{b}} \beta_{b\bar{b}}} \left[-\frac{1}{4} \ln^2 \left(\frac{1 + \beta_b}{1 - \beta_b} \right) + \frac{1}{4} \ln^2 \left(\frac{1 + \beta_{\bar{b}}}{1 - \beta_{\bar{b}}} \right) \right. \\ &\quad \left. - \text{Li}_2 \left(1 - \frac{\alpha_{b\bar{b}}}{v_{b\bar{b}}} p_b^0 (1 + \beta_b) \right) - \text{Li}_2 \left(1 - \frac{\alpha_{b\bar{b}}}{v_{b\bar{b}}} p_b^0 (1 - \beta_b) \right) \right. \\ &\quad \left. + \text{Li}_2 \left(1 - \frac{1}{v_{b\bar{b}}} p_b^0 (1 + \beta_{\bar{b}}) \right) + \text{Li}_2 \left(1 - \frac{1}{v_{b\bar{b}}} p_b^0 (1 - \beta_{\bar{b}}) \right) \right] \\ &\quad + -F_{qb} + F_{q\bar{b}} + F_{\bar{q}b} - F_{\bar{q}\bar{b}} \\ &\quad - \left[\frac{3}{2} + 2 \ln(\delta_s) \right] \ln \left(\frac{\mu^2}{m_b^2} \right) , \end{aligned} \quad (2.36)$$

while \mathcal{N}_b is defined in Eq. (2.19), Li_2 denotes the dilogarithm as described in Ref. [90] and X_{-2}^{virt} and X_{-1}^{virt} are given in Eq. (2.25). We have used the kinematical invariants defined in Eq. (2.23), $\beta_{b\bar{b}}$ and $\Lambda_{b\bar{b}}$ are defined in Eq. (2.26),

$$\alpha_{b\bar{b}} = \frac{1 + \beta_{b\bar{b}}}{1 - \beta_{b\bar{b}}} \quad \text{and} \quad v_{b\bar{b}} = \frac{m_b^2 (\alpha_{b\bar{b}}^2 - 1)}{2(\alpha_{b\bar{b}} p_b^0 - p_b^0)} , \quad (2.37)$$

while, for any initial parton i and final parton f , the function F_{if} can be written as:

$$F_{if} = \ln^2\left(\frac{1 - \beta_f}{1 - \beta_f \cos \theta_{if}}\right) - \frac{1}{2} \ln^2\left(\frac{1 + \beta_f}{1 - \beta_f}\right) + 2\text{Li}_2\left(-\frac{\beta_f(1 - \cos \theta_{if})}{1 - \beta_f}\right) - 2\text{Li}_2\left(-\frac{\beta_f(1 + \cos \theta_{if})}{1 - \beta_f \cos \theta_{if}}\right), \quad (2.38)$$

where θ_{if} is the angle between partons i and f in the center-of-mass frame of the initial state partons, and

$$\beta_f = \sqrt{1 - \frac{m_b^2}{(p_f^0)^2}}, \quad 1 - \beta_f \cos \theta_{if} = \frac{s_{if}}{p_f^0 \sqrt{s}}. \quad (2.39)$$

All the quantities in Eq. (2.38) can be expressed in terms of kinematic invariants, for details see Appendix F.

As can be easily seen from Eqs. (2.25) and (2.36), the IR poles of the virtual corrections are exactly canceled by the corresponding singularities in the soft gluon contribution. The remaining IR poles in $\hat{\sigma}^{soft}$ will be canceled by the PDF counterterms as described in detail in Sec. 2.3.3.

Hard gluon emission

The hard region of the gluon phase space is defined by requiring that the energy of the emitted gluon is above a given threshold. As we discussed earlier this is expressed by the condition that

$$E_g > \delta_s \frac{\sqrt{s}}{2}, \quad (2.40)$$

for an arbitrary small *soft* cutoff δ_s , which automatically assures that $\hat{\sigma}^{hard}$ does not contain soft singularities. However, a hard gluon can still yield singularities when it is emitted at a small angle, i.e. *collinear*, to a massless incoming or outgoing parton. In order to isolate these divergences and compute them analytically, we divide the hard region of the $q\bar{q}' \rightarrow Wb\bar{b}+g$ phase space into *hard/collinear* and *hard/non-collinear* regions, by introducing a small *collinear* cutoff δ_c . The *hard/non-collinear* region is defined by the conditions

$$\frac{2q_1 \cdot k}{E_g \sqrt{s}} > \delta_c \quad \text{and} \quad \frac{2q_2 \cdot k}{E_g \sqrt{s}} > \delta_c. \quad (2.41)$$

The contribution from the *hard/non-collinear* region, $\hat{\sigma}^{hard/non-coll}$, is finite and we compute it numerically using standard Monte Carlo integration techniques.

In the *hard/collinear* region, one of the conditions in Eq. (2.41) is not satisfied and the hard gluon is emitted collinear to one of the incoming partons. In this region, the initial-state parton i ($i=q, \bar{q}$) is considered to split into a hard parton i' and a collinear gluon g , $i \rightarrow i'g$, with $p_{i'} = zp_i$ and $k = (1-z)p_i$. The matrix element squared for $ij \rightarrow Wb\bar{b} + g$ factorizes into the LO matrix element squared and the Altarelli-Parisi splitting function for $i \rightarrow i'g$, i.e.:

$$\overline{\sum} |\mathcal{A}_{\text{real}}(ij \rightarrow Wb\bar{b} + g)|^2 \xrightarrow{\text{collinear}} (4\pi\alpha_s) \sum_{i'} \overline{\sum} |\mathcal{A}_0(i'j \rightarrow Wb\bar{b})|^2 \frac{2P_{ii'}(z)}{z s_{ig}}, \quad (2.42)$$

with $s_{ig} = 2p_i \cdot k$, and $P_{ii'}(z)$ is the unregulated Altarelli-Parisi splitting function for $q \rightarrow q + g$ at lowest order, including terms of $\mathcal{O}(\epsilon)$ as given by $P_{qq}(z) = P_{qq}^4 + \epsilon P'_{qq}$ with

$$\begin{aligned} P_{qq}^4(z) &= C_F \frac{1+z^2}{1-z}, \\ P'_{qq}(z) &= -C_F(1-z), \end{aligned} \quad (2.43)$$

where $C_F = 1/2(N - 1/N)$. Moreover, in the collinear limit, the $q\bar{q}' \rightarrow Wb\bar{b} + g$ phase space also factorizes as:

$$\begin{aligned} d(PS_4)(ij \rightarrow Wb\bar{b} + g) &\xrightarrow{\text{collinear}} d(PS_3)(i'j \rightarrow Wb\bar{b}) \frac{z d^{(d-1)}k}{(2\pi)^{(d-1)}2E_g} \theta\left(E_g - \delta_s \frac{\sqrt{s}}{2}\right) \times \\ &\quad \theta(\cos \theta_{ig} - (1 - \delta_c)) \\ &\stackrel{d=4-2\epsilon}{=} \frac{\Gamma(1-\epsilon)}{\Gamma(1-2\epsilon)} \frac{(4\pi)^\epsilon}{16\pi^2} z dz ds_{ig} [(1-z)s_{ig}]^{-\epsilon} \theta\left(\frac{(1-z)}{z} s' \frac{\delta_c}{2} - s_{ig}\right), \end{aligned} \quad (2.44)$$

where the integration range for s_{ig} in the collinear region is given in terms of the collinear cutoff, and we have defined $s' = 2p_{i'} \cdot p_j$. The integral over the collinear gluon degrees of freedom can then be performed separately, and this allows us to extract explicitly the collinear singularities of $\hat{\sigma}^{\text{hard}}$. $\hat{\sigma}^{\text{hard/coll}}$ turns out to be of the form [79, 91]:

$$\begin{aligned} \hat{\sigma}^{\text{hard/coll}} &= \left[\frac{\alpha_s}{2\pi} \frac{\Gamma(1-\epsilon)}{\Gamma(1-2\epsilon)} \left(\frac{4\pi\mu^2}{m_b^2} \right)^\epsilon \right] \left(-\frac{1}{\epsilon} \right) \delta_c^{-\epsilon} \times \\ &\quad \left\{ \int_0^{1-\delta_s} dz \left[\frac{(1-z)^2}{2z} \frac{s'}{m_b^2} \right]^{-\epsilon} P_{ii'}(z) \hat{\sigma}^{\text{LO}}(i'j \rightarrow Wb\bar{b}) + (i \leftrightarrow j) \right\}. \end{aligned} \quad (2.45)$$

The upper limit on the z integration ensures the exclusion of the soft gluon region. As usual, these initial-state collinear divergences are absorbed into the parton distribution functions as will be described in detail in the Sec. 2.3.3.

The tree level processes $(q, \bar{q})g \rightarrow Wb\bar{b} + (q', \bar{q}')$

The extraction of the collinear singularities of $\hat{\sigma}_{\text{real}}^{qg}$ is done in the same way as described in the previous subsection for the $q\bar{q}'$ initial state. In the collinear region, $\cos\theta_{iq} > 1 - \delta_c$, the initial state parton i with momentum q_i is considered to split into a hard parton i' and a collinear quark q , $i \rightarrow i'q$, with $q_{i'} = zq_i$ and $k = (1 - z)q_i$. The matrix element squared for $ij \rightarrow Wb\bar{b} + q$ factorizes into the unregulated Altarelli-Parisi splitting functions in d dimensions: $P_{ii'} = P_{ii'}^4 + \epsilon P_{ii'}'$ and the corresponding LO matrix elements squared. The $ij \rightarrow Wb\bar{b} + q$ phase space factorizes into the $i'j \rightarrow Wb\bar{b}$ phase space and the phase space of the collinear quark. As a result, after integrating over the phase space of the collinear quark, the collinear singularity of $\hat{\sigma}_{qg}^{\text{real}}$ can be extracted as:

$$\begin{aligned} \hat{\sigma}_{qg}^{\text{coll}} = & \left[\frac{\alpha_s}{2\pi} \frac{1}{\Gamma(1 - \epsilon)} \left(\frac{4\pi\mu^2}{m_b^2} \right)^\epsilon \right] \left(-\frac{1}{\epsilon} \right) \delta_c^{-\epsilon} \int_0^1 dz \left[\frac{(1 - z)^2}{2z} \frac{s'}{m_b^2} \right]^{-\epsilon} \times \\ & [P_{gq}(z) \hat{\sigma}_{q\bar{q}}^{\text{LO}}(q(q_1)\bar{q}(q_2) \rightarrow Wb\bar{b})] \quad . \end{aligned} \quad (2.46)$$

The collinear radiation of an antiquark in $\bar{q}g \rightarrow Wb\bar{b} + \bar{q}$ is treated analogously. In the case of $(q, \bar{q})g \rightarrow Wb\bar{b} + (q, \bar{q})$ we have the possible splitting $g \rightarrow q\bar{q}$. The $O(1)$ and $O(\epsilon)$ parts of the corresponding splitting function are:

$$\begin{aligned} P_{gq}^4(z) &= \frac{1}{2}(z^2 + (1 - z)^2), \\ P_{gq}'(z) &= -z(1 - z). \end{aligned} \quad (2.47)$$

Again, these initial state collinear divergences are absorbed into the parton distribution functions as will be described in detail in Section 2.3.3.

2.3.3 Total Cross Section for $p\bar{p}(pp) \rightarrow Wb\bar{b}$

As described in Sec. 2.1, the observable total cross section at NLO is obtained by convoluting the NLO parton level cross section with the NLO parton distribution functions $\mathcal{F}_q^{p,\bar{p}}(x, \mu)$, thereby absorbing the remaining initial-state singularities of $\delta\hat{\sigma}_{q\bar{q}}^{\text{NLO}}$ into the quark distribution functions. This can be understood as follows. First the parton cross section is convoluted with the *bare* quark/antiquark distribution functions $\mathcal{F}_{q,\bar{q}}^{p,\bar{p}}(x)$ and subsequently $\mathcal{F}_{q,\bar{q}}^{p,\bar{p}}(x)$ is replaced by the renormalized quark/antiquark distribution functions $\mathcal{F}_{q,\bar{q}}^{p,\bar{p}}(x, \mu)$ defined in some subtraction scheme. Using the \overline{MS} scheme, the scale-dependent NLO quark distribution functions are given in terms of $\mathcal{F}_{q,\bar{q}}^{p,\bar{p}}(x)$ and the QCD NLO parton distribution

function counterterms [79] as follows:

- (a) For the case where an initial state gluon g splits into a $q\bar{q}$ pair ($g \rightarrow q\bar{q}$):

$$\mathcal{F}_{q(\bar{q})}^{p,\bar{p}}(x, \mu_f) = \mathcal{F}_{q(\bar{q})}^{p,\bar{p}}(x) + \left[\frac{\alpha_s}{2\pi} \left(\frac{4\pi\mu_r^2}{\mu_f^2} \right)^\epsilon \frac{1}{\Gamma(1-\epsilon)} \right] \int_x^1 \frac{dz}{z} \left(-\frac{1}{\epsilon} \right) P_{gq(\bar{q})}^4(z) \mathcal{F}_g^{p,\bar{p}}\left(\frac{x}{z}\right) , \quad (2.48)$$

where P_{gq}^4 is defined in Eq. (2.47). This is relevant to process $q(\bar{q})g \rightarrow Wb\bar{b} + q'(\bar{q}')$ when the gluon becomes collinear with the final massless parton.

- (b) For the case of $q \rightarrow qg$ splitting:

$$\begin{aligned} \mathcal{F}_q^{p,\bar{p}}(x, \mu) &= \mathcal{F}_q^{p,\bar{p}}(x) \left[1 - \frac{\alpha_s}{2\pi} \frac{1}{\Gamma(1-\epsilon)} \left(\frac{4\pi\mu_r^2}{\mu_f^2} \right)^\epsilon \left(\frac{1}{\epsilon} \right) C_F \left(2 \ln(\delta_s) + \frac{3}{2} \right) \right] \\ &+ \left[\frac{\alpha_s}{2\pi} \frac{1}{\Gamma(1-\epsilon)} \left(\frac{4\pi\mu_r^2}{\mu_f^2} \right)^\epsilon \right] \int_x^{1-\delta_s} \frac{dz}{z} \left(-\frac{1}{\epsilon} \right) P_{qq}(z) \mathcal{F}_q^{p,\bar{p}}\left(\frac{x}{z}\right) , \end{aligned} \quad (2.49)$$

where the $\mathcal{O}(\alpha_s)$ terms in the previous equation are calculated from the $\mathcal{O}(\alpha_s)$ corrections to the $q \rightarrow qg$ splitting, in the two-cutoff PSS formalism, and $P_{qq}(z)$ is the Altarelli-Parisi splitting function of Eq. (2.43). This is relevant to process $q\bar{q}' \rightarrow Wb\bar{b} + g$ when the final gluon goes soft or when one of the initial partons become collinear with the gluon.

When convoluting the parton cross section with the renormalized quark/antiquark distribution functions of Eq. (2.49), the IR singular counterterm, that is the first term of the RHS of Eq. (2.49), exactly cancels the remaining IR poles of $\hat{\sigma}_{q\bar{q}}^{\text{virt}} + \hat{\sigma}^{\text{soft}}$ and $\hat{\sigma}^{\text{hard/coll}}$. Finally, the complete $\mathcal{O}(\alpha_s^3)$ inclusive total cross section for $p\bar{p}(pp) \rightarrow Wb\bar{b}$ in the \overline{MS} factorization scheme can be written as follows:

$$\sigma^{\text{NLO}} = \sigma_{q\bar{q}'}^{\text{NLO}} + \sigma_{qg+\bar{q}g}^{\text{NLO}} , \quad (2.50)$$

with $\sigma_{q\bar{q}'}^{\text{NLO}}$ and σ_{qg}^{NLO} defined in the following, Eqs. (2.51) and (2.53) respectively.

$$\begin{aligned}
\sigma_{q\bar{q}'}^{\text{NLO}} &= \sum_{q\bar{q}'} \int dx_1 dx_2 \mathcal{F}_q^p(x_1, \mu) \mathcal{F}_{\bar{q}'}^{\bar{p}(p)}(x_2, \mu) \left[\hat{\sigma}_{q\bar{q}'}^{\text{LO}}(x_1, x_2, \mu) + \hat{\sigma}_{q\bar{q}'}^{\text{virt}}(x_1, x_2, \mu) + \hat{\sigma}'^{\text{soft}}(x_1, x_2, \mu) \right] \\
&+ \frac{\alpha_s}{2\pi} C_F \sum_{q\bar{q}'} \int dx_1 dx_2 \left\{ \int_{x_1}^{1-\delta_s} \frac{dz}{z} \left[\mathcal{F}_q^p\left(\frac{x_1}{z}, \mu\right) \mathcal{F}_{\bar{q}'}^{\bar{p}(p)}(x_2, \mu) + \mathcal{F}_q^{\bar{p}(p)}(x_2, \mu) \mathcal{F}_{\bar{q}'}^p\left(\frac{x_1}{z}, \mu\right) \right] \right. \\
&\quad \times \hat{\sigma}_{q\bar{q}'}^{\text{LO}}(x_1, x_2, \mu) \left[\frac{1+z^2}{1-z} \ln\left(\frac{s}{\mu^2} \frac{(1-z)^2}{z} \frac{\delta_c}{2}\right) + 1-z \right] + (1 \leftrightarrow 2) \left. \right\} \\
&+ \sum_{q\bar{q}'} \int dx_1 dx_2 \mathcal{F}_q^p(x_1, \mu) \mathcal{F}_{\bar{q}'}^{\bar{p}(p)}(x_2, \mu) \hat{\sigma}^{\text{hard/non-coll}}(x_1, x_2, \mu) ,
\end{aligned} \tag{2.51}$$

with

$$\hat{\sigma}'^{\text{soft}} = \hat{\sigma}^{\text{soft}} + \frac{\alpha_s}{2\pi} \frac{1}{\Gamma(1-\epsilon)} (4\pi)^\epsilon \left(\frac{1}{\epsilon}\right) C_F [4 \ln(\delta_s) + 3] . \tag{2.52}$$

$$\begin{aligned}
\sigma_{qg+\bar{q}g}^{\text{NLO}} &= \frac{\alpha_s}{2\pi} \sum_{i=q,\bar{q}} \int dx_1 dx_2 \left\{ \int_{x_1}^1 \frac{dz}{z} \mathcal{F}_g^p\left(\frac{x_1}{z}, \mu\right) \mathcal{F}_i^{\bar{p}(p)}(x_2, \mu) \times \right. \\
&\quad \hat{\sigma}_{q\bar{q}}^{\text{LO}}(x_1, x_2, \mu) \left[P_{gi}^4(z) \ln\left(\frac{s}{\mu^2} \frac{(1-z)^2}{z} \frac{\delta_c}{2}\right) - P'_{gi}(z) \right] + (1 \leftrightarrow 2) \left. \right\} \\
&+ \sum_{i=q,\bar{q}} \int dx_1 dx_2 \left\{ \mathcal{F}_i^p(x_1, \mu) \mathcal{F}_g^{\bar{p}(p)}(x_2, \mu) \hat{\sigma}_{ig}^{\text{non-coll}}(x_1, x_2, \mu) + (1 \leftrightarrow 2) \right\} .
\end{aligned} \tag{2.53}$$

We note that σ^{NLO} is finite, since, after mass factorization, both soft and collinear singularities have been canceled between $\hat{\sigma}_{q\bar{q}}^{\text{virt}} + \hat{\sigma}'^{\text{soft}}$ and $\hat{\sigma}^{\text{hard/coll}}$. Note that the second term in Eq. (2.51), which is proportional to $\ln\left(\frac{s}{\mu^2}\right)$, corresponds exactly to the second and third terms of Eq. (2.7), as predicted by renormalization group arguments.

To finish this Section, and before we discuss in detail in Chapter 3 the numerical results for the NLO total cross section for $p\bar{p} \rightarrow Wb\bar{b}$, we first demonstrate that σ^{NLO} does not depend on the arbitrary cutoffs of the PSS method, i.e. on the soft and hard/collinear cutoffs δ_s and δ_c . We note that the cancellation of the cutoff dependence at the level of the total NLO cross section is a very delicate issue, since it involves both analytical and numerical contributions. It is crucial to study the behavior of σ^{NLO} in a region where the cutoffs are small enough to justify the approximations used in the analytical calculation of the IR-divergent part of $\hat{\sigma}_{q\bar{q}}^{\text{real}}$, but not so small to cause large numerical cancellations. The Monte Carlo phase space

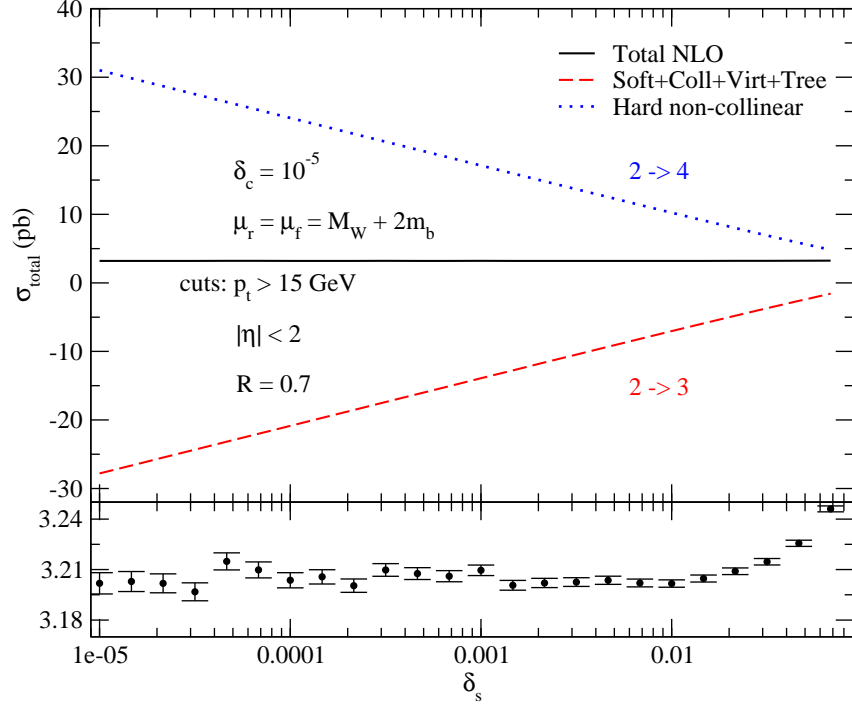


Figure 2.8: Dependence of $\sigma^{\text{NLO}}(p\bar{p} \rightarrow Wb\bar{b})$ on the δ_s PSS parameter, when δ_c is fixed at $\delta_c = 10^{-5}$. In the upper window we illustrate separately the cutoff dependence of the soft and hard-collinear part ($2 \rightarrow 3$, red dashed curve) and of the hard non-collinear part ($2 \rightarrow 4$, blue dotted curve) of the real corrections to the total cross section. The $2 \rightarrow 3$ curve also includes those parts of the $2 \rightarrow 3$ NLO cross section that do not depend on δ_c and δ_s , i.e. the tree level and one-loop virtual contributions. The sum of all the contributions corresponds to the black solid line. The lower window shows a blow-up of the black solid line in the upper plot, to illustrate the stability of the result. The error bars indicate the statistical uncertainty of the Monte Carlo integration.

integration has been performed using the adaptive multi-dimensional integration routine VEGAS [71].

Figures 2.8 and 2.9 illustrate the dependence of the total cross section on the two-cutoffs of the PSS method, using the setup outlined in Section 3.1. In Figure 2.8, we show the dependence of σ^{NLO} on the soft cutoff, δ_s , for a fixed value of the hard/collinear cutoff, $\delta_c = 10^{-5}$. In Figure 2.9, we show the dependence of σ^{NLO} on the hard/collinear cutoff, δ_c , for a fixed value of the soft cutoff, $\delta_s = 10^{-3}$. In the upper window of Figure 2.8(2.9) we illustrate

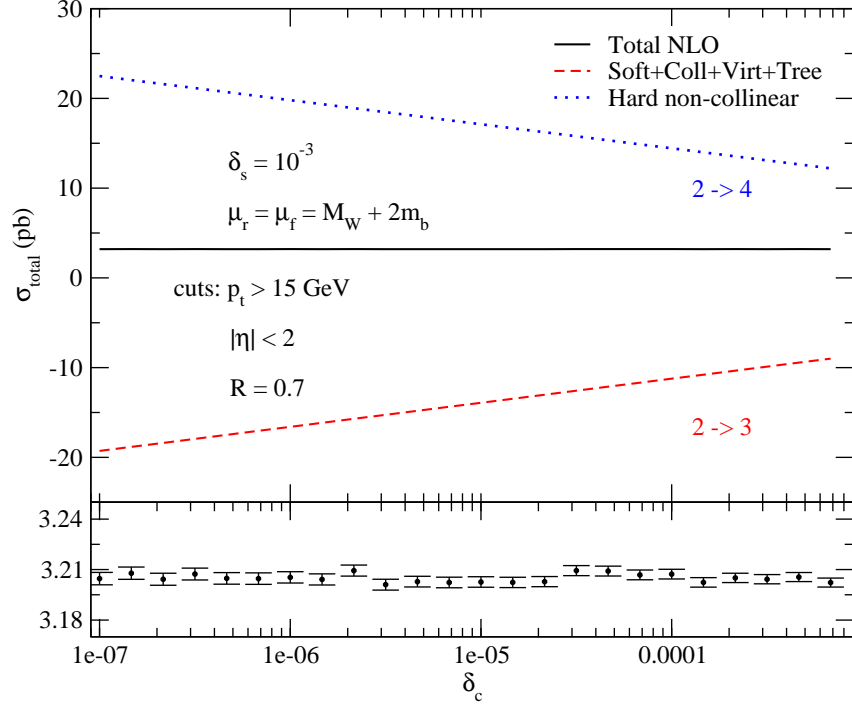


Figure 2.9: Dependence of $\sigma^{\text{NLO}}(p\bar{p} \rightarrow Wb\bar{b})$ on the δ_c PSS parameter, when δ_s is fixed at $\delta_s = 10^{-3}$. In the upper window we illustrate separately the cutoff dependence of the soft and hard-collinear part ($2 \rightarrow 3$, red dashed curve) and of the hard non-collinear part ($2 \rightarrow 4$, blue dotted curve) of the real corrections to the total cross section. The $2 \rightarrow 3$ curve also includes those parts of the $2 \rightarrow 3$ NLO cross section that do not depend on δ_c and δ_s , i.e. the tree level and one-loop virtual contributions. The sum of all the contributions corresponds to the black solid line. The lower window shows a blow-up of the black solid line in the upper plot, to illustrate the stability of the result. The error bars indicate the statistical uncertainty of the Monte Carlo integration.

the cancellation of the $\delta_s(\delta_c)$ dependence between $\sigma_{\text{soft}} + \sigma_{\text{hard/coll}}$ and $\sigma_{\text{hard/non-coll}}$, while in the lower window we show, on a larger scale, σ^{NLO} with the statistical errors from the Monte Carlo integration. As before, σ^{NLO} also includes the contribution from the LO and the virtual cross sections, which are both cutoff-independent. For δ_s in the range $10^{-5} - 10^{-2}$ and δ_c in the range $10^{-7} - 10^{-3}$, a clear plateau is reached and the NLO total cross section is independent of the arbitrary cutoffs of the two-cutoff PSS method. All the results presented in Chapter 3 are obtained using the two-cutoff PSS method with $\delta_s = 10^{-3}$ and $\delta_c = 10^{-5}$.

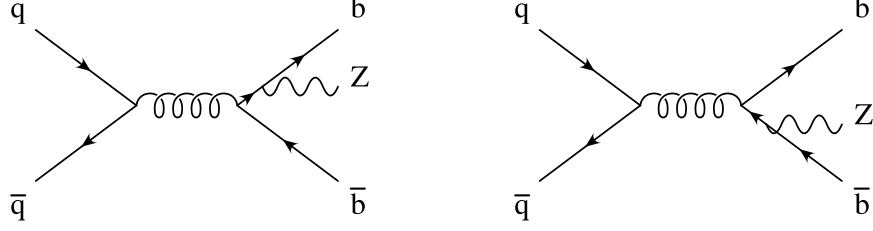


Figure 2.10: Tree level Feynman diagrams for $q\bar{q} \rightarrow Zb\bar{b}$, with Z emitted from final fermion line.

2.4 Calculation of NLO QCD Corrections to $Zb\bar{b}$ Production at Hadron Colliders

In this Section we present in detail the calculation of the partonic total and differential cross section $\hat{\sigma}^{\text{NLO}}(ij \rightarrow Zb\bar{b})$ [92], which can be decomposed as in Eq. (2.4). We work throughout in the 4-flavor number scheme, where only 4 massless quark flavors can be excited in the initial state, as we consider full b -quark mass contributions to the partonic cross section.

There are two subprocesses contributing to $\hat{\sigma}^{\text{LO}}$ in Eq. (2.4), namely $q\bar{q} \rightarrow Zb\bar{b}$ and $gg \rightarrow Zb\bar{b}$.

The tree level Feynman diagrams contributing to the LO cross section for subprocess $q\bar{q} \rightarrow Zb\bar{b}$ are shown in Figures 2.2 (with $V = Z$) and 2.10, when the Z weak boson is emitted from initial and final fermion lines respectively. In Figure 2.11 we show the tree level Feynman diagrams contributing to the $gg \rightarrow Zb\bar{b}$ subprocess. The corresponding amplitudes are presented in Section 2.4.1 and more details are summarized in Appendix B.

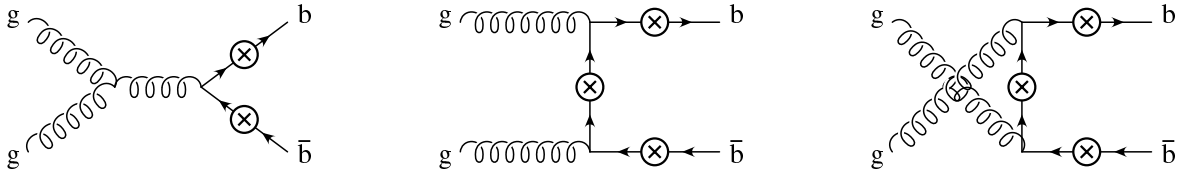


Figure 2.11: Tree level Feynman diagrams for $gg \rightarrow Zb\bar{b}$. The circled crosses correspond to all possible insertions of the Z boson, each one representing a different diagram.

We notice that the tree level diagrams for $q\bar{q}' \rightarrow Wb\bar{b}$ are a subset of the diagrams for

$q\bar{q} \rightarrow Zb\bar{b}$, namely the ones in which the Z boson is emitted from the initial quarks legs. The same holds at NLO: the NLO QCD corrections to $q\bar{q}' \rightarrow Wb\bar{b}$ discussed in Section 2.3 are a subset of the NLO QCD corrections to $q\bar{q} \rightarrow Zb\bar{b}$ discussed in this Section. The results derived for $q\bar{q}' \rightarrow Wb\bar{b}$ can be automatically translated to the $q\bar{q} \rightarrow Zb\bar{b}$ case by keeping the contributions of the vector and axial vector parts of the $Wq\bar{q}'$ vertex separate and substituting the corresponding values of vector and axial vector couplings of the $Zq\bar{q}$ vertex, as well as making the necessary changes to the PDFs of the initial partons in the hadronic cross section.

At NLO one has to consider five subprocesses: $q\bar{q} \rightarrow Zb\bar{b}$ and $gg \rightarrow Zb\bar{b}$ contributing at tree level to $\hat{\sigma}^{\text{LO}}$ in Eq. (2.4) and at one-loop to $\hat{\sigma}^{\text{virt}}$ in Eq. (2.5), as well as $q\bar{q} \rightarrow Zb\bar{b} + g$, $q(\bar{q})g \rightarrow Zb\bar{b} + q(\bar{q})$ and $gg \rightarrow Zb\bar{b} + g$ contributing at tree level to $\hat{\sigma}^{\text{real}}$ in Eq. (2.5).

The rest of this Section is organized as follows. We present in Section 2.4.1 results for the LO amplitudes. In Sections 2.4.2 and 2.4.3 we shall present results for the $\mathcal{O}(\alpha_s)$ virtual corrections to $Zb\bar{b}$ hadronic production. For details on the $\mathcal{O}(\alpha_s^3)$ subprocess $q\bar{q} \rightarrow Zb\bar{b} + g$ we refer the reader to Sections 2.3.2 and 2.3.3, as results are analogous to the $\mathcal{O}(\alpha_s^3)$ subprocess $q\bar{q}' \rightarrow Wb\bar{b} + g$. In Sections 2.4.4 and Section 2.4.5 we shall discuss the $\mathcal{O}(\alpha_s^3)$ subprocess $gg \rightarrow Zb\bar{b} + g$. $\mathcal{O}(\alpha_s^3)$ real subprocesses initiated by $q(\bar{q})g$ for $Zb\bar{b}$ are slightly different in structure with respect to the similar ones encountered in the $Wb\bar{b}$, as the LO structure of the former is more complex than the latter. For that reason we discuss their structure in detail in Sections 2.4.4 and 2.4.5.

2.4.1 Tree Level Cross Section for $Zb\bar{b}$ Hadronic Production

The contributing tree level Feynman diagrams for the LO $q\bar{q} \rightarrow Zb\bar{b}$ process are shown in Figures 2.2 (with $V = Z$) and 2.10 for subprocess $q\bar{q} \rightarrow Zb\bar{b}$ with the Z weak boson emitted from initial and final fermion lines, respectively. Given the assignment of momenta:

$$q(q_1)\bar{q}(q_2) \rightarrow b(p_b) + \bar{b}(p_{\bar{b}}) + Z(p_Z) \ ,$$

the LO amplitude can be written as:

$$\begin{aligned}
\mathcal{A}_0(q\bar{q} \rightarrow Zb\bar{b}) = & ig_s^2 \frac{g_w}{\cos \theta_w} \epsilon_\mu^*(p_Z) \frac{g_{\nu\rho}}{(p_b + p_{\bar{b}})^2} \bar{u}_b \gamma^\rho v_{\bar{b}} t_{ij}^a t_{kl}^a \\
& \left[\bar{v}_{\bar{q}} \gamma^\mu (g_V^q + g_A^q \gamma_5) \frac{-\not{q}_2 + \not{p}_Z}{(-q_2 + p_Z)^2} \gamma^\nu u_q \right. \\
& \left. + \bar{v}_{\bar{q}} \gamma^\nu \frac{\not{q}_1 - \not{p}_Z}{(q_1 - p_Z)^2} \gamma^\mu (g_V^q + g_A^q \gamma_5) u_q \right] \\
& + ig_s^2 \frac{g_w}{\cos \theta_w} \epsilon_\mu^*(p_Z) \frac{g_{\nu\rho}}{(q_1 + q_2)^2} \bar{v}_{\bar{q}} \gamma^\rho u_q t_{ij}^a t_{kl}^a \\
& \left[\bar{u}_b \gamma^\mu (g_V^b + g_A^b \gamma_5) \frac{\not{p}_b + \not{p}_Z + m_b}{[(p_b + p_Z)^2 - m_b^2]} \gamma^\nu v_{\bar{b}} \right. \\
& \left. + \bar{u}_b \gamma^\nu \frac{-\not{p}_{\bar{b}} - \not{p}_Z + m_b}{[(-p_{\bar{b}} - p_Z)^2 - m_b^2]} \gamma^\mu (g_V^b + g_A^b \gamma_5) v_{\bar{b}} \right]. \tag{2.54}
\end{aligned}$$

where g_s and g_w are the strong and weak coupling constant, respectively, $t^a = \lambda^a/2$ are given in terms of the Gell-Mann matrices λ^a and θ_w is the weak angle. The vector, g_V^f , and axial, g_A^f , couplings for the Zff vertex are given explicitly in Eq. (A.28) (for more details see Appendices A and B).

...

The tree level amplitude for the process

$$g^a(q_1) + g^b(q_2) \rightarrow b(p_b) + \bar{b}(p_{\bar{b}}) + Z(p_Z),$$

where $q_1 + q_2 = p_b + p_{\bar{b}} + p_Z$ and a, b denote the color of the incoming gluons, is obtained from the three classes of Feynman diagrams represented in Figure 2.11, identified as s -channel, t -channel, and u -channel diagrams, respectively. We find it convenient to organize the color structure of both the tree level amplitude and the one-loop virtual amplitude in terms of only two color factors, one symmetric and one antisymmetric in the color indices of the initial gluons. Following this prescription, the tree level amplitude for $gg \rightarrow Zb\bar{b}$ can be written as:

$$\mathcal{A}_0 = \mathcal{A}_0^{nab}[t^a, t^b] + \mathcal{A}_0^{ab}\{t^a, t^b\}, \tag{2.55}$$

where $t^{a,b} = \lambda^{a,b}/2$ are given in terms of the Gell-Mann matrices $\lambda^{a,b}$ ². \mathcal{A}_0^{ab} and \mathcal{A}_0^{nab} correspond to the terms in the amplitude that are proportional, respectively, to the *abelian*

²We note that the one-loop virtual amplitude can be expressed in terms of the same antisymmetric color factor $[t^a, t^b]$ and a symmetric color factor made of $\{t^a, t^b\}$ and δ^{ab} .

(or symmetric) and *non-abelian* (or antisymmetric) color factors and are given by:

$$\mathcal{A}_0^{ab} = \frac{1}{2}(\mathcal{A}_{0,t} + \mathcal{A}_{0,u}) \quad , \quad \mathcal{A}_0^{nab} = \mathcal{A}_{0,s} + \frac{1}{2}(\mathcal{A}_{0,t} - \mathcal{A}_{0,u}) \quad , \quad (2.56)$$

where $\mathcal{A}_{0,s}$, $\mathcal{A}_{0,t}$, and $\mathcal{A}_{0,u}$ are the amplitudes corresponding to the sum of the s -channel, t -channel, and u -channel tree level diagrams in Figure 2.11. Explicit expressions for them are shown in Eqs. (B.3)-(B.5).

Because of the *orthogonality* between symmetric and antisymmetric color factors, the tree level amplitude squared takes the very simple form:

$$\overline{\sum} |\mathcal{A}_0|^2 = \overline{\sum} \left[\frac{N}{2}(N^2 - 1) (|\mathcal{A}_0^{nab}|^2 + |\mathcal{A}_0^{ab}|^2) - \frac{1}{N}(N^2 - 1)|\mathcal{A}_0^{ab}|^2 \right] \quad . \quad (2.57)$$

The partonic LO cross section is obtained by integrating $|\mathcal{A}_0|^2$ over the $Zb\bar{b}$ final state phase space, as shown in Eq. (2.14). We perform the sum over polarizations of the Z gauge boson using the prescription shown in Eq. (2.15), keeping both terms.

When averaging over the polarization states of the initial gluons (in the $gg \rightarrow Zb\bar{b}$ case), the polarization sum of the gluon polarization vectors, $\epsilon_\mu(q_1, \lambda_1)$ and $\epsilon_\nu(q_2, \lambda_2)$, has to be performed in such a way that only the physical (transverse) polarization states of the gluons contribute to the matrix element squared. We adopt the general prescription:

$$\sum_{\lambda_i=1,2} \epsilon_\mu(q_i, \lambda_i) \epsilon_\nu^*(q_i, \lambda_i) = -g_{\mu\nu} + \frac{n_{i\mu}q_{i\nu} + q_{i\mu}n_{i\nu}}{n_i \cdot q_i} - \frac{n_i^2 q_{i\mu}q_{i\nu}}{(n_i \cdot q_i)^2} \quad , \quad (2.58)$$

where $i=1,2$ and the arbitrary vectors n_i have to satisfy the relations:

$$n_i^\mu \sum_{\lambda_i=1,2} \epsilon_\mu(q_i, \lambda_i) \epsilon_\nu^*(q_i, \lambda_i) = 0 \quad , \quad n_i^\nu \sum_{\lambda_i=1,2} \epsilon_\mu(q_i, \lambda_i) \epsilon_\nu^*(q_i, \lambda_i) = 0 \quad , \quad (2.59)$$

together with $n_i \cdot q_j \neq 0$ and $n_1 \neq n_2$. We choose $n_1 = q_2$ and $n_2 = q_1$, such that:

$$\sum_{\lambda_i=1,2} \epsilon_\mu(q_i, \lambda_i) \epsilon_\nu^*(q_i, \lambda_i) = -g_{\mu\nu} + \frac{q_{1\mu}q_{2\nu} + q_{2\mu}q_{1\nu}}{q_1 \cdot q_2} \quad . \quad (2.60)$$

Finally, the entire calculation is performed using the Feynman gauge for both internal and external gluons (for more details see Appendix A).

2.4.2 Virtual Corrections to $q\bar{q} \rightarrow Zb\bar{b}$

The $\mathcal{O}(\alpha_s)$ virtual corrections to the $q\bar{q} \rightarrow Zb\bar{b}$ tree level subprocess consist of the self energy, vertex, box and pentagon diagrams illustrated in Figures 2.3-2.6, when the Z weak boson is

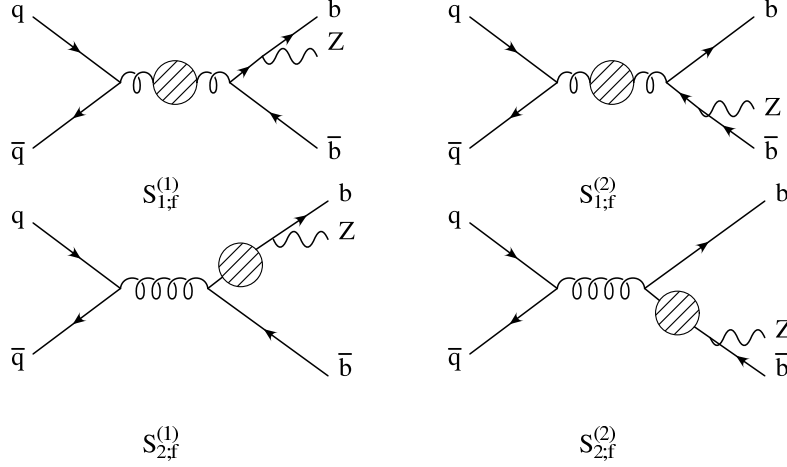


Figure 2.12: Gluon ($S_{1,f}^{(1,2)}$) and b -quark ($S_{2,f}^{(1,2)}$) $\mathcal{O}(\alpha_s)$ self energy corrections contributing to the $q\bar{q} \rightarrow Z b\bar{b}$ subprocess at NLO, when the Z boson is emitted from the final fermion line. The shaded blobs denote standard one-loop QCD corrections to the gluon and quark propagators respectively.

emitted from the initial fermion line (q or \bar{q}), and in Figures 2.12-2.15, when it is emitted from the final fermion line (b or \bar{b}). The contributions to the virtual amplitude squared of Eq. (2.5) can then be written as:

$$\overline{\sum} |\mathcal{A}_{\text{virt}}(q\bar{q} \rightarrow Z b\bar{b})|^2 = \sum_{D_i} \overline{\sum} \left(\mathcal{A}_0 \mathcal{A}_{D_i}^\dagger + \mathcal{A}_0^\dagger \mathcal{A}_{D_i} \right) = \sum_{D_i} \overline{\sum} 2\mathcal{R}e \left(\mathcal{A}_0 \mathcal{A}_{D_i}^\dagger \right), \quad (2.61)$$

where \mathcal{A}_0 is the tree level amplitude, corresponding to the diagrams shown in Figures 2.2 and 2.10, and \mathcal{A}_{D_i} denotes the amplitude for a one-loop diagram, with D_i running over all self-energy, vertex, box and pentagon diagrams illustrated in Figures 2.3, 2.4, 2.5, 2.6, 2.12, 2.13, 2.14 and 2.15.

The calculation of each virtual diagram (\mathcal{A}_{D_i}) is performed in the way explained in Sections 2.2.2 and 2.3.1. As mentioned there, one of the most challenging parts of the calculation is related to controlling the spurious divergences that appear when reducing tensor Feynman integrals. This is specially true when considering pentagon diagrams, like the ones in Figures 2.6 and 2.15. There were only two pentagon diagrams in the $W b\bar{b}$ calculation, but that number is doubled just by considering the one-loop diagrams for $q\bar{q} \rightarrow Z b\bar{b}$, and we will see in Section 2.4.3 that when considering one-loop diagrams for $gg \rightarrow Z b\bar{b}$ one has to add twelve more pentagon diagrams, some of them containing up to $E4$ -PV functions

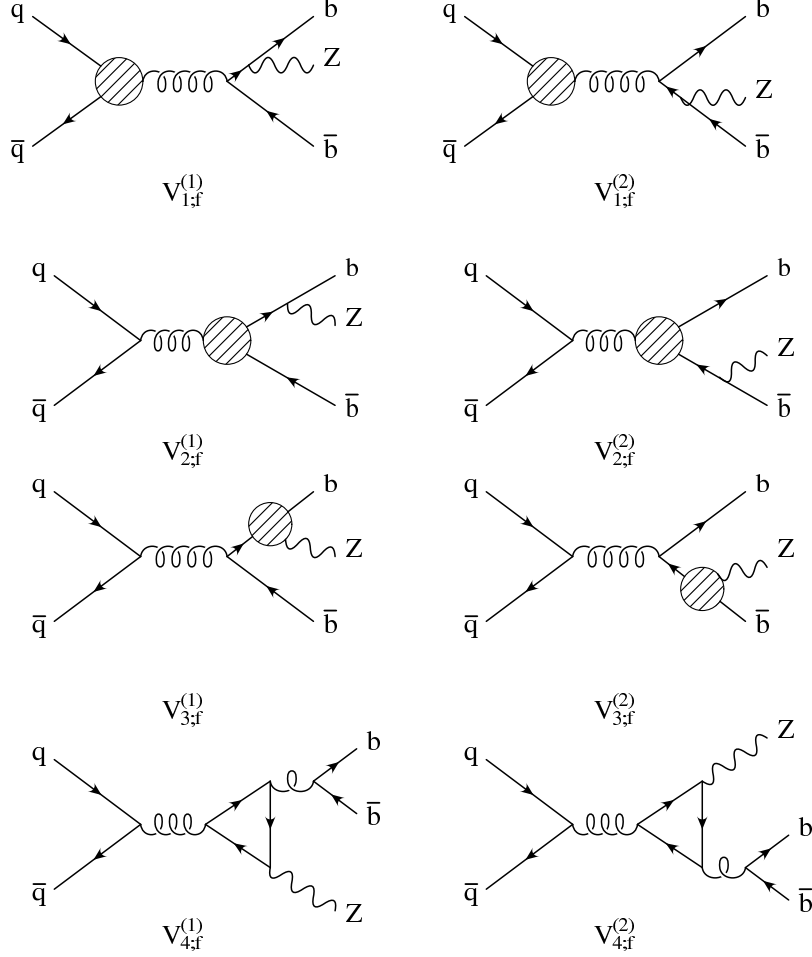


Figure 2.13: $\mathcal{O}(\alpha_s)$ vertex corrections contributing to the $q\bar{q} \rightarrow Zb\bar{b}$ subprocess at NLO when the Z boson is emitted from the final fermion line or from a closed fermion line. The shaded blobs denote standard one-loop QCD corrections to the $q\bar{q}g$ ($V_{1,f}^{(1,2)}$), $b\bar{b}g$ ($V_{2,f}^{(1,2)}$) and $q\bar{q}Z$ ($V_{3,f}^{(1,2)}$) vertices respectively. $V_{4,f}^{(1,2)}$ are b - and t -fermion loop vertices which are UV and IR finite (contributions of quarks from first and second family vanish).

(see Appendix D). All this increases considerably the stability problem. In the case of pentagon diagrams it is convenient to reduce consistently all E -PV functions by canceling systematically, at the level of the amplitude squared in Eq. (2.61), all possible vector products containing the loop momentum in the numerator with some denominators. This is possible as, in the pentagon topology of our process, each leg has an outgoing momentum which is on-shell, corresponding basically to one of the external initial or final particles of the

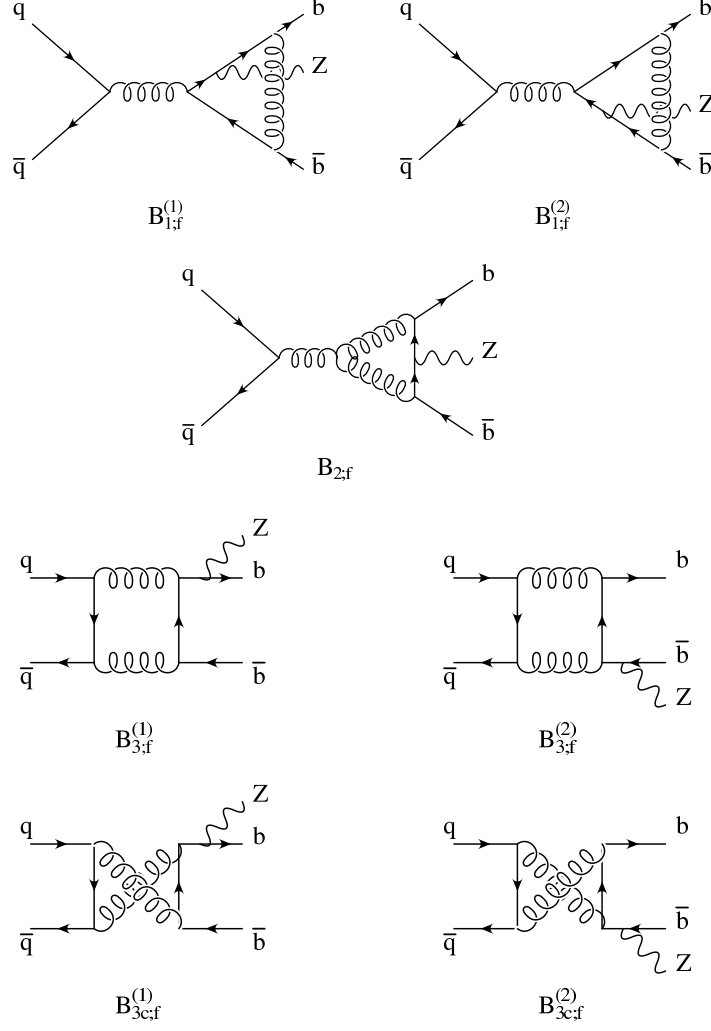


Figure 2.14: $\mathcal{O}(\alpha_s)$ box diagram corrections contributing to the $q\bar{q} \rightarrow Z b\bar{b}$ subprocess at NLO, when the Z boson emitted from the final fermion lines (b or \bar{b}).

subprocess. One then ends with expressions for each pentagon diagram containing purely scalar pentagon integrals, or tensor integrals with fewer than five denominators, improving considerably the behavior of the numerical code. We checked analytically these reductions with the non-reduced expressions by using the full reduction of all tensor integrals to scalar integrals, and found agreement. Another gain we had by doing the aforementioned reductions was a considerable speed up of all analytical and numerical computations.

In Section 2.4.2.1 we present the UV singularity structure of $\hat{\sigma}^{\text{virt}}(q\bar{q} \rightarrow Z b\bar{b})$ as it has a

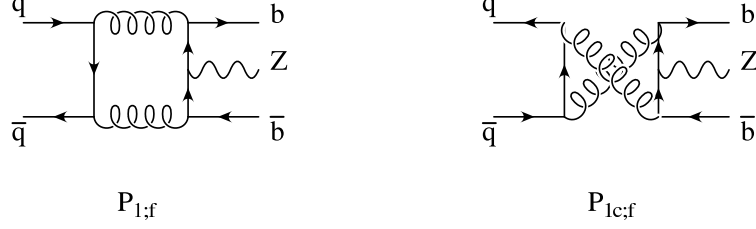


Figure 2.15: $\mathcal{O}(\alpha_s)$ pentagon diagram corrections contributing to the $q\bar{q} \rightarrow Zb\bar{b}$ subprocess at NLO, when the Z boson emitted from the final fermion lines (b or \bar{b}).

slightly different structure to what is discussed in Sections 2.3.1.1 due to the Z boson emission from the final fermion lines. The IR divergent structure on the other side is analogous to that presented in Section 2.3.1.2, to which we refer the reader for details.

2.4.2.1 Virtual corrections: UV singularities and counterterms

The UV singularities of the $\mathcal{O}(\alpha_s^3)$ total cross section for $q\bar{q} \rightarrow Zb\bar{b}$ originate from self-energy and vertex virtual corrections shown in Figures 2.3, 2.4, 2.12 and 2.13. These singularities are renormalized by introducing counterterms for the wave function of the external fields ($\delta Z_2^{(q)}$, $\delta Z_2^{(b)}$), the bottom-quark mass (δm_b), and the strong coupling constant (δZ_{α_s}). If we denote by $\Delta_{\text{UV}}(S_i^{(1,2)})$ and $\Delta_{\text{UV}}(V_i^{(1,2)})$ the UV-divergent contribution of each self-energy ($S_i^{(1,2)}$) or vertex diagram ($V_i^{(1,2)}$) to the virtual amplitude squared (see Eq. (2.61)), we can write the UV-singular part of the total virtual amplitude squared as:

$$\begin{aligned}
\overline{\sum |\mathcal{A}_{\text{virt}}^{\text{UV}}|^2} &= \overline{\sum |\mathcal{A}_0|^2} \left\{ \sum_{i=1}^2 \Delta_{\text{UV}} \left(S_i^{(1)} + S_i^{(2)} + S_{i;\text{f}}^{(1)} + S_{i;\text{f}}^{(2)} \right) \right. \\
&\quad + \sum_{i=1}^3 \Delta_{\text{UV}} \left(V_i^{(1)} + V_i^{(2)} + V_{i;\text{f}}^{(1)} + V_{i;\text{f}}^{(2)} \right) \\
&\quad \left. + 2 \left[\left(\delta Z_2^{(q)} \right)_{\text{UV}} + \left(\delta Z_2^{(b)} \right)_{\text{UV}} + \delta Z_{\alpha_s} \right] \right\} . \tag{2.62}
\end{aligned}$$

We denote by $|\mathcal{A}_0|^2$ the matrix element squared of the tree-level amplitude for $q\bar{q} \rightarrow Zb\bar{b}$, computed in $d = 4$ dimensions, as presented in Eq. (2.54).

The UV-divergent contributions due to the individual diagrams are explicitly given by:

$$\begin{aligned}
\Delta_{\text{UV}} \left(S_1^{(1)} + S_1^{(2)} + S_{1;\text{f}}^{(1)} + S_{1;\text{f}}^{(2)} \right) &= \frac{\alpha_s}{2\pi} \left[\mathcal{N}_s \left(\frac{5}{3}N - \frac{2}{3}n_{lf} \right) - \mathcal{N}_b \frac{2}{3} \right] \left(\frac{1}{\epsilon_{\text{UV}}} \right) , \\
\Delta_{\text{UV}} \left(S_2^{(1)} + S_2^{(2)} + S_{2;\text{f}}^{(1)} + S_{2;\text{f}}^{(2)} \right) &= -\frac{\alpha_s}{2\pi} \mathcal{N}_b \left(\frac{N}{2} - \frac{1}{2N} \right) \left(\frac{1}{\epsilon_{\text{UV}}} \right) , \\
\Delta_{\text{UV}} \left(V_1^{(1)} + V_1^{(2)} + V_{1;\text{f}}^{(1)} + V_{1;\text{f}}^{(2)} \right) &= \frac{\alpha_s}{2\pi} \mathcal{N}_s \left(\frac{3N}{2} - \frac{1}{2N} \right) \left(\frac{1}{\epsilon_{\text{UV}}} \right) , \\
\Delta_{\text{UV}} \left(V_2^{(1)} + V_2^{(2)} + V_{2;\text{f}}^{(1)} + V_{2;\text{f}}^{(2)} \right) &= \frac{\alpha_s}{2\pi} \mathcal{N}_b \left(\frac{3N}{2} - \frac{1}{2N} \right) \left(\frac{1}{\epsilon_{\text{UV}}} \right) , \\
\Delta_{\text{UV}} \left(V_3^{(1)} + V_3^{(2)} + V_{3;\text{f}}^{(1)} + V_{3;\text{f}}^{(2)} \right) &= \frac{\alpha_s}{2\pi} \mathcal{N}_b \left(\frac{N}{2} - \frac{1}{2N} \right) \left(\frac{1}{\epsilon_{\text{UV}}} \right) , \tag{2.63}
\end{aligned}$$

where \mathcal{N}_s and \mathcal{N}_b are standard normalization factors defined in Eq. (2.19).

We define the required counterterms according to the following convention. For the external fields, we fix the wave-function renormalization constants of the external fields ($Z_2^{(i)} = 1 + \delta Z_2^{(i)}$, $i=q, b$) using on-shell subtraction, given expressions as in Eq. (2.20). We notice that both $\delta Z_2^{(q)}$ and $\delta Z_2^{(b)}$, as well as some of the vertex corrections ($V_1^{(1,2)}$, $V_{1;\text{f}}^{(1,2)}$ and $V_2^{(1,2)}$, $V_{2;\text{f}}^{(1,2)}$), have also IR singularities. In this section, we limit the discussion to the UV singularities only, while the IR structure of these terms are analogous to what is shown in Section 2.3.1.2.

We define the subtraction condition for the bottom-quark mass m_b in such a way that m_b is the pole mass, in which case the bottom-mass counterterm is given by:

$$\frac{\delta m_b}{m_b} = -\frac{\alpha_s}{4\pi} \mathcal{N}_b \left(\frac{N}{2} - \frac{1}{2N} \right) \left(\frac{3}{\epsilon_{\text{UV}}} + 4 \right) , \tag{2.64}$$

this counterterm have been already included into the term $\Delta_{\text{UV}} \left(S_2^{(1)} + S_2^{(2)} + S_{2;\text{f}}^{(1)} + S_{2;\text{f}}^{(2)} \right)$ in Eq. (2.63).

The structure of the remaining counterterms that appear in this case is the same as presented in Section 2.3.1.1, and we refer the reader to it.

2.4.3 Virtual Corrections to $gg \rightarrow Zb\bar{b}$

The $\mathcal{O}(\alpha_s)$ virtual corrections to the $gg \rightarrow Zb\bar{b}$ tree level subprocess consist of the self-energy, vertex, box, and pentagon diagrams illustrated in Figures 2.16-2.19. The $\mathcal{O}(\alpha_s^3)$ contribution

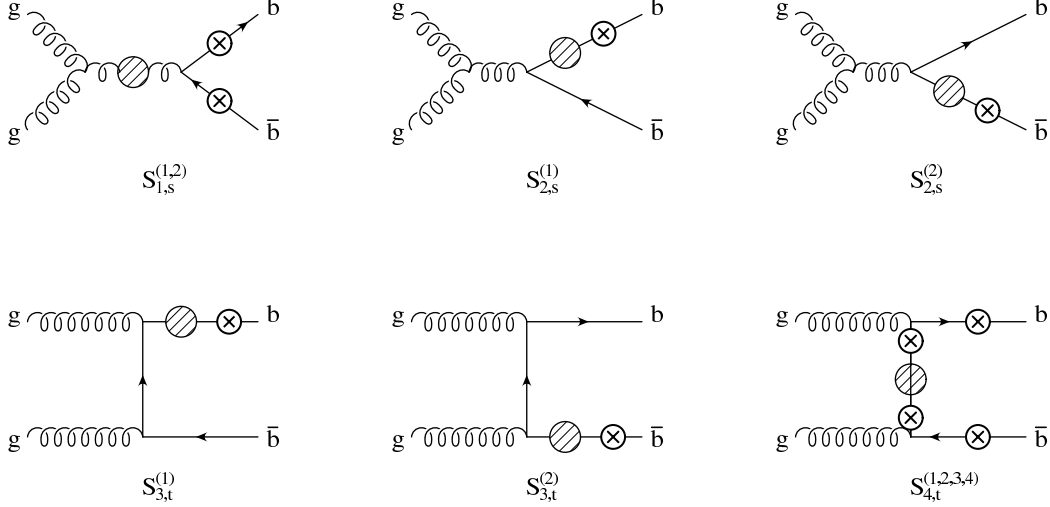


Figure 2.16: Gluon ($S_{1,s}^{(1,2)}$) and quark ($S_{1,s}^{(1,2)}$, $S_{2,s}^{(1,2)}$, $S_{3,(t,u)}^{(1,2)}$, and $S_{4,(t,u)}^{(1,2,3,4)}$) $\mathcal{O}(\alpha_s)$ self energy corrections contributing to the $gg \rightarrow Zb\bar{b}$ subprocess at NLO. The circled crosses correspond to all possible insertions of the Z boson, each one representing a different diagram.

to the virtual amplitude squared of Eq. (2.5) can then be written as:

$$\overline{\sum} |\mathcal{A}_{\text{virt}}(gg \rightarrow Zb\bar{b})|^2 = \sum_{D_{i,j}} \overline{\sum} \left(\mathcal{A}_0 \mathcal{A}_{D_{i,j}}^* + \mathcal{A}_0^* \mathcal{A}_{D_{i,j}} \right) = \sum_{D_{i,j}} \overline{\sum} 2 \text{Re} \left(\mathcal{A}_0 \mathcal{A}_{D_{i,j}}^* \right) , \quad (2.65)$$

where \mathcal{A}_0 is the tree level amplitude given in Eq. (2.55), while $\mathcal{A}_{D_{i,j}}$ denotes the amplitude for a class of virtual diagrams that only differ by the insertion of the final state Z boson leg, i.e. $D_{i,j} = \sum_k D_{i,j}^{(k)}$ with $D_i = S_i, V_i, B_i, P_i$, $j = s, t, u$, and k running over all possible Z boson insertions, as illustrated in Figures 2.16-2.19.

The calculation of each virtual diagram ($\mathcal{A}_{D_{i,j}}$) is performed in the way we have explained in Sections 2.2.2, 2.3.1 and 2.4.2. We refer to those sections for details. We note that the greatest complexity for virtual diagrams in our calculation is encountered in the $gg \rightarrow Zb\bar{b}$ subprocess. This is due to the higher number of one-loop diagrams that need to be considered and to the presence of two external gluons. For this reason we have chosen to organize the diagrams, at certain stages, into gauge invariant color amplitudes, that is, into coefficients of the same color structure. This allows a better handling of the spurious singularities and a natural way to make internal cross checks and cross checks with new techniques (see Section 2.2.2 and Appendix E).

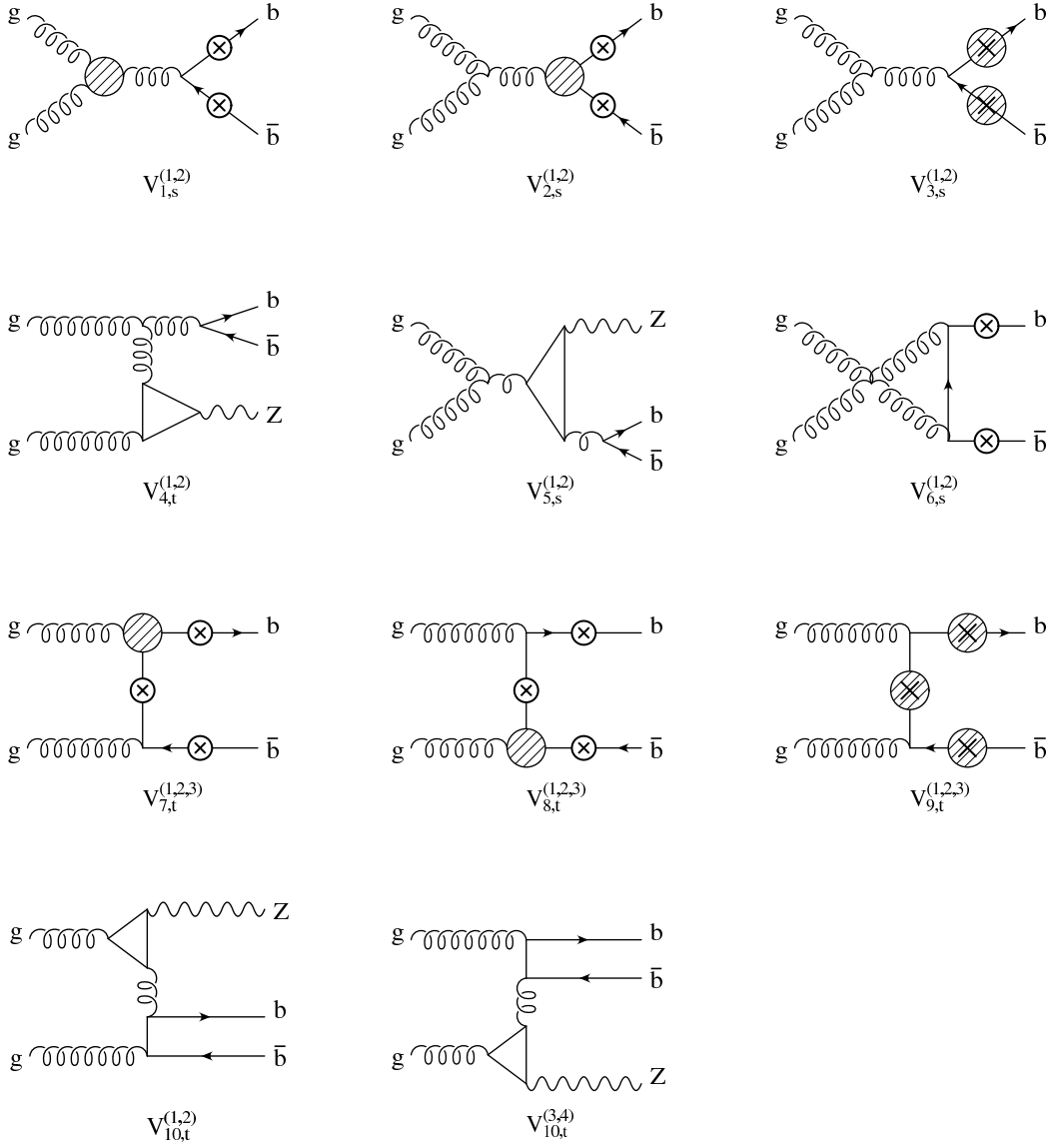


Figure 2.17: $\mathcal{O}(\alpha_s)$ vertex corrections contributing to the $gg \rightarrow Zb\bar{b}$ subprocess at NLO. The shaded blobs denote standard one-loop QCD corrections to the ggg ($V_{1,s}^{(1,2)}$), $b\bar{b}g$ ($V_{2,s}^{(1,2)}$, $V_{7,(t,u)}^{(1,2,3)}$, and $V_{8,(t,u)}^{(1,2,3)}$) and $b\bar{b}Z$ ($V_{3,s}^{(1,2)}$ and $V_{9,(t,u)}^{(1,2,3)}$) vertices. The circled crosses correspond to all possible insertions of the Z boson, each one representing a different diagram.

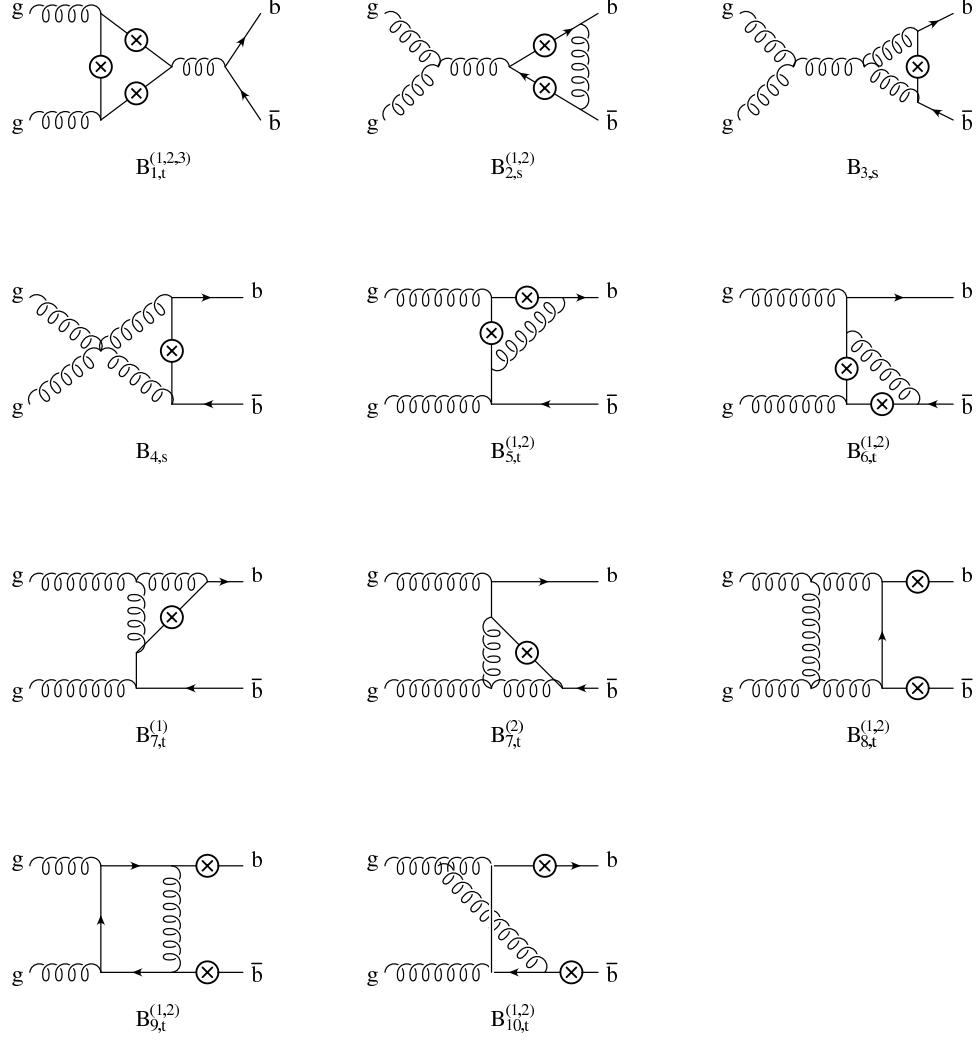


Figure 2.18: $\mathcal{O}(\alpha_s)$ box diagram corrections contributing to the $gg \rightarrow Z b \bar{b}$ subprocess at NLO. The circled crosses correspond to all possible insertions of the Z boson, each one representing a different diagram.

We introduce the leading and sub-leading color factors:

$$\begin{aligned}
C_1 &= \frac{N^2}{4}(N^2 - 1) , \\
C_2 &= -\frac{1}{4}(N^2 - 1) , \\
C_3 &= \left(1 + \frac{1}{N^2}\right)(N^2 - 1) ,
\end{aligned} \tag{2.66}$$

and use them to group the different diagrams when interfered, as in Eq. (2.65), with the LO

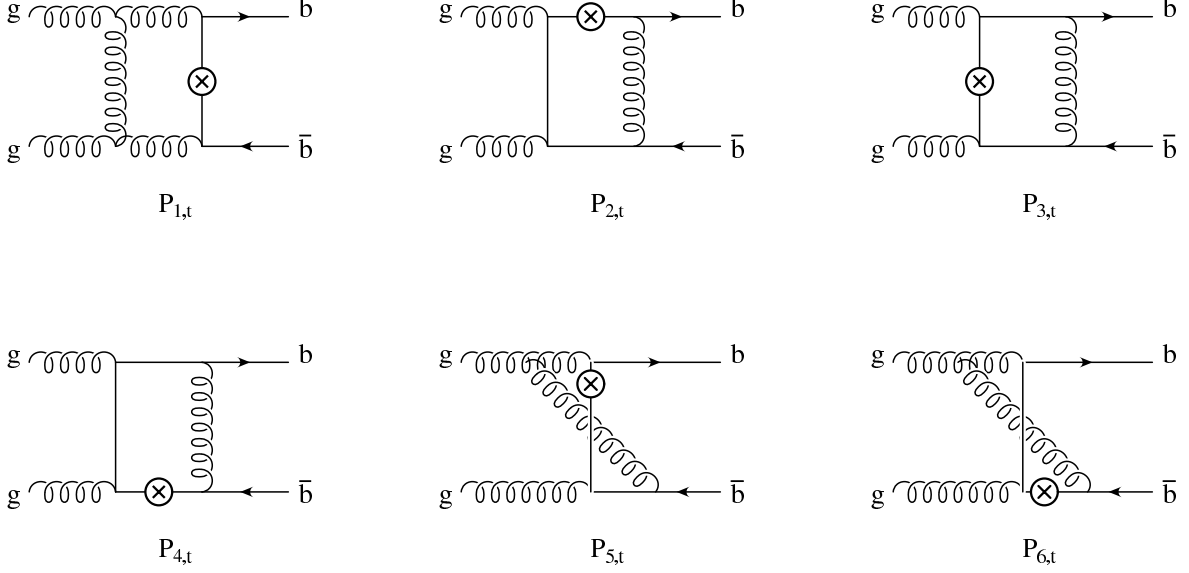


Figure 2.19: $\mathcal{O}(\alpha_s)$ pentagon diagram corrections contributing to the $gg \rightarrow Z b \bar{b}$ subprocess at NLO. The circled crosses correspond to all possible insertions of the Z boson, each one representing a different diagram.

amplitudes in Eq. (2.55), \mathcal{A}_0^{ab} and \mathcal{A}_0^{nab} , independently. This leads to the seven sets of color amplitudes $A_i^{ab/nab}$ ($i = 1, \dots, 5$), whose diagram content is shown in Tables 2.1-2.5.

Table 2.1: Diagram content of color amplitudes A_1^{ab} and A_1^{nab} whose color factor, when interfered with \mathcal{A}_0^{ab} or \mathcal{A}_0^{nab} respectively, is C_1 .

Color Factor: C_1	self energy	vertex	box	pentagon
A_1^{ab}	$S_{3,(t,u)}^{(1,2)}, S_{4,(t,u)}^{(1,2,3,4)}$	$V_{6,s}^{(1,2)}, V_{(7,8),(t,u)}^{(1,2,3)}, V_{9,(t,u)}^{(1,2,3)}$	$B_{4,s}, B_{(7,8),(t,u)}^{(1,2)}$	$P_{1,(t,u)}$
A_1^{nab}	$S_{1,s}^{(1,2)}, S_{2,s}^{(1,2)}, S_{3,(t,u)}^{(1,2)}, S_{4,(t,u)}^{(1,2,3,4)}$	$V_{1,s}^{(1,2)}, V_{2,s}^{(1,2)}, V_{3,s}^{(1,2)}, V_{6,s}^{(1,2)}, V_{(7,8),(t,u)}^{(1,2,3)}, V_{9,(t,u)}^{(1,2,3)}$	$B_{3,s}, B_{4,s}, B_{(7,8),(t,u)}^{(1,2)}$	$P_{1,(t,u)}$

Table 2.2: Diagram of content color amplitudes A_2^{ab} and A_2^{nab} whose color factor, when interfered with \mathcal{A}_0^{ab} or \mathcal{A}_0^{nab} respectively, is C_2 .

Color Factor: C_2	self energy	vertex	box	pentagon
A_2^{ab}	$S_{3,(t,u)}^{(1,2)}, S_{4,(t,u)}^{(1,2,3,4)}$	$V_{(7,8),(t,u)}^{(1,2,3)}, V_{9,(t,u)}^{(1,2,3)}$	$B_{(5,6),(t,u)}^{(1,2)}, B_{7,(t,u)}^{(1,2)}$ $B_{(9,10),(t,u)}^{(1,2)}$	$P_{(2,3,4),(t,u)},$ $P_{(5,6),(t,u)}$
A_2^{nab}	$S_{2,s}^{(1,2)}$ $S_{3,(t,u)}^{(1,2)}, S_{4,(t,u)}^{(1,2,3,4)}$	$V_{(2,3),s}^{(1,2)}$ $V_{(7,8),(t,u)}^{(1,2,3)}, V_{9,(t,u)}^{(1,2,3)}$	$B_{2,s}^{(1,2)}, B_{(5,6),(t,u)}^{(1,2)}$ $B_{9,(t,u)}^{(1,2)}$	$P_{(2,3,4),(t,u)}$

Table 2.3: Diagram content of color amplitude A_3^{ab} whose color factor, when interfered with \mathcal{A}_0^{ab} or \mathcal{A}_0^{nab} respectively, is C_3 .

Color Factor: C_3	self energy	vertex	box	pentagon
A_3^{ab}	$S_{3,(t,u)}^{(1,2)}, S_{4,(t,u)}^{(1,2,3,4)}$	$V_{(7,8),(t,u)}^{(1,2,3)}, V_{9,(t,u)}^{(1,2,3)}$	$B_{(5,6),(t,u)}^{(1,2)}, B_{(9),(t,u)}^{(1,2)}$	$P_{(2,3,4),(t,u)}$

Table 2.4: Diagram content of color amplitude A_4^{nab} whose color factor, when interfered with \mathcal{A}_0^{ab} or \mathcal{A}_0^{nab} respectively, is NC_2 .

Color Factor: NC_2	self energy	vertex	box	pentagon
A_4^{nab}	$S_{1,s}^{(1,2)}$	$V_{1,s}^{(1,2)}, V_{4,(t,u)}^{(1,2)}$ $V_{5,s}^{(1,2)}, V_{10,(t,u)}^{(1,2,3,4)}$	$B_{1,t}^{(1,2,3)}$	—

Table 2.5: Diagram content of color amplitude A_5^{ab} whose color factor, when interfered with \mathcal{A}_0^{ab} or \mathcal{A}_0^{nab} respectively, is $(N - 2/N)C_2$.

Color Factor: $(N - 2/N)C_2$	self energy	vertex	box	pentagon
A_5^{ab}	—	$V_{10,(t,u)}^{(1,2,3,4)}$	$B_{1,t}^{(1,2,3)}$	—

The structure of the UV singularities for the virtual cross section of the $gg \rightarrow Zb\bar{b}$ subprocess is presented in Section 2.4.3.1. The structure of the IR singular part on the other hand is presented in Section 2.4.3.2, while the IR singularities of the real cross section are discussed in Section 2.4.4. The explicit cancellation of IR singularities in the total inclusive NLO cross section for $gg \rightarrow Zb\bar{b}$ is outlined in Sections 2.4.4 and 2.4.5.

2.4.3.1 Virtual corrections: UV singularities and counterterms

Self-energy and vertex one-loop corrections to the tree level $gg \rightarrow Zb\bar{b}$ process (see Figures 2.16 and 2.17) give rise to UV divergences. These singularities are canceled by a set of counterterms fixed by well defined renormalization conditions. We need to introduce counterterms for the external field wave functions of bottom quarks and gluons ($\delta Z_2^{(b)}$, δZ_3), for the bottom mass (δm_b), and for the strong coupling constant (δZ_{α_s}).

By carefully grouping subsets of self-energy and vertex diagrams, we can factor out the UV singularities of the $\mathcal{O}(\alpha_s^3)$ virtual amplitude and write them in terms of the tree level partial amplitudes $\mathcal{A}_{0,s}$, $\mathcal{A}_{0,t}$, and $\mathcal{A}_{0,u}$ introduced in Eq. (2.56). According to the notation introduced in Figures 2.16-2.19, we denote by $D_{i,j}$ (with $D=S, V$, $i=1, 2, \dots$, and $j=s, t, u$) a class of diagrams with a given self-energy or vertex correction insertion, summed over all possible insertions of the external Z boson, one for each different diagram. We now define $\Delta_{\text{UV}}(\mathcal{A}_{D_{i,j}})$ to be the UV pole part of the corresponding amplitude. Using this notation, we find:

$$\begin{aligned}
\Delta_{\text{UV}}(\mathcal{A}_{S_{1,s}}) &= \frac{\alpha_s}{4\pi} \left[\mathcal{N}_s \left(\frac{5}{3}N - \frac{2}{3}n_{lf} \right) - \mathcal{N}_b \frac{2}{3} \right] \left(\frac{1}{\epsilon_{\text{UV}}} \right) [t^a, t^b] \mathcal{A}_{0,s} , \\
\Delta_{\text{UV}}(\mathcal{A}_{V_{1,s}}) &= \frac{\alpha_s}{4\pi} \left[\mathcal{N}_s \left(-\frac{2}{3}N + \frac{2}{3}n_{lf} \right) + \mathcal{N}_b \frac{2}{3} \right] \left(\frac{1}{\epsilon_{\text{UV}}} \right) [t^a, t^b] \mathcal{A}_{0,s} , \\
\Delta_{\text{UV}}(\mathcal{A}_{V_{2,s}} + \mathcal{A}_{V_{7,t}} + \mathcal{A}_{V_{7,u}}) &= \frac{\alpha_s}{4\pi} \mathcal{N}_b \left(\frac{3}{2}N - \frac{1}{2N} \right) \left(\frac{1}{\epsilon_{\text{UV}}} \right) \mathcal{A}_0 , \\
\Delta_{\text{UV}}(\mathcal{A}_{V_{8,t}} + \mathcal{A}_{V_{8,u}}) &= \frac{\alpha_s}{4\pi} \mathcal{N}_b \left(\frac{3}{2}N - \frac{1}{2N} \right) \left(\frac{1}{\epsilon_{\text{UV}}} \right) \times \\
&\quad \left(\frac{1}{2}(\mathcal{A}_{0,t} - \mathcal{A}_{0,u})[t^a, t^b] + \frac{1}{2}(\mathcal{A}_{0,t} + \mathcal{A}_{0,u})\{t^a, t^b\} \right) , \\
\Delta_{\text{UV}}(\mathcal{A}_{V_{3,s}} + \mathcal{A}_{V_{9,t}} + \mathcal{A}_{V_{9,u}}) &= \frac{\alpha_s}{4\pi} \mathcal{N}_b \left(\frac{N}{2} - \frac{1}{2N} \right) \left(\frac{1}{\epsilon_{\text{UV}}} \right) \mathcal{A}_0 , \\
\Delta_{\text{UV}}(\mathcal{A}_{S_{2,s}} + \mathcal{A}_{S_{3,t}} + \mathcal{A}_{S_{3,u}} + \mathcal{A}_{S_{4,t}} + \mathcal{A}_{S_{4,u}}) &= -\frac{\alpha_s}{4\pi} \mathcal{N}_b \left(\frac{N}{2} - \frac{1}{2N} \right) \left(\frac{1}{\epsilon_{\text{UV}}} \right) \times \\
&\quad \left(\mathcal{A}_0 + \frac{1}{2}(\mathcal{A}_{0,t} - \mathcal{A}_{0,u})[t^a, t^b] + \frac{1}{2}(\mathcal{A}_{0,t} + \mathcal{A}_{0,u})\{t^a, t^b\} \right) ,
\end{aligned} \tag{2.67}$$

where $n_{lf}=5$ corresponds to the number of light quark flavors, $N=3$ is the number of colors and \mathcal{N}_s and \mathcal{N}_b are defined in Eq. (2.19).

We notice that some of the UV divergent virtual corrections ($V_{1,s}^{(1,2)}$, $V_{7,(t,u)}^{(1,2,3)}$, and $V_{8,(t,u)}^{(1,2,3)}$), as well as $\delta Z_2^{(b)}$ and δZ_3 in Eqs. (2.20) and (2.68) below, have also IR singularities. In this section, we limit the discussion to the UV singularities only, while the IR structure of these terms will be considered in Section 2.4.3.2. For this reason, we have explicitly denoted by ϵ_{UV} the pole parameter.

The corresponding counterterms are defined as follows. For the external fields, we fix the wave-function renormalization constant of the external bottom quark fields using the on-shell subtraction scheme, giving the expressions shown in Eq. (2.20), while we renormalize the wave-function of external gluons in the \overline{MS} subtraction scheme:

$$(\delta Z_3)_{\text{UV}} = \frac{\alpha_s}{4\pi} (4\pi)^\epsilon \Gamma(1+\epsilon) \left\{ \left(\frac{5}{3}N - \frac{2}{3}n_{lf} \right) \frac{1}{\epsilon_{\text{UV}}} - \frac{2}{3} \left[\frac{1}{\epsilon_{\text{UV}}} + \ln \left(\frac{\mu^2}{m_b^2} \right) \right] \right\} , \tag{2.68}$$

according to which we also need to consider the insertion of a finite self-energy correction on the external gluon legs. This amounts to an extra contribution

$$\delta_{\text{UV}} = \frac{\alpha_s}{4\pi} (4\pi)^\epsilon \Gamma(1+\epsilon) \left(\frac{5}{3}N - \frac{2}{3}n_{lf} \right) \ln \left(\frac{\mu^2}{m_b^2} \right) , \tag{2.69}$$

which is important in order to obtain the correct scale dependence of the NLO cross section.

The structure of the remaining counterterms that appear in this case is the same as presented in Sections 2.3.1.1 and 2.4.2.1, and we refer the reader to them.

Using the results in Sections 2.3.1.1 and 2.4.2.1 and in Eqs. (2.67)-(2.69), it is easy to verify that the UV pole part of $\hat{\sigma}_{gg}^{\text{virt}}$,

$$\begin{aligned} (\hat{\sigma}_{gg}^{\text{virt}})_{UV-pole} &= \int d(P S_3) \sum_{D_{i,j}} \overline{\sum} 2 \mathcal{R}e \left(\mathcal{A}_0 \Delta_{UV}(\mathcal{A}_{D_{i,j}}^*) \right) + \\ &2\hat{\sigma}_{gg}^{\text{LO}} \left[(\delta Z_2^{(b)})_{UV} + (\delta Z_3)_{UV} + \delta_{UV} + \frac{\delta m_b}{m_b} + \delta Z_{\alpha_s} \right], \end{aligned} \quad (2.70)$$

is free of UV singularities and has a residual renormalization scale dependence of the form:

$$\hat{\sigma}_{gg}^{\text{LO}} \frac{\alpha_s(\mu)}{2\pi} \left(-\frac{2}{3} n_{lf} + \frac{11}{3} N \right) \ln \left(\frac{\mu^2}{s} \right), \quad (2.71)$$

as expected by renormalization group arguments (see the first term of Eq. (2.7)). We note that the presence of s in the argument of the logarithm of Eq. (2.71) has no particular relevance as described at the end of Section 2.3.1.1.

2.4.3.2 Virtual corrections: IR singularities

The structure of the IR singularities originating from the $\mathcal{O}(\alpha_s)$ virtual corrections to the tree level amplitude for $gg \rightarrow Z b \bar{b}$ is more involved than that for the UV singularities. However it simplifies considerably when given at the level of the amplitude squared, and this is what we present in this section.

The IR divergent part of the $\mathcal{O}(\alpha_s^3)$ virtual amplitude squared of Eq. (2.65) can be written in the following compact form:

$$\sum_{D_{i,j}} \overline{\sum} 2 \mathcal{R}e \left(\mathcal{A}_0 \Delta_{\text{IR}}(\mathcal{A}_{D_{i,j}}^*) \right) = \frac{\alpha_s}{2\pi} \mathcal{N}_b \overline{\sum} \left(C_1 \mathcal{M}_{V,\epsilon}^{(1)} + C_2 \mathcal{M}_{V,\epsilon}^{(2)} + C_3 \mathcal{M}_{V,\epsilon}^{(3)} \right), \quad (2.72)$$

where \mathcal{N}_b is defined in Eq. (2.19) and we denote by $\Delta_{\text{IR}}(\mathcal{A}_{D_{i,j}})$ the IR pole part of the amplitude of a given $D_{i,j}$ class of diagrams. The result is organized in terms of leading and sub-leading color factors presented in Eq. (2.66), and the corresponding matrix elements

squared $M_{V,\epsilon}^{(1)}$, $M_{V,\epsilon}^{(2)}$, and $M_{V,\epsilon}^{(3)}$ are given by:

$$\begin{aligned}
\mathcal{M}_{V,\epsilon}^{(1)} &= \left[-\frac{4}{\epsilon_{\text{IR}}^2} + \frac{2}{\epsilon_{\text{IR}}}(-2 + \Lambda_s) \right] (|\mathcal{A}_0^{nab}|^2 + |\mathcal{A}_0^{ab}|^2) \\
&+ \frac{1}{\epsilon_{\text{IR}}} [(\Lambda_{\tau_1} + \Lambda_{\tau_2}) |\mathcal{A}_{0,s} + \mathcal{A}_{0,t}|^2 + (\Lambda_{\tau_3} + \Lambda_{\tau_4}) |\mathcal{A}_{0,u} - \mathcal{A}_{0,s}|^2] , \\
\mathcal{M}_{V,\epsilon}^{(2)} &= \left[-\frac{8}{\epsilon_{\text{IR}}^2} + \frac{4}{\epsilon_{\text{IR}}}(-2 + \Lambda_{\tau_1} + \Lambda_{\tau_2} + \Lambda_{\tau_3} + \Lambda_{\tau_4}) \right] |\mathcal{A}_0^{ab}|^2 \\
&+ \frac{2}{\epsilon_{\text{IR}}} \frac{\bar{s}_{b\bar{b}} - 2m_b^2}{\bar{s}_{b\bar{b}}\beta_{b\bar{b}}} \Lambda_{b\bar{b}} (|\mathcal{A}_0^{nab}|^2 + |\mathcal{A}_0^{ab}|^2) , \\
\mathcal{M}_{V,\epsilon}^{(3)} &= \frac{1}{\epsilon_{\text{IR}}} \frac{\bar{s}_{b\bar{b}} - 2m_b^2}{\bar{s}_{b\bar{b}}\beta_{b\bar{b}}} \Lambda_{b\bar{b}} |\mathcal{A}_0^{ab}|^2 ,
\end{aligned} \tag{2.73}$$

where the IR nature of the pole terms has been made explicit. \mathcal{A}_0^{ab} and \mathcal{A}_0^{nab} are defined in Eq. (2.56), while $\mathcal{A}_{0,s}$, $\mathcal{A}_{0,t}$, and $\mathcal{A}_{0,u}$ are given explicitly in Appendix B. We have introduced the notation $\Lambda_s = \ln(s/m_b^2)$ and $\Lambda_{\tau_i} = \ln(\tau_i/m_b^2)$, where the invariants have been defined in Eq. (2.23), and $\beta_{b\bar{b}}$ and $\Lambda_{b\bar{b}}$ are defined in Eq. (2.26).

We write explicitly here the IR divergent structure of the (δZ_3) counterterm, as it is the only one that has not appeared previously. We get:

$$(\delta Z_3)_{\text{IR}} = \mathcal{N}_b \left(-\frac{5}{3}N + \frac{2}{3}n_{lf} \right) \frac{1}{\epsilon_{\text{IR}}} . \tag{2.74}$$

When we add the IR singularities coming from the counterterms we have introduced in Section 2.4.3.1, we can write the complete pole part of the IR singular $\mathcal{O}(\alpha_s^3)$ virtual cross section as:

$$\begin{aligned}
(\hat{\sigma}_{gg}^{\text{virt}})_{\text{IR-pole}} &= \int d(P S_3) \sum_{D_{i,j}} \overline{\sum} 2\mathcal{R}e \left(\mathcal{A}_0 \Delta_{\text{IR}}(\mathcal{A}_{D_{i,j}}^*) \right) + 2\hat{\sigma}_{\text{LO}}^{gg} \left((\delta Z_2^{(b)})_{\text{IR}} + (\delta Z_3)_{\text{IR}} \right) \\
&= \int d(P S_3) \frac{\alpha_s}{2\pi} \mathcal{N}_b \overline{\sum} \left(C_1 \mathcal{M}_{V,\epsilon}^{(1)} + C_2 \mathcal{M}_{V,\epsilon}^{(2)} + C_3 \mathcal{M}_{V,\epsilon}^{(3)} \right) \\
&+ \frac{\alpha_s}{2\pi} \mathcal{N}_b \left(\frac{2}{3}n_{lf} - \frac{8}{3}N + \frac{1}{N} \right) \frac{1}{\epsilon_{\text{IR}}} \hat{\sigma}_{gg}^{\text{LO}} .
\end{aligned} \tag{2.75}$$

As will be demonstrated in Section 2.4.4, the IR singularities of $\hat{\sigma}_{gg}^{\text{virt}}$ are canceled by the corresponding IR singularities of $\hat{\sigma}_{gg}^{\text{real}}$.

2.4.4 Real Corrections to $Zb\bar{b}$ Production

The real corrections to $Zb\bar{b}$ production is built up of three $\mathcal{O}(\alpha_s^3)$ subprocesses, namely $q\bar{q} \rightarrow Zb\bar{b} + g$, $gg \rightarrow Zb\bar{b} + g$ and $(q, \bar{q})g \rightarrow Zb\bar{b} + (q, \bar{q})$.

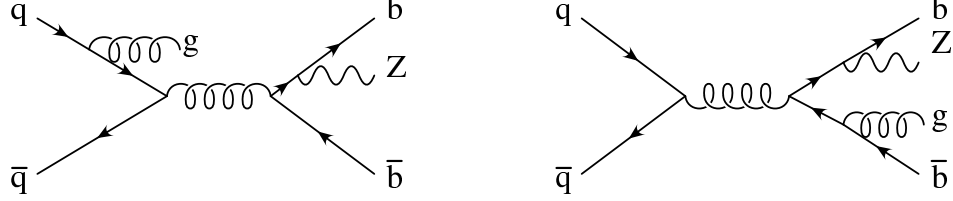


Figure 2.20: Examples of $\mathcal{O}(\alpha_s)$ real corrections to $q\bar{q} \rightarrow Zb\bar{b}$ production, with Z emitted from the final fermion line.

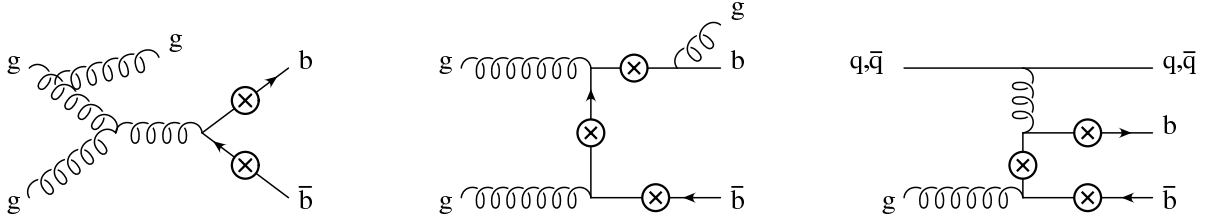


Figure 2.21: Examples of $\mathcal{O}(\alpha_s)$ real corrections to $Zb\bar{b}$ production. The circled crosses denote all possible insertions of a Z weak boson, each insertion corresponding to a different diagram.

The real cross section for the $q\bar{q} \rightarrow Zb\bar{b} + g$ subprocess is analogous to the $q\bar{q}' \rightarrow Wb\bar{b} + g$ subprocess, although it contains a set of diagrams with the Z boson emitted from the b -quark fermion line, as shown in Figure 2.20. We refer the reader to the discussion in Sections 2.3.2 and 2.3.3 for details.

The NLO real cross section $\hat{\sigma}_{gg}^{\text{real}}$ in Eq. (2.5) corresponds to the $\mathcal{O}(\alpha_s)$ corrections to $gg \rightarrow Zb\bar{b}$ due to the emission of a real gluon, i.e. to the process $gg \rightarrow Zb\bar{b} + g$, examples of which are illustrated in Figure 2.21. It contains IR singularities that cancel the analogous singularities present in the $\mathcal{O}(\alpha_s)$ virtual corrections (see Section 2.4.3.2) and in the NLO parton distribution functions. These singularities can be either *soft*, when the energy of the emitted gluon becomes very small, or *collinear*, when the final state gluon is emitted collinear to one of the initial gluons. There is no collinear radiation from the final b and \bar{b} quarks because they are massive. At the same order in α_s , the $\hat{\sigma}_{qg}^{\text{real}}$ cross section corresponds to the tree level processes $(q, \bar{q})g \rightarrow Zb\bar{b} + (q, \bar{q})$, an example of which is also illustrated in Figure 2.21. This part of the NLO cross section develops IR singularities entirely due to the

collinear emission of a final state quark or antiquark from one of the initial state massless partons. The IR singularities can be conveniently isolated by *slicing* the $gg \rightarrow Zb\bar{b} + g$ and $(q, \bar{q})g \rightarrow Zb\bar{b} + (q, \bar{q})$ phase spaces into different regions defined by suitable cutoffs (as was done in Section 2.3.2). The dependence on the arbitrary cutoffs introduced in *slicing* the phase space of the final state particles is not physical, and cancels at the level of the total real hadronic cross section, i.e. in σ^{real} , as well as at the level of the real cross section for each separate channel, i.e., in $\sigma_{q\bar{q}}^{\text{real}}$, $\sigma_{gg}^{\text{real}}$, and $\sigma_{qg}^{\text{real}}$. This cancellation constitutes an important check of the calculation and will be discussed in detail in Section 2.4.5.

We have calculated the cross section for the processes

$$g(q_1) + g(q_2) \rightarrow b(p_b) + \bar{b}(p_{\bar{b}}) + Z(p_Z) + g(k) ,$$

and

$$(q, \bar{q})(q_1) + g(q_2) \rightarrow b(p_b) + \bar{b}(p_{\bar{b}}) + Z(p_Z) + (q, \bar{q})(k) ,$$

with $q_1 + q_2 = p_b + p_{\bar{b}} + p_Z + k$, using the PSS method with *two cutoffs*, as in Section 2.3.2.

In the next section we discuss the application of the two-cutoff PSS method to the $gg \rightarrow Zb\bar{b} + g$ and $q(\bar{q})g \rightarrow Zb\bar{b} + q(\bar{q})$ subprocesses.

Real gluon emission, $gg \rightarrow Zb\bar{b} + g$: soft region

The soft region of the phase space for the gluon emission process

$$g^a(q_1) + g^b(q_2) \rightarrow b(p_b) + \bar{b}(p_{\bar{b}}) + Z(p_Z) + g^c(k) \quad (2.76)$$

is defined by demanding that the energy of the emitted gluon ($k^0 = E_g$) satisfies the condition

$$E_g \leq \delta_s \frac{\sqrt{s}}{2} \quad (2.77)$$

for an arbitrary small value of the *soft* cutoff δ_s . In the *soft limit* ($E_g \rightarrow 0$), the amplitude for this process can be written as:

$$\begin{aligned} \mathcal{A}_{\text{soft}}(gg \rightarrow Zb\bar{b} + g) = & t^c t^a t^b \left(\frac{p_b \cdot \epsilon^*}{p_b \cdot k} - \frac{q_1 \cdot \epsilon^*}{q_1 \cdot k} \right) (\mathcal{A}_{0,t} + \mathcal{A}_{0,s}) + t^c t^b t^a \left(\frac{p_{\bar{b}} \cdot \epsilon^*}{p_{\bar{b}} \cdot k} - \frac{q_2 \cdot \epsilon^*}{q_2 \cdot k} \right) (\mathcal{A}_{0,u} - \mathcal{A}_{0,s}) \\ & - t^a t^b t^c \left(\frac{p_{\bar{b}} \cdot \epsilon^*}{p_{\bar{b}} \cdot k} - \frac{q_2 \cdot \epsilon^*}{q_2 \cdot k} \right) (\mathcal{A}_{0,t} + \mathcal{A}_{0,s}) - t^b t^a t^c \left(\frac{p_b \cdot \epsilon^*}{p_b \cdot k} - \frac{q_1 \cdot \epsilon^*}{q_1 \cdot k} \right) (\mathcal{A}_{0,u} - \mathcal{A}_{0,s}) \\ & + t^a t^c t^b \left(\frac{q_1 \cdot \epsilon^*}{q_1 \cdot k} - \frac{q_2 \cdot \epsilon^*}{q_2 \cdot k} \right) (\mathcal{A}_{0,t} + \mathcal{A}_{0,s}) + t^b t^c t^a \left(\frac{q_2 \cdot \epsilon^*}{q_2 \cdot k} - \frac{q_1 \cdot \epsilon^*}{q_1 \cdot k} \right) (\mathcal{A}_{0,u} - \mathcal{A}_{0,s}) , \end{aligned} \quad (2.78)$$

where a, b , and c are the color indices of the external gluons, while $\epsilon^\mu(k, \lambda)$ (for $\lambda=1, 2$) is the polarization vector of the emitted soft gluon. Moreover, in the soft region the $gg \rightarrow Zb\bar{b} + g$ phase space factorizes as:

$$\begin{aligned} d(PS_4)(gg \rightarrow Zb\bar{b} + g) &\xrightarrow{soft} d(PS_3)(gg \rightarrow Zb\bar{b})d(PS_g)_{soft} \\ &= d(PS_3)(gg \rightarrow Zb\bar{b}) \frac{d^{(d-1)}k}{(2\pi)^{(d-1)}2E_g} \theta\left(\delta_s \frac{\sqrt{s}}{2} - E_g\right) , \end{aligned} \quad (2.79)$$

where $d(PS_4)$ and $d(PS_3)$ have been defined in Section 2.1, while $d(PS_g)_{soft}$ denotes the the phase space measure of the soft gluon. Since the contribution of the soft gluon is now completely factorized, we can perform the integration over $d(PS_g)_{soft}$ analytically, using dimensional regularization in $d = 4 - 2\epsilon$ to extract the soft poles that will cancel the corresponding singularities in Eq. (2.75). For completeness, the integrals that we have used to perform the integration over the phase space of the soft gluon are collected in Appendix F.

After squaring the soft amplitude \mathcal{A}_{soft} , summing over the polarization of the radiated soft gluon, and integrating over the soft gluon momentum, the pole part of the parton level soft cross section reads

$$\begin{aligned} (\hat{\sigma}_{gg}^{soft})_{pole} &= \int d(PS_3) \left(\int d(PS_g)_{soft} \overline{\sum} |\mathcal{A}_{soft}(gg \rightarrow Zb\bar{b} + g)|^2 \right)_{pole} \\ &= \int d(PS_3) \frac{\alpha_s}{2\pi} \mathcal{N}_b \overline{\sum} \left(C_1 \mathcal{M}_{S,\epsilon}^{(1)} + C_2 \mathcal{M}_{S,\epsilon}^{(2)} + C_3 \mathcal{M}_{S,\epsilon}^{(3)} \right) , \end{aligned} \quad (2.80)$$

where C_1 , C_2 , and C_3 are defined in Eq. (2.66), while $\mathcal{M}_{S,\epsilon}^{(1)}$, $\mathcal{M}_{S,\epsilon}^{(2)}$, and $\mathcal{M}_{S,\epsilon}^{(3)}$ represent the IR pole parts of the corresponding matrix elements squared, and can be written as:

$$\begin{aligned} \mathcal{M}_{S,\epsilon}^{(1)} &= -\mathcal{M}_{V,\epsilon}^{(1)} - \frac{2}{\epsilon} (1 + 4 \ln(\delta_s)) (|\mathcal{A}_0^{nab}|^2 + |\mathcal{A}_0^{ab}|^2) , \\ \mathcal{M}_{S,\epsilon}^{(2)} &= -\mathcal{M}_{V,\epsilon}^{(2)} - \frac{16}{\epsilon} \ln(\delta_s) |\mathcal{A}_0^{ab}|^2 + \frac{2}{\epsilon} (|\mathcal{A}_0^{nab}|^2 + |\mathcal{A}_0^{ab}|^2) , \\ \mathcal{M}_{S,\epsilon}^{(3)} &= -\mathcal{M}_{V,\epsilon}^{(3)} + \frac{1}{\epsilon} |\mathcal{A}_0^{ab}|^2 . \end{aligned} \quad (2.81)$$

Note that in this section we do not explicitly denote the IR poles as poles in ϵ_{IR} , since all singularities present in $\sigma_{gg,qg}^{real}$ are of IR origin.

After adding the IR divergent part of the parton level virtual cross section of Eq. (2.75)

we obtain:

$$\hat{\sigma}_{gg}^{s+v} \equiv (\hat{\sigma}_{gg}^{soft})_{pole} + (\hat{\sigma}_{gg}^{virt})_{IR-pole} = \frac{\alpha_s}{2\pi} \mathcal{N}_b \left[-4N \ln(\delta_s) - \frac{1}{3}(11N - 2n_{lf}) \right] \frac{1}{\epsilon} \hat{\sigma}_{gg}^{LO} , \quad (2.82)$$

where we can see that the IR poles of the parton level virtual cross section are exactly canceled by the corresponding singularities in the parton level soft gluon emission cross section. The residual divergences will be canceled by the soft+virtual part of the PDF counterterm when convoluting with the gluon PDFs, as will be demonstrated in Section 2.4.5. The finite contribution to the parton level soft cross section is finally given by

$$\begin{aligned} (\hat{\sigma}_{gg}^{soft})_{finite} &= \int d(P S_3) \left(\int d(P S_g)_{soft} \overline{\sum} |\mathcal{A}_{soft}(gg \rightarrow Z b \bar{b} + g)|^2 \right)_{finite} \\ &= \int d(P S_3) \frac{\alpha_s}{2\pi} \mathcal{N}_b \overline{\sum} \left(C_1 \mathcal{M}_S^{(1)} + C_2 \mathcal{M}_S^{(2)} + C_3 \mathcal{M}_S^{(3)} \right) , \end{aligned} \quad (2.83)$$

where the finite parts of the $\mathcal{M}_S^{(1)}$, $\mathcal{M}_S^{(2)}$, and $\mathcal{M}_S^{(3)}$ matrix element squared are explicitly given by:

$$\begin{aligned}
\mathcal{M}_S^{(1)} &= \left[-\frac{4}{3}\pi^2 + 4\Lambda_s \ln(\delta_s) + 8\ln^2(\delta_s) - 2\Lambda_s - 4\ln(\delta_s) \right. \\
&\quad \left. + \frac{1}{\beta_b} \ln\left(\frac{1+\beta_b}{1-\beta_b}\right) + \frac{1}{\beta_{\bar{b}}} \ln\left(\frac{1+\beta_{\bar{b}}}{1-\beta_{\bar{b}}}\right) \right] (|\mathcal{A}_0^{nab}|^2 + |\mathcal{A}_0^{ab}|^2) \\
&\quad + \left[(\Lambda_s + 2\ln(\delta_s)) (\Lambda_{\tau_1} + \Lambda_{\tau_2}) + \frac{1}{2}F(q_1, p_b) + \frac{1}{2}F(q_2, p_{\bar{b}}) \right] |\mathcal{A}_0^{nab} + \mathcal{A}_0^{ab}|^2 \\
&\quad + \left[(\Lambda_s + 2\ln(\delta_s)) (\Lambda_{\tau_3} + \Lambda_{\tau_4}) + \frac{1}{2}F(q_2, p_b) + \frac{1}{2}F(q_1, p_{\bar{b}}) \right] |\mathcal{A}_0^{nab} - \mathcal{A}_0^{ab}|^2, \\
\mathcal{M}_S^{(2)} &= \left\{ \frac{\bar{s}_{b\bar{b}} - 2m_b^2}{\bar{s}_{b\bar{b}}} \left[(2\Lambda_s + 4\ln(\delta_s)) \frac{1}{\beta_{b\bar{b}}} \Lambda_{b\bar{b}} + \frac{1}{2}\ln^2\left(\frac{1+\beta_b}{1-\beta_b}\right) - \frac{1}{2}\ln^2\left(\frac{1+\beta_{\bar{b}}}{1-\beta_{\bar{b}}}\right) \right. \right. \\
&\quad \left. + 2\text{Li}_2\left(1 - \frac{\alpha_{b\bar{b}}}{v_{b\bar{b}}} p_b^0(1+\beta_b)\right) + 2\text{Li}_2\left(1 - \frac{\alpha_{b\bar{b}}}{v_{b\bar{b}}} p_b^0(1-\beta_b)\right) \right. \\
&\quad \left. - 2\text{Li}_2\left(1 - \frac{1}{v_{b\bar{b}}} p_{\bar{b}}^0(1+\beta_{\bar{b}})\right) - 2\text{Li}_2\left(1 - \frac{1}{v_{b\bar{b}}} p_{\bar{b}}^0(1-\beta_{\bar{b}})\right) \right] \\
&\quad \left. - 2\Lambda_s - 4\ln(\delta_s) + \frac{2}{\beta_{b\bar{b}}} \Lambda_{b\bar{b}} \right\} (|\mathcal{A}_0^{nab}|^2 + |\mathcal{A}_0^{ab}|^2) \\
&\quad + 2 \left[-\frac{4}{3}\pi^2 - 2\Lambda_s^2 + 8\ln^2(\delta_s) + 2(\Lambda_s + 2\ln(\delta_s)) (\Lambda_{\tau_1} + \Lambda_{\tau_2} + \Lambda_{\tau_3} + \Lambda_{\tau_4}) \right. \\
&\quad \left. + F(q_1, p_b) + F(q_2, p_{\bar{b}}) + F(q_2, p_b) + F(q_1, p_{\bar{b}}) \right. \\
&\quad \left. - 4\Lambda_s - 8\ln(\delta_s) + \frac{2}{\beta_b} \ln\left(\frac{1+\beta_b}{1-\beta_b}\right) + \frac{2}{\beta_{\bar{b}}} \ln\left(\frac{1+\beta_{\bar{b}}}{1-\beta_{\bar{b}}}\right) \right] |\mathcal{A}_0^{ab}|^2, \\
\mathcal{M}_S^{(3)} &= \frac{1}{2} \left\{ \frac{\bar{s}_{b\bar{b}} - 2m_b^2}{\bar{s}_{b\bar{b}}} \left[(2\Lambda_s + 4\ln(\delta_s)) \frac{1}{\beta_{b\bar{b}}} \Lambda_{b\bar{b}} + \frac{1}{2}\ln^2\left(\frac{1+\beta_b}{1-\beta_b}\right) - \frac{1}{2}\ln^2\left(\frac{1+\beta_{\bar{b}}}{1-\beta_{\bar{b}}}\right) \right. \right. \\
&\quad \left. + 2\text{Li}_2\left(1 - \frac{\alpha_{b\bar{b}}}{v_{b\bar{b}}} p_b^0(1+\beta_b)\right) + 2\text{Li}_2\left(1 - \frac{\alpha_{b\bar{b}}}{v_{b\bar{b}}} p_b^0(1-\beta_b)\right) \right. \\
&\quad \left. - 2\text{Li}_2\left(1 - \frac{1}{v_{b\bar{b}}} p_{\bar{b}}^0(1+\beta_{\bar{b}})\right) - 2\text{Li}_2\left(1 - \frac{1}{v_{b\bar{b}}} p_{\bar{b}}^0(1-\beta_{\bar{b}})\right) \right] \\
&\quad \left. - 2\Lambda_s - 4\ln(\delta_s) + \frac{1}{\beta_b} \ln\left(\frac{1+\beta_b}{1-\beta_b}\right) + \frac{1}{\beta_{\bar{b}}} \ln\left(\frac{1+\beta_{\bar{b}}}{1-\beta_{\bar{b}}}\right) \right\} |\mathcal{A}_0^{ab}|^2, \tag{2.84}
\end{aligned}$$

where

$$\beta_i = \sqrt{1 - \frac{m_b^2}{(p_i^0)^2}}, \tag{2.85}$$

$$\alpha_{b\bar{b}} = \frac{1 + \beta_{b\bar{b}}}{1 - \beta_{b\bar{b}}}, \quad v_{b\bar{b}} = \frac{m_b^2(\alpha_{b\bar{b}}^2 - 1)}{2(\alpha_{b\bar{b}} p_b^0 - p_{\bar{b}}^0)}, \tag{2.86}$$

$\Lambda_\delta = \ln(\delta/m_b^2)$, with δ a given kinematic invariant, and $\bar{s}_{b\bar{b}}$, $\beta_{b\bar{b}}$, and $\Lambda_{b\bar{b}}$ are defined in Eq. (2.26), while the function $F(p_i, p_f)$ can be found in Eq. (F.9) (see Appendix F for more details). We have used the set of kinematic invariants presented in Eq. (2.23).

Real gluon emission, $gg \rightarrow Zb\bar{b} + g$: hard region

The matrix element squared for $ij \rightarrow Zb\bar{b} + g$ factorizes into the LO matrix element squared and the unregulated Altarelli-Parisi splitting function $P_{ii'} = P_{ii'}^4 + \epsilon P'_{ii'}$ for $i \rightarrow i'g$, i.e.:

$$\overline{\sum} |\mathcal{A}_{\text{real}}(ij \rightarrow Zb\bar{b} + g)|^2 \xrightarrow{\text{collinear}} (4\pi\alpha_s) \overline{\sum} |\mathcal{A}_0(i'j \rightarrow Zb\bar{b})|^2 \frac{2P_{ii'}(z)}{z s_{ig}}, \quad (2.87)$$

where $s_{ig} = 2q_i \cdot k$ and $P_{ii'}^4$ and $P'_{ii'}$ are the Altarelli-Parisi splitting functions, which in the gg case are given by:

$$\begin{aligned} P_{gg}^4(z) &= 2N \left(\frac{z}{1-z} + \frac{1-z}{z} + z(1-z) \right), \\ P'_{gg}(z) &= 0. \end{aligned} \quad (2.88)$$

Moreover, in the collinear limit, the $ij \rightarrow Zb\bar{b} + g$ phase space also factorizes as:

$$\begin{aligned} d(PS_4)(ij \rightarrow Zb\bar{b} + g) &\xrightarrow{\text{collinear}} d(PS_3)(i'j \rightarrow Zb\bar{b}) \frac{z d^{(d-1)}k}{(2\pi)^{(d-1)}2E_g} \theta \left(E_g - \delta_s \frac{\sqrt{s}}{2} \right) \times \\ &\quad \theta(\cos \theta_{ig} - (1 - \delta_c)) \\ &\stackrel{d=4-2\epsilon}{=} d(PS_3)(i'j \rightarrow Zb\bar{b}) \frac{1}{\Gamma(1-\epsilon)} \frac{(4\pi)^\epsilon}{16\pi^2} z dz ds_{ig} [(1-z)s_{ig}]^{-\epsilon} \times \\ &\quad \theta \left(\frac{(1-z)}{z} s' \frac{\delta_c}{2} - s_{ig} \right), \end{aligned} \quad (2.89)$$

where $d(PS_4)$ and $d(PS_3)$ have been defined in Section 2.1, while the integration range for s_{ig} in the collinear region is given in terms of the collinear cutoff, and we have defined $s' = 2q_{i'} \cdot q_j$. The integral over the collinear gluon degrees of freedom can then be performed analytically, and this allows us to extract explicitly the collinear singularities of $\hat{\sigma}_{gg}^{\text{hard}}$ [79, 91], which can be written as:

$$\begin{aligned} \hat{\sigma}_{gg}^{\text{hard/coll}} &= \left[\frac{\alpha_s}{2\pi} \frac{1}{\Gamma(1-\epsilon)} \left(\frac{4\pi\mu^2}{m_b^2} \right)^\epsilon \right] \left(-\frac{1}{\epsilon} \right) \delta_c^{-\epsilon} \times \\ &\quad \left\{ \int_0^{1-\delta_s} dz \left[\frac{(1-z)^2}{2z} \frac{s'}{m_b^2} \right]^{-\epsilon} P_{ii'}(z) \hat{\sigma}_{gg}^{\text{LO}}(i'j \rightarrow Zb\bar{b}) + (i \leftrightarrow j) \right\}, \end{aligned} \quad (2.90)$$

where i, i' , and j are all gluons. As usual, these initial state collinear divergences are absorbed into the gluon distribution functions as will be described in detail in Section 2.4.5.

The tree level processes $(q, \bar{q})g \rightarrow Zb\bar{b} + (q, \bar{q})$

The extraction of the collinear singularities of $\hat{\sigma}_{gg}^{\text{real}}$ is done in the same way as described in the previous subsection for the gg initial state. In the collinear region, $\cos\theta_{iq} > 1 - \delta_c$, the initial state parton i with momentum q_i is considered to split into a hard parton i' and a collinear quark q , $i \rightarrow i'q$, with $q_{i'} = zq_i$ and $k = (1-z)q_i$. The matrix element squared for $ij \rightarrow Zb\bar{b} + q$ factorizes into the unregulated Altarelli-Parisi splitting functions in d dimensions, $P_{ii'} = P_{ii'}^4 + \epsilon P_{ii'}'$, shown in Eq.(2.47) for the $g \rightarrow q\bar{q}$ splitting and in Eq. (2.92) for the $(q, \bar{q}) \rightarrow g(q, \bar{q})$ splitting, and the corresponding LO matrix elements squared. The $ij \rightarrow Zb\bar{b} + q$ phase space factorizes into the $i'j \rightarrow Zb\bar{b}$ phase space and the phase space of the collinear quark. As a result, after integrating over the phase space of the collinear quark, the collinear singularity of $\hat{\sigma}_{\text{real}}^{gg}$ can be extracted as:

$$\begin{aligned} \hat{\sigma}_{gg}^{\text{coll}} = & \left[\frac{\alpha_s}{2\pi} \frac{1}{\Gamma(1-\epsilon)} \left(\frac{4\pi\mu^2}{m_b^2} \right)^\epsilon \right] \left(-\frac{1}{\epsilon} \right) \delta_c^{-\epsilon} \int_0^1 dz \left[\frac{(1-z)^2}{2z} \frac{s'}{m_b^2} \right]^{-\epsilon} \times \\ & [P_{qg}(z) \hat{\sigma}_{gg}^{\text{LO}}(g(q_{1'})g(q_2) \rightarrow Zb\bar{b}) + P_{gq}(z) \hat{\sigma}_{q\bar{q}}^{\text{LO}}(q(q_1)\bar{q}(q_{2'}) \rightarrow Zb\bar{b})] \quad . \quad (2.91) \end{aligned}$$

The collinear radiation of an antiquark in $\bar{q}g \rightarrow Zb\bar{b} + \bar{q}$ is treated analogously. The $O(1)$ and $O(\epsilon)$ parts of the P_{qg} splitting function are given by:

$$\begin{aligned} P_{qg}^4(z) &= C_F \left(\frac{1 + (1-z)^2}{z} \right) , \\ P_{qg}'(z) &= -C_F z, \end{aligned} \quad (2.92)$$

and by Eq. (2.47) for P_{gq} .

Again, these initial state collinear divergences are absorbed into the parton distribution functions as will be described in detail in Section 2.4.5.

2.4.5 Total Cross Section of $p\bar{p}(pp) \rightarrow Zb\bar{b}$

The total inclusive hadronic cross section for $p\bar{p}(pp) \rightarrow Zb\bar{b}$ is the sum of the contributions from the $q\bar{q}$, the gg and the $(q, \bar{q})g$ initial states:

$$\sigma^{\text{NLO}}(p\bar{p}(pp) \rightarrow Zb\bar{b}) = \sigma_{q\bar{q}}^{\text{NLO}}(p\bar{p}(pp) \rightarrow Zb\bar{b}) + \sigma_{gg}^{\text{NLO}}(p\bar{p}(pp) \rightarrow Zb\bar{b}) + \sigma_{qg}^{\text{NLO}}(p\bar{p}(pp) \rightarrow Zb\bar{b}) \quad . \quad (2.93)$$

As described in Section 2.1, $\sigma_{ij}^{\text{NLO}}(p\bar{p}(pp) \rightarrow Zb\bar{b})$ is obtained by convoluting the parton level NLO cross section $\hat{\sigma}_{ij}^{\text{NLO}}(p\bar{p}(pp) \rightarrow Zb\bar{b})$ with the NLO PDFs $\mathcal{F}_i^{p,\bar{p}}(x, \mu)$ ($i = q, g$), thereby

absorbing the remaining initial state singularities of $\delta\hat{\sigma}_{ij}^{\text{NLO}}$ into the renormalized PDFs. In the following we demonstrate in detail how this cancellation works in the case of the gg and $(q, \bar{q})g$ initiated processes. The case of the $q\bar{q}$ initiated process is discussed in Section 2.3.3, where we presented in detail the contribution of the $q\bar{q}$ initial state to $\sigma^{\text{NLO}}(p\bar{p}(pp) \rightarrow Wb\bar{b})$. $\sigma_{q\bar{q}}^{\text{NLO}}(p\bar{p}(pp) \rightarrow Zb\bar{b})$ can be obtained from there with obvious modifications, and will not be repeated here.

Similarly to the discussion in Section 2.3.3, first the parton level cross section is convoluted with the *bare* parton distribution functions $\mathcal{F}_i^{p,\bar{p}}(x)$ and subsequently the $\mathcal{F}_i^{p,\bar{p}}(x)$ are replaced by the renormalized parton distribution functions, $\mathcal{F}_i^{p,\bar{p}}(x, \mu_f)$, defined in some subtraction scheme at a given factorization scale μ_f . Using the \overline{MS} scheme, the scale-dependent NLO parton distribution functions for the two-cutoff PSS are given in terms of the bare $\mathcal{F}_i^{p,\bar{p}}(x)$ and the QCD NLO parton distribution function counterterms [79] as follows:

- (a) For the case where an initial state gluon, quark or antiquark ($k = g, (q, \bar{q})$) splits, respectively, into a $q\bar{q}$ or $(q, \bar{q})g$ pair ($k' = (q, \bar{q}), g$):

$$\mathcal{F}_{k'}^{p,\bar{p}}(x, \mu_f) = \mathcal{F}_{k'}^{p,\bar{p}}(x) + \left[\frac{\alpha_s}{2\pi} \left(\frac{4\pi\mu_r^2}{\mu_f^2} \right)^\epsilon \frac{1}{\Gamma(1-\epsilon)} \right] \int_x^1 \frac{dz}{z} \left(-\frac{1}{\epsilon} \right) P_{kk'}^4(z) \mathcal{F}_k^{p,\bar{p}}\left(\frac{x}{z}\right), \quad (2.94)$$

where P_{ij}^A are defined in Eqs. (2.47) and (2.92).

- (b) For the case of $g \rightarrow gg$ splitting:

$$\begin{aligned} \mathcal{F}_g^{p,\bar{p}}(x, \mu_f) = & \mathcal{F}_g^{p,\bar{p}}(x) \left[1 - \frac{\alpha_s}{2\pi} \left(\frac{4\pi\mu_r^2}{\mu_f^2} \right)^\epsilon \frac{1}{\Gamma(1-\epsilon)} \left(\frac{1}{\epsilon} \right) N \left(2\ln(\delta_s) + \frac{11}{6} - \frac{1}{3} \frac{n_{lf}}{N} \right) \right] \\ & + \left[\frac{\alpha_s}{2\pi} \left(\frac{4\pi\mu_r^2}{\mu_f^2} \right)^\epsilon \frac{1}{\Gamma(1-\epsilon)} \right] \int_x^{1-\delta_s} \frac{dz}{z} \left(-\frac{1}{\epsilon} \right) P_{gg}(z) \mathcal{F}_g^{p,\bar{p}}\left(\frac{x}{z}\right), \end{aligned} \quad (2.95)$$

where P_{gg} is Altarelli-Parisi splitting function given in Eq. (2.88).

The $\mathcal{O}(\alpha_s)$ terms in the previous equations are calculated from the $\mathcal{O}(\alpha_s)$ corrections to the $k \rightarrow k'j$ splittings, in the two-cutoffs PSS formalism. Moreover, note that in Eqs. (2.94) and (2.95) we have carefully separated the dependence on the factorization (μ_f) and renormalization scale (μ_r). It is understood that $\alpha_s = \alpha_s(\mu_r)$. The definition of the

subtracted PDFs is indeed the only place where both scales play a role, and the only place where we have a dependence on μ_f . In the rest of this section, we have always set $\mu_r = \mu_f = \mu$ and we will also give the master formulas for the total NLO cross section, Eq. (2.96), using $\mu_r = \mu_f = \mu$. In Chapter 3 we will study the explicit dependence of the total hadronic cross section on both scales μ_r and μ_f .

When convoluting the parton gg cross section with the renormalized gluon distribution function of Eq. (2.95), the IR singular counterterm of Eq. (2.95) exactly cancels the remaining IR poles of $\hat{\sigma}_{gg}^{\text{virt}} + \hat{\sigma}_{gg}^{\text{soft}}$ and $\hat{\sigma}_{gg}^{\text{hard/coll}}$, shown in Eq. (2.82). Finally, the complete $\mathcal{O}(\alpha_s^3)$ inclusive total cross section for $p\bar{p}(pp) \rightarrow Zb\bar{b}$ in the \overline{MS} factorization scheme when only the gg initial state is included, i.e. $\sigma_{gg}^{\text{NLO}}(p\bar{p}(pp) \rightarrow Zb\bar{b})$ of Eq. (2.93), can be written as follows:

$$\begin{aligned}
\sigma_{gg}^{\text{NLO}} = & \frac{1}{2} \int dx_1 dx_2 \left\{ \mathcal{F}_g^p(x_1, \mu) \mathcal{F}_g^{\bar{p}(p)}(x_2, \mu) \left[\hat{\sigma}_{gg}^{\text{LO}}(x_1, x_2, \mu) + (\hat{\sigma}_{gg}^{\text{virt}})_{\text{finite}}(x_1, x_2, \mu) \right. \right. \\
& + \left. (\hat{\sigma}_{gg}^{\text{soft}})_{\text{finite}}(x_1, x_2, \mu) + \hat{\sigma}_{gg}^{s+v+ct}(x_1, x_2, \mu) + (1 \leftrightarrow 2) \right\} \\
& + \frac{1}{2} \int dx_1 dx_2 \left\{ \int_{x_1}^{1-\delta_s} \frac{dz}{z} \left[\mathcal{F}_g^p\left(\frac{x_1}{z}, \mu\right) \mathcal{F}_g^{\bar{p}(p)}(x_2, \mu) + \mathcal{F}_g^p(x_2, \mu) \mathcal{F}_g^{\bar{p}(p)}\left(\frac{x_1}{z}, \mu\right) \right] \right. \\
& \times \hat{\sigma}_{gg}^{\text{LO}}(x_1, x_2, \mu) \frac{\alpha_s}{2\pi} \ln \left(\frac{s}{\mu^2} \frac{(1-z)^2 \delta_c}{z} \frac{\delta_c}{2} \right) P_{gg}(z) + (1 \leftrightarrow 2) \left. \right\} \\
& + \frac{1}{2} \int dx_1 dx_2 \left\{ \mathcal{F}_g^p(x_1, \mu) \mathcal{F}_g^{\bar{p}(p)}(x_2, \mu) \hat{\sigma}_{gg}^{\text{hard/non-coll}}(x_1, x_2, \mu) + (1 \leftrightarrow 2) \right\} ,
\end{aligned} \tag{2.96}$$

where $\hat{\sigma}_{gg}^{s+v+ct}$ is obtained from the sum of $(\hat{\sigma}_{gg}^{\text{virt}})_{UV\text{-pole}}$ of Eq. (2.70), $\hat{\sigma}_{gg}^{s+v}$ of Eq. (2.82), and the PDF counterterm in Eq. (2.95) as follows

$$\hat{\sigma}_{gg}^{s+v+ct} = \frac{\alpha_s}{2\pi} \left[4N \ln(\delta_s) \ln \left(\frac{s}{\mu^2} \right) + \left(\frac{11}{3}N - \frac{2n_{lf}}{3} + 4N \ln(\delta_s) \right) \ln \left(\frac{m_b^2}{s} \right) \right] \hat{\sigma}_{gg}^{\text{LO}} . \tag{2.97}$$

We note that σ_{gg}^{NLO} is finite, since, after mass factorization, both soft and collinear singularities have been canceled between $\hat{\sigma}_{gg}^{\text{virt}} + \hat{\sigma}_{gg}^{\text{soft}}$ and $\hat{\sigma}_{gg}^{\text{hard/coll}}$. The last terms respectively describe the finite real gluon emission of Eq. (2.12). Note that when collecting all the terms in Eq. (2.96) that are proportional to $\ln(\mu^2/s)$, one obtains exactly the last two terms in Eq. (2.7), as predicted by renormalization group arguments.

For the $(q, \bar{q})g$ initiated processes we find

$$\begin{aligned}
\sigma_{\text{NLO}}^{qg} = & \frac{\alpha_s}{2\pi} \sum_{i=q, \bar{q}} \int dx_1 dx_2 \left\{ \int_{x_1}^1 \frac{dz}{z} \mathcal{F}_i^p\left(\frac{x_1}{z}, \mu\right) \mathcal{F}_g^{\bar{p}(p)}(x_2, \mu) \times \right. \\
& \hat{\sigma}_{g\bar{q}}^{\text{LO}}(x_1, x_2, \mu) \left[P_{ig}^4(z) \ln\left(\frac{s}{\mu^2} \frac{(1-z)^2}{z} \frac{\delta_c}{2}\right) - P'_{ig}(z) \right] \\
& + \int_{x_1}^1 \frac{dz}{z} \mathcal{F}_g^p\left(\frac{x_1}{z}, \mu\right) \mathcal{F}_i^{\bar{p}(p)}(x_2, \mu) \times \\
& \hat{\sigma}_{q\bar{q}}^{\text{LO}}(x_1, x_2, \mu) \left[P_{gi}^4(z) \ln\left(\frac{s}{\mu^2} \frac{(1-z)^2}{z} \frac{\delta_c}{2}\right) - P'_{gi}(z) \right] + (1 \leftrightarrow 2) \Big\} \\
& + \sum_{i=q, \bar{q}} \int dx_1 dx_2 \left\{ \mathcal{F}_i^p(x_1, \mu) \mathcal{F}_g^{\bar{p}(p)}(x_2, \mu) \hat{\sigma}_{ig}^{\text{non-coll}}(x_1, x_2, \mu) + (1 \leftrightarrow 2) \right\} ,
\end{aligned} \tag{2.98}$$

We would like to conclude this section by showing explicitly that the total NLO cross section, σ^{NLO} , does not depend on the arbitrary cutoffs introduced by the PSS method, i.e. on δ_s and δ_c . The cancellation of the PSS cutoff dependence is realized in σ^{real} by matching contributions that are calculated either analytically, in the IR-unsafe region below the cutoffs, or numerically, in the IR-safe region above the cutoffs. While the analytical calculation in the IR-unsafe region reproduces the form of the cross section in the soft or collinear limits and is therefore only accurate for small values of the cutoffs, the numerical integration in the IR-safe region becomes unstable for very small values of the cutoffs. Therefore, obtaining a convincing cutoff independence involves a delicate balance between the previous antagonistic requirements and ultimately dictates the choice of values that are neither too large nor too small for the cutoffs. The Monte Carlo phase space integration has been performed using the adaptive multi-dimensional integration routine VEGAS [71].

Figures 2.22 and 2.23 illustrate the dependence of the total cross section $\sigma^{\text{NLO}}(p\bar{p} \rightarrow Zb\bar{b})$ on the two-cutoffs of the PSS method, using the setup outlined in Section 3.1. In Figure 2.22, δ_s is varied between 10^{-5} and 10^{-2} with $\delta_c = 10^{-5}$, while in Figure 2.23, δ_c is varied between 10^{-7} and 10^{-4} with $\delta_s = 10^{-3}$. In both plots, we show in the upper window the overall cutoff dependence cancellation between $\sigma^{\text{soft}} + \sigma^{\text{hard/coll}}$ and $\sigma^{\text{hard/non-coll}}$ in σ^{real} including all channels, gg , $q\bar{q}$ and qg . We include too contributions from the LO and the virtual cross sections which are cutoff independent. In the lower window of the same plots we complement this information by reproducing the full σ^{NLO} , including all channels, on a larger scale that magnifies the details of the cutoff dependence cancellation. The statistical errors from the

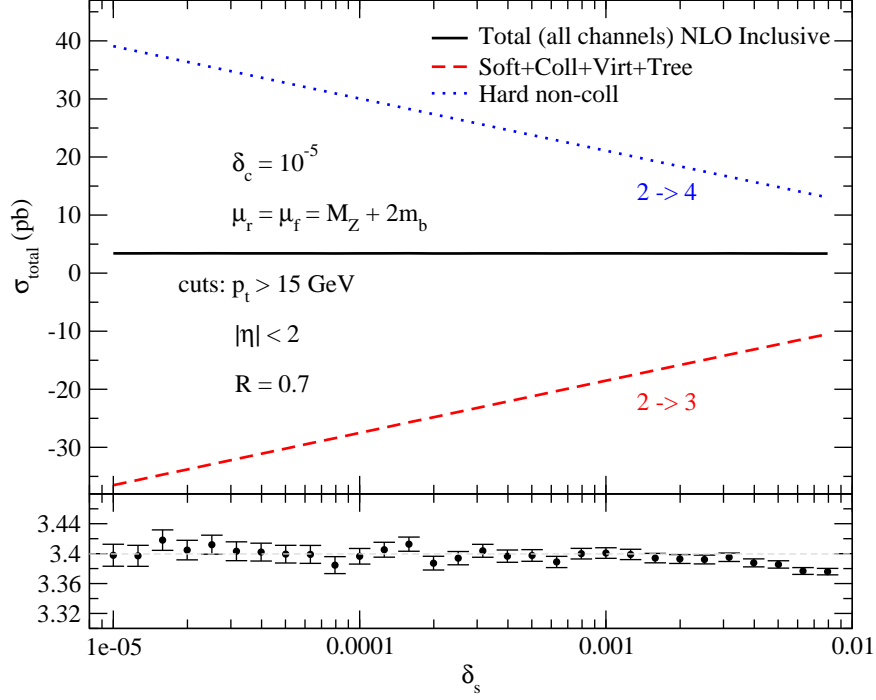


Figure 2.22: Dependence of $\sigma^{\text{NLO}}(p\bar{p} \rightarrow Zb\bar{b})$ on the soft cutoff δ_s of the two-cutoff PSS method for $\mu = M_Z + 2m_b$, and $\delta_c = 10^{-5}$. The upper plot shows the cancellation of the δ_s -dependence between $\sigma^{\text{soft}} + \sigma^{\text{hard/coll}}$ and $\sigma^{\text{hard/non-coll}}$. The lower plot shows, on an enlarged scale, the dependence of the full $\sigma^{\text{NLO}} = \sigma_{gg}^{\text{NLO}} + \sigma_{q\bar{q}}^{\text{NLO}} + \sigma_{qg}^{\text{NLO}}$ on δ_s with the corresponding statistical errors.

Monte Carlo phase space integration are also shown. Both Figures 2.22 and 2.23 show a clear plateau over a wide range of δ_s and δ_c and the NLO cross section is proven to be cutoff independent. The results presented in Chapter 3 have been obtained by using $\delta_s = 10^{-3}$ and $\delta_c = 10^{-5}$.

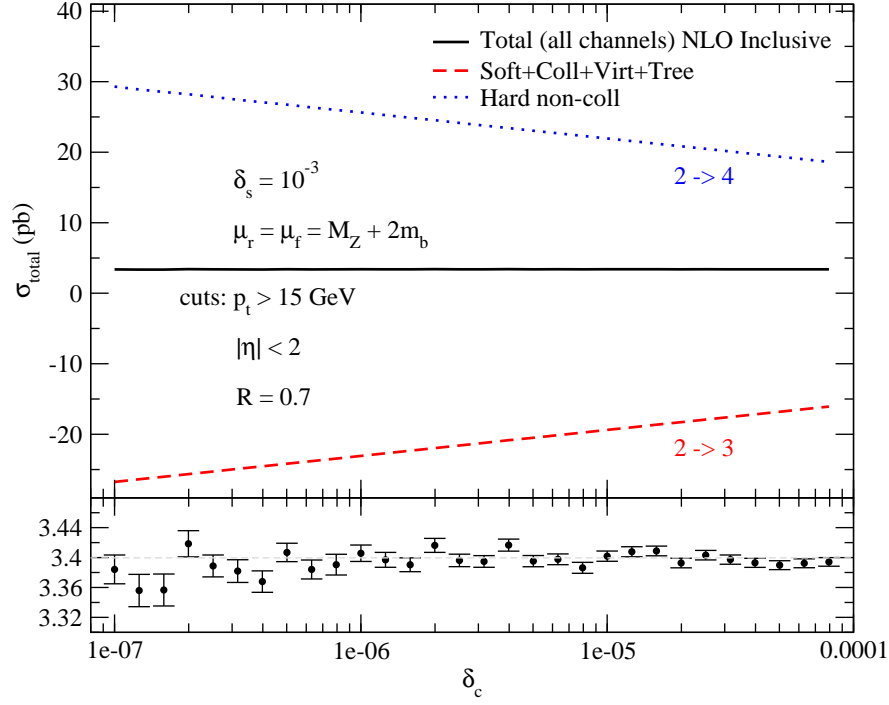


Figure 2.23: Dependence of $\sigma^{\text{NLO}}(p\bar{p} \rightarrow Zb\bar{b})$ on the collinear cutoff δ_c of the two-cutoff PSS method, for $\mu = M_Z + 2m_b$, and $\delta_s = 10^{-3}$. The upper plot shows the cancellation of the δ_s -dependence between $\sigma^{\text{soft}} + \sigma^{\text{hard/coll}}$, and $\sigma^{\text{hard/non-coll}}$. The lower plot shows, on an enlarged scale, the dependence of the full $\sigma^{\text{NLO}} = \sigma_{gg}^{\text{NLO}} + \sigma_{q\bar{q}}^{\text{NLO}} + \sigma_{qg}^{\text{NLO}}$ on δ_c with the corresponding statistical errors.

CHAPTER 3

Numerical Results

In this Chapter, we present numerical results for the total cross sections and distributions for $W/Z\ b\bar{b}$ production including NLO QCD corrections and complete bottom-quark mass effects [84, 92]. We specialize our discussion to the case of the Tevatron collider, because this is at the moment the most interesting phenomenological environment (see introduction in Chapter 1). We also investigate the stability of the NLO QCD results by studying the dependence of the total cross section on the renormalization (μ_r) and factorization (μ_f) scales. Finally, we carefully compare our results with results obtained from a NLO calculation that considers massless bottom quarks by using the MCFM code [49].

In Section 3.1 we specify the setup used to produce the plots, while in Sections 3.2 and 3.3 we present and discuss results for $Wb\bar{b}$ and $Zb\bar{b}$ production respectively.

3.1 The Setup

We present NLO QCD results for $W/Z\ b\bar{b}$ production at the Tevatron using a non-zero bottom-quark mass fixed at $m_b=4.62$ GeV. The W and Z bosons are considered on-shell and their masses are taken to be $M_W = 80.410$ GeV and $M_Z = 91.1876$ GeV. The mass of the top quark, entering in virtual corrections, is set to $m_t = 170.9$ GeV. The LO results use the one-loop evolution of α_s and the CTEQ6L1 set of PDF [93], with $\alpha_s^{\text{LO}}(M_Z) = 0.130$, while the NLO results use the two-loop evolution of α_s and the CTEQ6M set of PDF, with $\alpha_s^{\text{NLO}}(M_Z) = 0.118$. The W boson coupling to quarks is proportional to the Cabibbo-Kobayashi-Maskawa (CKM) matrix elements. We take $V_{ud} = V_{cs} = 0.975$ and $V_{us} = V_{cd} = 0.222$, while we neglect the contribution of the third generation of quarks, since it is suppressed either by the initial state quark densities or by the corresponding CKM matrix elements.

Table 3.1: LO and NLO total $Wb\bar{b}$ cross sections at the Tevatron for massive and massless bottom quarks, using $\mu_r = \mu_f = M_W + 2m_b$. The numbers in square brackets are the ratios of the NLO and LO cross sections, the so called K -factors. Statistical errors of the MC integration amount to about 0.1%.

Cross Section	$m_b \neq 0$ (pb) [ratio]	$m_b = 0$ (pb) [ratio]
σ_{LO}	2.20[–]	2.38[–]
$\sigma_{\text{NLO}} \text{ inclusive}$	3.20[1.45]	3.45[1.45]
$\sigma_{\text{NLO}} \text{ exclusive}$	2.64[1.20]	2.84[1.19]

Partons cannot be detected as they are always confined in hadrons. For this reason, any phenomenological collider study, including final hadronic states, must implement a jet algorithm to recombine partons into jets, in a way consistent with factorization (see Section 2.1) and with experimental techniques. The jet algorithm basically assigns a “separation” between partons, and, based on it, defines criteria to decide whether to group a set of partons in the final state into a “proto-jet”. Finally, kinematic cuts are applied depending on the experimental setup, to decide if a proto-jet is in an observable region, in which case the proto-jet is promoted to a jet. We will consider in our study b -type and *light*-type jets, where the former contains either a b or a \bar{b} quark and the latter can only contain massless quarks or gluons.

We implement the k_T jet algorithm [94, 95, 96, 97] with a pseudo-cone size $R = 0.7$ and we recombine the parton momenta within a jet using the so called covariant E -scheme [95]. We checked that our implementation of the k_T jet algorithm coincides with the one in MCFM. We require all events to have a $b\bar{b}$ jet pair in the final state, with each jet having a transverse momentum larger than 15 GeV ($p_T^{b,\bar{b}} > 15$ GeV) and a pseudorapidity that satisfies $|\eta^{b,\bar{b}}| < 2$. We impose the same p_T and $|\eta|$ cuts also on the extra jet that may arise due to hard non-collinear real emission of a parton, i.e. in the processes $W/Z \ b\bar{b} + g$ or $W/Z \ b\bar{b} + q(\bar{q})$. This hard non-collinear extra parton is treated either *inclusively* or *exclusively*. In the *inclusive* case we include both two- and three-jet events, while in the *exclusive* case we require exactly two jets in the event. Two-jet events consist of a bottom-quark jet pair that may also include a final-state light parton (gluon or quark) due to the applied jet algorithm. Results in the massless bottom-quark approximation have been obtained using the MCFM code [49].

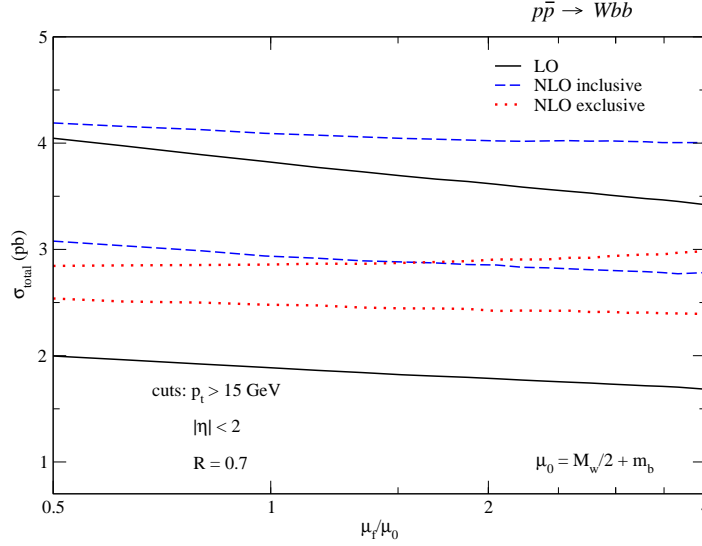


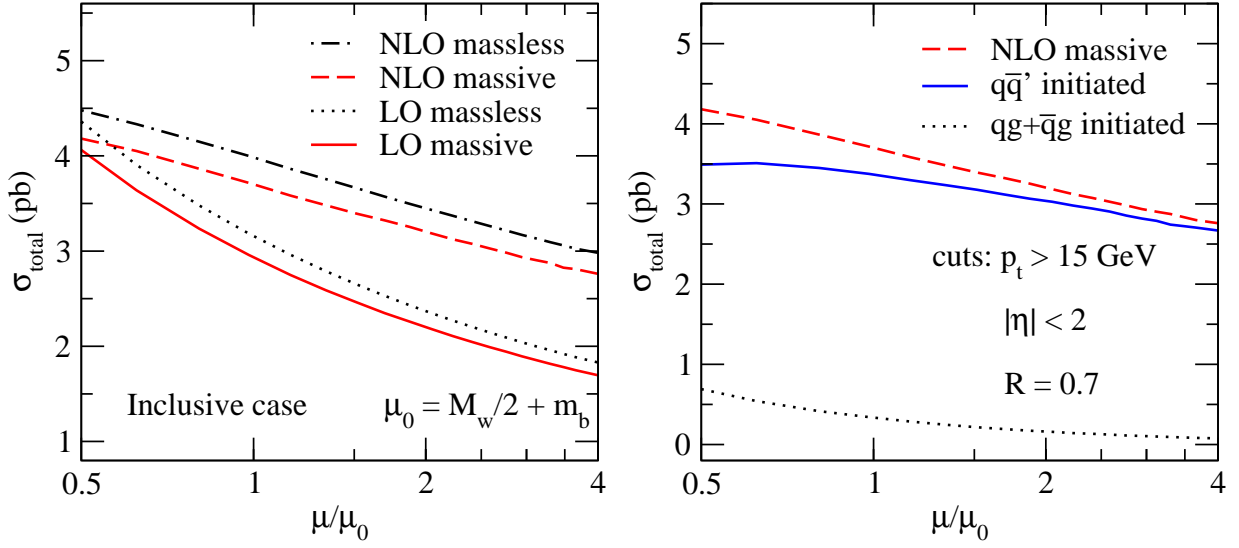
Figure 3.1: Dependence of the LO (black solid band), NLO *inclusive* (blue dashed band), and NLO *exclusive* (red dotted band) $Wb\bar{b}$ total cross sections on the renormalization/factorization scales, including full bottom-quark mass effects. The bands are obtained by independently varying both μ_r and μ_f between $\mu_0/2$ and $4\mu_0$ (with $\mu_0 = m_b + M_W/2$).

3.2 $Wb\bar{b}$ Production at the Tevatron

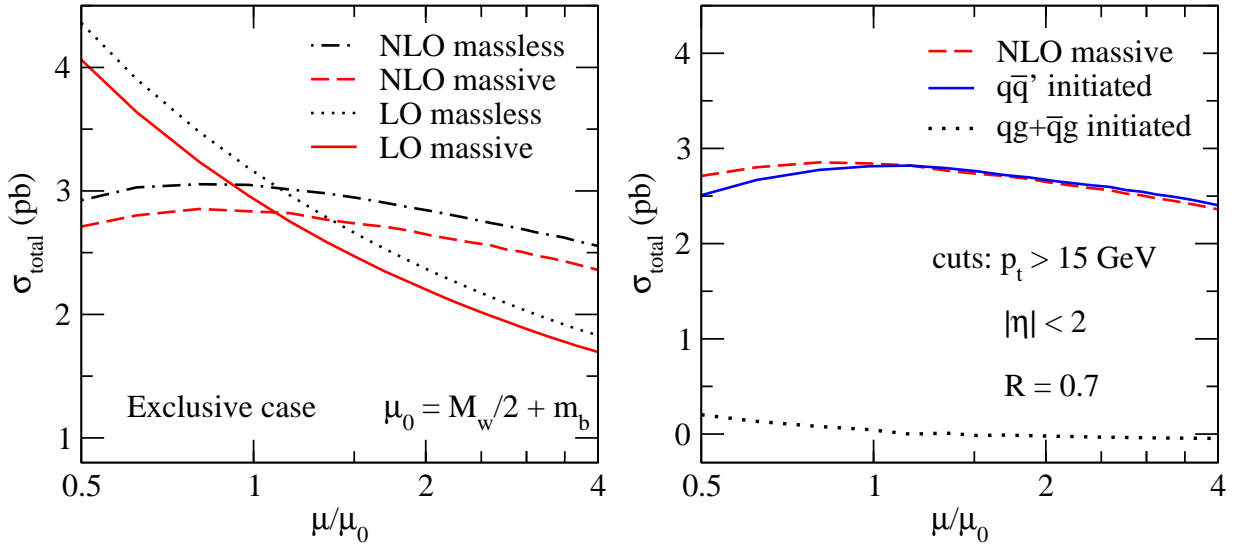
Let us first consider the influence of the NLO QCD corrections on the total cross section. In Table 3.1 we present the results obtained for both LO and NLO total cross sections, at a reference scale $\mu_r = \mu_f = M_W + 2m_b$, both in our fully massive calculation and in the massless approximation.

It can be seen that, given the setup explained in Section 3.1, the NLO QCD corrections increase considerably the total cross section, with NLO/LO ratios (K -factors) of about 1.45 and 1.2 for the inclusive and exclusive case respectively (for both the massive and massless calculations). We can see also that, in general, the massless approximation overestimates the total cross section. In the following we will study in detail where these corrections are more important, and we will show that, in the case of distributions, a global rescaling (or K -factor) does not properly simulate the NLO corrections.

In Figures 3.1 and 3.2, we illustrate the renormalization and factorization scale dependence of the LO and NLO total cross sections, both in the *inclusive* and *exclusive* case.



(a) *Inclusive case*



(b) *Exclusive case*

Figure 3.2: Dependence of the LO and NLO *inclusive* and *exclusive* $p\bar{p} \rightarrow Wb\bar{b}$ total cross section on the renormalization/factorization scale, when $\mu_r = \mu_f = \mu$. The left hand side plot compares both LO and NLO total cross sections for the case in which the bottom quark is treated as massless (MCFM) or massive (our calculation). The right hand side plot shows separately, for the massive case only, the scale dependence of the $q\bar{q}'$ and $qg + \bar{q}g$ contributions, as well as their sum.

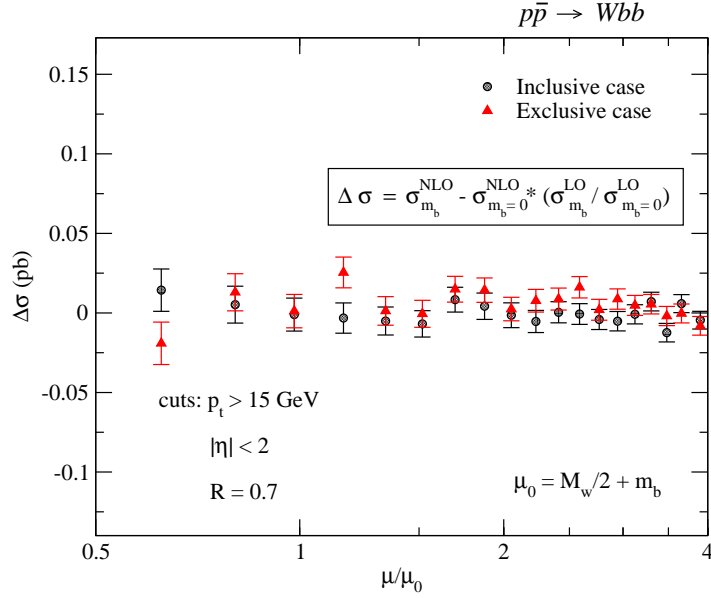


Figure 3.3: Dependence on the renormalization/factorization scale of the rescaled difference between our NLO calculation (with $m_b \neq 0$) of the total $Wb\bar{b}$ cross section and the corresponding result computed using MCFM (with $m_b = 0$) for the *inclusive* and *exclusive* cases (with $\mu_r = \mu_f = \mu_0$) respectively. The error bars indicate the statistical uncertainty of the Monte Carlo integration.

Figure 3.1 shows the overall scale dependence of both LO, NLO *inclusive* and NLO *exclusive* total cross sections, when both μ_r and μ_f are varied independently between $\mu_0/2$ and $4\mu_0$ (with $\mu_0 = m_b + M_W/2$), including full bottom-quark mass effects. We notice that the NLO cross sections have a reduced scale dependence over the range of scales shown, and the *exclusive* NLO cross section is more stable than the *inclusive* one especially at low scales. This is consistent with the fact that the *inclusive* NLO cross section integrates over the entire phase space of the $qg(\bar{q}g) \rightarrow b\bar{b}W + q(\bar{q})$ channels that are evaluated with NLO α_s and NLO PDFs, but are actually tree-level processes and retain therefore a strong scale dependence. In the *exclusive* case only the $2 \rightarrow 3$ collinear kinematic of these processes is retained, since 3-jets events are discarded, and this makes the overall renormalization and factorization scale dependence milder. To better illustrate this point, we show in the right hand side plots of Figures 3.2(a) and 3.2(b) the μ -dependence of the total cross section and of the partial cross sections corresponding to the $q\bar{q}'$ and the $qg + \bar{q}g$ initiated channels separately, for $\mu_r = \mu_f$,

both for the *inclusive* and for the *exclusive* case. It is clear that the low scale behavior of the *inclusive* cross section is mainly driven by the $qg + \bar{q}g$ contribution. In the left hand side plots of Figures 3.2(a) and 3.2(b), we also compare the scale dependence of our results to the scale dependence of the corresponding results obtained with $m_b = 0$ (using MCFM), both at LO and at NLO. Using a non-zero value of m_b is not expected to have any impact on the scale dependence of the result¹ and, indeed, the scale dependence of the LO and NLO pair of curves is very similar, with a shift due to the bottom-quark mass effects.

While the LO cross section still has a 40% uncertainty due to scale dependence, this uncertainty is reduced at NLO to about 20% for the *inclusive* and to about 10% for the *exclusive* cross sections. The uncertainties have been estimated as the positive/negative deviation with respect to the mid-point of the bands plotted in Figure 3.1, where each band range is defined by the minimum and maximum value in the band. We notice incidentally that the difference due to finite bottom-quark mass effects is less significant than the theoretical uncertainty due to the residual scale dependence in the *inclusive* case, but is comparable in size in the *exclusive* case. Indeed, the finite bottom-quark mass effects amount to about 8% in both *inclusive* and *exclusive* cases.

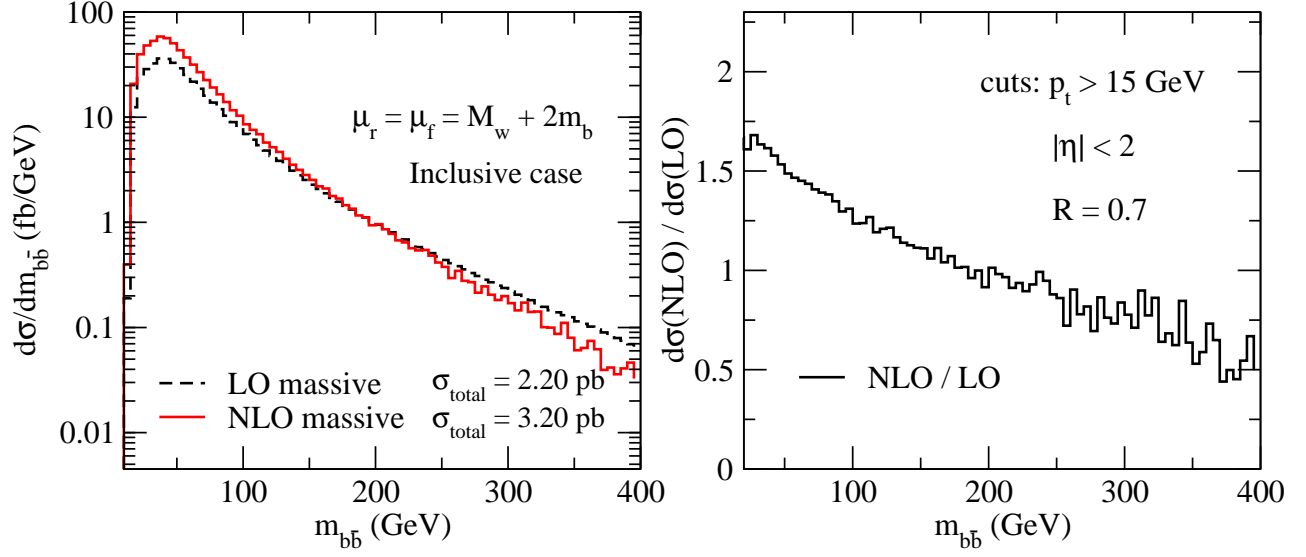
In Figure 3.3 we show the rescaled difference between the NLO total cross sections obtained from our calculation (with $m_b \neq 0$) and with MCFM (with $m_b = 0$) defined as follows:

$$\Delta\sigma = \sigma^{\text{NLO}}(m_b \neq 0) - \sigma^{\text{NLO}}(m_b = 0) \frac{\sigma^{\text{LO}}(m_b \neq 0)}{\sigma^{\text{LO}}(m_b = 0)}. \quad (3.1)$$

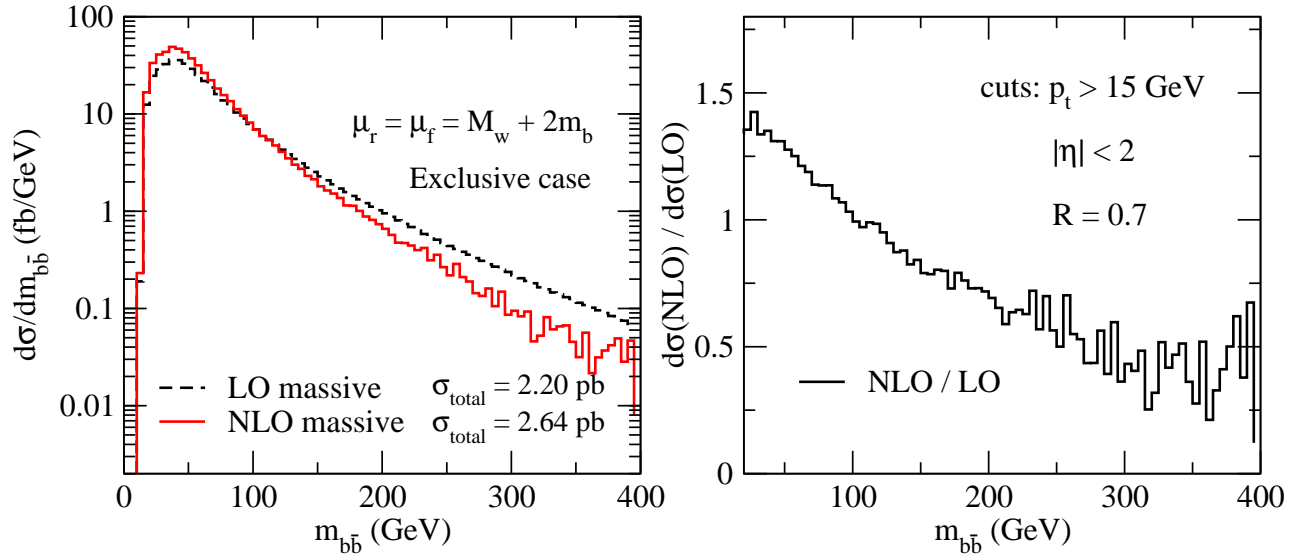
As can be seen, within the statistical errors of the Monte Carlo integration, the finite bottom-quark mass effects on the total cross sections at NLO are well described by the corresponding effects at LO.

Finally, in Figures 3.4-3.6 we study the distribution $d\sigma/dm_{b\bar{b}}$, where $m_{b\bar{b}}$ is the invariant mass of the $b\bar{b}$ jet pair. The impact of NLO QCD corrections on this distribution is illustrated in Figures 3.4(a) and 3.4(b) for the *inclusive* and *exclusive* case, respectively. We see that the NLO QCD corrections affects the cross section quite substantially in particular for low values of $m_{b\bar{b}}$. In each figure the right hand side plot gives the ratio of the NLO and LO distributions, providing a sort of K -factor bin by bin. Figures 3.5(a) and 3.5(b) compare the NLO $d\sigma/dm_{b\bar{b}}$ distributions obtained from the massive and massless bottom-quark calculations. The results

¹Note that we always use $m_b = 4.62$ GeV in the determination of the scales in terms of $\mu_0 = m_b + M_W/2$ even in the results obtained with $m_b = 0$.

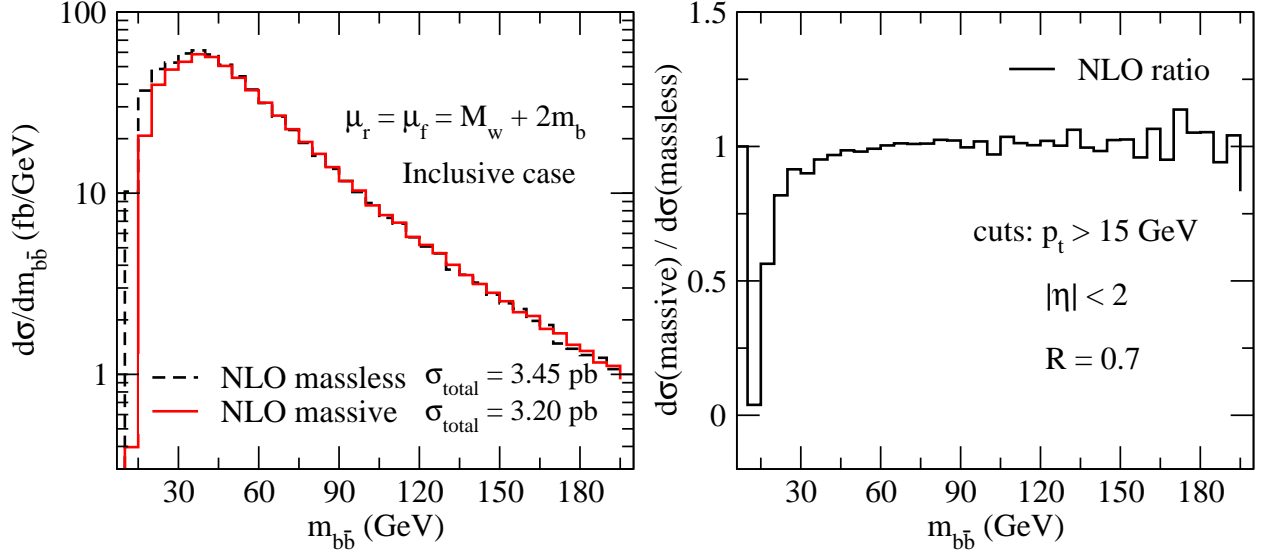


(a) *Inclusive case*

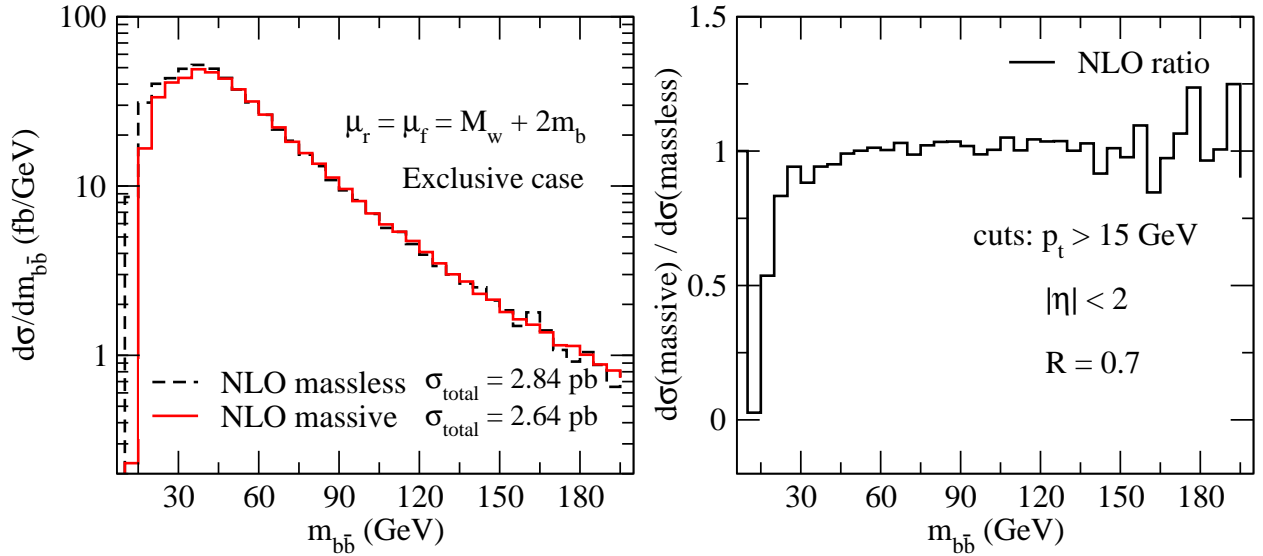


(b) *Exclusive case*

Figure 3.4: The distribution $d\sigma(p\bar{p} \rightarrow Wb\bar{b})/dm_{b\bar{b}}$ in LO and NLO QCD. The right hand side plot shows the ratio of the LO and NLO distributions.



(a) *Inclusive case*



(b) *Exclusive case*

Figure 3.5: The *inclusive* and *exclusive* distributions $d\sigma(p\bar{p} \rightarrow Wb\bar{b})/dm_{b\bar{b}}$ derived from our calculation (with $m_b \neq 0$) and from MCFM (with $m_b = 0$). The right hand side plot shows the ratio of the two distributions, $d\sigma(m_b \neq 0)/d\sigma(m_b = 0)$.

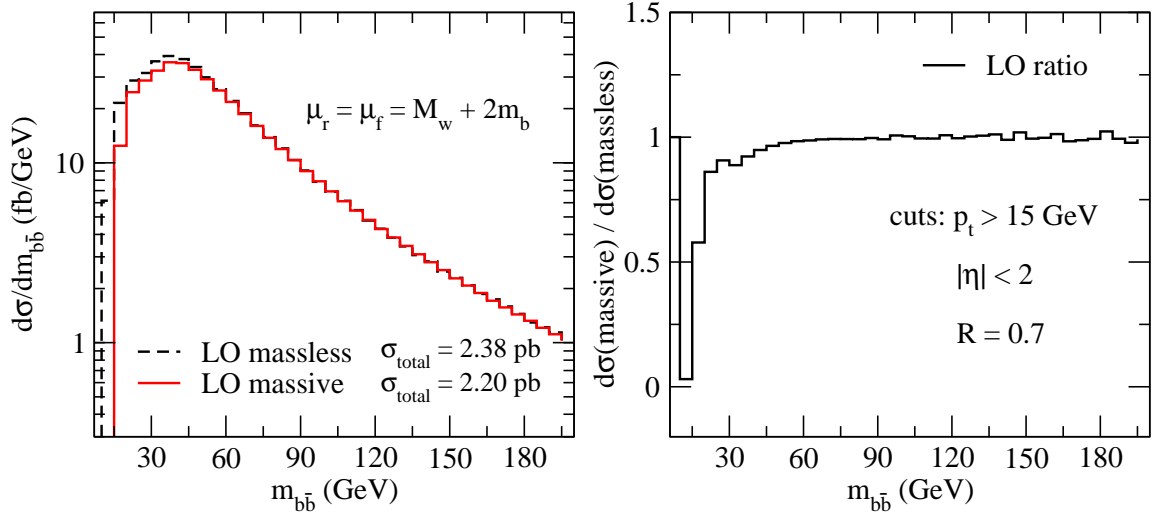


Figure 3.6: The LO distribution $d\sigma(p\bar{p} \rightarrow Wb\bar{b})/dm_{b\bar{b}}$ derived from our calculation (with $m_b \neq 0$) and from MCFM (with $m_b = 0$). The right hand side plot shows the ratio of the two distributions, $d\sigma(m_b \neq 0)/d\sigma(m_b = 0)$.

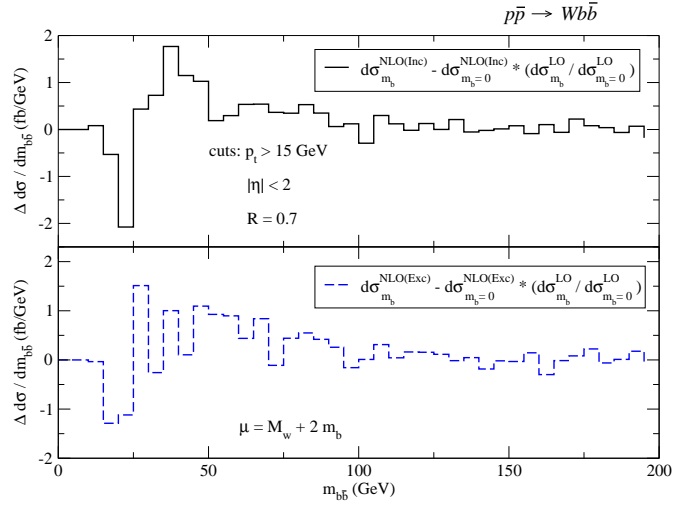


Figure 3.7: The $m_{b\bar{b}}$ distribution of the rescaled difference between our NLO calculation (with $m_b \neq 0$) and MCFM (with $m_b = 0$) for the *inclusive* (upper plot) and *exclusive* (lower plot) $p\bar{p} \rightarrow Wb\bar{b}$ production.

with $m_b = 0$ have been obtained using MCFM. As expected, most of the difference between the massless and massive bottom-quark cross sections is coming from the region of low invariant mass $m_{b\bar{b}}$, both for the inclusive and exclusive case, where the cross sections for $m_b \neq 0$ are consistently below the ones with $m_b = 0$. For completeness, we also show in Figure 3.6 the comparison between massive ($m_b \neq 0$) and massless ($m_b = 0$) calculations at LO in QCD. The LO $m_{b\bar{b}}$ distribution for massive bottom-quarks has been obtained both from our calculation and from MCFM, which implements the $m_b \neq 0$ option at tree level, and both results have been found in perfect agreement. As can be seen by comparing Figures 3.5(a)-3.5(b) and Figure 3.6, the impact of a non-zero bottom-quark mass is almost not affected by including NLO QCD corrections. To illustrate this in more detail, we show in Figure 3.7 the rescaled difference between the $m_{b\bar{b}}$ distributions obtained with our NLO calculation (with $m_b \neq 0$) and with MCFM (with $m_b = 0$) defined as follows:

$$\Delta \frac{d\sigma}{dm_{b\bar{b}}} = \frac{d\sigma^{\text{NLO}}}{dm_{b\bar{b}}}(m_b \neq 0) - \frac{d\sigma^{\text{NLO}}}{dm_{b\bar{b}}}(m_b = 0) \frac{d\sigma^{\text{LO}}(m_b \neq 0)}{d\sigma^{\text{LO}}(m_b = 0)}. \quad (3.2)$$

We notice that finite bottom-quark mass effects are particularly relevant for values of the $m_{b\bar{b}}$ invariant mass below about 60 GeV and that they appear to be of the same order at LO and NLO.

3.3 $Zb\bar{b}$ Production at the Tevatron

To start, let us have a look at the influence of the NLO QCD corrections on the total cross section. In Table 3.2 we present the values obtained with the scale $\mu_r = \mu_f = M_Z + 2m_b$, considering LO and NLO total cross sections, both in our fully massive calculation and in the massless approximation.

It can be seen that, given the setup explained in Section 3.1, the NLO QCD corrections increase considerably the total cross section, with NLO vs. LO ratios (K -factors) of about 1.5 and 1.27 for the inclusive and exclusive case respectively (for both the massive and massless calculations). We can also see that, in general, the massless approximation overestimates the total cross section. In the following we will study in detail where these corrections are more important, and especially we show that, in the case of distributions, a global rescaling (or K -factor) does not properly simulate the NLO corrections.

In Figures 3.8 and 3.9 we illustrate the renormalization and factorization scale dependence of the LO and NLO total cross sections, both in the *inclusive* and *exclusive* case. Figure 3.8

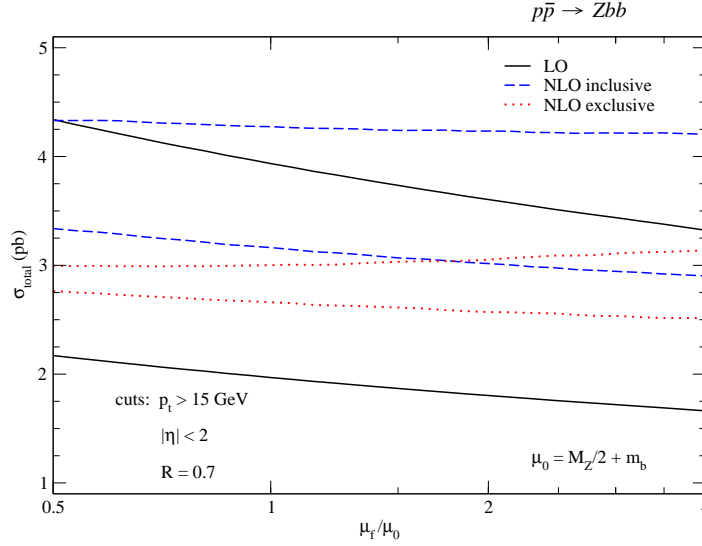


Figure 3.8: Dependence of the LO (black solid band), NLO *inclusive* (blue dashed band), and NLO *exclusive* (red dotted band) $Zb\bar{b}$ total cross sections on the renormalization/factorization scales, including full bottom-quark mass effects. The bands are obtained by independently varying both μ_r and μ_f between $\mu_0/2$ and $4\mu_0$ (with $\mu_0 = m_b + M_Z/2$).

shows the overall scale dependence of both LO, NLO *inclusive* and NLO *exclusive* total cross sections, when both μ_r and μ_f are varied independently between $\mu_0/2$ and $4\mu_0$ (with $\mu_0 = m_b + M_Z/2$), including full bottom-quark mass effects. We notice that the NLO cross sections have a reduced scale dependence over the range of scales shown, and the *exclusive* NLO cross section is more stable than the *inclusive*. Similarly to what we have discussed in the $Wb\bar{b}$ case, this effect is mainly driven by the tree level subprocess $q(\bar{q})g \rightarrow Zb\bar{b} + q(\bar{q})$ contributing to the real corrections. In the $Zb\bar{b}$ case, we also have a new initial state, namely gg . Its scale dependence behavior is similar to the $q\bar{q}$ initiated subprocess. To illustrate the independent contributions, we show in the right hand side plots of Figures 3.9(a) and 3.9(b) the μ -dependence of the total cross section and of the partial cross sections corresponding to the $q\bar{q}$, $qg + \bar{q}g$ and gg initiated channels separately, for $\mu_r = \mu_f$, both for the *inclusive* and for the *exclusive* case. It is clear that the low scale behavior of the *inclusive* cross section is considerably affected by the $qg + \bar{q}g$ contribution, which show a monotonic dependence on μ (i.e. with no plateau) characteristic of tree level processes. In the left hand side plots of Figures 3.9(a) and 3.9(b) we also compare the scale dependence of our results to

Table 3.2: LO and NLO total $Zb\bar{b}$ cross sections at the Tevatron for massive and massless bottom quarks, using $\mu_r = \mu_f = M_Z + 2m_b$. The numbers in square brackets are the ratios of the NLO and LO cross sections, the so called K -factors. Statistical errors of the MC integration amount to about 0.1%.

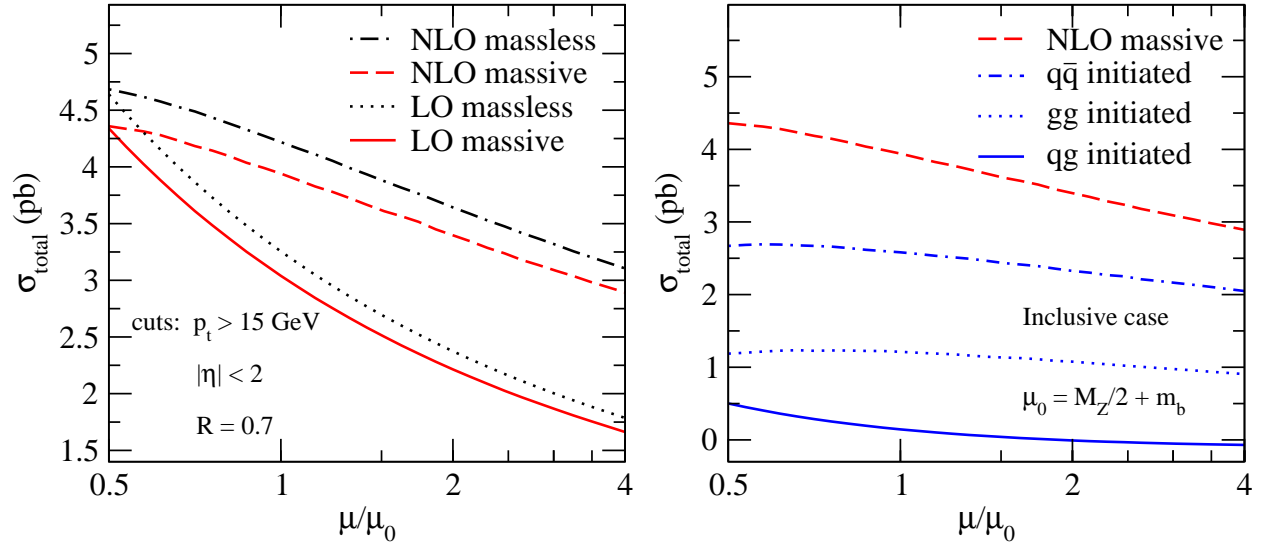
Cross Section	$m_b \neq 0$ (pb) [ratio]	$m_b = 0$ (pb) [ratio]
σ_{LO}	2.21[–]	2.37[–]
$\sigma_{\text{NLO}} \text{ inclusive}$	3.40[1.54]	3.64[1.54]
$\sigma_{\text{NLO}} \text{ exclusive}$	2.80[1.27]	3.01[1.27]

the scale dependence of the corresponding results obtained with $m_b = 0$ (using MCFM), both at LO and at NLO. Using a non-zero value of m_b is expected to have a mild impact on the scale dependence of the results, as the only modification to the renormalization scale dependence comes from the bottom quark mass renormalization, as shown in the subsections of Section 2.4 in Chapter 2. Indeed, the scale dependence of the LO and NLO curves is very similar.

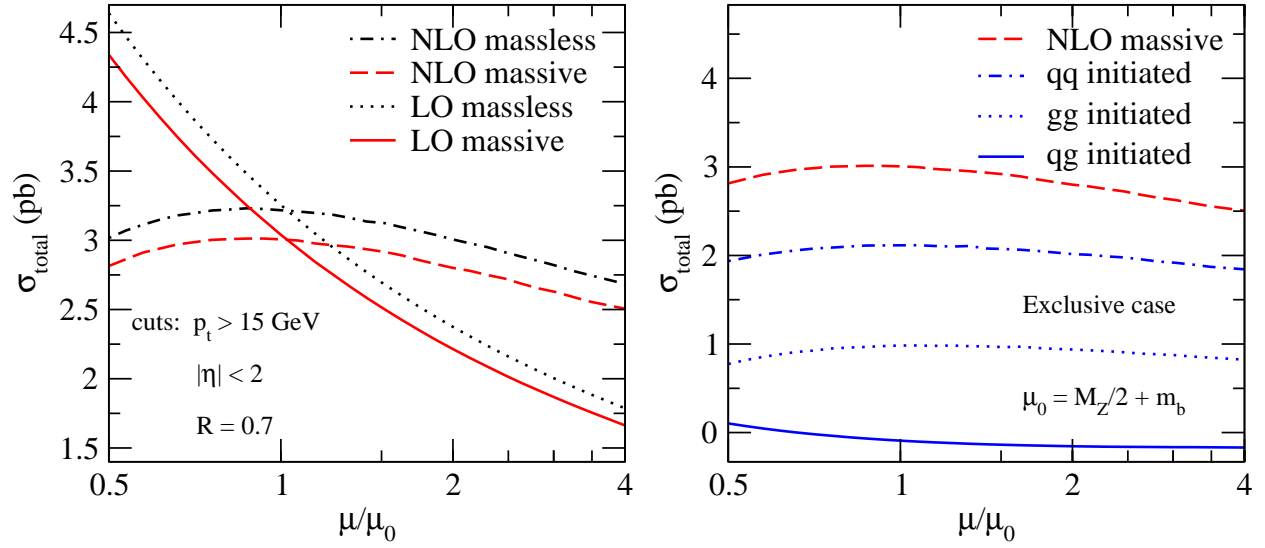
While the LO cross section still has a 45% uncertainty due to scale dependence, this uncertainty is reduced at NLO to about 20% for the *inclusive* and to about 11% for the *exclusive* cross sections. As before, the uncertainties have been estimated as the positive/negative deviation with respect to the mid-point of the bands plotted in Figure 3.8, where each band range is defined by the minimum and maximum value in the band. We notice incidentally that the difference due to finite bottom-quark mass effects is less significant than the theoretical uncertainty due to the residual scale dependence in the *inclusive* case, but is comparable in size in the *exclusive* case. Indeed, the finite bottom-quark mass effects amount to a reduction of the total cross sections by about 7% compared to the massless case at both LO and NLO QCD.

In Figure 3.10, we show the rescaled difference between the total cross sections obtained from our calculation (with $m_b \neq 0$) and with MCFM (with $m_b = 0$) defined as in Eq. (3.1). As can be seen, within the statistical errors of the MC integration, the finite bottom-quark mass effects on the total cross sections at NLO are well described by the corresponding effects at LO, similarly to what is observed in the $Wb\bar{b}$ case.

Finally, in Figures 3.11 to 3.13 we study the distribution $d\sigma/dm_{b\bar{b}}$, where $m_{b\bar{b}}$ is the invariant mass of the $b\bar{b}$ jet pair. The impact of NLO QCD corrections on this distribution



(a) *Inclusive case*



(b) *Exclusive case*

Figure 3.9: Dependence of the LO and NLO *inclusive* and *exclusive* $p\bar{p} \rightarrow Zb\bar{b}$ total cross section on the renormalization/factorization scale, when $\mu_r = \mu_f = \mu$. The LHS plots compare both LO and NLO total cross sections for the case in which the bottom quark is treated as massless (MCFM) or massive (our calculation). The RHS plots show separately, for the massive case only, the scale dependence of the $q\bar{q}$, gg and $qg + \bar{q}g$ contributions, as well as their sum.

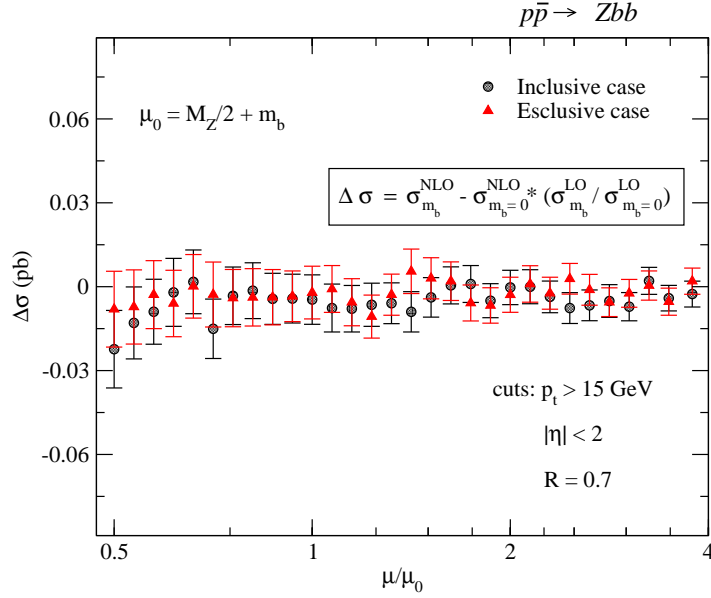


Figure 3.10: Dependence on the renormalization/factorization scale of the rescaled difference between our NLO calculation (with $m_b \neq 0$) of the total $Zb\bar{b}$ cross section and the corresponding result computed using MCFM (with $m_b = 0$) for the *inclusive* and *exclusive* cases (with $\mu_r = \mu_f = \mu_0$) respectively. The error bars indicate the statistical uncertainty of the Monte Carlo integration.

is illustrated in Figures 3.11(a) and 3.11(b) for the *inclusive* and *exclusive* case, respectively. We see that the NLO QCD corrections affects the cross section quite substantially, in particular, for low values of the $m_{b\bar{b}}$ invariant mass. In each figure the right hand side plot gives the ratio of the NLO and LO distributions. We stress the fact that the LO and NLO distributions are not just rescaled, which is clear from the RHS plots of Figures 3.11.

Figures 3.12(a) and 3.12(b) compare the NLO $d\sigma/dm_{b\bar{b}}$ distributions obtained from the massive and massless bottom-quark calculations. The results with $m_b = 0$ have been obtained using MCFM. As expected, most of the difference between the massless and massive bottom-quark cross sections is coming from the region of low $m_{b\bar{b}}$ invariant mass, both for the inclusive and exclusive case, where the cross sections for $m_b \neq 0$ are consistently below the ones with $m_b = 0$. This is better emphasized in the right hand side plots, where we show the ratio of the two distributions, $d\sigma(m_b \neq 0)/d\sigma(m_b = 0)$. For completeness, we also show in Figure 3.13 the comparison between massive ($m_b \neq 0$) and massless ($m_b = 0$)

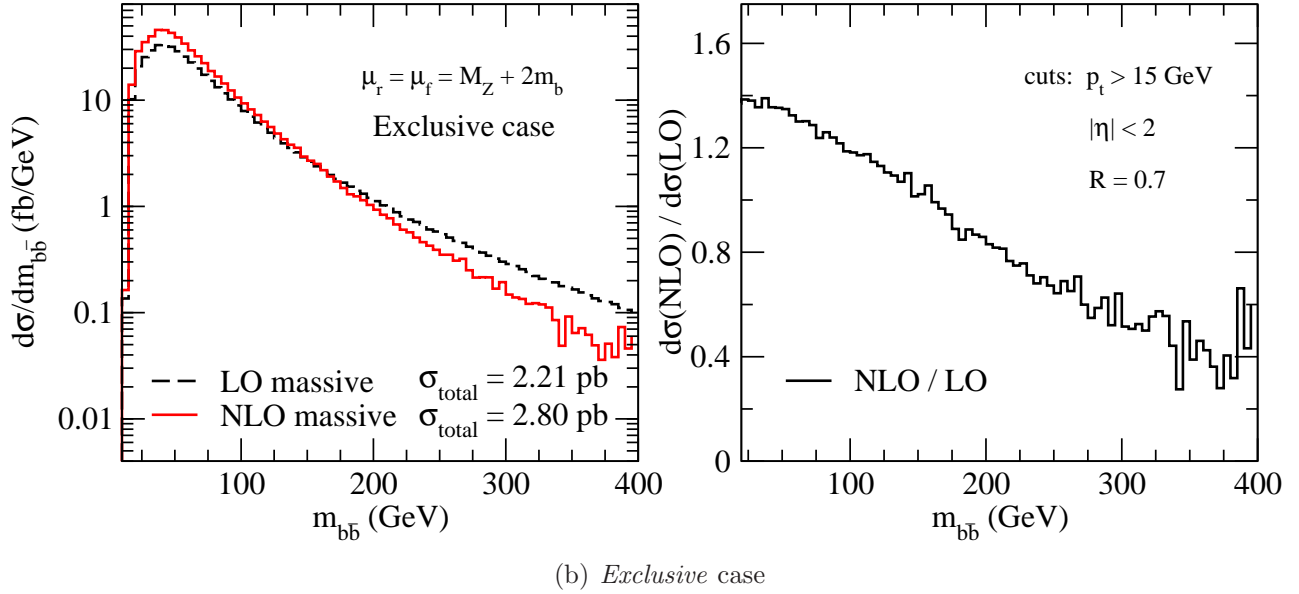
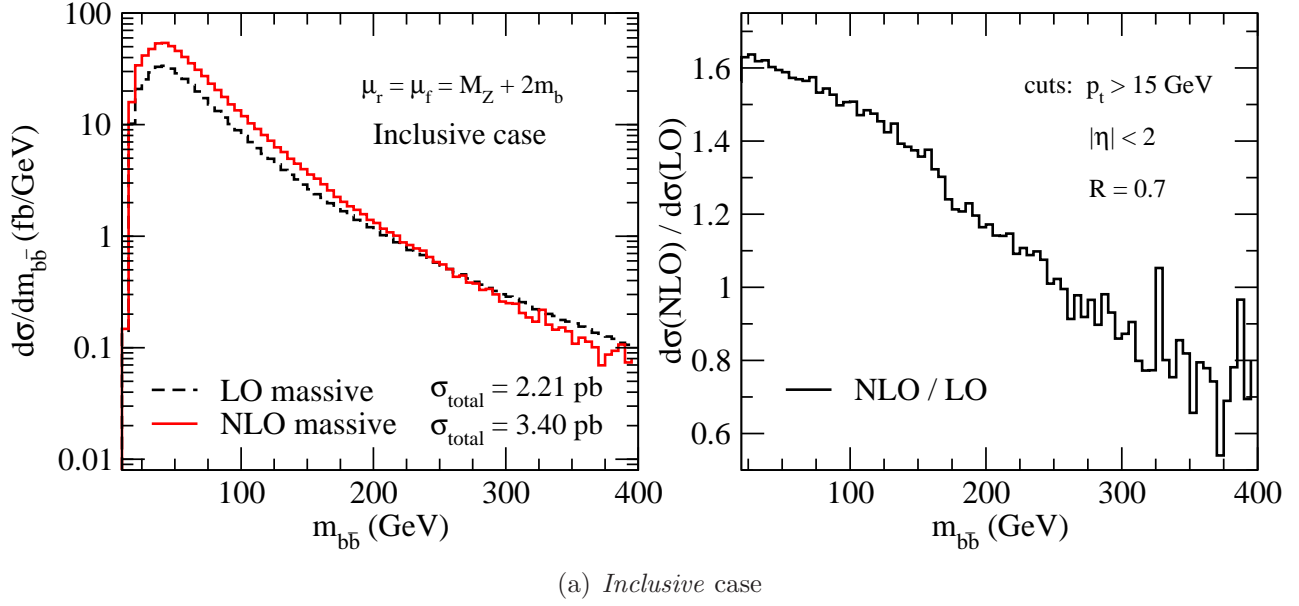
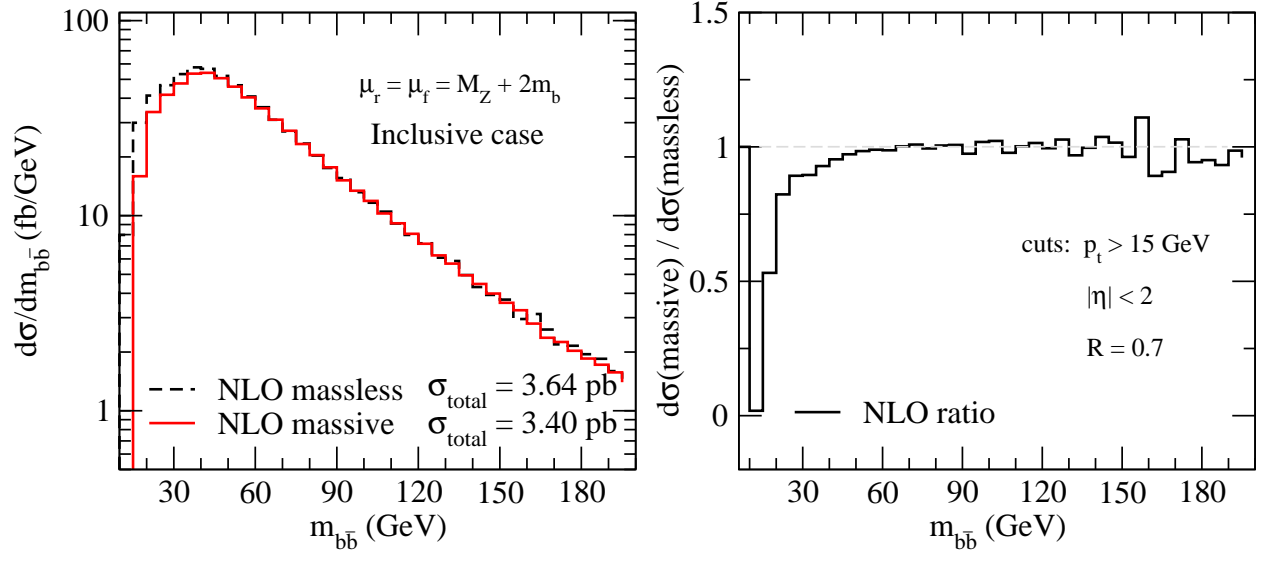
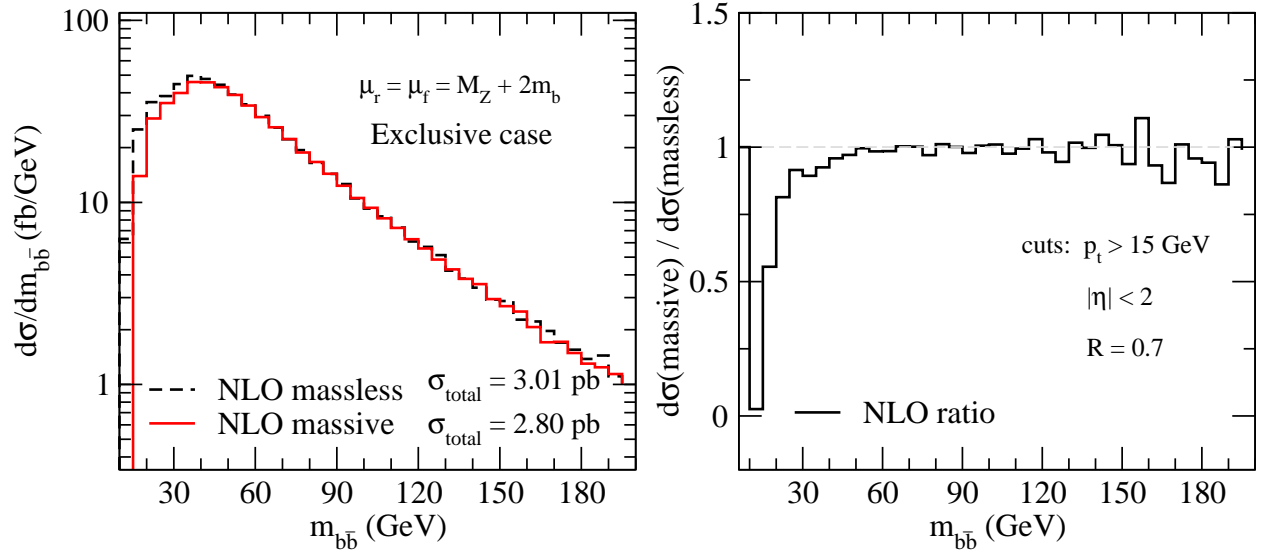


Figure 3.11: The distribution $d\sigma(p\bar{p} \rightarrow Zb\bar{b})/dm_{b\bar{b}}$ in LO and NLO QCD. The right hand side plot shows the ratio of the LO and NLO distributions.



(a) *Inclusive case*



(b) *Exclusive case*

Figure 3.12: The *inclusive* and *exclusive* distributions $d\sigma(p\bar{p} \rightarrow Zb\bar{b})/dm_{b\bar{b}}$ derived from our calculation (with $m_b \neq 0$) and from MCFM (with $m_b = 0$). The right hand side plot shows the ratio of the two distributions, $d\sigma(m_b \neq 0)/d\sigma(m_b = 0)$.

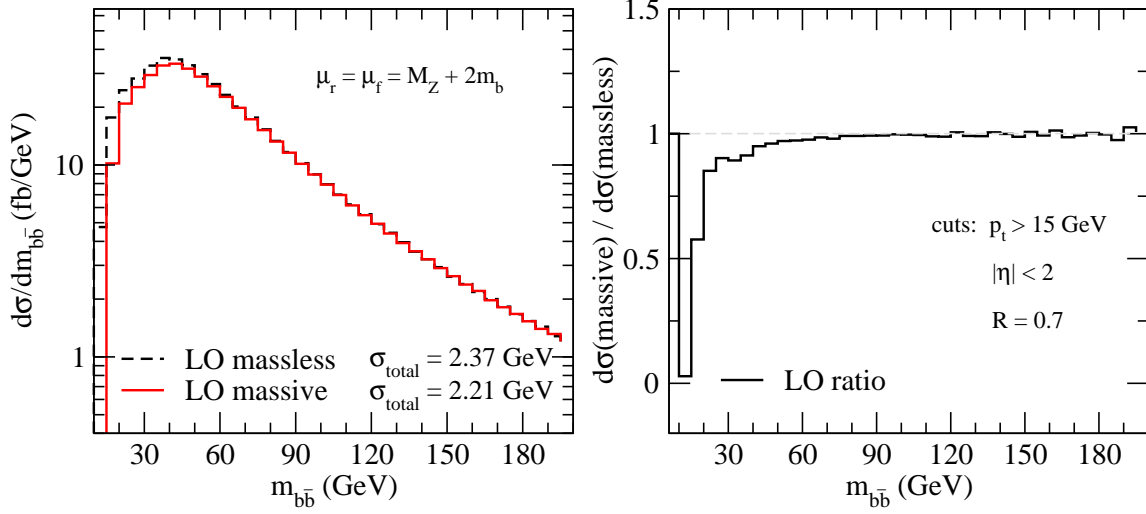


Figure 3.13: The LO distribution $d\sigma(p\bar{p} \rightarrow Zb\bar{b})/dm_{b\bar{b}}$ derived from our calculation (with $m_b \neq 0$) and from MCFM (with $m_b = 0$). The right hand side plot shows the ratio of the two distributions, $d\sigma(m_b \neq 0)/d\sigma(m_b = 0)$.

calculations at LO in QCD. The LO $m_{b\bar{b}}$ distribution for massive bottom-quarks has been obtained both from our calculation and from MCFM, which implements the $m_b \neq 0$ option at tree level, and both results agree perfectly. In general, mass effects are similar at LO and NLO. To illustrate this in more detail we show in Figure 3.14 the rescaled difference between the $m_{b\bar{b}}$ distributions obtained with our NLO calculation (with $m_b \neq 0$) and with MCFM (with $m_b = 0$) defined as in Eq. (3.2). We notice that, in the $Zb\bar{b}$ case, finite bottom-quark mass effects are relevant up to values of the $m_{b\bar{b}}$ invariant mass around 50 GeV.

For ongoing searches of a light SM Higgs boson, regions with small $m_{b\bar{b}}$ invariant mass are of relevance, as in many cases only one b -jet is tagged (semi-inclusive studies) in order to increase the experimental statistics. In such studies $m_{b\bar{b}}$ invariant mass distributions are produced by using the leading two jets in the event, one of them being the only tagged b -jet. In such case, a possible signal can come from a real emission in which the $b\bar{b}$ quark pair is recombined into a single b -jet (that is the partonic $m_{b\bar{b}}$ invariant mass is small) and the extra light parton is seen as another jet.

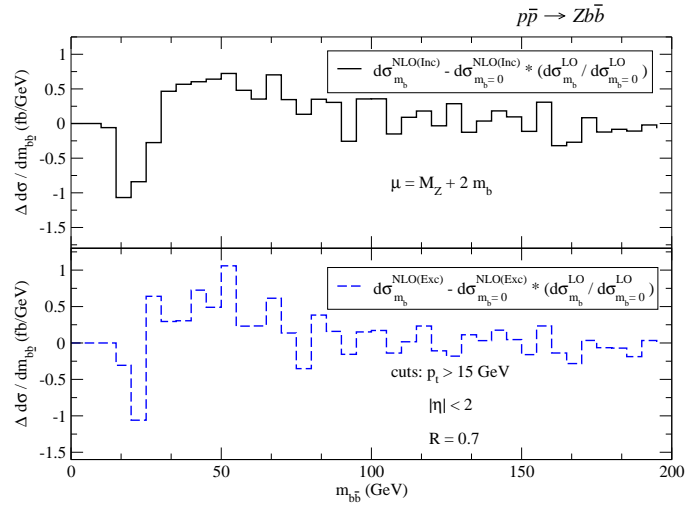


Figure 3.14: The $m_{b\bar{b}}$ distribution of the rescaled difference between our NLO calculation (with $m_b \neq 0$) and MCFM (with $m_b = 0$) for the *inclusive* (upper plot) and *exclusive* (lower plot) $p\bar{p} \rightarrow Zb\bar{b}$ production.

CHAPTER 4

CONCLUSION

We have presented a full review of our calculation of NLO QCD corrections to $W/Z\ b\bar{b}$ production at hadron colliders including full bottom-quark mass effects [84, 92]. We have shown results for total cross sections and $b\bar{b}$ invariant mass ($m_{b\bar{b}}$) distributions at the Tevatron Fermilab collider. We have found that, for such collider, the NLO QCD corrections reduce considerably the dependence on factorization and renormalization scales, in particular when considering exclusive cross sections where exactly two b -quark jets are tagged in the final state. This then reduces the theoretical uncertainty of the cross section, from about 40% at LO to 20% and 10% at NLO for the inclusive and exclusive cases, respectively. Even more importantly, we have found that NLO corrections change considerably the shape of LO distributions; that is, the NLO distributions are not simply a rescaling of those at LO.

We have systematically compared our results to a calculation that considers massless bottom quarks and have found that this approximation overestimates the total cross section by about 8% for $Wb\bar{b}$ production and 10% for $Zb\bar{b}$ production. The mass effects are particularly relevant in regions with small $m_{b\bar{b}}$ invariant mass. On the other hand, the massless calculation shows very similar dependence on the factorization and renormalization scales, as including mass effects is expected to affect very mildly such dependence.

4.1 Outlook

As we have stressed, our results are of relevance to the search for a SM-like Higgs particle in the VH ($V = W, Z$) associated production channel and to the measurement of single-top production, both processes of great interest to the high energy physics community. The low $m_{b\bar{b}}$ invariant mass region, where bottom-quark mass effects are most relevant, is important when a light SM-like Higgs particle ($M_H \sim 100 - 140$ GeV) is searched semi-inclusively and

by tagging only one b -quark, in order to increase the experimental statistics. The low $m_{b\bar{b}}$ invariant mass region is of course relevant for single-top production since in this case the whole $m_{b\bar{b}}$ spectrum is relevant, as the kinematics of the process is broader and semi-inclusive searches are essential.

We are currently studying the impact of our calculation on searches for single-top production, where we also consider final states with fewer than two b -quarks. We study modifications in the total cross sections and implications for b -tagging efficiency¹.

The next natural step is to implement our calculation for the LHC and study its phenomenological impact. Since at the LHC gluon initiated processes are enhanced, we expect some fundamental differences to appear. In particular, $q(\bar{q})g$ initiated subprocesses will play a bigger role and, given their tree level nature, will increase the dependence on renormalization and factorization scales and, to some extent, increase the theoretical uncertainty of the cross sections.

Finally, we want to emphasize that the calculation performed can be naturally extended to other important processes, such as $\gamma t\bar{t}$ production, which might be studied at the LHC and could give a direct measurement of the electric charge of the t -quark. In the same direction, we can study $\gamma b\bar{b}$ production at NLO in QCD. This process has considerable phenomenological implications, as it can put direct constraints on the b -quark PDF, which so far has only been derived from the gluon PDF evolution.

We can also study the associated production of a pseudo-scalar with heavy quarks, which is of relevance to searches for physics beyond the SM, particularly models with an extended Higgs sector, like supersymmetric models.

On the theoretical side, we expect to extend the checks performed on box coefficients by using generalized unitarity, to triangle, bubble and tadpole coefficients. Even more, we can extract analytically expressions for the contributing rational pieces. This will be of importance in the development of efficient new techniques for their extraction, as they will represent a playground to, for example, recursion relation techniques when massive external and internal particles are present in multi-leg processes.

¹Since the completion of this Dissertation, we have shown in Ref. [98] explicit results for NLO QCD corrections to Wb production both at the Tevatron and at the LHC.

APPENDIX A

Standard Model of Particle Physics

The Standard Model of particle physics is a quantum field theory based on the gauge groups SU_3 for color, SU_2 for weak isospin, and U_1 for hypercharge, as dictated by the local gauge symmetry invariance observed in the behavior of fundamental particles. The color quantum number is associated with the dynamics of the strong interactions, which by itself is the subject of Quantum Chromodynamics (QCD), while the weak isospin and hypercharge quantum numbers are fundamental to the dynamics of electroweak interactions.

The SM Lagrangian can be written as

$$\mathcal{L}_{SM} = \mathcal{L}_{YM} + \mathcal{L}_f + \mathcal{L}_H + \mathcal{L}_{\text{Yuk}} , \quad (\text{A.1})$$

where \mathcal{L}_{YM} is the Yang-Mills Lagrangian, \mathcal{L}_f the fermion Lagrangian, \mathcal{L}_H the Higgs Lagrangian and \mathcal{L}_{Yuk} contains the Yukawa interactions of the theory. \mathcal{L}_{YM} describes the dynamics of the gauge fields (kinetic terms + self-interactions) and includes the following terms

$$\begin{aligned} \mathcal{L}_{YM} &= \mathcal{L}_{QCD} + \mathcal{L}_{I_w} + \mathcal{L}_Y \\ &= -\frac{1}{4} \sum_{a=1}^8 G_{\mu\nu}^a G^{a\mu\nu} - \frac{1}{4} \sum_{i=1}^3 F_{\mu\nu}^i F^{i\mu\nu} - \frac{1}{4} B_{\mu\nu} B^{\mu\nu} . \end{aligned} \quad (\text{A.2})$$

The color field strength tensor is given by

$$G_{\mu\nu}^a = \partial_\mu A_\nu^a - \partial_\nu A_\mu^a + g_1 f^{abc} A_\mu^b A_\nu^c , \quad a, b, c = 1, \dots, 8 , \quad (\text{A.3})$$

with A_μ^b the eight color gauge fields (so called gluons), g_1 the dimensionless strong coupling constant and f^{abc} the structure constants of SU_3 . Analogously, the weak isospin, $F_{\mu\nu}^i$, and hypercharge, $B_{\mu\nu}$, field strength tensors are given by

$$F_{\mu\nu}^i = \partial_\mu W_\nu^i - \partial_\nu W_\mu^i + g_2 \epsilon^{ijk} W_\mu^j W_\nu^k , \quad i, j, k = 1, 2, 3 , \quad (\text{A.4})$$

$$B_{\mu\nu} = \partial_\mu B_\nu - \partial_\nu B_\mu , \quad (\text{A.5})$$

where W_μ^i and B_μ are the 4 electroweak gauge bosons (a linear combination of which will become the weak W_μ^\pm and Z_μ^0 weak gauge bosons plus the photon A_μ , as shown in Eq. (A.16)), g_2 is the dimensionless weak isospin coupling constant and ϵ^{ijk} are the structure constants of SU_2 .

Throughout the body of this dissertation we have denoted the strong coupling g_1 as g_s , and the weak isospin coupling g_2 as g_w . We also use the conventional definition $\alpha_s = g_s^2/(4\pi)$.

The second part of the SM Lagrangian in Eq. (A.1), \mathcal{L}_f , describes the fermion fields and their interactions with the gauge bosons. The fermion fields are classified as quarks, which are triplets under the color gauge group, and leptons, which have no color. Taking into account the fact that the W boson couples only to left-handed helicity states of quarks and leptons, this part of the Lagrangian is built such that right-handed and left-handed components of the fermion fields couple independently to the gauge bosons. Using the notation $(SU_2, SU_3)_Y$, to denote weak isospin, color, and hypercharge quantum number assignments of the fermion fields, we can write that a quark weak doublet, $\mathbf{Q}_L = \begin{pmatrix} u \\ d \end{pmatrix}_L$, is a $(\mathbf{2}, \mathbf{3})_{y_1}$ and a quark weak singlet, \mathbf{u}_R , is a $(\mathbf{1}, \mathbf{3})_{y_2}$ (and similar for \mathbf{d}_R). On the other side, a weak doublet of leptons, $L_L = \begin{pmatrix} \nu \\ e \end{pmatrix}_L$, is a $(\mathbf{2}, \mathbf{1})_{y_4}$ and a lepton weak singlet, e_R , is a $(\mathbf{1}, \mathbf{1})_{y_5}$. The fermion Lagrangian \mathcal{L}_f then can be written as

$$\begin{aligned} \mathcal{L}_f = & \bar{\mathbf{Q}}_L \sigma^\mu \mathcal{D}_\mu \mathbf{Q}_L + \bar{\mathbf{u}}_R \sigma^\mu \mathcal{D}_\mu \mathbf{u}_R + \bar{\mathbf{d}}_R \sigma^\mu \mathcal{D}_\mu \mathbf{d}_R \\ & + \bar{L}_L \sigma^\mu \mathcal{D}_\mu L_L + \bar{e}_R \sigma^\mu \mathcal{D}_\mu e_R + \dots , \end{aligned} \quad (\text{A.6})$$

where the dots stand for similar terms for the remaining quarks and leptons. In Eq. (A.6) σ^μ are the Pauli matrices ($\sigma^0 = \mathbf{1}$), and \mathcal{D}_μ are the covariant derivatives corresponding to each field,

$$\begin{aligned} \mathcal{D}_\mu \mathbf{Q}_L &= (\partial_\mu + g_1 \frac{i}{2} A_\mu^a \lambda^a + g_2 \frac{i}{2} W_\mu^i \tau^i + g_3 \frac{i}{2} y_1 B_\mu) \mathbf{Q}_L , \\ \mathcal{D}_\mu \mathbf{u}_R &= (\partial_\mu + g_1 \frac{i}{2} A_\mu^a \lambda^a + g_3 \frac{i}{2} y_2 B_\mu) \mathbf{u}_R , \\ \mathcal{D}_\mu \mathbf{d}_R &= (\partial_\mu + g_1 \frac{i}{2} A_\mu^a \lambda^a + g_3 \frac{i}{2} y_3 B_\mu) \mathbf{d}_R , \\ \mathcal{D}_\mu L_L &= (\partial_\mu + g_2 \frac{i}{2} W_\mu^i \tau^i + g_3 \frac{i}{2} y_4 B_\mu) L_L , \\ \mathcal{D}_\mu e_R &= (\partial_\mu + g_3 \frac{i}{2} y_5 B_\mu) e_R , \end{aligned} \quad (\text{A.7})$$

where g_3 is the dimensionless hypercharge coupling constant, and τ^i and λ^a are the Pauli and Gell-Mann matrices for SU_2 and SU_3 respectively.

Notice that a mass term for the fermion fields and for the vector boson fields (as needed for the weak vector bosons W_μ^\pm and Z_μ^0) is not allowed by gauge invariance. The last two terms in the Standard Model Lagrangian shown in Eq. (A.1) are introduced to remedy this problem. Indeed, the simplest way to preserve the gauge symmetry of the SM while generating massive electroweak gauge bosons is the so called Higgs mechanism, which we explain in the following. A separate step needs to be taken to introduce massive fermions, and we will discuss this below.

The Higgs mechanism, in its simplest version [99, 100, 101, 102], starts by adding to the model another field, called the Higgs field H , which transforms as a weak isospin doublet, a color singlet, and it has hypercharge y_h :

$$H = \begin{pmatrix} H_1 \\ H_2 \end{pmatrix} \sim (\mathbf{2}, \mathbf{1})_{y_h} . \quad (\text{A.8})$$

Its dynamics is dictated by the \mathcal{L}_H term in Eq. (A.1), which can be written as

$$\mathcal{L}_H = (\mathcal{D}_\mu H)^\dagger (\mathcal{D}^\mu H) - V(H) , \quad (\text{A.9})$$

where $\mathcal{D}_\mu H = (\partial_\mu + g_2 \frac{i}{2} W_\mu^i \tau^i + g_3 \frac{i}{2} y_h B_\mu) H$ is the covariant derivative of H and $V(H)$ is the most general renormalizable potential invariant under $SU_2 \times U_1$,

$$V(H) = \mu^2 H^\dagger H + \lambda (H^\dagger H)^2 , \quad (\text{A.10})$$

with μ^2 and λ real parameters. λ is a dimensionless parameter.

If $\mu^2 < 0$ the field configurations that minimize the potential $V(H)$ has to satisfy:

$$H_{vac}^\dagger H_{vac} = \frac{-\mu^2}{2\lambda} \equiv \frac{v^2}{2} . \quad (\text{A.11})$$

So, once $\mu^2 < 0$ the Higgs field develops a vacuum expectation value (VEV), which is degenerate over the sphere defined in the last equation. Picking one configuration breaks this degeneracy, causing the vacuum of the theory not to be $SU_2 \times U_1$ symmetric anymore. To illustrate the consequences, let us choose:

$$\langle H \rangle = \frac{v}{\sqrt{2}} \begin{pmatrix} 0 \\ 1 \end{pmatrix} . \quad (\text{A.12})$$

Indeed one can verify that this choice breaks the original gauge symmetry:

$$SU_2 \times U_1 \rightarrow U_1^{EM} , \quad (\text{A.13})$$

where U_1^{EM} is the electromagnetic U_1 symmetry.

When \mathcal{L}_H is expanded in the vicinity of the chosen minimum, by shifting the Higgs field as follows

$$H = \frac{1}{\sqrt{2}} \begin{pmatrix} 0 \\ v + h \end{pmatrix} , \quad (\text{A.14})$$

\mathcal{L}_H becomes the Lagrangian of a real scalar field with mass $m_h = 2v^2\lambda$, the physical Higgs boson. Moreover, a mass term for the gauge bosons is generated by the first term in Eq. (A.9), coming from

$$\frac{1}{2}(0, v) \left| \frac{1}{2}g_2 W_\mu^i \tau^i + \frac{1}{2}g_3 B_\mu \right|^2 \begin{pmatrix} 0 \\ v \end{pmatrix} . \quad (\text{A.15})$$

The corresponding mass eigenstates, i.e. the physical gauge fields, are obtained by diagonalizing the mass matrix of the vector fields W_μ^a and B_μ . The EW gauge bosons W_μ^\pm and Z_μ^0 , as well as the photon A_μ , are expressed as:

$$\begin{aligned} W_\mu^\pm &= \frac{1}{\sqrt{2}}(W_\mu^1 \mp iW_\mu^2) , \\ Z_\mu &= \frac{-g_3 B_\mu + g_2 W_\mu^3}{\sqrt{g_2^2 + g_3^2}} , \\ A_\mu &= \frac{g_2 B_\mu + g_3 W_\mu^3}{\sqrt{g_2^2 + g_3^2}} , \end{aligned} \quad (\text{A.16})$$

with the associated masses:

$$\begin{aligned} M_W^2 &= \frac{1}{4}g_2^2 v^2 , \\ M_Z^2 &= \frac{1}{4}(g_2^2 + g_3^2)v^2 , \\ M_A^2 &= 0 . \end{aligned} \quad (\text{A.17})$$

These simple relations are found to agree with experiment ($M_W = 80.4$ GeV, $M_Z = 91.2$ GeV) with $v \approx 174\sqrt{2}$ GeV. This is, of course, approximate as they are results based on the classical, or leading order level of the theory.

Finally let us focus on the last part of the SM Lagrangian presented in Eq. (A.1). This term, \mathcal{L}_{Yuk} , couples massive fermion fields to the Higgs field via Yukawa type interaction.

For example, the gauge invariant Yukawa coupling of the Higgs boson to the down quark, \mathbf{d} , is

$$-\lambda_d \overline{\mathbf{Q}}_L H \mathbf{d}_R + h.c. ,$$

where $\overline{\mathbf{Q}}_L = (\overline{\mathbf{u}}, \overline{\mathbf{d}})_L$ and λ_d is the Yukawa coupling for the down quark. After the shift of Eq. (A.14) this term gives the effective coupling

$$-\lambda_d \frac{1}{\sqrt{2}} \overline{\mathbf{Q}}_L \begin{pmatrix} 0 \\ v+h \end{pmatrix} \mathbf{d}_R + h.c. , \quad (\text{A.18})$$

which gives a mass term to the down quark with

$$m_d = \frac{\lambda_d v}{\sqrt{2}} , \quad (\text{A.19})$$

and defines the coupling between the down quark and the physical Higgs particle to be $-\lambda_d/\sqrt{2}$.

Similar terms are added for each massive fermion field. Then \mathcal{L}_{Yuk} will contain 9 arbitrary parameters, the Yukawa couplings, standing for 6 quark masses and 3 lepton masses. This completes the classical SM Lagrangian, which is the main theory used throughout this dissertation. Several extensions of the SM follow the same prescription and ultimately break the EW symmetry spontaneously by introducing several Higgs fields. On the other hand, alternative mechanisms to break the EW symmetry have also been proposed like ‘‘Technicolor’’, where scalars are seen as strongly bound states of fermions, ‘‘Little Higgs’’ models, where more complex global symmetries of the fundamental fields are considered to justify the existence of a relatively light Higgs, or more speculative theories that explain the breaking of the EW gauge symmetry in terms of extra dimensions. However, most alternatives to the Higgs mechanism encounter phenomenological difficulties and till now the most successful theory in describing experimental data is still the SM with a weakly coupled Higgs boson.

Feynman Rules

From the Lagrangian one can readily extract the Feynman rules of the theory. Now we present the set of rules we have employed throughout our calculation.

Let us start by writing the propagators for quarks and gluons, this last one in the Feynman gauge:

$$\begin{array}{c} a \\ \mu \end{array} \text{---}\text{ooooo}\text{---}\begin{array}{c} b \\ \nu \end{array} \\ p \rightarrow$$
$$= \frac{-ig_{\mu\nu}}{p^2 + i\epsilon} \delta^{ab}, \quad (\text{A.20})$$

$$i \xrightarrow[p]{\quad} j = \frac{i(\not{p} + m)}{p^2 - m^2 + i\epsilon} \delta_{ij} . \quad (\text{A.21})$$

For the coupling between quarks and gluons and gluon self-interactions we have the vertices:

$$\begin{array}{c} \text{\tiny a,μ} \\ | \\ \text{\scriptsize \circ} \\ | \\ \text{\scriptsize \circ} \\ | \\ \text{\scriptsize \circ} \\ | \\ \text{\scriptsize \circ} \\ | \\ \text{\scriptsize \circ} \\ | \\ \bullet \\ / \quad \backslash \\ i \qquad j \end{array} = ig_1 \gamma^\mu t_{ij}^a , \tag{A.22}$$

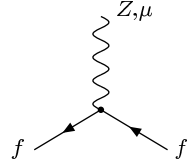
$$\begin{aligned}
& \text{Diagram: A vertex with three external lines. The top line is labeled } a, \mu \text{ and has a downward arrow } k. \text{ The bottom-left line is labeled } b, \nu \text{ and has an upward arrow } p. \text{ The bottom-right line is labeled } c, \rho \text{ and has an upward arrow } q. \\
& = g_1 f^{abc} [g^{\mu\nu}(k-p)^\rho + g^{\nu\rho}(p-q)^\mu + g^{\mu\rho}(q-k)^\nu] \ ,
\end{aligned}
\tag{A.23}$$

$$\begin{aligned}
& \begin{array}{c} a, \mu \\ \diagup \\ \text{---} \\ \diagdown \\ c, \rho \end{array} \quad \begin{array}{c} b, \nu \\ \diagdown \\ \text{---} \\ \diagup \\ d, \sigma \end{array} \\
&= -ig_1^2 [f^{abc} f^{cde} (g^{\mu\rho} g^{\nu\sigma} - g^{\mu\sigma} g^{\nu\rho}) \\
&\quad + f^{ace} f^{bde} (g^{\mu\nu} g^{\rho\sigma} - g^{\mu\sigma} g^{\nu\rho}) \\
&\quad + f^{ade} f^{bce} (g^{\mu\nu} g^{\rho\sigma} - g^{\mu\rho} g^{\nu\sigma})] \ , \tag{A.24}
\end{aligned}$$

where $2t_{ij}^a$ are the Gell-Mann matrices and f^{abc} the structure constants of $SU(3)$.

The weak boson couplings to fermions are given by the vertices (stripped of color indices):

$$\begin{array}{c}
W, \mu \\
\uparrow \\
f \quad \bullet \quad f'
\end{array}
= \frac{-ig_2}{2\sqrt{2}} \gamma^\mu (1 - \gamma_5) V_{ff'} , \quad (\text{A.25})$$



A Feynman diagram showing a vertex where a fermion line (labeled f) enters from the bottom left and a fermion line (labeled f) exits to the bottom right. A wavy line representing a Z boson, labeled Z, μ , exits from the top of the vertex.

$$= \frac{-ig_2}{\cos \theta_w} \gamma^\mu (g_V^f + g_A^f \gamma_5) , \quad (\text{A.26})$$

where $V_{ff'}$ are the entries of the CKM mixing matrix, and the vector, g_V^f , and axial, g_A^f , couplings for the Zff vertex are given by:

$$\begin{aligned} g_V^f &= \frac{1}{2} T_3^f - \sin^2 \theta_w Q_f , \\ g_A^f &= -\frac{1}{2} T_3^f , \end{aligned} \quad (\text{A.27})$$

where $\sin \theta_w = g_3 / \sqrt{g_2^2 + g_3^2}$, T_3^f is the third component of the weak isospin matrix for the fermion f , and Q_f is the charge of the fermion.

APPENDIX B

Tree Level Amplitudes for $W/Z \ b\bar{b}$ Production

In this Appendix we present explicit expressions for the tree level amplitudes that appear in the full calculation of $W/Z \ b\bar{b}$ production. This is a straightforward application of the Feynman rules shown in the last section of Appendix A. As we mentioned there, we denote the strong coupling g_1 as g_s , and the weak isospin coupling g_2 as g_w .

Tree level amplitude for $q\bar{q}' \rightarrow Wb\bar{b}$

The contributing tree level Feynman diagrams are shown in Figure 2.2.

Given the momenta assignment:

$$q(q_1)\bar{q}'(q_2) \rightarrow b(p_b) + \bar{b}(p_{\bar{b}}) + W(p_w) \ ,$$

the LO amplitude can be written as:

$$\begin{aligned} \mathcal{A}_0(q\bar{q}' \rightarrow Wb\bar{b}) = & \ i g_s^2 \frac{g_w}{2\sqrt{2}} V_{q\bar{q}'} \epsilon_\mu^*(p_w) \frac{g_{\nu\rho}}{(p_b + p_{\bar{b}})^2} \bar{u}_b \gamma^\rho v_{\bar{b}} t_{ij}^a t_{kl}^a \\ & \left[\bar{v}_{\bar{q}'} \gamma^\mu (1 - \gamma_5) \frac{-\not{q}_2 + \not{p}_w}{(-q_2 + p_w)^2} \gamma^\nu u_q \right. \\ & \left. + \bar{v}_{\bar{q}'} \gamma^\nu \frac{\not{q}_1 - \not{p}_w}{(q_1 - p_w)^2} \gamma^\mu (1 - \gamma_5) u_q \right] \ , \end{aligned} \quad (\text{B.1})$$

where $V_{q\bar{q}'}$ is the CKM mixing matrix, $\epsilon_\mu(p_w)$ is the polarization vector of the W boson and we denote by v and u the spinors for the external fermionic fields (for more details look at the Feynman rules in Appendix A).

Tree level amplitude for $q\bar{q} \rightarrow Zb\bar{b}$

The contributing tree level Feynman diagrams are shown in Figures 2.2 (with $V = Z$) and 2.10 for subprocess $q\bar{q} \rightarrow Zb\bar{b}$ with the Z weak boson emitted from initial and final fermion lines respectively.

Given the momenta assignment:

$$q(q_1)\bar{q}(q_2) \rightarrow b(p_b) + \bar{b}(p_{\bar{b}}) + Z(p_z) \ ,$$

the LO amplitude can be written as:

$$\begin{aligned} \mathcal{A}_0(q\bar{q} \rightarrow Zb\bar{b}) = & ig_s^2 \frac{g_W}{\cos \theta_W} \epsilon_\mu^*(p_z) \frac{g_{\nu\rho}}{(p_b + p_{\bar{b}})^2} \bar{u}_b \gamma^\rho v_{\bar{b}} t_{ij}^a t_{kl}^a \\ & \left[\bar{v}_{\bar{q}} \gamma^\mu (g_V^q + g_A^q \gamma_5) \frac{-\not{q}_2 + \not{p}_z}{(-q_2 + p_z)^2} \gamma^\nu u_q \right. \\ & \left. + \bar{v}_{\bar{q}} \gamma^\nu \frac{\not{q}_1 - \not{p}_z}{(q_1 - p_z)^2} \gamma^\mu (g_V^q + g_A^q \gamma_5) u_q \right] \\ & + ig_s^2 \frac{g_W}{\cos \theta_W} \epsilon_\mu^*(p_z) \frac{g_{\nu\rho}}{(q_1 + q_2)^2} \bar{v}_{\bar{q}} \gamma^\rho u_q t_{ij}^a t_{kl}^a \\ & \left[\bar{u}_b \gamma^\mu (g_V^b + g_A^b \gamma_5) \frac{\not{p}_b + \not{p}_z + m_b}{[(p_b + p_z)^2 - m_b^2]} \gamma^\nu v_{\bar{b}} \right. \\ & \left. + \bar{u}_b \gamma^\nu \frac{-\not{p}_{\bar{b}} - \not{p}_z + m_b}{[(-p_{\bar{b}} - p_z)^2 - m_b^2]} \gamma^\mu (g_V^b + g_A^b \gamma_5) v_{\bar{b}} \right] . \end{aligned} \quad (\text{B.2})$$

where g_V^f and g_A^f are the vector and axial coupling constants for fermion f , $\epsilon_\mu(p_z)$ is the polarization vector of the Z boson and we denote by v and u the spinors for the external fermionic fields (for more details look at the Feynman rules in Appendix A).

Tree level amplitude for $gg \rightarrow Zb\bar{b}$

The amplitudes $\mathcal{A}_{0,s}$, $\mathcal{A}_{0,t}$, and $\mathcal{A}_{0,u}$ introduced in Section 2.4.1 can be written as:

$$\begin{aligned} \mathcal{A}_{0,s} &= ig_s^2 \frac{g_W}{\cos \theta_W} \epsilon_\mu(q_1) \epsilon_\nu(q_2) \epsilon_\rho^*(p_z) \bar{u}_b \mathcal{A}_{0,s}^{\mu\nu\rho} v_{\bar{b}} \ , \\ \mathcal{A}_{0,t} &= ig_s^2 \frac{g_W}{\cos \theta_W} \epsilon_\mu(q_1) \epsilon_\nu(q_2) \epsilon_\rho^*(p_z) \bar{u}_b \mathcal{A}_{0,t}^{\mu\nu\rho} v_{\bar{b}} \ , \\ \mathcal{A}_{0,u} &= ig_s^2 \frac{g_W}{\cos \theta_W} \epsilon_\mu(q_1) \epsilon_\nu(q_2) \epsilon_\rho^*(p_z) \bar{u}_b \mathcal{A}_{0,u}^{\mu\nu\rho} v_{\bar{b}} \ , \end{aligned} \quad (\text{B.3})$$

where $\epsilon_\mu(p_z)$ is the polarization vector of the Z boson, v and u are the spinors for the external fermionic fields, and $\mathcal{A}_{0,s}^{\mu\nu\rho}$, $\mathcal{A}_{0,t}^{\mu\nu\rho}$, and $\mathcal{A}_{0,u}^{\mu\nu\rho}$ represent the total s -channel, t -channel, and u -channel amplitudes, corresponding to the diagrams in Figure 2.11. More explicitly:

$$\begin{aligned} \mathcal{A}_{0,s}^{\mu\nu\rho} &= \mathcal{A}_{0,s}^{(1)\mu\nu\rho} + \mathcal{A}_{0,s}^{(2)\mu\nu\rho} \ , \\ \mathcal{A}_{0,t}^{\mu\nu\rho} &= \mathcal{A}_{0,t}^{(1)\mu\nu\rho} + \mathcal{A}_{0,t}^{(2)\mu\nu\rho} + \mathcal{A}_{0,t}^{(3)\mu\nu\rho} \ , \\ \mathcal{A}_{0,u}^{\mu\nu\rho} &= \mathcal{A}_{0,u}^{(1)\mu\nu\rho} + \mathcal{A}_{0,u}^{(2)\mu\nu\rho} + \mathcal{A}_{0,u}^{(3)\mu\nu\rho} \ , \end{aligned} \quad (\text{B.4})$$

where

$$\begin{aligned}
\mathcal{A}_{0,s}^{(1),\mu\nu\rho} &= \frac{1}{s} \gamma^\rho (g_V^b + g_A^b \gamma_5) \frac{\not{p}_b + \not{p}_z + m_b}{[(p_b + p_z)^2 - m_b^2]} \gamma_\alpha V^{\mu\nu\alpha} , \\
\mathcal{A}_{0,s}^{(2),\mu\nu\rho} &= \frac{1}{s} \gamma_\alpha \frac{-\not{p}_{\bar{b}} - \not{p}_z + m_b}{[(p_{\bar{b}} + p_z)^2 - m_b^2]} \gamma^\rho (g_V^b + g_A^b \gamma_5) V^{\mu\nu\alpha} , \\
\mathcal{A}_{0,t}^{(1),\mu\nu\rho} &= \gamma^\rho (g_V^b + g_A^b \gamma_5) \frac{\not{p}_b + \not{p}_z + m_b}{[(p_b + p_z)^2 - m_b^2]} \gamma^\mu \frac{\not{q}_2 - \not{p}_{\bar{b}} + m_b}{[(q_2 - p_{\bar{b}})^2 - m_b^2]} \gamma^\nu , \\
\mathcal{A}_{0,t}^{(2),\mu\nu\rho} &= \gamma^\mu \frac{\not{p}_b - \not{q}_1 + m_b}{[(p_b - q_1)^2 - m_b^2]} \gamma^\rho (g_V^b + g_A^b \gamma_5) \frac{\not{q}_2 - \not{p}_{\bar{b}} + m_b}{[(q_2 - p_{\bar{b}})^2 - m_b^2]} \gamma^\nu , \\
\mathcal{A}_{0,t}^{(3),\mu\nu\rho} &= \gamma^\mu \frac{\not{p}_b - \not{q}_1 + m_b}{[(p_b - q_1)^2 - m_b^2]} \gamma^\nu \frac{-\not{p}_{\bar{b}} - \not{p}_z + m_b}{[(p_{\bar{b}} + p_z)^2 - m_b^2]} \gamma^\rho (g_V^b + g_A^b \gamma_5) , \\
\mathcal{A}_{0,u}^{(1),\mu\nu\rho} &= \mathcal{A}_{0,t}^{(1),\mu\nu\rho} (\mu \leftrightarrow \nu, q_1 \leftrightarrow q_2) , \\
\mathcal{A}_{0,u}^{(2),\mu\nu\rho} &= \mathcal{A}_{0,t}^{(2),\mu\nu\rho} (\mu \leftrightarrow \nu, q_1 \leftrightarrow q_2) , \\
\mathcal{A}_{0,u}^{(3),\mu\nu\rho} &= \mathcal{A}_{0,t}^{(3),\mu\nu\rho} (\mu \leftrightarrow \nu, q_1 \leftrightarrow q_2) ,
\end{aligned} \tag{B.5}$$

with

$$V^{\mu\nu\alpha} = (q_1 - q_2)^\alpha g^{\mu\nu} + (q_1 + 2q_2)^\mu g^{\nu\alpha} - (2q_1 + q_2)^\nu g^{\mu\alpha} ,$$

are the individual amplitudes for the s -channel, t -channel, and u -channel diagrams in Figure 2.11.

APPENDIX C

Scalar Integrals for $W/Z \, b\bar{b}$ Production

In this Appendix we present a collection of all the one-loop IR-divergent scalar integrals that appear in the $W/Z \, b\bar{b}$ NLO QCD calculation. For completeness we will also include the UV-structure of the UV-divergent scalar integrals, namely tadpoles and self-energies. We will use the following notation for the scalar m -point integral:

$$I0(q_1, \dots, q_{m-1}; m_0, \dots, m_{m-1}) = \mu^{4-d} \int \frac{d^d t}{(2\pi)^d} \frac{1}{[t^2 - m_0^2][(t + q_1)^2 - m_1^2] \cdots [(t + q_1 + \cdots + q_{m-1})^2 - m_{m-1}^2]} , \quad (\text{C.1})$$

which corresponds to the topology illustrated in Figure C.1. We have denoted by t the loop momentum, by $\{q_i\}$ ($i = 1, \dots, m$, $q_m = -\sum_{j=1}^{m-1} q_j$) the set of incoming momenta to the diagram and by $\{m_i\}$ ($i = 0, \dots, m-1$) the set of masses corresponding to the propagators in the loop. The integration over the loop momentum is performed over $d = 4 - 2\epsilon$ ($\epsilon = \epsilon_{\text{IR}}$

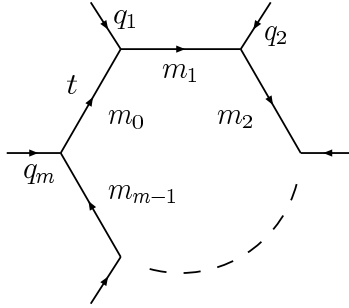


Figure C.1: Topology of one-loop Feynman integrals. We denote by t the loop momentum, by $\{q_i\}$ the set of incoming momenta and by $\{m_i\}$ the set of masses in the internal propagators.

unless stated differently) dimensions. We will denote integrals $I0$ with $m = 1, 2, 3, 4$ and 5 denominators by $A0, B0, C0, D0$ and $E0$ respectively, as conventional.

Most of the expressions presented in this Appendix exist in the literature (see for example [103, 76, 77, 104, 80]), except for the box integrals labelled in the following as II.2 and II.3, which as far as we know have not been presented explicitly¹. We have calculated these integrals using two independent techniques and found agreement. For IR-finite integrals we have used expressions from [103] and cross checked them with the FF-package [57].

The expressions presented below are correct up to $\mathcal{O}(\epsilon)$, since this is what is needed for a full NLO calculation. We include only the real pieces² of the integrals (according to the kinematics we use) as the imaginary parts do not contribute to the NLO partonic cross section. We will use the kinematics of the process:

$$i(q_1) + j(q_2) \rightarrow V(p_V) + b(p_b) + \bar{b}(p_{\bar{b}}) ,$$

with $p_V = q_1 + q_2 - p_b - p_{\bar{b}}$ and the on-shell conditions $q_1^2 = q_2^2 = 0$ and $p_b^2 = p_{\bar{b}}^2 = m_b^2$. Although in this dissertation we treat the V vector boson as on-shell (i.e. $p_V^2 = M_V^2$), the integrals in this Appendix are correct also for the case of an off-shell V boson, as we always eliminate p_V by using conservation of momentum. Therefore they can be used also if one had to include leptonic decays of the V boson. Moreover, all the following results are expressed in terms of the invariants $s_{ij} = (q_i + q_j)^2$, where q_i and q_j are two of the external momenta.

Scalar integrals can be related by rotation or reflection of the integration momentum:

$$\begin{aligned} I0(q_1, \dots, q_{m-1}; m_0, \dots, m_{m-1}) &= I0\left(-\sum_{i=1}^{m-1} q_i, q_1, \dots, q_{m-2}; m_{m-1}, m_0, \dots, m_{m-2}\right) \\ &= I0(q_{m-1}, \dots, q_1, m_{m-1}, \dots, m_0) . \end{aligned} \quad (\text{C.2})$$

In the following we therefore give the minimal set of scalar integrals appearing in our calculation.

Finally we will always factor out of the integrals the factor:

$$\mathcal{N}_b = \left(\frac{4\pi\mu^2}{m_b^2}\right)^\epsilon \Gamma(1 + \epsilon) . \quad (\text{C.3})$$

¹Since the completion of this Dissertation a full set of IR-divergent scalar integrals have been presented in Ref. [105], and we found agreement with the corresponding box expressions presented there.

²By real pieces we mean the real pieces of the integrals after factorizing $i/(16\pi^2)$.

A0 integral

$A0$ and $B0$ integrals are the only scalar UV-divergent integrals. The 1-point integral is IR-finite, and it is given by:

$$A0(m_b) = \frac{i}{16\pi^2} \mathcal{N}_b \, m_b^2 \left(\frac{1}{\epsilon_{\text{UV}}} + 1 \right) . \quad (\text{C.4})$$

We notice that $A0(m \rightarrow 0) = 0$, as it can be inferred from the fact that such dimensionful integral cannot be built from any kinematic invariant. We mention that the only other 1-point integral appearing in our calculation is $A0(m_t)$, which can be obtained from the previous expression replacing m_b and \mathcal{N}_b by m_t and \mathcal{N}_t respectively.

B0 integrals

All $B0$ integrals are UV-divergent and their corresponding UV-pole part is:

$$B0(p; m_0, m_1) \Big|_{\text{UV-pole}} = \frac{i}{16\pi^2} \mathcal{N}_b \, \frac{1}{\epsilon_{\text{UV}}} . \quad (\text{C.5})$$

The only IR-divergent $B0$ integral is the one with zero internal masses and with a light-like ($q_1^2 = 0$) external momentum $B0(q_1; 0, 0)$. Indeed, there is no invariant available to build this integral, so it should vanish. One can understand this vanishing as a cancellation between the UV and IR behavior of this integral of the form:

$$B0(q_1; 0, 0) = \frac{i}{16\pi^2} \mathcal{N}_b \left(\frac{1}{\epsilon_{\text{UV}}} - \frac{1}{\epsilon_{\text{IR}}} \right) , \quad (\text{C.6})$$

where we have made explicitly the UV or IR nature of the two single poles. Notice that the overall constant in front of the integral is a matter of convention.

IR-divergent C0 integrals

Let us organize the integrals by the number of internal masses.

I. All internal masses equal to zero

1. $C0(q_1, q_2; 0, 0, 0)$, two on-shell massless legs:

$$C0(q_1, q_2; 0, 0, 0) = \frac{i}{16\pi^2} \mathcal{N}_b \, \frac{1}{s_{12}} \left(\frac{1}{\epsilon^2} + \frac{1}{\epsilon} \ln \frac{m_b^2}{s_{12}} + \frac{1}{2} \ln^2 \frac{m_b^2}{s_{12}} - \frac{\pi^2}{6} \right) . \quad (\text{C.7})$$

2. $C0(q_1, -p_b - p_{\bar{b}}; 0, 0, 0)$, one on-shell massless leg:

$$C0(q_1, -p_b - p_{\bar{b}}; 0, 0, 0) = \frac{i}{16\pi^2} \mathcal{N}_b \frac{1}{2 q_1 \cdot (-p_b - p_{\bar{b}})} \left(\frac{1}{\epsilon} \left[\ln \frac{m_b^2}{|s_{12}|} - \ln \frac{m_b^2}{(-p_b - p_{\bar{b}})^2} \right] + \frac{1}{2} \left[\ln^2 \frac{m_b^2}{|s_{12}|} - \pi^2 - \ln^2 \frac{m_b^2}{(-p_b - p_{\bar{b}})^2} \right] \right), \quad (C.8)$$

notice that for this case, in our kinematics, $s_{12} < 0$ so we have included absolute values in the logarithm arguments to avoid negative arguments.

II. One non-zero internal mass

1. $C0(q_1, -p_b; 0, 0, m_b)$, One on-shell massless leg and one on-shell massive leg:

$$C0(q_1, -p_b; 0, 0, m_b) = \frac{i}{16\pi^2} \mathcal{N}_b \frac{1}{s_{12} - m_b^2} \left\{ \frac{1}{2\epsilon^2} + \frac{1}{\epsilon} \ln \left| \frac{m_b^2}{s_{12} - m_b^2} \right| + \frac{1}{2} \ln^2 \left(1 - \frac{s_{12}}{m_b^2} \right) + \text{Li}_2 \left(\frac{1}{1 - \frac{s_{12}}{m_b^2}} \right) + \ln \left(1 - \frac{m_b^2}{s_{12}} \right) \ln \left(1 - \frac{s_{12}}{m_b^2} \right) - \frac{\pi^2}{6} \right\}. \quad (C.9)$$

2. $C0(q_1, q_2 - p_b; 0, 0, m_b)$, One on-shell massless leg:

$$C0(q_1, q_2 - p_b; 0, 0, m_b) = \frac{i}{16\pi^2} \mathcal{N}_b \frac{1}{s_{12} - (q_2 - p_b)^2} \left\{ \frac{1}{\epsilon} \left(\ln \frac{m_b^2}{s_{12} - m_b^2} - \ln \frac{m_b^2}{|(q_2 - p_b)^2 - m_b^2|} \right) + \ln^2 \frac{m_b^2}{s_{12} - m_b^2} - \ln^2 \frac{m_b^2}{|(q_2 - p_b)^2 - m_b^2|} - \ln \left(\frac{m_b^2}{|(q_2 - p_b)^2 - m_b^2|} \right) \ln \left(1 - \frac{(q_2 - p_b)^2 - m_b^2}{m_b^2} \right) + \text{Li}_2 \left(1 + \frac{s_{12} - m_b^2}{m_b^2} \right) + \text{Li}_2 \left(\frac{m_b^2 - (q_2 - p_b)^2}{m_b^2} \right) - \frac{7}{6} \pi^2 \right\}. \quad (C.10)$$

III. Two non-zero internal masses

1. $C0(-p_b, p_b + p_{\bar{b}}; 0, m_b, m_b)$, Two on-shell massive legs:

$$C0(-p_b, p_b + p_{\bar{b}}; 0, m_b, m_b) = \frac{i}{16\pi^2} \mathcal{N}_b \frac{1}{\beta(p_b + p_{\bar{b}})^2} \left\{ \frac{1}{\epsilon} \ln \left(\frac{1 - \beta}{1 + \beta} \right) - \ln \left(\frac{(p_b + p_{\bar{b}})^2}{m_b^2} \right) \ln \left(\frac{1 - \beta}{1 + \beta} \right) - \frac{1}{2} I_2 - \pi^2 \right\}, \quad (C.11)$$

where we have defined:

$$\beta = \sqrt{1 - \frac{4 m_b^2}{(p_b + p_{\bar{b}})^2}},$$

and

$$\begin{aligned} I_2 = & -\ln^2 \left(\frac{1}{2}(1 + \beta) \right) + \ln^2 \left(\frac{1}{2}(1 - \beta) \right) - \pi^2 + 2 \ln \beta \ln \left(\frac{1 - \beta}{1 + \beta} \right) \\ & - 2 \text{Li}_2 \left(-\frac{1 - \beta}{2\beta} \right) + 2 \text{Li}_2 \left(\frac{1 + \beta}{2\beta} \right). \end{aligned}$$

IR-divergent $D0$ integrals

I. All internal masses equal to zero

We write the massless box expressions following the results of [77].

1. $D0(q_1, q_2, -p_b - p_{\bar{b}}; 0, 0, 0, 0)$, two adjacent on-shell massless legs:

$$\begin{aligned} D0(q_1, q_2, -p_b - p_{\bar{b}}; 0, 0, 0, 0) = & \frac{i}{16\pi^2} \mathcal{N}_b \frac{1}{s_{12}s_{23}} \left\{ \right. \\ & \frac{2}{\epsilon^2} \left[\left(\frac{m_b^2}{-s_{12}} \right)^\epsilon + \left(\frac{m_b^2}{-s_{23}} \right)^\epsilon - \left(\frac{m_b^2}{-(p_b + p_{\bar{b}})^2} \right)^\epsilon - \left(\frac{m_b^2}{-(-q_1 - q_2 + p_b + p_{\bar{b}})^2} \right)^\epsilon \right] \\ & + \frac{1}{\epsilon^2} \left[\left(-\frac{m_b^2 s_{12}}{(p_b + p_{\bar{b}})^2 (-q_1 - q_2 + p_b + p_{\bar{b}})^2} \right)^\epsilon \right] \\ & - 2 \text{Li}_2 \left(1 - \frac{(-q_1 - q_2 + p_b + p_{\bar{b}})^2}{s_{23}} \right) - 2 \text{Li}_2 \left(1 - \frac{(-q_1 - q_2 + p_b + p_{\bar{b}})^2}{s_{12}} \right) - \ln^2 \left(\frac{-s_{12}}{-s_{23}} \right) \\ & \left. - \frac{\pi^2}{6} \right\}. \end{aligned} \tag{C.12}$$

2. $D0(q_1, -p_b - p_{\bar{b}}, q_2; 0, 0, 0, 0)$, two opposite on-shell massless legs:

$$\begin{aligned} D0(q_1, -p_b - p_{\bar{b}}, q_2; 0, 0, 0, 0) = & \frac{i}{16\pi^2} \mathcal{N}_b \frac{1}{s_{12}s_{23} - M_2^2 M_4^2} \left\{ \right. \\ & \frac{2}{\epsilon^2} \left[\left(\frac{m_b^2}{-s_{12}} \right)^\epsilon + \left(\frac{m_b^2}{-s_{23}} \right)^\epsilon - \left(\frac{m_b^2}{-M_2^2} \right)^\epsilon - \left(\frac{m_b^2}{-M_4^2} \right)^\epsilon \right] \\ & - 2 \text{Li}_2 \left(1 - \frac{M_2^2}{s_{12}} \right) - 2 \text{Li}_2 \left(1 - \frac{M_2^2}{s_{23}} \right) - 2 \text{Li}_2 \left(1 - \frac{M_4^2}{s_{12}} \right) - 2 \text{Li}_2 \left(1 - \frac{M_4^2}{s_{23}} \right) \\ & + 2 \text{Li}_2 \left(1 - \frac{M_2^2 M_4^2}{s_{12}s_{23}} \right) - \ln^2 \left(\frac{-s_{12}}{-s_{23}} \right) \left. \right\}, \end{aligned} \tag{C.13}$$

with $M_2^2 = (p_b + p_{\bar{b}})^2$ and $M_4^2 = (q_1 + q_2 - p_b - p_{\bar{b}})^2$.

II. One non-zero internal mass

1. $D0(q_1, q_2, -p_{\bar{b}}; 0, 0, 0, m_b)$, two adjacent on-shell massless legs and one one-shell massive leg:

$$D0(q_1, q_2, -p_{\bar{b}}; 0, 0, 0, m_b) = \frac{i}{16\pi^2} \mathcal{N}_b \frac{1}{s_{12}(s_{23} - m_b^2)} \left\{ \begin{aligned} & \frac{3}{2\epsilon^2} + \frac{1}{\epsilon} \left[2 \ln \frac{m_b^2}{m_b^2 - s_{23}} + \ln \frac{m_b^2}{s_{12}} - \ln \frac{m_b^2}{(q_1 + q_2 - p_{\bar{b}})^2 - m_b^2} \right] \\ & + 2 \ln \left(\frac{m_b^2}{m_b^2 - s_{23}} \right) \ln \left(\frac{m_b^2}{\sigma} \right) - \ln^2 \left(\frac{m_b^2}{(q_1 + q_2 - p_{\bar{b}})^2 - m_b^2} \right) \\ & - 2 \text{Li}_2 \left(1 + \frac{(q_1 + q_2 - p_{\bar{b}})^2 - m_b^2}{m_b^2 - s_{23}} \right) + \frac{\pi^2}{3} \end{aligned} \right\}. \quad (\text{C.14})$$

2. $D0(q_1, -q_1 + p_b + p_{\bar{b}}, -p_{\bar{b}}; 0, 0, 0, m_b)$, one on-shell massless leg and two one-shell massive legs:

$$D0(q_1, -q_1 + p_b + p_{\bar{b}}, -p_{\bar{b}}; 0, 0, 0, m_b) = \frac{i}{16\pi^2} \mathcal{N}_b \frac{1}{s_{12}(s_{23} - m_b^2)} \left\{ \begin{aligned} & \frac{1}{2\epsilon^2} + \frac{1}{\epsilon} \left[\ln \left(\frac{m_b^2}{-s_{12}} \right) + \ln \left(\frac{m_b^2}{m_b^2 - s_{23}} \right) - \ln \left(\frac{m_b^2}{-M_2^2} \right) \right] \\ & \ln^2 \left(\frac{m_b^2}{-s_{12}} \right) - \ln^2 \left(\frac{-M_2^2}{m_b^2 - s_{23}} \right) + \frac{\pi^2}{2} \\ & + \ln \left(\frac{-M_2^2 + s_{12}}{m_b^2 - s_{23}} \right) \ln \left(\frac{(m_b^2)^2}{s_{12}^2} \right) - 2 \ln \left(1 - \frac{-s_{12}}{-M_2^2} \right) \ln \left(\frac{m_b^2}{m_b^2 - s_{23}} \right) \\ & + 2 \left[\ln \left(\frac{-M_2^2}{m_b^2 - s_{23}} \right) \ln \left(1 - \frac{-M_2^2(-s_{12} + m_b^2 - s_{23} + M_2^2)}{(m_b^2 - s_{23})(-s_{12})} \right) \right. \\ & - \ln \left(\frac{-M_2^2}{m_b^2 - s_{23}} \right) \ln \left(\frac{-M_2^2 - m_b^2 + s_{23}}{-M_2^2} \right) + \ln \left(\frac{-M_2^2 + s_{12}}{m_b^2 - s_{23}} \right) \ln \left(1 - \frac{m_b^2 - s_{23}}{-M_2^2 + s_{12}} \right) \\ & - \text{Li}_2 \left(1 - \frac{m_b^2 - s_{23}}{-M_2^2 + s_{12}} \right) - \text{Li}_2 \left(1 - \frac{-M_2^2 + s_{12}}{m_b^2 - s_{23}} \right) - \text{Li}_2 \left(1 - \frac{-M_2^2 - m_b^2 + s_{23}}{-s_{12}} \right) \\ & \left. + \text{Li}_2 \left(\frac{-M_2^2(-s_{12} + m_b^2 - s_{23} + M_2^2)}{(m_b^2 - s_{23})(-s_{12})} \right) - \text{Li}_2 \left(\frac{m_b^2 - s_{23}}{-M_2^2 + s_{12}} \right) + \text{Li}_2 \left(\frac{m_b^2 - s_{23}}{-M_2^2} \right) \right] \end{aligned} \right\}, \quad (\text{C.15})$$

where we have defined the mass square of the second leg as $M_2^2 = (-q_1 + p_b + p_{\bar{b}})^2$.

3. $D0(q_1, -q_1 - q_2 + p_b + p_{\bar{b}}, q_2 - p_{\bar{b}}; 0, 0, 0, m_b)^3$, one on-shell massless leg and one one-shell massive leg:

$$\begin{aligned}
D0(q_1, -q_1 - q_2 + p_b + p_{\bar{b}}, q_2 - p_{\bar{b}}; 0, 0, 0, m_b) = & \frac{i}{16\pi^2} \mathcal{N}_b \frac{1}{s_{12}(s_{23} - m_b^2)} \left\{ \right. \\
& \frac{1}{2\epsilon^2} + \frac{1}{\epsilon} \left[\ln \left(\frac{m_b^2}{-s_{12}} \right) + \ln \left(\frac{m_b^2}{m_b^2 - s_{23}} \right) - \ln \left(\frac{m_b^2}{M_2^2} \right) \right] \\
& + \ln^2 \left(\frac{-s_{12}}{m_b^2} \right) + \ln^2 \left(\frac{m_b^2 - s_{23}}{m_b^2} \right) - \ln^2 \left(\frac{M_2^2}{m_b^2} \right) + \frac{4}{3}\pi^2 \\
& + 2 \ln \left(\frac{M_2^2}{m_b^2} \right) \ln \left(\frac{(-s_{12} + M_2^2)(m_b^2 - s_{23} + M_2^2)}{s_{12}(s_{23} - m_b^2)} \right) - 2 \ln \left(\frac{m_b^2 - s_{23}}{m_b^2} \right) \ln \left(-\frac{m_b^2 - s_{23} + M_2^2}{s_{12}} \right) \\
& + 2 \ln \left(-\frac{s_{12}}{m_b^2} \right) \ln \left(\frac{-s_{12} + M_2^2}{m_b^2 - s_{23}} \right) + \ln \left(\frac{m_b^2 - M_3^2}{m_b^2} \right) \ln \left(-\frac{M_2^2 M_3^2}{-m_b^2 M_2^2 - (s_{23} - m_b^2)(M_3^2 - m_b^2)} \right) \\
& + 2 \text{Li}_2 \left(1 - \frac{(-s_{12} + M_2^2)(m_b^2 - s_{23} + M_2^2)}{s_{12}(s_{23} - m_b^2)} \right) - 2 \text{Li}_2 \left(1 - \frac{m_b^2 - s_{23} + M_2^2}{s_{12}} \right) \\
& - 2 \text{Li}_2 \left(1 + \frac{-s_{12} + M_2^2}{m_b^2 - s_{23}} \right) - \text{Li}_2 \left(1 - \frac{s_{23} - m_b^2}{M_2^2} \right) \\
& - \text{Li}_2 \left(1 - \frac{(m_b^2 - s_{23})M_3^2}{-m_b^2 M_2^2 - (s_{23} - m_b^2)(M_3^2 - m_b^2)} \right) + \text{Li}_2 \left(1 - \frac{M_2^2 M_3^2}{m_b^2 M_2^2 + (s_{23} - m_b^2)(M_3^2 - m_b^2)} \right) \\
& - \text{Li}_2 \left(1 - \frac{(-M_2^2 + s_{12})M_3^2}{m_b^2(-M_2^2 + s_{12}) - (s_{23} - m_b^2)(M_3^2 - m_b^2)} \right) + \text{Li}_2 \left(1 - \frac{m_b^2 - M_3^2}{m_b^2} \right) \\
& + \text{Li}_2 \left(1 + \frac{(-s_{12} + M_2^2)M_3^2}{m_b^2(-M_2^2 + s_{12}) - (s_{23} - m_b^2)(M_3^2 - m_b^2)} \right) \left. \right\}, \tag{C.16}
\end{aligned}$$

where we have defined $M_2^2 = (-q_1 - q_2 + p_b + p_{\bar{b}})^2$ and $M_3^2 = (q_2 - p_{\bar{b}})^2$.

³ During the completion of this manuscript a compilation of one-loop scalar integrals has appeared on <http://qcdloop.fnal.gov/>, written and maintained by R.K. Ellis. The box integrals presented in sections II.2 and II.3 of this Appendix are presented in there with one expression, corresponding to B_9 in their notation. We have compared analytically the pole structure and numerically the finite real part of our expressions II.2 and II.3 with the expression of B_9 , and we found perfect agreement. (See footnote 1 in this Appendix).

III. Two non-zero internal masses

1. $D0(q_1, -p_{\bar{b}}, q_2; 0, 0, m_b, m_b)$, two opposite on-shell massless legs and one on-shell massive leg:

$$\begin{aligned}
D0(q_1, -p_{\bar{b}}, q_2; 0, 0, m_b, m_b) = & \frac{i}{16\pi^2} \mathcal{N}_b \frac{1}{(s_{12} - m_b^2)(s_{23} - m_b^2)} \left\{ \right. \\
& \frac{1}{2\epsilon^2} + \frac{1}{\epsilon} \left[\ln \left(\frac{m_b^2}{m_b^2 - s_{23}} \right) + \ln \left(\frac{m_b^2}{m_b^2 - s_{12}} \right) - \ln \left(\frac{m_b^2}{(q_1 + q_2 - p_{\bar{b}})^2 - m_b^2} \right) \right] \\
& + \ln^2 \left(\frac{m_b^2 - s_{23}}{m_b^2} \right) + \ln^2 \left(\frac{m_b^2 - s_{12}}{m_b^2} \right) - \ln^2 \left(\frac{(q_1 + q_2 - p_{\bar{b}})^2 - m_b^2}{m_b^2} \right) + \frac{3}{2} \pi^2 \\
& + 2 \ln \left(\frac{-s_{23} + (q_1 + q_2 - p_{\bar{b}})^2}{m_b^2 - s_{12}} \right) \ln \left(\frac{m_b^2 - s_{12}}{m_b^2 - s_{23} - s_{12} + (q_1 + q_2 - p_{\bar{b}})^2} \right) \\
& + 2 \ln \left(\frac{-s_{12} + (q_1 + q_2 - p_{\bar{b}})^2}{m_b^2 - s_{23}} \right) \ln \left(\frac{m_b^2 - s_{23}}{m_b^2 - s_{23} - s_{12} + (q_1 + q_2 - p_{\bar{b}})^2} \right) \\
& - 2 \text{Li}_2 \left(\frac{m_b^2 - s_{23} - s_{12} + (q_1 + q_2 - p_{\bar{b}})^2}{m_b^2 - s_{12}} \right) \\
& - 2 \text{Li}_2 \left(\frac{m_b^2 - s_{23} - s_{12} + (q_1 + q_2 - p_{\bar{b}})^2}{m_b^2 - s_{23}} \right) \\
& \left. - 2 \text{Li}_2 \left(\frac{(-s_{23} + (q_1 + q_2 - p_{\bar{b}})^2)(-s_{12} + (q_1 + q_2 - p_{\bar{b}})^2)}{(m_b^2 - s_{23})(m_b^2 - s_{12})} \right) \right\}.
\end{aligned} \tag{C.17}$$

2. $D0(q_1, -p_{\bar{b}}, -q_1 + p_b + p_{\bar{b}}; 0, 0, m_b, m_b)$, one on-shell massless legs and two opposite on-shell massive legs:

$$\begin{aligned}
D0(q_1, -p_{\bar{b}}, -q_1 + p_b + p_{\bar{b}}; 0, 0, m_b, m_b) = & \frac{i}{16\pi^2} \mathcal{N}_b \frac{1}{(s_{12} - m_b^2)(s_{23} - m_b^2)} \left\{ \right. \\
& \frac{1}{\epsilon^2} + \frac{1}{\epsilon} \left[\ln \left(\frac{m_b^2}{m_b^2 - s_{12}} \right) + \ln \left(\frac{m_b^2}{m_b^2 - s_{23}} \right) \right] + \left[\ln^2 \left(\frac{m_b^2}{m_b^2 - s_{12}} \right) + \ln^2 \left(\frac{m_b^2}{m_b^2 - s_{23}} \right) \right. \\
& \left. + \ln^2 \left(\frac{m_b^2 - s_{12}}{m_b^2 - s_{23}} \right) - \frac{2\pi^2}{3} + 2\text{Li}_2 \left(\frac{1}{z_+} \right) + 2\text{Li}_2 \left(\frac{1}{z_-} \right) \right] \left. \right\},
\end{aligned} \tag{C.18}$$

with

$$z_{\pm} = \frac{1}{2} \left(1 \pm \sqrt{1 - \frac{4 m_b^2}{(-q_1 + p_b + p_{\bar{b}})^2}} \right).$$

3. $D0(q_2, -p_{\bar{b}}, -q_1 - q_2 + p_b + p_{\bar{b}}; 0, 0, m_b, m_b)$, one on-shell massless leg and one on-shell massive leg:

$$\begin{aligned}
D0(q_2, -p_{\bar{b}}, -q_1 - q_2 + p_b + p_{\bar{b}}; 0, 0, m_b, m_b) = & \frac{i}{16\pi^2} \mathcal{N}_b \frac{1}{(s_{12} - m_b^2)(s_{23} - m_b^2)} \left\{ \right. \\
& \frac{1}{2\epsilon^2} + \frac{1}{\epsilon} \left[\ln \left(\frac{m_b^2}{m_b^2 - s_{12}} \right) + \ln \left(\frac{m_b^2}{s_{23} - m_b^2} \right) - \ln \left(\frac{m_b^2}{m_b^2 - M_4^2} \right) \right] \\
& + Re \left[-\frac{5}{6} \pi^2 + \ln^2 \left(\frac{s_{23} - m_b^2}{m_b^2} \right) + \ln^2 \left(\frac{m_b^2 - s_{12}}{m_b^2} \right) - \ln^2 \left(\frac{m_b^2 - M_4^2}{m_b^2} \right) \right. \\
& + 2 \ln \left(\frac{s_{23} - M_4^2}{m_b^2 - s_{12}} \right) \ln \left(\frac{m_b^2 - M_4^2}{s_{23} - m_b^2} \right) + 2 \ln \left(\frac{-s_{12} + M_4^2}{s_{23} - m_b^2} \right) \ln \left(\frac{m_b^2 - M_4^2}{m_b^2 - s_{12}} \right) \\
& - 2 \text{Li}_2 \left(\frac{-s_{12} + M_4^2 - s_{23} + m_b^2}{m_b^2 - s_{12}} \right) - 2 \text{Li}_2 \left(\frac{s_{23} - M_4^2 - m_b^2 + s_{12}}{s_{23} - m_b^2} \right) \\
& \left. + 2 \text{Li}_2 \left(\frac{(m_b^2 - M_4^2)(s_{23} - M_4^2 - m_b^2 + s_{12})}{(s_{23} - m_b^2)(m_b^2 - s_{12})} \right) - I_0 \right] \left. \right\}, \tag{C.19}
\end{aligned}$$

where $M_4^2 = (q_1 - p_b)^2$ is the mass square of the fourth leg,

$$\begin{aligned}
I_0 = & \ln \left(\frac{m_b^2 - s_{12}}{m_b^2 - M_4^2} \right) \ln \left(\frac{M_3^2}{m_b^2} \right) + \left\{ -\text{Li}_2 \left(\frac{1}{\lambda_+} \right) \right. \\
& + \ln \left(\frac{m_b^2 - s_{12}}{m_b^2 - M_4^2} \right) \ln \left(\frac{-(m_b^2 - M_4^2) - \lambda_+(-s_{12} + M_4^2)}{-s_{12} + M_4^2} \right) \\
& - \text{Li}_2 \left(\frac{m_b^2 - s_{12}}{\lambda_+(-s_{12} + M_4^2) + m_b^2 - M_4^2} \right) + \text{Li}_2 \left(\frac{m_b^2 - M_4^2}{\lambda_+(-s_{12} + M_4^2) + m_b^2 - M_4^2} \right) \\
& \left. + (\lambda_+ \leftrightarrow \lambda_-) \right\}, \tag{C.20}
\end{aligned}$$

$M_3^2 = (-q_1 - q_2 + p_b + p_{\bar{b}})^2$ is the mass square of the third leg and

$$\lambda_{\pm} = \frac{1}{2} \left(1 \pm \sqrt{1 - \frac{4m_b^2}{M_3^2}} \right). \tag{C.21}$$

IV. Three non-zero internal masses

1. $D0(-p_b, q_2, -q_2 + p_b + p_{\bar{b}}; 0, m_b, m_b, m_b)$, One on-shell massless leg and two adjacent on-shell massive legs:

$$\begin{aligned}
D0(-p_b, q_2, -q_2 + p_b + p_{\bar{b}}; 0, m_b, m_b, m_b) = & \frac{i}{16\pi^2} \mathcal{N}_b \frac{1}{s_{23}(s_{12} - m_b^2)\beta} \left\{ \right. \\
& \frac{1}{\epsilon} \ln \left(\frac{1 - \beta}{1 + \beta} \right) - \left[(-2 \ln(\mathcal{X}_s) \ln(m_b^2/(m_b^2 - s_{12})) + 2 \ln(\mathcal{X}_s) \ln(1 - \mathcal{X}_s^2) \right. \\
& + \pi^2/2 + \text{Li}_2(\mathcal{X}_s \mathcal{X}_3) + \ln^2(\mathcal{X}_3) \\
& - 2 \left(\text{Li}_2(\mathcal{X}_s \mathcal{X}_3) + \ln(\mathcal{X}_s) \ln(1 - \mathcal{X}_s \mathcal{X}_3) + \ln(\mathcal{X}_3) \ln(1 - \mathcal{X}_s \mathcal{X}_3) \right) \\
& \left. \left. - 2 \left(\text{Li}_2(\mathcal{X}_s/\mathcal{X}_3) + \ln(\mathcal{X}_s) \ln(1 - \mathcal{X}_s/\mathcal{X}_3) - \ln(\mathcal{X}_3) \ln(1 - \mathcal{X}_s/\mathcal{X}_3) \right) \right] \right\}, \quad (\text{C.22})
\end{aligned}$$

where, using $M_3^2 = (-q_2 + p_b + p_{\bar{b}})^2$ the mass square of the third leg, we have defined:

$$\beta = \sqrt{1 - \frac{4 m_b^2}{s_{23}}},$$

$$\beta_3 = \sqrt{1 - \frac{4 m_b^2}{M_3^2}},$$

$$\mathcal{X}_s = \frac{1 - \beta}{1 + \beta},$$

and

$$\mathcal{X}_3 = \frac{1 - \beta_3}{1 + \beta_3}.$$

2. $D0(-p_b, -q_1 - q_2 + p_b + p_{\bar{b}}, q_1 + q_2; 0, m_b, m_b, m_b)$, Two adjacent on-shell massive legs:

$$\begin{aligned}
D0(-p_b, -q_1 - q_2 + p_b + p_{\bar{b}}, q_1 + q_2; 0, m_b, m_b, m_b) = \\
\frac{i}{16\pi^2} \mathcal{N}_b \frac{1}{(s_{12} - m_b^2)s_{23}\beta} \left\{ \frac{1}{\epsilon} \ln \left(\frac{1 - \beta}{1 + \beta} \right) + X_0 \right\}, \quad (\text{C.23})
\end{aligned}$$

where we have defined:

$$\beta = \sqrt{1 - \frac{4 m_b^2}{s_{23}}}.$$

Defining $M_2^2 = (-q_1 - q_2 + p_b + p_{\bar{b}})^2$, $M_3^2 = (q_1 + q_2)^2$,

$$\beta_2 = \sqrt{1 - \frac{4 m_b^2}{M_2^2}},$$

$$\beta_3 = \sqrt{1 - \frac{4 m_b^2}{M_3^2}},$$

$$\mathcal{X}_s = \frac{1 - \beta}{1 + \beta},$$

$$\mathcal{X}_2 = \frac{1 - \beta_2}{1 + \beta_2},$$

and

$$\mathcal{X}_3 = \frac{1 - \beta_3}{1 + \beta_3},$$

we can express the finite piece X_0 as follows:

$$\begin{aligned} X_0 = & \frac{\mathcal{X}_s s_{23} \beta}{m_b^2 (1 - \mathcal{X}_s^2)} \left\{ \right. \\ & 2 \ln(\mathcal{X}_s) \ln(1 - \mathcal{X}_s^2) - 2 \ln(\mathcal{X}_s) \ln(m_b^2 / (m_b^2 - s_{12})) \\ & + \pi^2 / 2 + \text{Li}_2(\mathcal{X}_s^2) + \ln^2(\mathcal{X}_2) + \ln^2(\mathcal{X}_3) \\ & - \text{Li}_2(\mathcal{X}_s \mathcal{X}_2 \mathcal{X}_3) + \text{Li}_2(\mathcal{X}_s \mathcal{X}_2 / \mathcal{X}_3) + \text{Li}_2(\mathcal{X}_s \mathcal{X}_3 / \mathcal{X}_2) + \text{Li}_2(\mathcal{X}_s / \mathcal{X}_2 / \mathcal{X}_3) \\ & + \ln(1 - \mathcal{X}_s \mathcal{X}_2 \mathcal{X}_3) \ln(\mathcal{X}_s) + \ln(1 - \mathcal{X}_s \mathcal{X}_2 \mathcal{X}_3) \ln(\mathcal{X}_2) \\ & + \ln(1 - \mathcal{X}_s \mathcal{X}_2 \mathcal{X}_3) \ln(\mathcal{X}_3) + \ln(1 - \mathcal{X}_s \mathcal{X}_2 / \mathcal{X}_3) \ln(\mathcal{X}_s) \\ & + \ln(1 - \mathcal{X}_s \mathcal{X}_2 / \mathcal{X}_3) \ln(\mathcal{X}_2) + \ln(1 - \mathcal{X}_s \mathcal{X}_2 / \mathcal{X}_3) \ln(1 / \mathcal{X}_3) \\ & + \ln(1 - \mathcal{X}_s \mathcal{X}_3 / \mathcal{X}_2) \ln(\mathcal{X}_s) + \ln(1 - \mathcal{X}_s \mathcal{X}_3 / \mathcal{X}_2) \ln(1 / \mathcal{X}_2) \\ & + \ln(1 - \mathcal{X}_s \mathcal{X}_3 / \mathcal{X}_2) \ln(\mathcal{X}_3) + \ln(1 - \mathcal{X}_s / (\mathcal{X}_2 \mathcal{X}_3)) \ln(\mathcal{X}_s) \\ & \left. + \ln(1 - \mathcal{X}_s / (\mathcal{X}_2 \mathcal{X}_3)) \ln(1 / \mathcal{X}_2) + \ln(1 - \mathcal{X}_s / (\mathcal{X}_2 \mathcal{X}_3)) \ln(1 / \mathcal{X}_3) \right\}. \end{aligned} \tag{C.24}$$

Reduction of box and pentagon scalar integrals

An interesting property of m -point scalar integrals in $d = 4 - 2\epsilon$ dimensions is that they can be expressed as a linear combination of $(m - 1)$ -point scalar integrals in $d = 4 - 2\epsilon$ plus the

corresponding m -point scalar integral calculated in $d = 6 - 2\epsilon$ dimensions. This has been proved in Ref. [76] and is summarized in the following formula:

$$I_m = \frac{1}{2} \left[- \sum_{i=1}^m c_i I_{m-1}^{(i)} + (m - 5 + 2\epsilon) c_0 I_m^{(d=6-2\epsilon)} \right] , \quad (\text{C.25})$$

where the integral I_m on the left hand side corresponds to $(-1)^{m+1} I_0(q_1, \dots, q_{m-1}; m_0, \dots, m_{m-1})$, in the notation of Eq. (C.1), $I_m^{(d=6-2\epsilon)}$ denotes the same m -point integral calculated in $d = 6 - 2\epsilon$ dimension and $I_{m-1}^{(i)}$ correspond to the $(m-1)$ -point integrals obtained from I_m by taking out the i -th denominator and are calculated in $d = 4 - 2\epsilon$ dimensions.

The c_i ($i = 1, \dots, m$) coefficients in Eq. (C.25) are given by:

$$c_i = \sum_{j=1}^m S_{ij}^{-1} , \quad c_0 = \sum_{i=1}^m c_i = \sum_{i,j=1}^m S_{ij}^{-1} , \quad (\text{C.26})$$

where the matrix S_{ij} is built from invariants as:

$$S_{ij} = \frac{1}{2} (m_i^2 - m_j^2 - p_{ij}^2) . \quad (\text{C.27})$$

with $p_{ij}^2 = (q_i + \dots + q_j)^2$.

We have used Eq. (C.25) twice. First, using Eq. (C.25) we have cross checked our calculation of the IR-divergent box integrals II.2 and II.3 that did not exist in the literature. Second, we have used it to compute the pentagon scalar integrals. In the case of $E0$ -functions, Eq. (C.25) is particularly useful because the coefficients in front on $I_5^{(d=6-2\epsilon)}$ is of $\mathcal{O}(\epsilon)$ and therefore does not contribute (given that $I_5^{(d=6-2\epsilon)}$ is IR-finite). According to Eq. (C.25), $E0$ -functions are therefore calculated as the linear combination of five scalar integrals in $d = 4 - 2\epsilon$.

APPENDIX D

Reducing Tensor Feynman Integrals

At one-loop, Feynman diagrams with m external legs may contain Feynman tensor integrals with up to m denominators of the form:

$$In^{\mu_1 \dots \mu_n}(q_1, \dots, q_{m-1}, m_0, \dots, m_{m-1}) = \int \frac{d^d t}{(2\pi)^d} \frac{t^{\mu_1} \dots t^{\mu_n}}{[t^2 - m_0^2][(t + q_1)^2 - m_1^2] \dots [(t + q_1 + \dots + q_{m-1})^2 - m_{m-1}^2]} , \quad (\text{D.1})$$

which corresponds to the topology illustrated in Figure D.1. In Eq. (D.1) t is the loop momentum, $d = 4 - 2\epsilon$ is the dimension of the loop momentum integration, μ_1, \dots, μ_n are Lorentz indices associated to each power of loop momentum appearing in the numerator, $\{q_i\}$ ($i = 1, \dots, m$, $q_m = -\sum_{j=1}^{m-1} q_j$) is the set of incoming external momenta connected to the loop and $\{m_i\}$ ($i = 0, \dots, m-1$) is the set of masses associated with each propagator in the loop. The index “ n ” is associated with the rank of the tensor integral. As a short

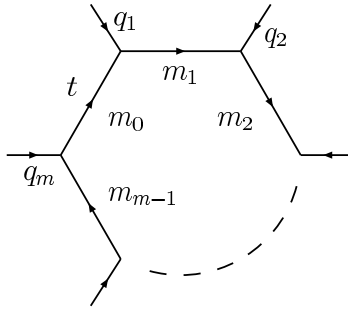


Figure D.1: Topology of one-loop Feynman Integrals. We denote by t the loop momentum, $\{q_i\}$ the set of incoming momenta and $\{m_i\}$ the set of masses in the internal propagators.

hand notation, depending on the number of denominators, or external momenta, we will write $I = A$ for one leg, $I = B$ for two legs, and so on. Integrals with no powers of loop momentum in the numerator are called “scalar” (see Appendix C) and are labelled by $n = 0$. So, for example, a scalar triangle integral will be denoted by $C0$, while a rank 4 box integral by $D4$.

One notices immediately that the tensor integral $In^{\mu_1 \dots \mu_n}$ is a symmetric tensor and it can be expressed as a linear combination of (symmetric) tensor Lorentz structures built from the external momenta $\{q_i\}$ and the metric tensor, $g^{\mu\nu}$, if the set $\{q_i\}$ is not complete. In this case (i.e. for $m \geq 5$) $g^{\mu\nu}$ can be expressed as a linear combination of momenta.

The coefficients of the Lorentz structures are rational functions of scalar integrals and invariants built from the external momenta $\{q_i\}$, the masses $\{m_i\}$ and the integration dimension d . For example, a straightforward computation of the $m = 2$, $n = 1$ tensor integral gives:

$$B1^\mu(q_1, m, m) = -\frac{1}{2}B0(q_1, m, m)q_1^\mu \equiv B^{(1)}(q_1, m, m)q_1^\mu, \quad (\text{D.2})$$

where we have defined the coefficient of the only Lorentz structure as $B^{(1)}(q_1, m, m) = -\frac{1}{2}B0(q_1, m, m)$.

The systematic reduction of tensor integrals to a linear combination of Lorentz structures is known as the Passarino-Veltman (PV) method [72], and consequently we will call the tensor integral coefficients In -PV functions, depending on the topology and rank of the integral. In the following we will write explicitly the tensor integrals we have encountered in our calculations and give an example of how they are recursively reduced (for a review see for example [73]).

Starting with 2-point integrals, we write (suppressing the arguments of the PV functions):

$$B1^\mu(q_1, m_0, m_1) = B^{(1)}q_1^\mu, \quad (\text{D.3})$$

$$B2^{\mu\nu}(q_1, m_0, m_1) = B^{(00)}g^{\mu\nu} + B^{(11)}q_1^\mu q_1^\nu. \quad (\text{D.4})$$

For 3-point integrals we write:

$$C1(q_1, q_2, m_0, m_1, m_2)^\mu = C^{(1)} q_1^\mu + C^{(2)} q_2^\mu, \quad (D.5)$$

$$C2(q_1, q_2, m_0, m_1, m_2)^{\mu\nu} = C^{(00)} g^{\mu\nu} + C^{(11)} q_1^\mu q_1^\nu + C^{(22)} q_2^\mu q_2^\nu \quad (D.6)$$

$$+ C^{(12)} (q_1^\mu q_2^\nu + q_1^\nu q_2^\mu), \quad (D.7)$$

$$\begin{aligned} C3(q_1, q_2, m_0, m_1, m_2)^{\mu\nu\rho} &= C^{(001)} (g^{\mu\nu} q_1^\rho + \text{perm}) + C^{(002)} (g^{\mu\nu} q_2^\rho + \text{perm}) \\ &+ C^{(111)} q_1^\mu q_1^\nu q_1^\rho + C^{(222)} q_2^\mu q_2^\nu q_2^\rho \\ &+ C^{(112)} (q_1^\mu q_1^\nu q_2^\rho + \text{perm}) + C^{(221)} (q_2^\mu q_2^\nu q_1^\rho + \text{perm}), \end{aligned} \quad (D.8)$$

where the term “perm” accounts for all terms, obtained from permutations of Lorentz indices, that are needed to obtain a symmetric tensor.

Finally for 4-point integrals we write:

$$D1(q_1, q_2, q_3, m_0, m_1, m_2, m_3)^\mu = D^{(1)} q_1^\mu + D^{(2)} q_2^\mu + D^{(3)} q_3^\mu, \quad (D.9)$$

$$\begin{aligned} D2(q_1, q_2, q_3, m_0, m_1, m_2, m_3)^{\mu\nu} &= D^{(00)} g^{\mu\nu} + D^{(11)} q_1^\mu q_1^\nu + D^{(22)} q_2^\mu q_2^\nu + D^{(33)} q_3^\mu q_3^\nu + \\ &D^{(12)} (q_1^\mu q_2^\nu + q_1^\nu q_2^\mu) + D^{(13)} (q_1^\mu q_3^\nu + q_1^\nu q_3^\mu) + \\ &D^{(23)} (q_2^\mu q_3^\nu + q_2^\nu q_3^\mu), \end{aligned} \quad (D.10)$$

$$\begin{aligned} D3(q_1, q_2, q_3, m_0, m_1, m_2, m_3)^{\mu\nu\rho} &= D^{(001)} (g^{\mu\nu} q_1^\rho + \text{perm}) + D^{(002)} (g^{\mu\nu} q_2^\rho + \text{perm}) + \\ &D^{(003)} (g^{\mu\nu} q_3^\rho + \text{perm}) + \\ &D^{(111)} q_1^\mu q_1^\nu q_1^\rho + D^{(222)} q_2^\mu q_2^\nu q_2^\rho + D^{(333)} q_3^\mu q_3^\nu q_3^\rho + \\ &D^{(112)} (q_1^\mu q_1^\nu q_2^\rho + \text{perm}) + D^{(113)} (q_1^\mu q_1^\nu q_3^\rho + \text{perm}) + \\ &D^{(221)} (q_2^\mu q_2^\nu q_1^\rho + \text{perm}) + D^{(223)} (q_2^\mu q_2^\nu q_3^\rho + \text{perm}) + \\ &D^{(331)} (q_3^\mu q_3^\nu q_1^\rho + \text{perm}) + D^{(332)} (q_3^\mu q_3^\nu q_2^\rho + \text{perm}) + \\ &D^{(123)} (q_1^\mu q_2^\nu q_3^\rho + \text{perm}), \end{aligned} \quad (D.11)$$

$$\begin{aligned}
D4(q_1, q_2, q_3, m_0, m_1, m_2, m_3)^{\mu\nu\rho\sigma} = & \\
& D^{(0000)}(g^{\mu\nu}g^{\rho\sigma} + \text{perm}) + \sum_{i \in \{1,2,3\}} D^{(00ii)}(g^{\mu\nu}q_i^\rho q_i^\sigma + \text{perm}) + \\
& \sum_{\substack{i,j \in \{1,2,3\} \\ i < j}} D^{(00ij)}(g^{\mu\nu}(q_i^\rho q_j^\sigma + q_j^\rho q_i^\sigma) + \text{perm}) + \sum_{i \in \{1,2,3\}} D^{(iiii)}(q_i^\mu q_i^\nu q_i^\rho q_i^\sigma) + \\
& \sum_{\substack{i,j \in \{1,2,3\} \\ i \neq j}} D^{(iiij)}(q_i^\mu q_i^\nu q_i^\rho q_j^\sigma + \text{perm}) + \sum_{\substack{i,j \in \{1,2,3\} \\ i < j}} D^{(iijj)}(q_i^\mu q_i^\nu q_j^\rho q_j^\sigma + \text{perm}) + \\
& \sum_{\substack{i,j,k \in \{1,2,3\} \\ i \neq j, k \neq i, j < k}} D^{(iijk)}(q_i^\mu q_i^\nu q_j^\rho q_k^\sigma + \text{perm}) . \tag{D.12}
\end{aligned}$$

Naturally, the calculation of pentagon diagrams (like the ones shown in Figures 2.6, 2.15 and 2.19) involves up to $E4$ -PV functions, but, as explained in Sections 2.2.2, 2.3.1 and 2.4.2, we have only used directly these functions for cross checks, due to the large numerical instabilities associated with them. Their structure can be easily inferred from previous PV functions, by just omitting terms with $g^{\mu\nu}$ tensors, and will not be presented here.

Expressions for the In -PV functions can be obtained recursively by saturating the tensor Lorentz indices of Eq. (D.1) and Eqs. (D.3)-(D.12) with the same external momentum or $g^{\mu\nu}$ tensor. Using relations like

$$t \cdot q_1 = \frac{1}{2} [(t + q_1)^2 - m_1^2] - (t^2 - m_0^2) - (q_1^2 + m_0^2 - m_1^2) , \tag{D.13}$$

allows one to simplify the loop momentum dependence in the numerator of Eq. (D.1) against some of the denominators, thereby relating higher rank m -point tensor integrals to lower rank and/or less external point ones.

Comparing the coefficients of the reduced tensor structures obtained by saturating Eq. (D.1) and the corresponding expressions in Eqs. (D.3)-(D.12) with the same external momentum or $g^{\mu\nu}$ tensor provides a set of equations that fully determines the coefficients of the tensor integrals represented in Eqs. (D.3)-(D.12).

Let us consider as an example the case of $D4^{\mu\nu\rho\sigma}$. The set of $D4$ -PV functions is one of the most demanding irreducible pieces that appear in the $W/Z \, b\bar{b}$ NLO QCD calculation (without taking into account the reducible E -PV functions). They are needed to account for the abelian contributions of the box diagrams $B_{1,t}^{(1,2,3)}$ to A_5^{ab} , shown in Table 2.5.

To write the set of equations that allow the expression of all 22 $D4$ -PV functions in terms of lower rank functions, let us denote by $\mathcal{I}_i^{(jkl)}$ the term proportional to the tensor structure

$q_j^\mu q_k^\nu q_l^\rho$ from the contraction of $D4^{\mu\nu\rho\sigma}$ in Eq. (D.1) with $q_{i\sigma}$ ($i, j, k, l = 1, 2, 3$), that is for example:

$$\mathcal{I}_3^{(112)} = \text{coefficient } q_1^\mu q_1^\nu q_2^\rho \text{ of in } D4^{\mu\nu\rho\sigma} q_{3\sigma} . \quad (\text{D.14})$$

We will denote by $\mathcal{I}_i^{(00k)}$ the coefficients of the structure $g^{\mu\nu} q_k^\rho$ obtained from the contraction of $D4^{\mu\nu\rho\sigma}$ with $q_{i\sigma}$.

More explicitly, here is what one obtains by contracting $D4^{\mu\nu\rho\sigma}$ of Eq. (D.1) with the external momenta q_i ($i = 1, 2, 3$):

$$\begin{aligned} D4^{\mu\nu\rho\sigma}(q_1, q_2, q_3, m_0, m_1, m_2, m_3) q_{1\sigma} = & \frac{1}{2} \left[\right. \\ & C3^{\mu\nu\rho}(q_1 + q_2, q_3, m_0, m_2, m_3) - C3^{\mu\nu\rho}(q_2, q_3, m_1, m_2, m_3) \\ & + q_1^\mu C2^{\nu\rho}(q_2, q_3, m_1, m_2, m_3) + q_1^\nu C2^{\mu\rho}(q_2, q_3, m_1, m_2, m_3) + q_1^\rho C2^{\mu\nu}(q_2, q_3, m_1, m_2, m_3) \\ & - q_1^\mu q_1^\nu C1^\rho(q_2, q_3, m_1, m_2, m_3) - q_1^\mu q_1^\rho C1^\nu(q_2, q_3, m_1, m_2, m_3) \\ & - q_1^\rho q_1^\nu C1^\mu(q_2, q_3, m_1, m_2, m_3) \\ & \left. + q_1^\mu q_1^\nu q_1^\rho C0(q_2, q_3, m_1, m_2, m_3) - (q_1 \cdot q_1 + m_0^2 - m_1^2) D3^{\mu\nu\rho}(q_1, q_2, q_3, m_0, m_1, m_2, m_3) \right] . \end{aligned} \quad (\text{D.15})$$

$$\begin{aligned} D4^{\mu\nu\rho\sigma}(q_1, q_2, q_3, m_0, m_1, m_2, m_3) q_{2\sigma} = & \frac{1}{2} \left[\right. \\ & C3^{\mu\nu\rho}(q_1, q_2 + q_3, m_0, m_1, m_3) - C3^{\mu\nu\rho}(q_1 + q_2, q_3, m_0, m_2, m_3) \\ & \left. - (q_2 \cdot q_2 + 2q_2 \cdot q_1 + m_1^2 - m_2^2) D3^{\mu\nu\rho}(q_1, q_2, q_3, m_0, m_1, m_2, m_3) \right] . \end{aligned} \quad (\text{D.16})$$

$$\begin{aligned} D4^{\mu\nu\rho\sigma}(q_1, q_2, q_3, m_0, m_1, m_2, m_3) q_{3\sigma} = & \frac{1}{2} \left[\right. \\ & C3^{\mu\nu\rho}(q_1, q_2, m_0, m_1, m_2) - C3^{\mu\nu\rho}(q_1, q_2 + q_3, m_0, m_1, m_3) \\ & \left. - (q_3 \cdot q_3 + 2q_3 \cdot (q_1 + q_2) + m_2^2 - m_3^2) D3^{\mu\nu\rho}(q_1, q_2, q_3, m_0, m_1, m_2, m_3) \right] , \end{aligned} \quad (\text{D.17})$$

where all the m -point tensor integrals used are defined in Eq. (D.1). Expressing the Dn and Cn tensor integrals in Eqs. (D.15)-(D.17) using Eqs. (D.5)-(D.11), one reduces them to linear combinations of symmetric tensor structures with three Lorentz, built of external momenta and the metric tensor, whose coefficients are precisely the $\mathcal{I}_i^{(jkl)}$ defined before Eq. (D.14).

Eqs. (D.15)-(D.17) in this form have them to be compared to the expressions obtained from Eq. (D.12) when contracting $D4^{\mu\nu\rho\sigma}$ in there with $q_{i\sigma}$ ($i = 1, 2, 3$). The result of the

comparison can be cast into the following matrix formula:

$$\begin{aligned}
& \begin{pmatrix} q_1^2 & q_1 \cdot q_2 & q_1 \cdot q_3 \\ q_1 \cdot q_2 & q_2^2 & q_2 \cdot q_3 \\ q_1 \cdot q_3 & q_2 \cdot q_3 & q_3^2 \end{pmatrix} \times \\
& \begin{pmatrix} D^{(0011)} & D^{(0012)} & D^{(0013)} & D^{(1111)} & D^{(2221)} & D^{(3331)} & D^{(1112)} & D^{(1113)} & D^{(1122)} & D^{(2213)} & D^{(1133)} \\ D^{(0012)} & D^{(0022)} & D^{(0023)} & D^{(1112)} & D^{(2222)} & D^{(3332)} & D^{(1122)} & D^{(1122)} & D^{(2221)} & D^{(2223)} & D^{(3312)} \\ D^{(0013)} & D^{(0023)} & D^{(0033)} & D^{(1113)} & D^{(2223)} & D^{(3333)} & D^{(1123)} & D^{(1123)} & D^{(2213)} & D^{(2233)} & D^{(3331)} \end{pmatrix} \\
& = \begin{pmatrix} \mathcal{I}_1^{(001)} - D^{(0000)} & \mathcal{I}_2^{(001)} & \mathcal{I}_3^{(001)} & \mathcal{I}_1^{(111)} - 3D^{(0011)} \\ \mathcal{I}_1^{(002)} & \mathcal{I}_2^{(002)} - D^{(0000)} & \mathcal{I}_3^{(002)} & \mathcal{I}_1^{(222)} \\ \mathcal{I}_1^{(003)} & \mathcal{I}_2^{(003)} & \mathcal{I}_3^{(003)} - D^{(0000)} & \mathcal{I}_1^{(333)} \\ \\ \mathcal{I}_2^{(111)} & \mathcal{I}_3^{(111)} & \mathcal{I}_1^{(112)} - 2D^{(0012)} & \mathcal{I}_1^{(113)} - 2D^{(0013)} \\ \mathcal{I}_2^{(222)} - 3D^{(0022)} & \mathcal{I}_3^{(222)} & \mathcal{I}_2^{(112)} - D^{(0011)} & \mathcal{I}_2^{(113)} \\ \mathcal{I}_2^{(333)} & \mathcal{I}_3^{(333)} - 3D^{(0033)} & \mathcal{I}_3^{(112)} & \mathcal{I}_3^{(113)} - D^{(0011)} \\ \\ \mathcal{I}_1^{(221)} - D^{(0022)} & \mathcal{I}_1^{(223)} & \mathcal{I}_1^{(331)} - D^{(0033)} \\ \mathcal{I}_2^{(221)} - 2D^{(0012)} & \mathcal{I}_2^{(223)} - 2D^{(0023)} & \mathcal{I}_2^{(331)} \\ \mathcal{I}_3^{(221)} & \mathcal{I}_3^{(223)} - D^{(0022)} & \mathcal{I}_3^{(331)} - 2D^{(0013)} \end{pmatrix}, \tag{D.18}
\end{aligned}$$

where $\mathcal{I}_i^{(jkl)}$ is defined before Eq. (D.14). The solution of this equation determines almost all 22 $D4$ -PV coefficients in terms of lower-rank, lower-point PV functions. More accurately, Eq. (D.18) can be solved for all the coefficients $D^{(ijkl)}$, except for $D^{(0000)}$. In fact, all other coefficients will depend on it. To solve completely all $D4$ -PV functions, we need then another relation for $D^{(0000)}$. This relation can be obtained by contracting $D4^{\mu\nu\rho\sigma}$ with $g_{\rho\sigma}$ and applying a relation like Eq. (D.13). The result is:

$$\begin{aligned}
& D4^{\mu\nu\rho\sigma}(q_1, q_2, q_3, m_0, m_1, m_2, m_3) g_{\rho\sigma} = \\
& C2^{\mu\nu}(q_2, q_3, m_1, m_2, m_3) - q_1^\mu C1^\nu(q_2, q_3, m_1, m_2, m_3) - q_1^\nu C1^\mu(q_2, q_3, m_1, m_2, m_3) \\
& + q_1^\mu q_1^\nu C0(q_2, q_3, m_1, m_2, m_3) \\
& + m_0^2 D2^{\mu\nu}(q_1, q_2, q_3, m_0, m_1, m_2, m_3). \tag{D.19}
\end{aligned}$$

Notice that all terms on the RHS of the previous equation depend on Cm -PV functions ($m < 4$), and $D2$ -PV functions. From this relation one then obtains the desired relation for

$D^{(0000)}$, namely:

$$\sum_i q_i \cdot q_i D^{(00ii)} + \sum_{i < j} 2q_i \cdot q_j D^{(00ij)} + D^{(0000)}(d+2) = C^{(00)}(q_2, q_3, m_1, m_2, m_3) + m_0^2 D^{(00)}, \quad (\text{D.20})$$

after which all the 22 $D4$ -PV functions are determined in terms of lower rank and lower point PV functions, kinematic invariants built from the external momenta and internal masses as well as the dimension of the momentum space d .

When the same procedure is repeated for all the PV functions, one ends up with a full reduction to scalar integrals and rational functions depending on the external momenta, the internal masses and the dimension d .

Finally, it is evident from Eq. (D.18) how the Gram determinants (GDs) that we discussed extensively in Section 2.4.2, appear in the PV-reductions. The GD for 4-point functions is indeed the determinant of the first matrix on the LHS of Eq. (D.18). The solution of Eq. (D.18) involves at least one inverse power of it for each coefficient $D^{(ijkl)}$. Even two powers can appear in those cases when some entries of the RHS depend on $D^{(00ij)}$ ($i, j = 0, 1, 2, 3$). So at least one power of GD appears in the reduction of $D4$ -PV functions to $D3$ -PV functions and other lower rank and lower point coefficients. By the time they are completely reduced to scalar integrals, the $D^{(ijkl)}$ tensor integral coefficients will contain at least four power of the 4-point GD.

APPENDIX E

Using Quadruple Unitarity Cuts to Check Coefficients of Scalar Box Integrals

In this Appendix we review a set of non-trivial cross checks performed on pieces of our calculation of NLO QCD corrections to $W/Z \, b\bar{b}$ production including full b -quark mass effects. By using generalized unitarity cuts, specifically quadruple cuts as presented by Britto, Cachazo and Feng (BCF) [23], we have been able to check results for the coefficients of scalar box integrals, which we have computed analytically using Passarino-Veltman (PV) reduction (see Appendix D).

The Calculation

We show now explicit results for the quadruple cut involving a top loop, which contributes to the virtual corrections to the subprocess $gg \rightarrow Zb\bar{b}$ (see Section 2.4.3) shown in Figure E.1, with the kinematics:

$$g(q_1)g(q_2) \rightarrow Z(p_z)b(p_b)\bar{b}(p_{\bar{b}}), \quad q_1^2 = q_2^2 = p_b^2 - m_b^2 = p_{\bar{b}}^2 - m_b^2 = p_z^2 - M_Z^2 = 0. \quad (\text{E.1})$$

This quadruple cut has the feature that only the $B_{1,t}^{(1)}$ Feynman diagrams with a top loop (see Figure 2.18) contribute to it, that is all pentagon diagrams in the subprocess vanish under the cut. We notice that this box topology is of particular interest because it involves the most intricate irreducible tensor integrals of the computation, namely $D4$ -PV functions, as described in Appendix D.

To extract coefficient $d_{1,t}^{(1)}$ of the scalar box $B_{1,t}^{(1)}$, from the quadruple, we simply use a similar approach to the example given in Section 3 of Ref. [23]. We get, analogously to BCF's Eq. (3.1), the expression:

$$d_{1,t}^{(1)} = \sum_{\ell=\ell_{\pm}} (\ell^2 - m_t^2) ((\ell + q_1)^2 - m_t^2) ((\ell + q_1 + q_2)^2 - m_t^2) ((\ell + p_z)^2 - m_t^2) B_{1,t}^{(1)} \Big|_{\ell}, \quad (\text{E.2})$$

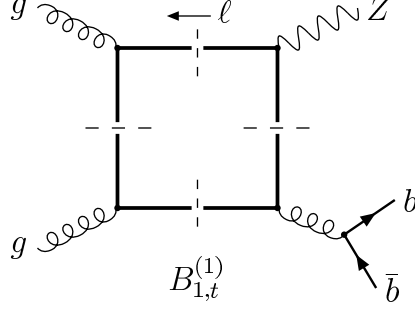


Figure E.1: Topology of the example presented. It corresponds to two Feynman Diagrams given by the two possible orientations of the fermion line. The loop in the fermion is a top quark (with mass m_t).

where ℓ_{\pm} corresponds to the two solutions of the on-shell conditions:

$$\{\ell \mid \ell^2 = m_t^2, \quad (\ell + q_1)^2 = m_t^2, \quad (\ell + q_1 + q_2)^2 = m_t^2, \quad (\ell + p_z)^2 = m_t^2\} \quad , \quad (\text{E.3})$$

which we solve (following BCF [23]) by using the parametrization:

$$\ell = \alpha q_1 + \beta q_2 + \sigma p_z + \rho P_4 \quad , \quad P_4^\mu = \epsilon^{\mu\nu\rho\sigma} q_{1\nu} q_{2\rho} p_{z\sigma} \quad . \quad (\text{E.4})$$

The term $B_{1,t}^{(1)}|_{\ell}$ in the RHS of Eq. (E.2) corresponds to the expression of the Feynman diagrams where the loop integral is frozen, i.e. the one obtained by substituting the loop momentum with the solutions $\ell = \ell_{\pm}$. We show the solutions to the on-shell conditions in Eq. (E.3) in the following subsection.

We have compared analytically both results for the box coefficient $d_{1,t}^{(1)}$, from our standard computation and from the generalized unitarity technique, and they agree. We do not write such expressions, as they are quite cumbersome and not too illuminating.

We have performed similar checks for other coefficients of scalar boxes. In general, we have calculated, using PV reduction, all diagrams in such way that all tensor integrals are reduced to a set of 1-, 2-, 3- and 4-point scalar integrals. So we can actually extract tadpole, bubble, triangle and box coefficients, as well as rational functions, from any given set of Feynman diagrams. They can be used as a playground for on-shell one-loop techniques like, for example, the ones discussed in Ref. [2].

Solutions to on-shell conditions

Here we write explicitly the solutions to the on-shell conditions in Eq. (E.3), by using the parametrization shown in Eq. (E.4). One obtains a set of four quadratic equations for α , β , σ and ρ which can be solved straightforwardly. The two solutions ℓ_{\pm} are given by:

$$\begin{aligned}
\alpha &= -\frac{1}{2} \left(v_{23}^2 + 2v_{13}v_{23} + 2v_{14}v_{23} + 2v_{24}v_{23} - v_{23}v_{12} - v_{23}v_{34} - v_{23}m_b^2 + 2v_{13}v_{24} \right. \\
&\quad \left. - v_{24}v_{34} - v_{12}m_b^2 + v_{24}^2 + 2v_{14}v_{24} - v_{24}m_b^2 - v_{12}v_{34} - v_{24}v_{12} \right) / \Delta, \\
\beta &= \frac{1}{2} \frac{(v_{24} + v_{23} - m_b^2 - v_{34})(v_{12} - v_{13} - v_{14})}{\Delta}, \\
\sigma &= -\frac{1}{2} v_{12} \frac{(v_{24} + v_{23} - m_b^2 - v_{34})}{\Delta}, \\
\rho &= \pm \frac{1}{2} \frac{\delta}{\Delta},
\end{aligned} \tag{E.5}$$

for the two possible signs in the ρ expression. We have defined:

$$\begin{aligned}
\delta &= \left[\left(v_{12}v_{23}^2 + 2v_{23}m_t^2v_{13} - 2v_{23}v_{12}v_{34} + 2v_{23}m_t^2v_{14} - 2v_{23}v_{12}m_b^2 + 2v_{23}v_{24}v_{12} \right. \right. \\
&\quad \left. \left. + 2m_t^2v_{24}v_{13} - 2m_t^2v_{12}v_{34} - 2v_{24}v_{12}m_b^2 - 2m_t^2v_{12}m_b^2 + v_{12}v_{24}^2 - 2v_{24}v_{12}v_{34} \right. \right. \\
&\quad \left. \left. + 2v_{12}m_b^2v_{34} + v_{12}m_b^4 + v_{12}v_{34}^2 + 2m_t^2v_{14}v_{24} \right) / v_{12} \right]^{\frac{1}{2}},
\end{aligned} \tag{E.6}$$

and

$$\Delta = P_4 \cdot P_4 = v_{13}v_{23} + v_{13}v_{24} + v_{14}v_{23} - v_{12}m_b^2 - v_{12}v_{34} + v_{14}v_{24}, \tag{E.7}$$

which corresponds to the Gram determinant of the process. The invariants v_{ij} are defined as $v_{ij} = q_i \cdot q_j$, with q_1 and q_2 as in Eq. (E.1), $q_3 = p_b$ and $q_4 = p_{\bar{b}}$.

We mention that the box coefficient in Eq. (E.2) depends only on even powers of ρ , giving then a solution which is a rational function of invariants as expected.

APPENDIX F

Phase Space Integrals for the Emission of a Soft Gluon in the two Cutoff PSS Method

Phase space soft integrals for $q\bar{q}'$ initiated W/Z $b\bar{b}$ production

In this appendix we collect the integrals which we have used in calculating the results in Eq. (2.36) starting from Eq. (2.34). For a more exhaustive treatment of the formalism used we refer to Refs. [79, 89], from which the results in this appendix have been taken.

We parameterize the soft gluon d -momentum in the $q\bar{q}'$ rest frame as:

$$k = E_g(1, \dots, \sin \theta_1 \sin \theta_2, \sin \theta_1 \cos \theta_2, \cos \theta_1) \ , \quad (\text{F.1})$$

such that the phase space of the soft gluon in $d=4-2\epsilon$ dimensions can be written as:

$$\begin{aligned} d(PS_g)_{soft} &= \frac{\Gamma(1-\epsilon)}{\Gamma(1-2\epsilon)} \frac{\pi^\epsilon}{(2\pi)^3} \int_0^{\delta_s \sqrt{s}/2} dE_g E_g^{1-2\epsilon} \times \\ &\quad \int_0^\pi d\theta_1 \sin^{1-2\epsilon} \theta_1 \int_0^\pi d\theta_2 \sin^{-2\epsilon} \theta_2 \ . \end{aligned} \quad (\text{F.2})$$

Then, all the integrals we need are of the form:

$$\begin{aligned} I_n^{(k,l)} &= \int_0^\pi d\theta_1 \sin^{d-3} \theta_1 \int_0^\pi d\theta_2 \sin^{d-4} \theta_2 \times \\ &\quad \frac{(a + b \cos \theta_1)^{-k}}{(A + B \cos \theta_1 + C \sin \theta_1 \cos \theta_2)^l} \ . \end{aligned} \quad (\text{F.3})$$

In particular we need the following four cases. When $A^2 \neq B^2 + C^2$, and $b = -a$, we use

(dropping terms of order $\mathcal{O}((d-4)^2)$):

$$\begin{aligned}
I_n^{(1,1)} &= \frac{\pi}{a(A+B)} \left\{ \frac{2}{d-4} + \ln \left[\frac{(A+B)^2}{A^2 - B^2 - C^2} \right] \right. \\
&+ \frac{1}{2}(d-4) \left[\ln^2 \left(\frac{A - \sqrt{B^2 + C^2}}{A+B} \right) \right. \\
&- \frac{1}{2} \ln^2 \left(\frac{A + \sqrt{B^2 + C^2}}{A - \sqrt{B^2 + C^2}} \right) \\
&+ 2 \text{Li}_2 \left(-\frac{B + \sqrt{B^2 + C^2}}{A - \sqrt{B^2 + C^2}} \right) \\
&- \left. \left. 2 \text{Li}_2 \left(\frac{B - \sqrt{B^2 + C^2}}{A+B} \right) \right] \right\} , \tag{F.4}
\end{aligned}$$

while when $b \neq -a$ we use:

$$\begin{aligned}
I_n^{(0,1)} &= \frac{\pi}{\sqrt{B^2 + C^2}} \left\{ \ln \left(\frac{A + \sqrt{B^2 + C^2}}{A - \sqrt{B^2 + C^2}} \right) \right. \\
&- (d-4) \left[\text{Li}_2 \left(\frac{2\sqrt{B^2 + C^2}}{A + \sqrt{B^2 + C^2}} \right) \right. \\
&+ \left. \left. \frac{1}{4} \ln^2 \left(\frac{A + \sqrt{B^2 + C^2}}{A - \sqrt{B^2 + C^2}} \right) \right] \right\} , \tag{F.5}
\end{aligned}$$

$$\begin{aligned}
I_n^{(0,2)} &= \frac{2\pi}{A^2 - B^2 - C^2} \times \\
&\left[1 - \frac{1}{2}(d-4) \frac{A}{\sqrt{B^2 + C^2}} \ln \left(\frac{A + \sqrt{B^2 + C^2}}{A - \sqrt{B^2 + C^2}} \right) \right] . \tag{F.6}
\end{aligned}$$

Finally, when $A^2 = B^2 + C^2$, and $b = -a$, we have:

$$\begin{aligned}
I_n^{(1,1)} &= 2\pi \frac{1}{aA} \frac{1}{d-4} \left(\frac{A+B}{2A} \right)^{d/2-3} \times \\
&\left[1 + \frac{1}{4}(d-4)^2 \text{Li}_2 \left(\frac{A-B}{2A} \right) \right] . \tag{F.7}
\end{aligned}$$

Phase space soft integrals for $gg \rightarrow Zb\bar{b}$

In this Appendix we collect the phase space integrals for a final state soft gluon that are used in calculating the results reported in Eqs. (2.81) and (2.84). We parameterize the soft

gluon d -momentum in the gg rest frame as shown in Eq. (F.1). We have seen that the phase space of the soft gluon in $d=4-2\epsilon$ dimensions can be written as in Eq. (F.2).

Then all the integrals we need are the following four:

$$\begin{aligned}
\int d(P S_g)_{soft} \frac{(q_1 \cdot q_2)}{(q_1 \cdot k)(q_2 \cdot k)} &= \frac{1}{(4\pi)^2} \mathcal{N}_b 2 \left[\frac{1}{\epsilon^2} - \frac{2}{\epsilon} \ln(\delta_s) - \frac{1}{\epsilon} \Lambda_s \right. \\
&\quad \left. - \frac{\pi^2}{3} + \frac{1}{2} (\Lambda_s^2 + 4\Lambda_s \ln(\delta_s) + 4 \ln^2(\delta_s)) \right] , \\
\int d(P S_g)_{soft} \frac{(q_1 \cdot p_b)}{(q_1 \cdot k)(p_b \cdot k)} &= \frac{1}{(4\pi)^2} \mathcal{N}_b \left[\frac{1}{\epsilon^2} - \frac{2}{\epsilon} \Lambda_{\tau_1} - \frac{2}{\epsilon} \ln(\delta_s) - \frac{\pi^2}{3} \right. \\
&\quad \left. - \frac{1}{2} \Lambda_s^2 + 2\Lambda_{\tau_1} \Lambda_s + 2 \ln^2(\delta_s) + 4\Lambda_{\tau_1} \ln(\delta_s) + F(q_1, p_b) \right] , \\
\int d(P S_g)_{soft} \frac{(p_b \cdot \bar{p}_b)}{(p_b \cdot k)(\bar{p}_b \cdot k)} &= \frac{1}{(4\pi)^2} \mathcal{N}_b \left(\frac{\bar{s}_{b\bar{b}} - 2m_b^2}{\bar{s}_{b\bar{b}}} \right) \left[\left(-\frac{2}{\epsilon} + 2\Lambda_s + 4 \ln(\delta_s) \right) \frac{1}{\beta_{b\bar{b}}} \Lambda_{b\bar{b}} \right. \\
&\quad \left. - \frac{1}{\beta_{b\bar{b}}} \Lambda_{b\bar{b}}^2 - \frac{4}{\beta_{b\bar{b}}} \text{Li}_2 \left(\frac{2\beta_{b\bar{b}}}{1 + \beta_{b\bar{b}}} \right) \right] , \\
\int d(P S_g)_{soft} \frac{p_b^2}{(p_b \cdot k)^2} &= \frac{1}{(4\pi)^2} \mathcal{N}_b \left[-\frac{2}{\epsilon} + 2\Lambda_s + 4 \ln(\delta_s) - 2 \frac{1}{\beta_{b\bar{b}}} \Lambda_{b\bar{b}} \right] , \tag{F.8}
\end{aligned}$$

where we have used the set of kinematic invariants in Eq. (2.23), $\beta_{b\bar{b}}$ and $\Lambda_{b\bar{b}}$ are defined in Eq. (2.26), Λ_s and Λ_{τ_i} after Eq. (2.86) and \mathcal{N}_b in Eq. (2.19). Moreover we have denoted by $F(p_i, p_f)$ the function:

$$\begin{aligned}
F(p_i, p_f) &= \ln^2 \left(\frac{1 - \beta_f}{1 - \beta_f \cos \theta_{if}} \right) - \frac{1}{2} \ln^2 \left(\frac{1 + \beta_f}{1 - \beta_f} \right) \\
&\quad + 2\text{Li}_2 \left(-\frac{\beta_f(1 - \cos \theta_{if})}{1 - \beta_f} \right) - 2\text{Li}_2 \left(-\frac{\beta_f(1 + \cos \theta_{if})}{1 - \beta_f \cos \theta_{if}} \right) , \tag{F.9}
\end{aligned}$$

where θ_{if} is the angle between partons i and f in the center-of-mass frame of the initial state partons, and

$$\beta_f = \sqrt{1 - \frac{m_b^2}{(p_f^0)^2}} , \quad 1 - \beta_f \cos \theta_{if} = \frac{s_{if}}{p_f^0 \sqrt{s}} . \tag{F.10}$$

All the quantities in Eq. (F.9) can be expressed in terms of kinematical invariants, once we use $s_{if} = 2p_i \cdot p_f$ and:

$$p_b^0 = \frac{s - \bar{s}_{bV} + m_b^2}{2\sqrt{s}} \quad \text{and} \quad p_{\bar{b}}^0 = \frac{s - \bar{s}_{bV} + m_b^2}{2\sqrt{s}} , \tag{F.11}$$

with $\bar{s}_{fV} = (p_f + p_V)^2$ ($V = Z$).

REFERENCES

- [1] W. M. Yao et al. Review of particle physics. *J. Phys.*, G33:1–1232, 2006.
- [2] Zvi Bern, Lance J. Dixon, and David A. Kosower. On-Shell Methods in Perturbative QCD. *Annals Phys.*, 322:1587–1634, 2007, arXiv:0704.2798 [hep-ph].
- [3] H. Murayama, I. Watanabe, and K. Hagiwara. HELAS: HELicity amplitude subroutines for Feynman diagram evaluations. 1992. KEK-91-11.
- [4] T. Stelzer and W. F. Long. Automatic generation of tree level helicity amplitudes. *Comput. Phys. Commun.*, 81:357–371, 1994, hep-ph/9401258.
- [5] Fabio Maltoni and Tim Stelzer. MadEvent: Automatic event generation with MadGraph. *JHEP*, 02:027, 2003, hep-ph/0208156.
- [6] A. Pukhov et al. Comphep: A package for evaluation of feynman diagrams and integration over multi-particle phase space. user’s manual for version 33. 1999, hep-ph/9908288.
- [7] F. Krauss, R. Kuhn, and G. Soff. AMEGIC++ 1.0: A matrix element generator in C++. *JHEP*, 02:044, 2002, hep-ph/0109036.
- [8] Stephen J. Parke and T. R. Taylor. An Amplitude for n Gluon Scattering. *Phys. Rev. Lett.*, 56:2459, 1986.
- [9] Frits A. Berends and W. T. Giele. Recursive Calculations for Processes with n Gluons. *Nucl. Phys.*, B306:759, 1988.
- [10] Lance J. Dixon. Calculating scattering amplitudes efficiently. 1996, hep-ph/9601359.
- [11] Edward Witten. Perturbative gauge theory as a string theory in twistor space. *Commun. Math. Phys.*, 252:189–258, 2004, hep-th/0312171.
- [12] Zvi Bern, Lance J. Dixon, and David A. Kosower. Progress in one-loop QCD computations. *Ann. Rev. Nucl. Part. Sci.*, 46:109–148, 1996, hep-ph/9602280.
- [13] Carola F. Berger. Bootstrapping one-loop QCD amplitudes. *AIP Conf. Proc.*, 903:157–160, 2007, hep-ph/0608027.
- [14] Zvi Bern, Lance J. Dixon, David C. Dunbar, and David A. Kosower. One loop n point gauge theory amplitudes, unitarity and collinear limits. *Nucl. Phys.*, B425:217–260, 1994, hep-ph/9403226.

- [15] Zvi Bern, Lance J. Dixon, David C. Dunbar, and David A. Kosower. Fusing gauge theory tree amplitudes into loop amplitudes. *Nucl. Phys.*, B435:59–101, 1995, hep-ph/9409265.
- [16] Steven J. Bidder, N. E. J. Bjerrum-Bohr, Lance J. Dixon, and David C. Dunbar. $N = 1$ supersymmetric one-loop amplitudes and the holomorphic anomaly of unitarity cuts. *Phys. Lett.*, B606:189–201, 2005, hep-th/0410296.
- [17] Steven J. Bidder, N. E. J. Bjerrum-Bohr, David C. Dunbar, and Warren B. Perkins. One-loop gluon scattering amplitudes in theories with $N \leq 4$ supersymmetries. *Phys. Lett.*, B612:75–88, 2005, hep-th/0502028.
- [18] Ruth Britto, Evgeny Buchbinder, Freddy Cachazo, and Bo Feng. One-loop amplitudes of gluons in SQCD. *Phys. Rev.*, D72:065012, 2005, hep-ph/0503132.
- [19] Ruth Britto, Bo Feng, and Pierpaolo Mastrolia. The cut-constructible part of QCD amplitudes. *Phys. Rev.*, D73:105004, 2006, hep-ph/0602178.
- [20] Carola F. Berger, Zvi Bern, Lance J. Dixon, Darren Forde, and David A. Kosower. Bootstrapping one-loop QCD amplitudes with general helicities. *Phys. Rev.*, D74:036009, 2006, hep-ph/0604195.
- [21] Carola F. Berger, Zvi Bern, Lance J. Dixon, Darren Forde, and David A. Kosower. All one-loop maximally helicity violating gluonic amplitudes in QCD. *Phys. Rev.*, D75:016006, 2007, hep-ph/0607014.
- [22] Zhiguang Xiao, Gang Yang, and Chuan-Jie Zhu. The rational part of QCD amplitude. III: The six-gluon. *Nucl. Phys.*, B758:53–89, 2006, hep-ph/0607017.
- [23] Ruth Britto, Freddy Cachazo, and Bo Feng. Generalized unitarity and one-loop amplitudes in $N = 4$ super-Yang-Mills. *Nucl. Phys.*, B725:275–305, 2005, hep-th/0412103.
- [24] A. Abulencia et al. Search for $H \rightarrow b \text{ anti-}b$ produced in association with W bosons in $p \text{ anti-}p$ collisions at $\sqrt{s} = 1.96\text{-TeV}$. *Phys. Rev. Lett.*, 96:081803, 2006, hep-ex/0512051.
- [25] CDF Note 8240. Search for Standard Model Higgs boson production in association with W boson at CDF with 695 pb^{-1} . 2006.
- [26] V. M. Abazov et al. A search for $W b \text{ anti-}b$ and $W H$ production in $p \text{ anti-}p$ collisions at $\sqrt{s} = 1.96\text{-TeV}$. *Phys. Rev. Lett.*, 94:091802, 2005, hep-ex/0410062.
- [27] $D0$ Notes 4896-CONF and 5054-CONF. A search for WH production at $\sqrt{s} = 1.96\text{-TeV}$. 2006.
- [28] A. Patwa. W and Z production and standard model Higgs search from the Fermilab Tevatron. 2006, hep-ex/0605082.

- [29] L. Sonnenschein. Talk given at HCP 2006, <http://hcp2006.phy.duke.edu>.
- [30] D. Acosta et al. Search for electroweak single top quark production in p anti-p collisions at $\sqrt{s} = 1.96$ -TeV. *Phys. Rev.*, D71:012005, 2005, hep-ex/0410058.
- [31] V. M. Abazov et al. Search for single top quark production in p anti-p collisions at $\sqrt{s} = 1.96$ -TeV. *Phys. Lett.*, B622:265–276, 2005, hep-ex/0505063.
- [32] A. Gresele. Search for single top production at the Tevatron. 2006, hep-ex/0605041.
- [33] Aran Garcia-Bellido. Evidence for single top quark production at D0. 2007, arXiv:0706.0037 [hep-ex].
- [34] V. M. Abazov et al. Evidence for production of single top quarks and first direct measurement of $\sigma(\text{tb})$. *Phys. Rev. Lett.*, 98:181802, 2007, hep-ex/0612052.
- [35] Tao Han and S. Willenbrock. QCD correction to the $p p \rightarrow W H$ and $Z H$ total cross-sections. *Phys. Lett.*, B273:167–172, 1991.
- [36] S. Mrenna and C. P. Yuan. Effects of QCD resummation on $W + h$ and t anti- b production at the Tevatron. *Phys. Lett.*, B416:200–207, 1998, hep-ph/9703224.
- [37] Oliver Brein, Abdelhak Djouadi, and Robert Harlander. NNLO QCD corrections to the Higgs-strahlung processes at hadron colliders. *Phys. Lett.*, B579:149–156, 2004, hep-ph/0307206.
- [38] M. L. Ciccolini, S. Dittmaier, and M. Krämer. Electroweak radiative corrections to associated $W H$ and $Z H$ production at hadron colliders. *Phys. Rev.*, D68:073003, 2003, hep-ph/0306234.
- [39] T. Stelzer, Z. Sullivan, and S. Willenbrock. Single-top-quark production via W -gluon fusion at next-to-leading order. *Phys. Rev.*, D56:5919–5927, 1997, hep-ph/9705398.
- [40] T. Stelzer, Z. Sullivan, and S. Willenbrock. Single top quark production at hadron colliders. *Phys. Rev.*, D58:094021, 1998, hep-ph/9807340.
- [41] Martin C. Smith and S. Willenbrock. QCD and Yukawa Corrections to Single-Top-Quark Production via $q \bar{q} \rightarrow t \bar{b}$. *Phys. Rev.*, D54:6696–6702, 1996, hep-ph/9604223.
- [42] B. W. Harris, E. Laenen, L. Phaf, Z. Sullivan, and S. Weinzierl. The fully differential single top quark cross section in next-to-leading order QCD. *Phys. Rev.*, D66:054024, 2002, hep-ph/0207055.
- [43] Zack Sullivan. Understanding single-top-quark production and jets at hadron colliders. *Phys. Rev.*, D70:114012, 2004, hep-ph/0408049.
- [44] Qing-Hong Cao and C. P. Yuan. Single top quark production and decay at next-to-leading order in hadron collision. *Phys. Rev.*, D71:054022, 2005, hep-ph/0408180.

- [45] Qing-Hong Cao, Reinhard Schwienhorst, and C. P. Yuan. Next-to-leading order corrections to single top quark production and decay at Tevatron. I: s-channel process. *Phys. Rev.*, D71:054023, 2005, hep-ph/0409040.
- [46] Qing-Hong Cao, Reinhard Schwienhorst, Jorge A. Benitez, Raymond Brock, and C. P. Yuan. Next-to-leading order corrections to single top quark production and decay at the tevatron. ii: t-channel process. *Phys. Rev.*, D72:094027, 2005, hep-ph/0504230.
- [47] Zack Sullivan. Angular correlations in single-top-quark and Wjj production at next-to-leading order. *Phys. Rev.*, D72:094034, 2005, hep-ph/0510224.
- [48] M. Beccaria, G. Macorini, F. M. Renard, and C. Verzegnassi. Single top production in the t-channel at LHC: A realistic test of electroweak models. 2006, hep-ph/0605108.
- [49] J. Campbell and R.K. Ellis. webpage: mcfm.fnal.gov.
- [50] R. K. Ellis and Sinisa Veseli. Strong radiative corrections to Wb anti- b production in p anti- p collisions. *Phys. Rev.*, D60:011501, 1999, hep-ph/9810489.
- [51] John M. Campbell and R. K. Ellis. Radiative corrections to Zb anti- b production. *Phys. Rev.*, D62:114012, 2000, hep-ph/0006304.
- [52] John Campbell and R. K. Ellis. Next-to-leading order corrections to $W + 2\text{jet}$ and $Z + 2\text{jet}$ production at hadron colliders. *Phys. Rev.*, D65:113007, 2002, hep-ph/0202176.
- [53] Zvi Bern, Lance J. Dixon, David A. Kosower, and Stefan Weinzierl. One-loop amplitudes for $e^+e^- \rightarrow \text{anti-}q\,q\,\text{anti-}Q\,Q$. *Nucl. Phys.*, B489:3–23, 1997, hep-ph/9610370.
- [54] Zvi Bern, Lance J. Dixon, and David A. Kosower. One-loop amplitudes for e^+e^- to four partons. *Nucl. Phys.*, B513:3–86, 1998, hep-ph/9708239.
- [55] J. A. M. Vermaseren. New features of FORM. 2000, math-ph/0010025.
- [56] Matthias Jamin and Markus E. Lautenbacher. TRACER: Version 1.1: A Mathematica package for gamma algebra in arbitrary dimensions. *Comput. Phys. Commun.*, 74:265–288, 1993.
- [57] G. J. van Oldenborgh. FF: A Package to evaluate one loop Feynman diagrams. *Comput. Phys. Commun.*, 66:1–15, 1991.
- [58] J. A. M. Vermaseren. Axodraw. *Comput. Phys. Commun.*, 83:45–58, 1994.
- [59] See the webpage: <http://feyndiagram.com/>.
- [60] See the webpage: <http://plasma-gate.weizmann.ac.il/Grace/>.
- [61] Richard P. Feynman. Very high-energy collisions of hadrons. *Phys. Rev. Lett.*, 23:1415–1417, 1969.

- [62] R. P. Feynman. Photon-hadron interactions. Reading 1972, 282p.
- [63] Michael E. Peskin and D. V. Schroeder. An Introduction to quantum field theory. Reading, USA: Addison-Wesley (1995) 842 p.
- [64] Steven Weinberg. The quantum theory of fields. Vol. 2: Modern applications. Cambridge, UK: Univ. Pr. (1996) 489 p.
- [65] John C. Collins, Davison E. Soper, and George Sterman. Factorization of Hard Processes in QCD. *Adv. Ser. Direct. High Energy Phys.*, 5:1–91, 1988, hep-ph/0409313.
- [66] John Collins and Jian-Wei Qiu. $k(t)$ factorization is violated in production of high-transverse-momentum particles in hadron-hadron collisions. *Phys. Rev.*, D75:114014, 2007, arXiv:0705.2141 [hep-ph].
- [67] John Collins. 2-soft-gluon exchange and factorization breaking. 2007, arXiv:0708.4410 [hep-ph].
- [68] George Sterman. Partons, factorization and resummation. 1995, hep-ph/9606312.
- [69] Davison E. Soper. Basics of QCD perturbation theory. 1996, hep-ph/9702203.
- [70] W. K. Tung. Perturbative QCD and the parton structure of the nucleon. In *Shifman, M. (ed.): At the frontier of particle physics, vol. 2* 887-971.
- [71] G. Peter Lepage. A New Algorithm for Adaptive Multidimensional Integration. *J. Comput. Phys.*, 27:192, 1978.
- [72] G. Passarino and M. J. G. Veltman. One Loop Corrections for $e^+ e^-$ Annihilation Into $\mu^+ \mu^-$ in the Weinberg Model. *Nucl. Phys.*, B160:151, 1979.
- [73] A. Denner. Techniques for calculation of electroweak radiative corrections at the one loop level and results for w physics at lep-200. *Fortsch. Phys.*, 41:307–420, 1993.
- [74] Giovanni Ossola, Costas G. Papadopoulos, and Roberto Pittau. Reducing full one-loop amplitudes to scalar integrals at the integrand level. *Nucl. Phys.*, B763:147–169, 2007, hep-ph/0609007.
- [75] S. A. Larin. The Renormalization of the axial anomaly in dimensional regularization. *Phys. Lett.*, B303:113–118, 1993, hep-ph/9302240.
- [76] Zvi Bern, Lance J. Dixon, and David A. Kosower. Dimensionally regulated one loop integrals. *Phys. Lett.*, B302:299–308, 1993, hep-ph/9212308.
- [77] Zvi Bern, Lance J. Dixon, and David A. Kosower. Dimensionally regulated pentagon integrals. *Nucl. Phys.*, B412:751–816, 1994, hep-ph/9306240.
- [78] Lewis J. Bergmann. NEXT-TO-LEADING LOG QCD CALCULATION OF SYMMETRIC DIHADRON PRODUCTION. UMI-89-15738.

- [79] B. W. Harris and J. F. Owens. The two cutoff phase space slicing method. *Phys. Rev.*, D65:094032, 2002, hep-ph/0102128.
- [80] L. Reina, S. Dawson, and D. Wackeroth. QCD corrections to associated t anti- t h production at the Tevatron. *Phys. Rev.*, D65:053017, 2002, hep-ph/0109066.
- [81] S. Dawson, C. Jackson, L. H. Orr, L. Reina, and D. Wackeroth. Associated Higgs production with top quarks at the Large Hadron Collider: NLO QCD corrections. *Phys. Rev.*, D68:034022, 2003, hep-ph/0305087.
- [82] W. Beenakker et al. Higgs radiation off top quarks at the Tevatron and the LHC. *Phys. Rev. Lett.*, 87:201805, 2001, hep-ph/0107081.
- [83] W. Beenakker et al. NLO QCD corrections to t anti- t H production in hadron collisions. ((U)). *Nucl. Phys.*, B653:151–203, 2003, hep-ph/0211352.
- [84] F. Febres Cordero, L. Reina, and D. Wackeroth. NLO QCD corrections to W boson production with a massive b - quark jet pair at the Tevatron p anti- p collider. *Phys. Rev.*, D74:034007, 2006, hep-ph/0606102.
- [85] John C. Collins, Frank Wilczek, and A. Zee. Low-Energy Manifestations of Heavy Particles: Application to the Neutral Current. *Phys. Rev.*, D18:242, 1978.
- [86] F. Bloch and A. Nordsieck. Note on the radiation field of the electron. *Phys. Rev.*, 52(2):54–59, Jul 1937.
- [87] T. Kinoshita. Mass singularities of Feynman amplitudes. *J. Math. Phys.*, 3:650–677, 1962.
- [88] T. D. Lee and M. Nauenberg. Degenerate Systems and Mass Singularities. *Phys. Rev.*, 133:B1549–B1562, 1964.
- [89] W. Beenakker, H. Kuijf, W. L. van Neerven, and J. Smith. QCD Corrections to Heavy Quark Production in p anti- p Collisions. *Phys. Rev.*, D40:54–82, 1989.
- [90] L. Lewin. Dilogarithms and Associated Functions. MacDonald, London, 1958.
- [91] U. Baur, S. Keller, and D. Wackeroth. Electroweak radiative corrections to W boson production in hadronic collisions. *Phys. Rev.*, D59:013002, 1999, hep-ph/9807417.
- [92] F. Febres Cordero, L. Reina, and D. Wackeroth. NLO QCD corrections to Z b anti- b production with massive bottom quarks at the Fermilab Tevatron. 2008, 0806.0808.
- [93] J. Pumplin et al. New generation of parton distributions with uncertainties from global QCD analysis. *JHEP*, 07:012, 2002, hep-ph/0201195.
- [94] S. Catani, Yuri L. Dokshitzer, and B. R. Webber. The K -perpendicular clustering algorithm for jets in deep inelastic scattering and hadron collisions. *Phys. Lett.*, B285:291–299, 1992.

- [95] S. Catani, Yuri L. Dokshitzer, M. H. Seymour, and B. R. Webber. Longitudinally invariant $K(t)$ clustering algorithms for hadron hadron collisions. *Nucl. Phys.*, B406:187–224, 1993.
- [96] Stephen D. Ellis and Davison E. Soper. Successive combination jet algorithm for hadron collisions. *Phys. Rev.*, D48:3160–3166, 1993, hep-ph/9305266.
- [97] William B. Kilgore and W. T. Giele. Next-to-leading order gluonic three jet production at hadron colliders. *Phys. Rev.*, D55:7183–7190, 1997, hep-ph/9610433.
- [98] J. Campbell et al. Associated Production of a W Boson and One b Jet. 2008, 0809.3003.
- [99] F. Englert and R. Brout. Broken symmetry and the mass of gauge vector mesons. *Phys. Rev. Lett.*, 13(9):321, 1964.
- [100] Peter W. Higgs. Broken symmetries and the masses of gauge bosons. *Phys. Rev. Lett.*, 13(16):508, 1964.
- [101] G. S. Guralnik, C. R. Hagen, and T. W. B. Kibble. GLOBAL CONSERVATION LAWS AND MASSLESS PARTICLES. *Phys. Rev. Lett.*, 13:585–587, 1964.
- [102] T. W. B. Kibble. Symmetry breaking in non-Abelian gauge theories. *Phys. Rev.*, 155:1554–1561, 1967.
- [103] W. Beenakker and Ansgar Denner. INFRARED DIVERGENT SCALAR BOX INTEGRALS WITH APPLICATIONS IN THE ELECTROWEAK STANDARD MODEL. *Nucl. Phys.*, B338:349–370, 1990.
- [104] Carlo Oleari. Next-to-leading-order corrections to the production of heavy-flavour jets in $e^+ e^-$ collisions. 1997, hep-ph/9802431.
- [105] R. Keith Ellis and Giulia Zanderighi. Scalar one-loop integrals for QCD. *JHEP*, 02:002, 2008, 0712.1851.